

University of Southampton Research Repository

Copyright © and Moral Rights for this thesis and, where applicable, any accompanying data are retained by the author and/or other copyright owners. A copy can be downloaded for personal non-commercial research or study, without prior permission or charge. This thesis and the accompanying data cannot be reproduced or quoted extensively from without first obtaining permission in writing from the copyright holder/s. The content of the thesis and accompanying research data (where applicable) must not be changed in any way or sold commercially in any format or medium without the formal permission of the copyright holder/s.

When referring to this thesis and any accompanying data, full bibliographic details must be given, e.g.

Thesis: Author (Year of Submission) "Full thesis title", University of Southampton, name of the University Faculty or School or Department, PhD Thesis, pagination.

Data: Author (Year) Title. URI [dataset]

University of Southampton

Faculty of Engineering and Physical Sciences

School of Engineering and School of Chemistry

Development of Silver Nanomaterials as Spectrally Selective Absorbers

by

Bilal Amin Mughal

ORCID ID <u>0009-0009-6527-2764</u>

Thesis for the degree of Doctor of Philosophy

April 2025

University of Southampton

Abstract

Faculty of Engineering and Physical Sciences

Thesis for the degree of Doctor of Philosophy

Development of Silver Nanomaterials as Spectrally Selective Absorbers

by

Bilal Amin Mughal

This research presents a novel approach to the synthesis and characterisation of silver nanoparticles (AgNPs), with a specific focus on anisotropic silver nanorods (AgNRs). Unlike previous studies that primarily concentrated on batch synthesis methods, this work pioneers the integration of continuous flow synthesis for scalable, controlled production of AgNRs. The continuous flow method ensures improved reproducibility, scalability, and control over reaction conditions, addressing major challenges in batch synthesis. This research also introduces innovative reactor designs, including 3D-printed continuous flow reactors, demonstrating their efficiency in producing AgNRs with aspect ratios tailored for near-infrared (NIR) absorption.

A key contribution of this thesis is the systematic optimisation of synthesis parameters to achieve enhanced control over the size, shape, and optical properties of AgNRs. This optimisation fine-tunes the aspect ratio of AgNRs to ensure NIR absorption, which is critical for applications such as stealth technology and photonic devices. The research also establishes strong correlations between synthesis conditions and localised surface plasmon resonance (LSPR), leading to precise optical performance.

Furthermore, the thesis advances the application of AgNRs by successfully integrating them into polymer matrices. The development of a silver-polymer nanocomposite was achieved by embedding AgNRs within a polymethyl methacrylate (PMMA) matrix, enhancing the composite's optical properties. These nanocomposites exhibit enhanced NIR absorption, positioning them as potential candidates for infrared shielding materials, solar energy harvesting, and stealth technology.

The findings contribute to the field of nanomaterials by demonstrating the effectiveness of continuous flow synthesis in producing functionalised AgNRs for industrial applications. Future research is recommended to focus on the further improvement of flow process and functionalisation of AgNRs and refining the polymer nanocomposite technology for enhanced performance in optical and related applications. The potential for scaling up the continuous flow synthesis for silver nanoparticle production are also discussed as crucial steps towards sustainable development in nanotechnology.

Table of Contents

Abstract	iii
List of Figures	xi
List of Tables	xviii
List of Equations	XX
Research Thesis: Declaration of Authorship	xxi
Acknowledgements	xxiii
Definitions and Abbreviations	XXV
Chapter 1 Introduction	1
1.1 Background	1
1.2 Anisotropic nanoparticles	4
1.3 Motivation	7
1.4 Aim & objectives	9
Chapter 2 Background and Literature Review	11
2.1 Light properties	11
2.2 Localised surface plasmon resonance	13
2.3 Synthesis of silver nanoparticles	18
2.3.1 Top-down & bottom-up methods	18
2.3.2 Chemical methods	19
2.3.3 Physical methods	33
2.3.4 Biological methods	36
2.3.5 Continuous flow synthesis of silver nanoparticles	38
2.3.6 Summary	43
2.4 Applications	44
2.4.1 Antibacterial applications	44
2.4.2 Applications in catalysis	46
2.4.3 Applications in bioconjugation	47

2.4.4 Photothermal applications	48
2.4.5 Cancer cell imaging	50
2.4.6 Surface-enhanced Raman scattering (SERS) substrate	51
2.4.7 Hydrophobic surfaces	52
2.4.8 Infrared absorbent material	53
2.5 Stealth	53
2.5.1 Active stealth	54
2.5.2 Passive stealth	54
2.5.3 Threat detectors	55
2.5.4 Summary	57
2.6 Conclusions	58
Chapter 3 Batch Synthesis of Silver Nanoparticles	60
3.1 Introduction	60
3.2 Synthesis of silver nanoparticles	60
3.2.1 Chemicals	60
3.2.2 General seed-mediated synthesis procedure	61
Preparation of seed particles	61
Procedure of silver nanorod growth	62
3.2.3 Method 1 – Rekha method	63
3.2.4 Method 2 – Murphy method	64
3.2.5 Purification method	66
3.3 Characterisation	67
3.3.1 Optical Spectrometry	67
3.3.2 Transmission Electron Microscopy	68
Batch synthesis results	69
3.4 Batch synthesis using method 1	69
3.4.1 Effects of silver nitrate added during seed particles formation	69

3.4.2 Effects of reducing agent during seed particles formation	75
3.4.3 Effects of silver nitrate added in growth solution	79
3.4.4 Effects of surfactant added in growth solution	81
3.4.5 Effects of ascorbic acid (AA) in growth solution	83
3.4.6 Effects of sodium hydroxide added in growth solution	84
3.4.7 Optimisation of reaction conditions in method 1	86
3.4.8 Stability testing	94
3.5 Batch synthesis using method 2	95
3.5.1 Influence of silver nitrate added in seed solution	95
3.5.2 Effects of silver nitrate added in growth solution	97
3.5.3 Effects of CTAB added in growth solution	99
3.5.4 Effects of ascorbic acid (AA) added in growth solution	101
3.5.5 Effects of sodium hydroxide added in growth solution	102
3.5.6 Trialling optimal parameters in method 2	104
3.6 Comparison of batch synthesis methods: method 1 vs method 2	108
3.7 Conclusions	109
Chapter 4 Flow Synthesis Experiments	112
Chapter overview	112
4.1 Justification of reactor design choices and iterative development strategy	112
4.2 Materials and reagent preparation steps used in all flow synthesis experiments	113
4.2.1 List of the components:	113
4.2.2 List of reagents used in all flow synthesis experiments	114
4.2.3 Flow synthesis steps	115
4.2.4 Flow regime in the flow reactors	116
4.2.5 Residence time and post-synthesis handling	117
4.3 Flow synthesis using design 1	117
4.3.1 Design 1 details	117

4.3.2 Flow rates for design 1	119
4.3.3 Results for design 1	120
4.3.4 Modification of flow synthesis using design 1	122
4.3.5 Modifying reagent concentrations for modified design 1 .	124
4.4 Flow synthesis using design 2	127
4.4.1 Design 2 details	127
4.4.2 Flow rates for design 2	128
4.4.3 Results for flow synthesis using design 2	129
4.4.4 Modified design 2 flow synthesis	130
4.4.5 Results for modified design 2 flow synthesis	131
4.5 Flow synthesis using design 3	133
4.5.1 Design 3 details	133
4.5.2 Flow rates for design 3	135
4.5.3 Design 3 flow synthesis results	135
4.5.4 Modifying design 3 parameters	136
4.5.5. Flow synthesis results for modified design 3	137
4.6 Flow synthesis using design 4	138
4.6.1 Flow rates for design 4	139
4.6.2 Results for design 4	140
4.6.3 Modifying reagent concentration in design 4 flow synthes	sis141
4.6.4 Results for modified design 4	142
4.7 Optimised flow synthesis experiments	145
4.7.1 Optimised synthesis using design 1	146
Comparison of optimised design 1 with batch Method 1	150
4.7.2 Optimised synthesis using design 4	151
Comparison of optimised design 4 with batch Method 1 at 0.1	mL seed volume154
4.8 Overall discussion	156

4.9 Conclusions	157
Chapter 5 Development of Silver/polymer Nanocomposite	159
5.1 Introduction to metal-polymer nanocomposites	159
5.2 Materials and methods	162
5.2.1 Materials	162
5.2.2 Synthesis of silver nanorods	163
5.2.3 Coating of silver nanorods with silica	164
5.2.4 Development of AgNR@SiO ₂ /PMMA nanocomposite	165
5.2.5 Preparation of PDMS mould and nanocomposite film	167
5.3 Results and discussion	168
5.3.1 AgNR synthesis	168
5.3.2 AgNR coating with silica	169
5.3.3 AgNR@SiO ₂ -PMMA nanocomposite	171
5.3.4 AgNR@SiO ₂ -PMMA nanocomposite FTIR	172
5.3.5 Novelty and contribution of the work	176
5.4 Conclusions and future research directions	177
Chapter 6 Conclusions	180
Chapter 7 Future Recommendations	183
Appendix A Details of Flow Synthesis Designs	186
Publications and Presentations	192
References	194

List of Figures

Figure 1.1. Nanometre scale compared to some larger structures [4]
Figure 1.2. Number of publications with 'silver nanoparticles' in the article title, abstract or keywords (data obtained from scopus.com).
Figure 1.3. Schematic of localised surface plasmon resonance (LSPR) in a spherical metal particle [15,16]
Figure 1.4. (A) Colloidal AgNPs with different colours. (B) Absorption spectra of corresponding colloid [17]
Figure 1.5. Different morphologies of gold nanoparticles: A) nanocubes; B) branched nanoparticles; C) dodecahedral; D) nanoprisms; E) nanorods; F) nanostars [28]6
Figure 2.1. Interaction of light with an object
Figure 2.2. Schematic of localised surface plasmon resonance (LSPR). Coherent oscillations in the free electrons of the material may be induced by the oscillating electric field of the incident light [16]
Figure 2.3. Schematic illustration of LSPR excitation for nanorods and (b) LSPR absorption bands of nanorods: longitudinal and transverse plasmon bands [47]
Figure 2.4. Example UV-Vis-NIR absorption spectra for common silver nanoparticle morphologies. (a) yellow- 10nm spherical particles; orange- 35 nm long nanoprisms; violet-40 nm long nanoprisms; and blue- 64 nm long nanoprisms [49]. (b) black- 10 nm silver seed particles; pink- nanorods with aspect ratio 6; purple- nanorods with aspect ratio 11; and green-nanorods with aspect ratio 15 [48]
Figure 2.5. UV–vis absorption spectra and absorption shift of gold nanoparticles. (A) UV–vis absorption spectrum of the synthesised gold nanoparticles. (B) Shift in absorption λrps of gold nanoparticles with particle size [51].
Figure 2.6. Various synthesis routes of silver nanoparticles. (A) Top-down and bottom-up methods. (B) Physical synthesis method. (C) Chemical synthesis method. (D) Plausible synthesis mechanisms of green chemistry. [58]
Figure 2.7. Seed-mediated growth approach used by Murphy and co-workers to synthesise gold and silver nanorods. (bottom right) Transmission electron micrograph of gold nanorods that are an average of 500 nm long. [66]

Figure 2.8. Molecular structure of Hexadecyltrimethylammonium bromide (CTAB), a cationic
surfactant used in nanorod synthesis. [72]
Figure 2.9. Schematic representation of the polyol synthesis of Ag nanowires [79]25
Figure 2.10. Electrochemical growth of gold nanorods [87]27
Figure 2.11. Apparatus used for the microwave-assisted synthesis of metallic nanostructures [94]
Figure 2.12. Porous membrane-templated synthesis of gold nanorods. (a) schematic of gold deposition, template membrane formation and nanorod (b) SEM image of porous alumina membrane. (c) SEM image of free-standing array of gold nanorods [98]
Figure 2.13. List of various bacteria, fungi, plants and algae used to synthesise AgNPs [127]
Figure 2.14. Different-sized silver nanoparticles tested in diffusion disks against E. coli MTCC 443 strain [166]
Figure 2.15. (a) Silver nanoparticles attached to silica spheres. (b) The absorbance spectrum of the dyes decreases as the dyes are reduced. [175]
Figure 2.16. Schematic illustration of the protocol used to conjugate antibodies to the surface of Au nanocages. [181]
Figure 2.17. (A, B) SK-BR-3 breast cancer cells treated with immuno- Au nanocages, then irradiated with 810 nm light at a power density of 1.5 W/cm ² for 5 min. (C, D) SK-BR-3 cells irradiated under the same conditions but without immuno-Au nanocage treatment. [185]49
Figure 2.18. (A) Light scattering images of anti-EGFR/Au nanospheres; (B) Light scattering images of anti-EGFR/Au nanorods (C) Average extinction spectra of anti-EGFR/Au nanorods. [189]
Figure 2.19. Water droplets on the Ag dendritic film surface, Ni surface, and Cu surface. All surfaces were modified with n-dodecanethiol. [200]
Figure 2.20. Mid-wavelength infrared signature of a commercial aircraft showing engine emissions – vulnerable to IR- seeking missiles [208]
Figure 3.1. The Schematic illustration of the seed-mediated synthesis of silver nanorods. The seed solution includes silver nitrate (AgNO ₃), sodium borohydride (NaBH ₄), and CTAB. The growth solution comprises CTAB. AgNO ₃ , ascorbic acid (AA), NaOH, and seed solution. 61

Figure 3.2. Colloidal solution of Ag seeds
Figure 3.3. Ag nanorod solutions prepared using varied seed volume
Figure 3.4. Absorption spectra of silver nanorods prepared with different concentrations of seed particles: (a) 0.25 mL, (b) 0.125 mL, and (c) 0.1 mL The three spectra correspond to aspect ratios of (a) 6 ± 0.86 , (b) 11 ± 0.43 and (c) 15 ± 2.87 [48]
Figure 3.5. UV-vis spectra of silver nanorods: Effect of changing amount of seed. (1) = 2.0 mL, (2) = 1.0 mL, (3) = 0.5 mL, (4) = 0.25 mL, (5) = 0.125 mL and (6) = 0.06 mL of seed solution [64]
Figure 3.6. Perkin Elmer Lambda 750S UV-VIS-IR spectrophotometer
Figure 3.7. FEI Tecnai T12 transmission electron microscope
Figure 3.8. UV-Vis spectra of silver seed particles obtained at 1, 5, 10 and 20 mM of silver nitrate
Figure 3.9. TEM images of Ag nanoparticles synthesised at lowest and high AgNO3 concentrations: (A) 1 mM; (B) 20 mM
Figure 3.10. UV-Vis spectra of the final nanoparticle growth at different concentrations of silver nitrate in the seed solution. For each concentration, the seed amount was varied between 0.01 to 0.2 mL
Figure 3.11. TEM images of nanoparticles produced using different amount of AgNO3 in seed solution: (A) 1 mM AgNO3, 0.01 mL seed; (B) 5 mM AgNO3, 0.01 mL seed; (C) 10 mM AgNO3, 0.01 mL seed; (D) 20 mM AgNO3, 0.01 mL seed
Figure 3.12. UV-Vis spectra of silver seed particles obtained at 1, 5, 10 and 20 mM of sodium borohydride
Figure 3.13. TEM image of Ag nanoparticles synthesised at lowest and high sodium borohydride concentrations: (A) 1 mM; (B) 20 mM.
Figure 3.14. UV-Vis spectra of the final nanoparticle growth at different concentrations of sodium borohydride in the seed solution. For each concentration, the seed amount was varied between 0.01 to 0.2 mL
Figure 3.15. UV-Vis spectra of the final nanoparticle growth at different concentrations of AgNO3 in the growth solution. For each concentration, the seed amount was varied between 0.01 to 0.2 mL.

Figure 3.16. UV-Vis spectra of nanoparticles synthesised at different concentrations of CTAB
in the growth solution. For each concentration, the seed amount was varied between 0.01 to 0.2
mL83
Figure 3.17. UV-Vis spectra of nanoparticles synthesised at different concentrations of ascorbic
acid in the growth solution. For each concentration, the seed amount was varied between 0.01
to 0.2 mL84
Figure 3.18. UV-Vis spectra of nanoparticles synthesised at different concentrations of NaOH
in the growth solution. For each concentration, the seed amount was varied between 0.01 to 0.2 mL
Figure 3.19. Absorption spectra of nanoparticles synthesised using parameters in Trial 188
Figure 3.20. Absorption spectra of nanoparticles synthesised using parameters in Trial 289
Figure 3.21. TEM images of nanoparticles synthesised using parameters in Trial 2. (A) 0.01
mL seed sample; (B) 0.02 mL seed sample; (C) 0.1 mL seed sample; (D) 0.2 mL seed sample
89
Figure 3.22. Absorption spectra of nanoparticles synthesised using parameters in Trial 391
Figure 3.23. TEM images of nanoparticles synthesised using parameters in trial 3. (A) 0.01 mL
seed sample; (B) 0.02 mL seed sample; (C) 0.1 mL seed sample; (D) 0.2 mL seed sample92
Figure 3.24. UV-vis absorption spectra of nanoparticles measured 12 weeks apart94
Figure 3.25. UV-Vis spectra of silver seed particles obtained at 0.25, 0.50, 1.0 and 2.0 mM of
silver nitrate96
Figure 3.26. UV-Vis spectra of the final nanoparticle growth at different concentrations of
silver nitrate in the seed solution. For each concentration, the seed amount was varied between
0.025 to 0.5 mL
Figure 3.27. UV-Vis spectra of the final nanoparticle growth at different concentrations of
AgNO3 in the growth solution. For each concentration, the seed amount was varied between
0.05 to 1.0 mL
Figure 3.28. UV-Vis spectra of nanoparticles synthesised at different concentrations of CTAB
added in the growth solution. For each concentration, the seed amount was varied between 0.05
42 1 0 mJ

Figure 3.29. UV-Vis spectra of nanoparticles synthesised at different concentrations of ascorbic
acid in the growth solution. For each concentration, the seed amount was varied between 0.05
to 1.0 mL
Figure 3.30. UV-Vis spectra of nanoparticles synthesised at different concentrations of NaOH
in the growth solution. For each concentration, the seed amount was varied between 0.05 to 1.0
mL
Figure 3.31. Absorption spectra of nanoparticles synthesised using optimal parameters in
Method 2
Figure 3.32. TEM images of nanoparticles synthesised using parameters in Method 2. (A) &
(B) 0.01 mL seed sample; (C) 0.05 mL seed sample; (D) 0.2 mL seed sample106
Figure 4.1. Flow synthesis apparatus for silver nanorods utilising syringe pumps, y-type
fittings, and PTFE tubing118
Figure 4.2. Absorption spectra for D1_2 and D1_3120
Figure 4.3. TEM images of nanoparticles produced using design 1 : (A) D1_2; (B) D1_3121
Figure 4.4. Schematic of modified design 1 for synthesis of silver nanorods
Figure 4.5. Absorption spectra for D1_5 and D1_6123
Figure 4.6. Absorption spectra for D1_8, D1_9 and D1_10
Figure 4.7. TEM images of nanoparticles produced using modified design 1 : (A) D1_9; (B)
D1_10126
Figure 4.8. Flow synthesis apparatus for silver nanorods utilising syringe pumps, t-type fittings,
and PTFE tubing
Figure 4.9. Absorption spectra for D2_1, and D2_2129
Figure 4.10. Schematic of modified design 2
Figure 4.11. Absorption spectra for D2_4 and D2_5131
Figure 4.12. Flow synthesis apparatus for silver nanorods utilising syringe pumps, 3D-printed
three-inlet reactor, and PTFE tubing
Figure 4.13. Absorption spectra for D3_2 and D3_3
Figure 4.14. Absorption spectra for 3 4 and D3 5

Figure 4.15. Flow synthesis apparatus for silver nanorods utilising syringe pumps, 3D-printed
y-type reactor, and PTFE tubing
Figure 4.16. Absorption spectra for D4_2 and D4_3141
Figure 4.17. Absorption spectra for D4_4, D4_5 and D4_6142
Figure 4.18. TEM images of nanoparticles produced using modified design 4 : (A) D4_5; (B) D4_6
Figure 4.19. Schematic and set up of 3D-printed mixing reactor used in optimised flow synthesis experiments. Top two figures show the actual reactor. Below are cad models, with the image in bottom right showing a magnet bar in the base part
Figure 4.20. Flow synthesis apparatus for silver nanorods utilising syringe pumps, y-type fittings, PTFE tubing, and 3D-printed mixing reactor
Figure 4.21. Absorption spectra for D5_1, D5_2 and D5_3149
Figure 4.22. TEM images of nanoparticles produced using optimised design 1 : (A) D5_2; (B) D5_3
Figure 4.23. Flow synthesis apparatus for silver nanorods utilising syringe pumps, 3D-printed y-type reactor, PTFE tubing, and 3D-printed mixing reactor
Figure 4.24. Absorption spectra for D6_1, D6_2 and D6_3153
Figure 4.25. TEM images of nanoparticles produced using optimised design 4 : (A) D6_1; (B) D6_2; (C) D6_3
Figure 5.1. Structures of MMA and PMMA.[237]
Figure 5.2. A simple depiction of the steps to modify the silver nanorod surface164
Figure 5.3. Schematic representation of surface modification of silver nanorods. The process involves thiol-based ligand exchange with MHA, silica coating through TEOS hydrolysis and condensation, and final dispersion in PMMA
Figure 5.4. Example of a glass slide-PDMS mould
Figure 5.5. Normalised absorbance spectra for silver nanoparticles
Figure 5.6. TEM image of silver nanoparticles prepared for AgNR/PMMA synthesis169
Figure 5.7. TEM results showing silver nanorods coated in a silica shell

Figure 5.8. Absorbance spectra AgNR/PMMA nanocomposites	172
Figure 5.9. FTIR spectrum of PMMA	174
Figure 5.10. FTIR spectrum of AgNR/PMMA nanocomposite containing 5% AgNRs	175
Figure 5.11. FTIR spectrum of AgNR/PMMA nanocomposite containing 10% AgNRs	176

List of Tables

Table 2-1 Some of the physical methods of AgNPs synthesis, along with their advantage and applications
Table 2-2 Examples of sensors for detecting different electromagnetic wavelengths55
Table 2-3 Some studies showing combination of materials used for IR stealth purposes57
Table 3-1 Parameters for Method 1
Table 3-2 Parameters for Method 2
Table 3-3 Summary of morphological and optical characteristics of silver nanoparticles synthesised using Method 1 under varying AgNO ₃ concentrations. The table includes seed volume, observed longitudinal surface plasmon resonance (LSPR) peak wavelengths from UV-Vis spectra, corresponding nanoparticle morphology, and particle size or aspect ratio as determined from TEM analysis.
Table 3-4 Parameters used to synthesise nanoparticles in trial 1
Table 3-5 Parameters used to synthesise nanoparticles in trial 2
Table 3-6 Summary of morphological and optical characteristics from Method 1 – Trial 2, showing the effect of seed volume on LSPR peak position and nanoparticle shape90
Table 3-7 Parameters used to synthesise nanoparticles in trial 3
Table 3-8 Comparison of UV-Vis LSPR peak positions and nanoparticle morphologies obtained using 0.1 mL seed volume in three experimental trials (Method 1), against a reference silver nanorod sample reported in literature.
Table 3-9 Optimal parameters used to synthesis nanoparticles in Method 2
Table 3-10 Comparison between LSPR responses and morphologies of silver nanoparticles synthesised using Optimised Method 2 and the reference method by Murphy et al. [64]. Both methods varied seed volume while maintaining similar growth conditions. Observed LSPR wavelengths and particle morphologies are presented along with known size or aspect ratio data where available
Table 4-1. Reagent concentrations used in the flow synthesis experiments114
Table 4-2 Tubing details for flow synthesis using design 1
Table 4-3 Flow rates utilised in design 1

Table 4-4 Tubing details for modified design 1
Table 4-5 Flow rates used in modified design 1 flow synthesis
Table 4-6 Flow rates used in the modified design 1
Table 4-7 Tubing details for design 2
Table 4-8 Flow rates used in flow synthesis using design 2
Table 4-9 Tubing details in the modified design 2 set up
Table 4-10 Flow rates used in modified design 2
Table 4-11 Tubing details for design 3
Table 4-12 Flow rates used in flow synthesis design 3
Table 4-13 Flow rates used in the modified design 3
Table 4-14 Tubing details for design 4
Table 4-15 Flow rates for flow synthesis using design 4
Table 4-16 Flow rates for flow synthesis using modified design 4
Table 4-17 Tubing details for optimised design 1 flow synthesis
Table 4-18 Flow rates and seed concentrations used in optimised design 1 flow synthesis .148
Table 4-19 Comparison of LSPR peak positions and nanoparticle morphologies between batch synthesis (Method 1) and Optimised Design 1 flow experiments across matched seed volumes of 0.1, 0.05, and 0.02 mL. While both methods demonstrate increasing LSPR redshift with decreasing seed volume, the flow synthesis yielded more uniform rod growth and narrower spectral features, reflecting enhanced control over aspect ratio and particle uniformity 150
Table 4-20 Flow rates for flow synthesis using optimised design 4
Table 4-21 Comparison of LSPR peak positions and nanoparticle morphologies between batch synthesis (Method 1) and Optimised Design 4 (D6_1 to D6_3) across seed volumes of 0.1 mL, 0.05 mL, and 0.02 mL.

List of Equations

(2-1)	12
(2-2)	12
(2-3)	12
(2-4)	12
(2-5)	12
(2-6)	12
(2-7)	12
(2-8)	16
(2-9)	17
(2-10)	17
(2-11)	17
(2-12)	

	Research Thesis: Declaration of Authorship
Print	name: Bilal Amin Mughal
Γitle	of thesis: Development of Silver Nanomaterials as Spectrally Selective Absorbers
	clare that this thesis and the work presented in it are my own and has been generated by me ne result of my own original research.
l cc	onfirm that:
1.	This work was done wholly or mainly while in candidature for a research degree at this University;
2.	Where any part of this thesis has previously been submitted for a degree or any other qualification at this University or any other institution, this has been clearly stated;
3.	Where I have consulted the published work of others, this is always clearly attributed;
4.	Where I have quoted from the work of others, the source is always given. With the exception of such quotations, this thesis is entirely my own work;
5.	I have acknowledged all main sources of help;
6.	Where the thesis is based on work done by myself jointly with others, I have made clear exactly what was done by others and what I have contributed myself;
7.	Either none of this work has been published before submission, or parts of this work have been published as: [please list references below]:
Sign	ed:
Date	y:
-	



Acknowledgements

The journey of PhD research has been a challenging but rewarding experience. It would not have been possible without the incredible amount of support I have received over the years. I would like to express my sincere gratitude to Prof. Xunli Zhang for his patient guidance and untiring support on my writing, experimental design, results analysis, paper writing and presentations throughout the academic research journey, and also encouraging health-consciousness outside the academia. Many thanks to Dr. Eugen Stulz for his assistance in supervision and training in the chemistry laboratory. I would like to thank my industrial sponsor Defence Science and Technology Laboratory (Dstl) for their financial support, and my technical partner Karl Lymer for his guidance and advice towards the project and extraacademic activities.

The experimental work could not have been possible without support from Dr. Harriet Kimpton and Dr. Xiaojuan Lai. I would like to express many thanks to them for helping with the synthesis procedure and also with the characterisation of nanoparticles. I would also like to acknowledge the staff at the Biomedical Imaging Unit (University Hospital Southampton) for their assistance with the TEM measurements.

The Bioengineering group has some incredible people who have helped with my research by suggesting ideas and offering to help when needed. A few individuals who stand out are Dr. Thomas Mabey, Dr Fatih Yanar and Selman Gultekin. I would also like to thank the staff and fellow PhD students of the Engineering and Chemistry research groups who have made the university such a welcoming and fun place to work.

Thanks to all my colleagues: Aran, Cici, Claire, Deepak, Dileep, Ebrahim, Eddy, Feng, Jeff, Kiro, Li-Mu, Li-Pan, Maruti, Mohammad, Neel, Ravi, Ren, Skylar, Shahbaz, Shamma, Sophia, Teresa, Tina, Xiyuan, ZaiHao, etc. for their technical assistance in my experiments and company during the research.

Life is easy when you have a caring and loving family as mine. I can never be grateful enough to my parents (Amin Moughal and Tasneem Mughal) for their love and support throughout my life. I'm lucky enough to have loving siblings (Feroz, Hassan, Mobeen and Rabia) who are always looking forward to my visit home and spending great times together.



Definitions and Abbreviations

AA Ascorbic acid

Ag Silver

AgNO₃ Silver nitrate

AgNPs Silver nanoparticles

AgNRs Silver nanorods

AIBN Azobisisobutyronitrile

A.R Aspect ratio

Au Gold

CTAB Hexadecyltrimethylammonium bromide

DMA Dimethylamine

EtOH Ethanol

LSPR Localised surface plasmon resonance

MEHQ Monomethyl ether of hydroquinone

MHA 6-Mercaptohexonic acid

mL Millilitre

mm Millimetre

MMA Methyl methacrylate

mM Millimolar

NaBH₄ Sodium borohydride

NaOH Sodium hydroxide

NIR Near-infrared

nm Nanometer

NPs Nanoparticles

PDMS Polydimethylsiloxane

PMMA Polymethyl methacrylate

PVP Polyvinylpyrrolidone

rpm Revolutions per minute

SPR Surface plasmon resonance

TEM Transmission electron microscope

TEOS Tetraethyl orthosilicate

TSC Trisodium citrate

UV-Vis Ultraviolet-visible

v/v Volume / Volume

wt. Weight



Chapter 1 Introduction

1.1 Background

Throughout the course of history, human civilisation has advanced and altered various materials to satisfy diverse needs. The development of technology has enabled the manipulation of material structures at the nanoscale, which has opened avenues for the integration of nanotechnology into various aspects of daily life. Nanotechnology is a field of research that has been extensively studied and utilised for a wide range of applications. Several methods are used to develop different nanostructures including nanoparticles, nanorods, and nanowires. By changing the nanostructure of the materials, their properties can be modified to perform a certain function or desired properties. Enhanced material properties (e.g. high strength, and lightweight) [1], microelectromechanical systems (MEMS) [2], photonics, medical devices/treatments [3] are some of the applications of nanotechnology.

A structure or component can only be called 'nano' if at least one of its dimensions is in the nanometre range of under 100 nm. For example, nanorods can be several micrometres in length, however their diameter is only tens of nanometres. Figure 1.1 depicts the nanometre scale in relation to some micrometre sized objects [4].

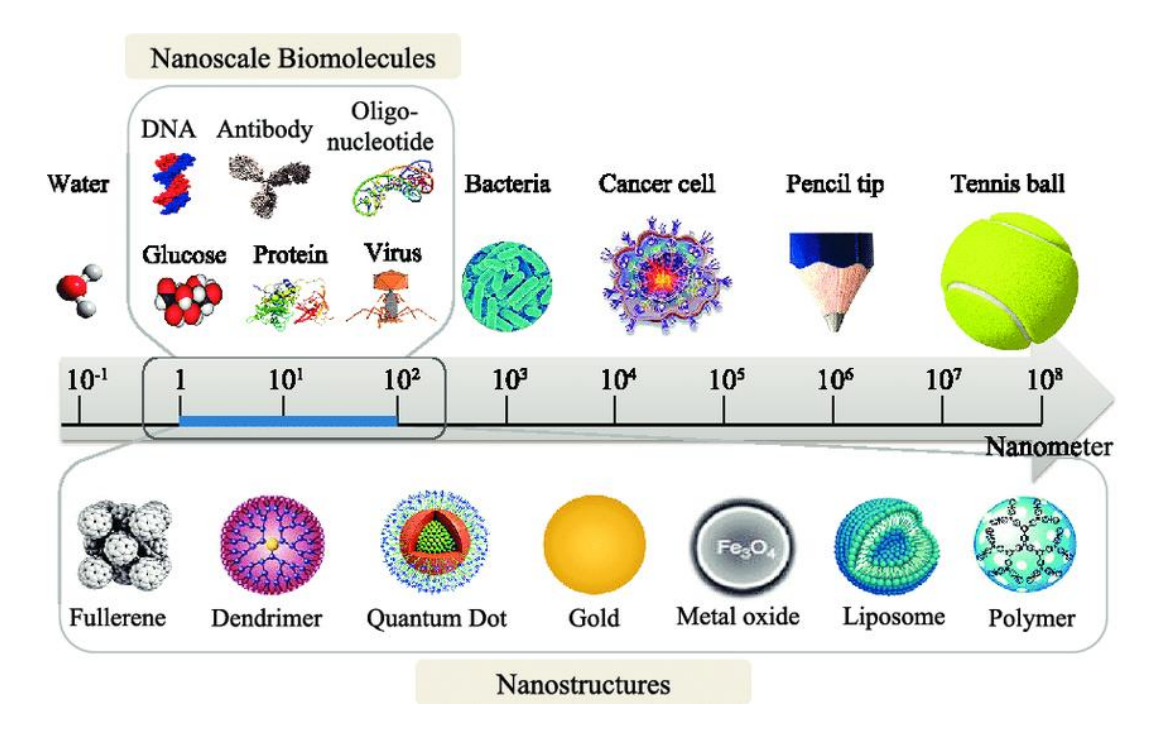


Figure 1.1. Nanometre scale compared to some larger structures [4]

In recent times, there has been a heightened focus on the creation of nanomaterials using noble metals, with silver (Ag) being a particularly sought-after option due to its exceptional plasmonic and antimicrobial characteristics. These properties enable the use of Ag nanoparticles (AgNPs) in a range of applications, such as Raman spectroscopy [5], electronics (sensors & supercapacitors), biochemical sensors, and antimicrobial agents [6]. The dimensions of AgNPs lie within the range of 1 nm to 100 nm. There are various methods for synthesising AgNPs, including chemical, physical, and biological. The growing research on AgNPs is demonstrated in Figure 1.2.

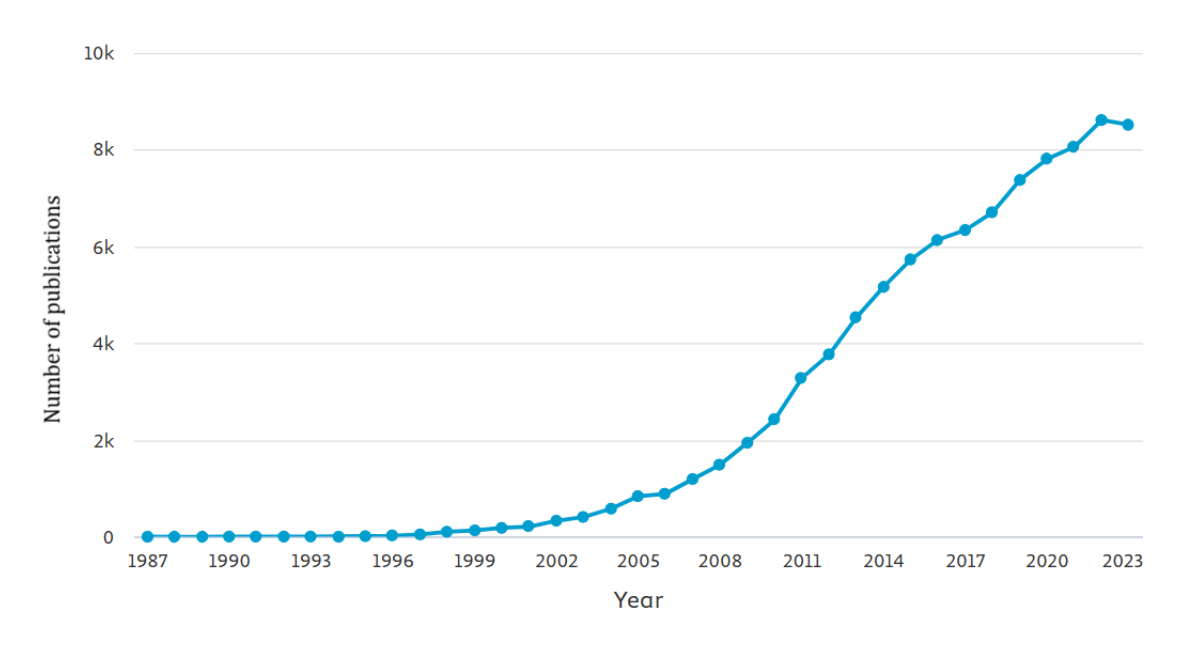


Figure 1.2. Number of publications with 'silver nanoparticles' in the article title, abstract or keywords (data obtained from scopus.com).

The utilisation of nanoscale materials can be optimised by manipulating their behaviour at the nanoscale. The behaviour and interactions of atoms are dictated by the forces present at the nano-level, which ultimately control the material's final properties. These forces differ from those operating at the macroscale and operate on a nanoscale. Unlike gravitational forces, which are proportional to mass, electrostatic forces are significantly affected by short distances.

One of the main differences at the nanoscale is the increased surface area to volume ratio (s/v ratio). Therefore, electrostatic forces are crucial components. This increase in the s/v ratio results in increased surface energy for nanomaterials. In a solution, these nanoparticles stick together and become lumped, which is not desired. As a result of the increased s/v ratio, the chemical reaction kinetics is also changed.

Because of few atoms close to each other at the surface, a band of loose valence electrons is open to binding to other atoms and result in increased chemical reaction rates.

Silver (Ag) is an excellent example of how noble materials at nanoscale offer great benefits. In bulk form, silver is inert. However, in nano-form, it finds numerous applications in various fields. One of its applications is that it is an excellent catalyst, for example in C-H and C-C bonding, reduction of nitroaromatics and carbonyl compounds, and oxidation of alcohols [7], [8]. Recently, there have been numerous studies carried out using noble metals as catalysts (see references for some examples) [9], [10], [11], [12]. One important point to take into consideration when utilising such materials is the controllability over reactions as high activity rates can lead to undesired reactions, i.e., oxidation.

The synthesis of nanomaterials with a specified structure and geometry is feasible. This capability is beneficial in the creation of nanomaterials with targeted functionality, such as catalysts. Molecular recognition sites, which dictate the bonding of other molecules, vary in number and arrangement, thereby the regulation of geometry, including edges and vertices, can lead to an augmented rate of reaction and stability [13].

When a material is reduced in size to the nano level, its optical properties are changed too. The size of particles governs their appearance. For example, AgNPs do not appear as bulk silver does. The geometry (i.e., shape and size) of the nanoparticles regulates the wavelength of light absorbed and reflected. For AgNPs in 30 nm diameter, the absorbance band is between 400 to 550 nm wavelength (blue to green region) of visible light, whereas the 700 nm wavelength (red) is reflect, which is why they appear red. AgNPs in 100 nm diameter, the absorbed wavelength is around 700 nm, so they appear blue [14]. The observed colour change is a result of optical phenomenon known as surface plasmon resonance (SPR). The phenomenon occurs for the nanoparticles having a smaller size than the wavelength of light. When such nanoparticles are irradiated by light, the oscillating electric field from light results in coherent oscillation of conduction band of electrons around the nanoparticle surface (as shown in Figure 1.3) [15].

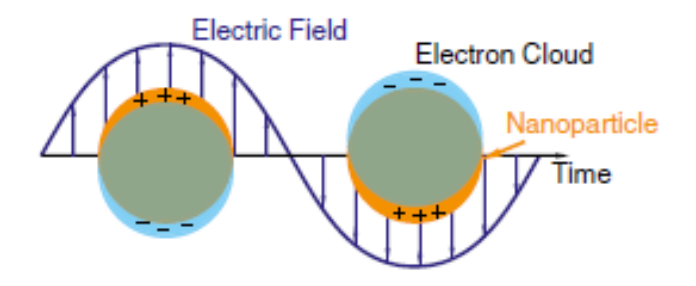


Figure 1.3. Schematic of localised surface plasmon resonance (LSPR) in a spherical metal particle [15,16].

The excitation of the electrons results in absorption of light at a resonant wavelength for the nanoparticles in the corresponding region of electromagnetic radiation. Factors such as geometry can affect the resonant frequency. The correlation of the colour variation observed and the absorbance spectra in the noble metal colloid are shown in Figure 1.4.

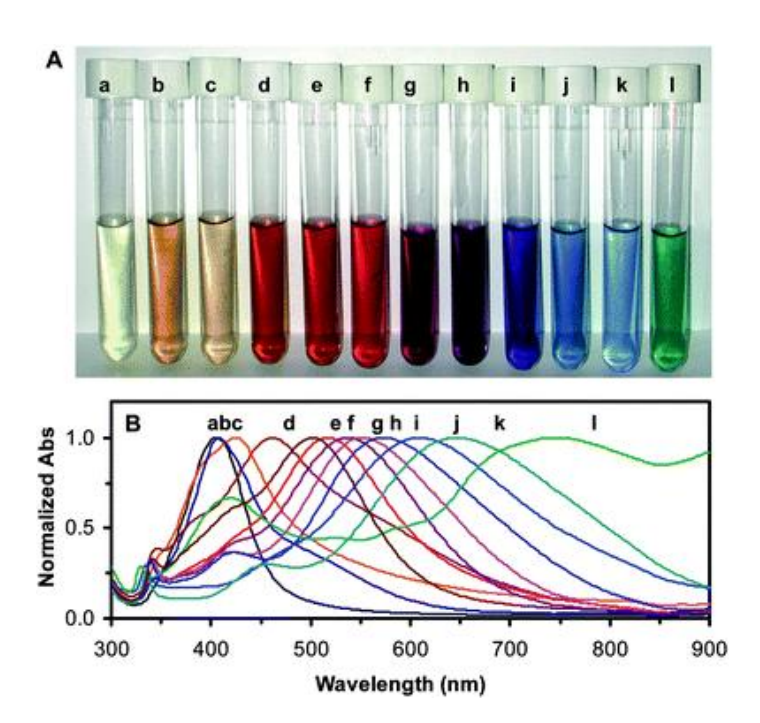


Figure 1.4. (A) Colloidal AgNPs with different colours. (B) Absorption spectra of corresponding colloid [17]

1.2 Anisotropic nanoparticles

Anisotropy, the property of an object that is direction-dependent, is present throughout the universe. It is the foundation of complex systems, which range from the formation of new galaxies in the universe to cell mitosis in eukaryotes. It is easy to overlook the importance of anisotropy at large scales, yet the formation of systems with complex functions is not possible without anisotropic building blocks. The rule is true for small scale structures, and examples of such structures are found throughout nature exploiting anisotropy for useful functional materials. Bird and insect wings display iridescence due to the interaction of light with their asymmetric nanoscale characteristics [18]. Bones exhibit high rigidity and toughness because its assembled from anisotropic components [19].

For many years, chemists have pursued the replication of the structural and functional complexity found in nature to obtain increasingly complex materials for a variety of applications including energy harvesting and drug delivery. The utilisation of nanoscale anisotropy has been demonstrated to yield substantial advancements in material performance, particularly. Solar cells based on anisotropic nanostructures, for example, can achieve greater efficiency in light harvesting than those constructed from simple isotropic building blocks [20]. *In vivo*, anisotropic nanoparticles exhibit different behaviour compared to their isotropic equivalents, and particle shape is increasingly recognised to be a critical design parameter for the next generation of nanomedicines to be realised [21].

The fundamental influence of anisotropy is well-known on the properties of nanoscale structures. Therefore, how can anisotropy be regulated to change the properties of the material? In biology, precise determination of anisotropy is important to unlock complex functionality. This can be seen in certain viruses like tobacco mosaic virus (TMV), the packaging in capsids consists of numerous copies of the capsomer protein [22]. This is a complicated process for chemists as they have to control the anisotropic nanoparticles. Over the past two decades, the rapid creation of new processes has been witnessed that allow highly accurate preparation of anisotropic nanoparticles. This has enabled research in nanoparticles based on their geometry-function combinations. Studies using well-defined anisotropic nanostructures (i.e., with a single morphology and small sizes) and insight into how the tuning form helps us to precisely monitor the material properties are a priority.

Inorganic nanosized particles have been the subject of great interest recently due to their unique properties [23]. With the mean free path of an electron in metals at room temperature being between 10-100 nm, it is predicted that as the metal particles are reduced to such nano-size scales, unique properties could be obtained [23]. Spherical gold and silver nanoparticles with a diameter of less than 100 nm appear red and

yellow respectively, when suspended in transparent media [23]. When they are less than 3 nm in diameter, they are non-reactive, but are able to catalyse chemical reactions [8]. As well as possessing unique valuable properties, inorganic nanowires exhibit exceptionally high strength, stiffness, and ductility combinations compared to bulk materials. One-dimensional nanoparticles such as nanorods and nanowires (see Figure 1.5 for different morphologies of nanoparticles) have promising applications in electronics, photonics, bio-chemical sensing and imaging, and drug delivery [17–19]. The optical properties of silver and gold nanoparticles can be tuned in the visible and near-infrared wavelengths according to their shape, size, and local di-electric environment [15]. In addition, molecules that adsorb to these nanoparticles' surface exhibit enhanced surface-enhanced Raman scattering (SERS) effects. This is because of the collective oscillation of electrons in the conduction band, a process known as surface plasmon resonance. Therefore, optical sensors are one emerging application of metallic nanoparticles [27].

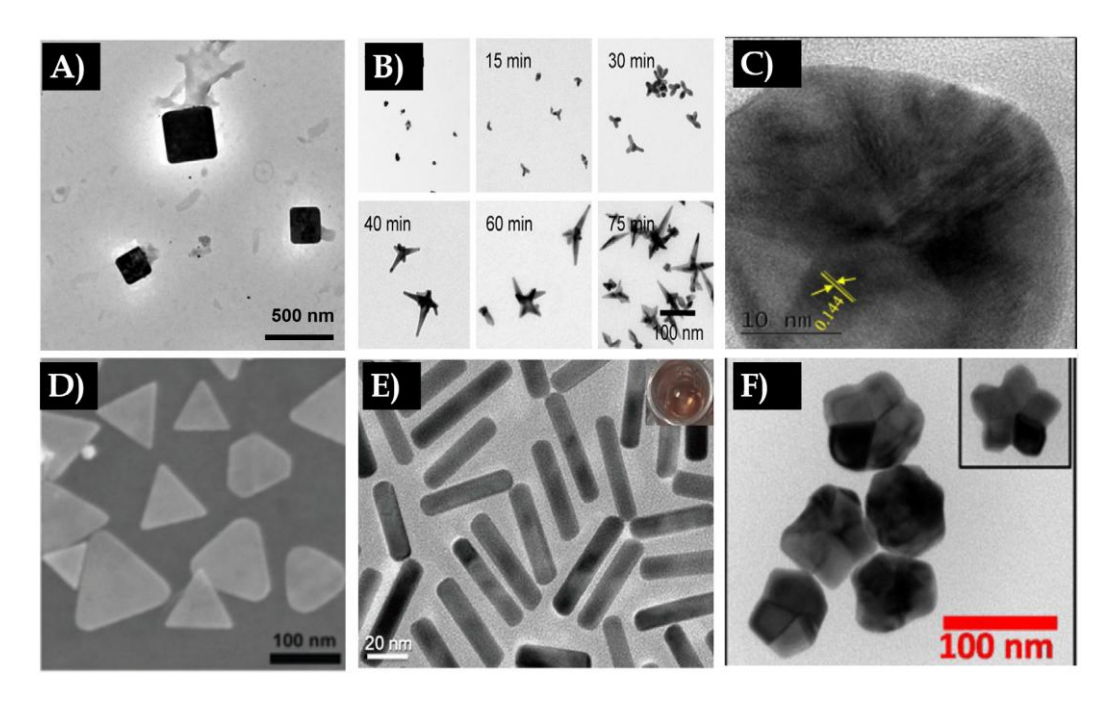


Figure 1.5. Different morphologies of gold nanoparticles: A) nanocubes; B) branched nanoparticles; C) dodecahedral; D) nanoprisms; E) nanorods; F) nanostars [28]

For 1-dimensional metallic nanoparticles such as nanorods and nanowires, there are two separate plasmon bands: the transverse plasmon band, which corresponds to light absorbance along the short axis of the particle, and the longitudinal plasmon band, which corresponds to light absorbance along the long axis of the particle. For non-spherical nanoparticles, other weaker bands are also seen due to quadrupoles. The

enhanced electric fields present at the tips of 1-dimensional nanoparticles lead to improved plasmonic properties, which can be useful for optical and electrical applications [27]. Gold and silver nanoparticles have been utilised as contrasting agents in electron microscopy due to their electron-dense property. They are also being used in biological optical imaging and sensing applications [27]. These applications are possible due to the elastic light-scattering properties of these nanoparticles, and they also depend on the shift of the plasmon band maxima with local dielectric constant.

Specifically, anisotropy yields a diverse range of physical, chemical, and biological properties that are unattainable in isotropic structures [29], [30]. Nevertheless, the majority of research in this area has been centred on contrasting isotropic particles with a solitary sample of anisotropic particles (typically dispersed). It is extremely limited to examine variations between different shapes and sizes of nanoparticles (isotropic and anisotropic) that are of the same surface chemistry. Such types of studies may lead to a much more thorough understanding of how the parameters of a nanoparticle are connected to its properties and how they can be further manipulated to achieve the end goals of the application.

1.3 Motivation

Technological advancements pose a formidable challenge to the endurance of military equipment and vehicles in hostile environments, such as warfare. The emergence of new detection methods and technologies has facilitated the detection of vehicles, including fighter aircraft, thereby granting the adversary an advantage. The susceptibility of military aircraft and other equipment can be reduced using methods such as, suppressing the vehicle signatures, damage enemy defence systems, employ systems that warn about threats and using electronic counter-measures [31]. Of these, signature suppression has gained attention due to the broad signature detection technologies available, including radar, infrared and acoustic.

It is already known that silver possesses plasmonic properties. Depending on the geometry, silver nanoparticles (AgNPs) can be used to absorb specific wavelengths of electromagnetic radiation. For example, spherical and triangular nanoparticles can

absorb in the ultraviolet to visible regions. Studies have shown that AgNPs can be tuned to absorb desired wavelengths of light, where silver nanorods can absorb in the NIR [32]. By increasing the aspect ratio, the absorption can be increased [33]. Therefore, this study aimed to develop AgNPs to absorb light in the near-infrared (NIR) wavelengths. Nanorods were chosen for this study because their anisotropic shape allows for precise tuning of their optical properties, particularly in the near-infrared (NIR) region. Unlike spherical nanoparticles, which have a single localised surface plasmon resonance (LSPR) peak, nanorods exhibit two distinct plasmonic modes: the transverse plasmon band (along the short axis) and the longitudinal plasmon band (along the long axis). The longitudinal plasmon band can be systematically shifted into the NIR region by controlling the nanorod's aspect ratio [34]. This makes them ideal candidates for applications requiring absorption and manipulation of NIR light, such as stealth coatings and photothermal energy conversion.

Additionally, silver nanorods (AgNRs) offer high plasmonic efficiency, meaning they strongly interact with light, leading to enhanced absorption and heat generation [35]. This is particularly important for stealth technology, where reducing reflections and controlling thermal signatures are critical, and for solar energy applications, where efficient light absorption can enhance energy harvesting. The ability to fine-tune their optical response via synthesis parameters makes AgNRs a superior choice over other nanoparticle morphologies.

Using the above nanoparticles, nanocomposite coatings can be developed for defence applications, especially for use on military vehicles such as aircraft. Apart from heat from engine and exhaust, radiation from sun, or velocity-generated heat is an issue as infrared-guided missiles can target the vehicles. It has been proposed that IR signature can be reduced by using coatings that absorb IR wavebands in the 0.2-2 μ m, 5-7 μ m and 8-14 μ m spectrum [36], [37], [38]. Such coating materials can be applied on military equipment and clothing to reduce the IR signature.

Despite there being a large number of studies about synthesis of silver nanoparticles for antimicrobial studies, as well as other medicinal studies and solar energy applications, there is very little if any literature about its applications for infrared absorption, or stealth purposes. Plasmonic research in this area is in very early stages, therefore a lot more research is required to explore and understand fully the absorption

processes for infrared applications. As mentioned above, the plasmonic response depends on the geometry of the nanoparticles, however, there are many other challenges that must be overcome during the synthesis. The common issue for nanorod synthesis is the difficulty to control the size, shape, aspect ratio. It is necessary to research and develop an optimised synthesis method for silver nanorods. The approach should consider the economic and environmental impact of synthesis.

Finally, there is a need to synthesise these nanomaterials on an industrial scale. One of the ways to achieve that is by using continuous flow reactors. A flow reactor (also called micro reactor) is an apparatus that has micro channels in which chemical reactions take place [39]. In comparison to batch synthesis, flow/micro reactors offer continuous production (contrast with/to a batch reactor). They offer many advantages over conventional scale reactors, including vast improvements in energy efficiency, reaction speed and yield, safety, reliability, scalability, on-site/on-demand production, and a much finer degree of process control.

The sensitive nature of the application may be another reason for the lack of published research in this field as governments would not want to publish such research in the public domain, risking leakage of classified information. It is therefore a requirement of this project to adhere to the non-disclosure agreement with the industrial sponsor, Defence Security and Technology Laboratory (Dstl).

1.4 Aim & objectives

The aim of this research project was to develop anisotropic silver nanoparticles (mainly silver nanorods) for near infrared (NIR) absorption. The specific objectives of the work were to:

- Synthesise Ag nanorods with improved control over their diameter, aspect ratio and arrangement;
- Optimise the synthesis of Ag nanorods to achieve stable productivity and absorption in NIR and higher wavelengths;
- Characterise the absorption and scattering properties of the nanorods by UV-IR spectroscopy;
- Characterise the morphology and geometry of nanorods using TEM;

- Design, construct, and test flow reactors for continuous production of Ag nanorods; and
- Synthesise and characterise AgNP/polymer nanocomposite.

Chapter 2 Background and Literature Review

This chapter provides a comprehensive overview of plasmonic nanoparticles, focusing especially on nanorods, and covering their properties, synthesis methods and applications. The chapter commences with a thorough literature review to explore the current understanding of the physical and chemical properties of plasmonic nanoparticles and the various synthesis methods used to produce them. Subsequently, the chapter delves into the diverse applications of silver nanoparticles, including their use in medicinal, electronics and catalysis applications. The primary objective of this chapter is to demonstrate an in-depth understanding of silver nanoparticle research, development, and applications, on which this research project is based.

2.1 Light properties

Electromagnetic radiation is an electric and magnetic disturbance travelling through space carrying energy in the form of waves. The wave comprises of electrical and magnetic fields at right angle to each other. The main characteristic to identify them is the wavelength (λ), which is the distance between two peaks or troughs. The wavelengths vary between femtometres (gamma rays) to kilometres (radio waves). Visible light ranges from 400 nm to 700 nm. Infrared (IR) radiation has a range between 700 nm and 1 mm; it is the region focused upon in this project.

Scottish scientist James Maxwell published a historic paper in 1865 entitled "A Dynamical Theory of the Electromagnetic Field" to explain the fundamentals of electromagnetic radiation [40]. Maxwell combined previously known laws (Ampere, Faraday and Gauss) into four equations named after him. The equations are listed below and use the following operators:

- i. D is the electric displacement field
- ii. ρv is the charge density
- iii. B is the magnetic flux density
- iv. E is the electric field
- v. H is the magnetic field and
- vi. *J* is the electric current density
- Vii. ∇ and ∇ × refer to the divergence and curl of a vector function

$$\nabla \cdot D = \rho v \tag{2-1}$$

$$\nabla \cdot B = 0 \tag{2-2}$$

$$\nabla \times E = -\frac{\delta B}{\delta t} \tag{2-3}$$

$$\nabla \times H = \frac{\delta D}{\delta t} + J \tag{2-4}$$

These equations allow physicists to understand the behaviour of electromagnetic waves and their interaction with media and velocity as they propagate through the different media. In a vacuum, these waves travel at the speed of light (i.e., 299,792,458 m/s). This velocity is different for different media and is related to the permittivity and permeability (ε , μ) of that medium. Using the difference in speed between vacuum and in a given medium, the refractive index (n) can be calculated using the following equation:

$$n = \frac{c}{v} \tag{2-5}$$

$$c = \lambda v \tag{2-6}$$

$$E = hv ag{2-7}$$

 λ = Wavelength of the electromagnetic wave

v = Frequency of the wave

Light is a form of electromagnetic radiation and one of number of waves travelling through space. It is part of the electromagnetic spectrum which comprises of longer wavelength waves (1 m - km), such as sound waves, to short wavelength waves such as gamma rays.

Interaction between light and the surface of an object results in one of the following: (i) transmission through the object, (ii) reflection off the surface, or (iii) absorbance (see Figure 2.1). A good example where light is manipulated is lenses on the sunglasses; an optical coating allows reflection of the harmful ultra-violet wavelength and transmission of visible wavelength.

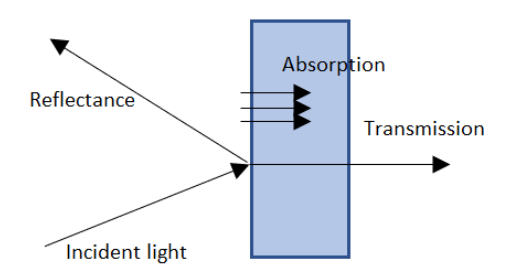


Figure 2.1. Interaction of light with an object

During absorption, the energy from the incident light is transformed into a different form, usually heat, thus the light does not emerge from the material. During transmission, the incident light simply travels through the material, entering one side and exiting from the other. The phenomenon of reflection causes the radiation to be re-emitted from the material. There are two forms of reflection, namely specular and diffuse (scattering). In the former, the angle of reflection is same as the incident angle, whereas in the latter the reflection is in many directions.

2.2 Localised surface plasmon resonance

Plasmonic nanomaterials exhibit absorption ranges that may closely resemble the absorption peaks of semiconductor nanomaterials. However, the absorption mechanisms of plasmonic nanomaterials are fundamentally distinct as they do not arise from transitions between quantized energy states, but rather from the excitation of the collective electron cloud motion [41]. The electric field effect prompts the occurrence of plasmon excitation at the electron cloud located on the surface. This excitation displays a resonance at a specific frequency of the incoming light, resulting in an optical absorption [42]. This phenomenon is known as localised surface plasmon resonance (LSPR) [43].

As the particles' size is reduced, the interaction of incident light with the conducted electrons takes place on the particle boundary. The optical properties are affected by this metal-dielectric boundary, becoming dependent on the size and shape. When light strikes nanoparticles, the electric field of light causes the conducted electrons to oscillate coherently (see Figure 2.2). When nanoparticles are much smaller than the light wavelength, the absorption range is very narrow, that region is known as plasmon band. [44]

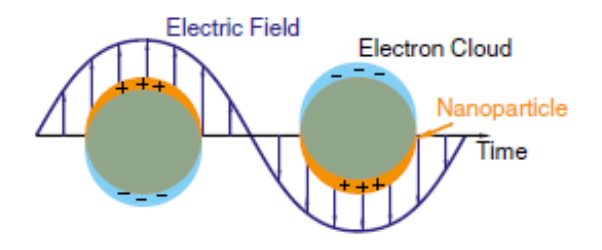


Figure 2.2. Schematic of localised surface plasmon resonance (LSPR). Coherent oscillations in the free electrons of the material may be induced by the oscillating electric field of the incident light [16].

Nanorods exhibit distinctive characteristics in their absorbance spectrum, as depicted in Figure 2.3(a) and (b). Specifically, two absorption bands are evident, known as the longitudinal plasmon band (LPB) and the transverse plasmon band (TPB). These bands correspond to electron oscillations along the nanorod's long and short axes, respectively. Notably, the TPB remains unaffected by changes in nanorod size or the surrounding refractive index. On the other hand, the LPB undergoes a red-shift with an increase in the nanorod's aspect ratio and is highly sensitive to changes in the refractive index [45]. The Localised Surface Plasmon Resonance (LSPR) properties are significantly influenced by factors such as nanoparticle size, shape, dielectric properties, and the surrounding medium [46]. These factors impact the electron charge density on the particle surface and consequently affect the LSPR response. Moreover, LSPR demonstrates high sensitivity to changes in the local dielectric environment's refractive index.

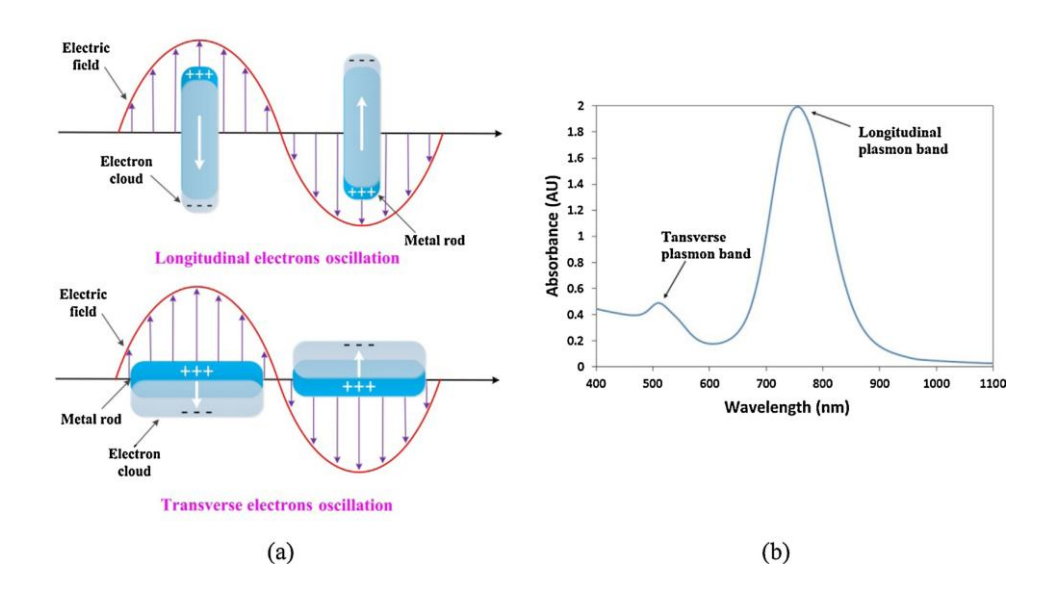


Figure 2.3. Schematic illustration of LSPR excitation for nanorods and (b) LSPR absorption bands of nanorods: longitudinal and transverse plasmon bands [47].

The optical properties of silver nanoparticles are highly sensitive to particle morphology. As shown in Figure 2.4, spherical AgNPs typically exhibit a single, sharp absorption peak around ~400 nm, corresponding to the dipolar localised surface plasmon resonance (LSPR). In contrast, anisotropic structures such as silver nanorods display two distinct LSPR bands: a transverse peak (similar to spheres, ~400 nm) and a longitudinal peak in the visible to near-infrared (NIR) region, the position of which shifts to longer wavelengths with increasing aspect ratio [48]. Silver nanoprisms, due to their planar geometry and multiple plasmon modes, exhibit broader and more complex spectral features, often spanning the 600–900 nm range [49].

Understanding these spectral signatures is essential for interpreting UV-Vis data presented in later chapters, where particle shape and uniformity are deduced from peak positions and relative intensities.

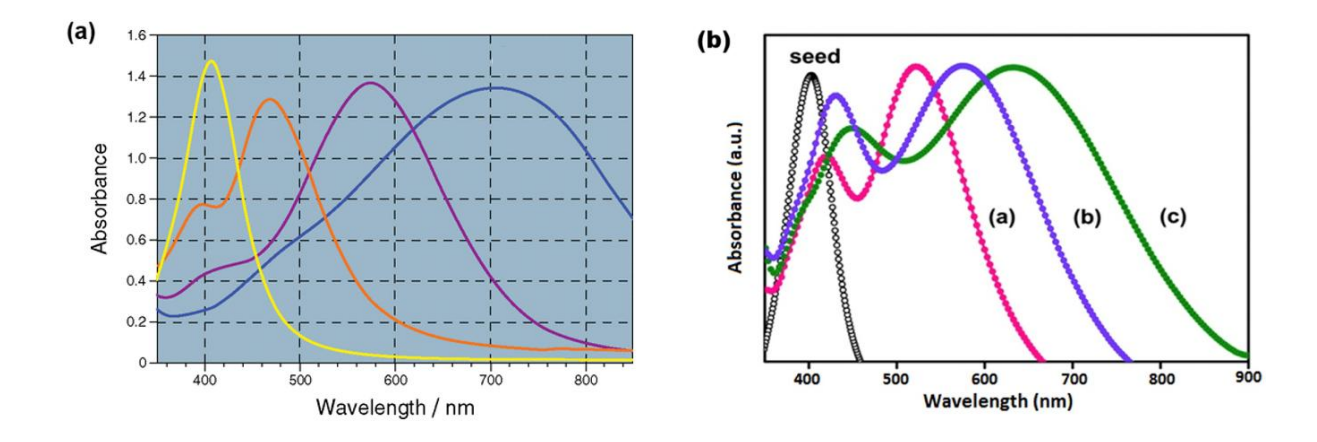


Figure 2.4. Example UV-Vis-NIR absorption spectra for common silver nanoparticle morphologies. (a) yellow- 10nm spherical particles; orange- 35 nm long nanoprisms; violet-40 nm long nanoprisms; and blue- 64 nm long nanoprisms [49]. (b) black- 10 nm silver seed particles; pink- nanorods with aspect ratio 6; purple- nanorods with aspect ratio 11; and green- nanorods with aspect ratio 15 [48].

The plasmon intensity during the interaction depends on the geometry, particle distribution and interface and dielectric function of the nanoparticle and host [42]. Taking into account these factors, it is possible to control the final properties of the material. The interaction is different depending on the material; therefore, they produce different colours. Two mechanisms that are associated with extinction of light are absorption and scattering, with the former being the more dominant factor.

Nanoparticles were used during the Roman era, with applications being glass using gold and silver nanoparticles [50].

Gold and silver are two of the most researched materials due to the pronounced plasmonic properties. An increase in their nanoparticle size results in the a red-shift of the absorption [43]. Compared to quantum dots, this variation due to size is small in metallic nanoparticles. For nanoparticles less than 30 nm in size, the shift is relatively small. For larger nanoparticles, this shift is larger, as illustrated in Figure 2.5A for the effect of size. The absorption band depends on the geometry of the nanoparticle. For example, in nanorods, the plasmon band exhibits two modes which results in oscillation of electrons in the longitudinal and perpendicular axis to the length. Therefore, in the nanorods, the absorption is dependent on the aspect ratio. An example of this increased size effect is displayed in Figure 2.5B, which shows the plasmon resonance absorptions of gold nanorods.

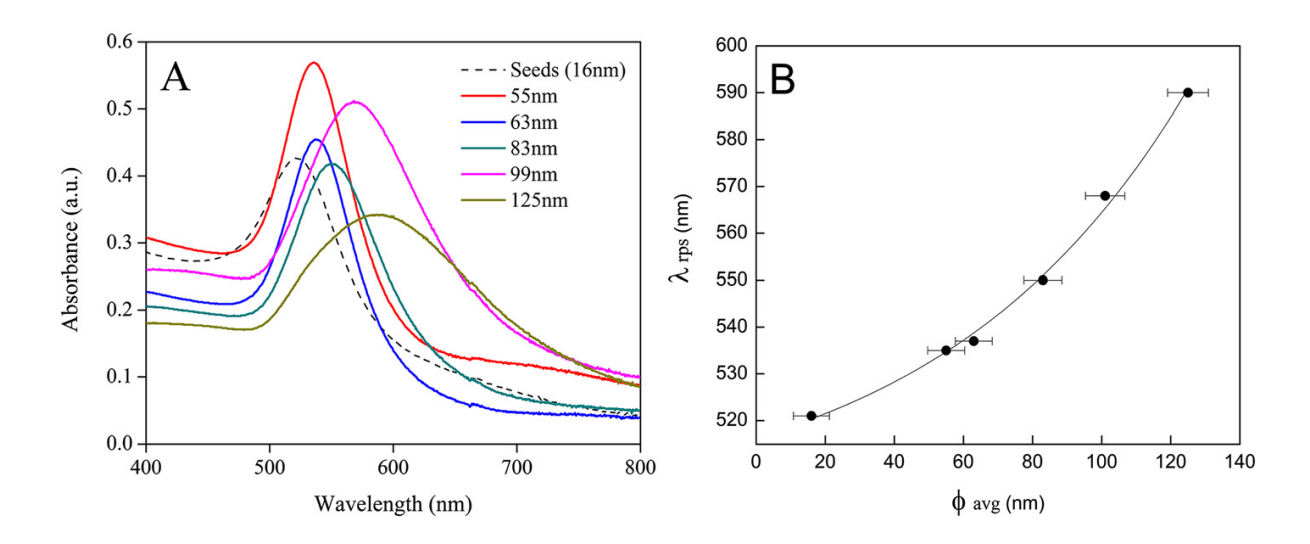


Figure 2.5. UV–vis absorption spectra and absorption shift of gold nanoparticles. (A) UV–vis absorption spectrum of the synthesised gold nanoparticles. (B) Shift in absorption λrps of gold nanoparticles with particle size [51].

The light absorption resulting from localized surface plasmon resonance (LSPR) in spherical nanoparticles can be described using the Mie solution to Maxwell's equations [52]. The Mie theory provides the following formula for the extinction cross-section, C_{ext} , of well-spaced spherical nanoparticles with a radius of R:

$$C_{ext} = \frac{24\pi^2 R^3 N \varepsilon_m^{3/2}}{\lambda} \frac{\varepsilon_i}{(\varepsilon_r + 2\varepsilon_m)^2 + \varepsilon_i^2}$$
(2-8)

where ε_m is the dielectric constant of the surrounding medium, ε_r and ε_i are the real and imaginary part of the dielectric function of the nanoparticles, respectively, and N is the number of spheres per unit volume.

Gans proposed that the surface plasmon mode of small metallic nanorods would divide into two modes because of their ellipsoidal shape and surface curvature, as predicted by the dipole approximation. To understand the optical characteristics of these rod-shaped particles, they have often been modelled as ellipsoids. Consequently, Gans' theory can be used to explain the optical behaviour of metallic nanorods. By employing Gans' formula, one can calculate the extinction cross-section for metallic nanorods [9,10]:

$$C_{ext} = \frac{2\pi V N \varepsilon_m^{3/2}}{3\lambda} \sum_j \frac{\binom{1}{p_j^2} \varepsilon_i}{(\varepsilon_r + \left(\frac{1 - p_j}{p_i}\right) \varepsilon_m)^2 + \varepsilon_i^2}$$
(2-9)

where V is the particle volume and P_j denotes the depolarization factor. The depolarization factor for elliptical particles may be described as following:

$$P_{length} = \frac{1 - e^2}{e^2} \left[\frac{1}{2e} ln \left(\frac{1 + e}{1 - e} \right) - 1 \right]$$
 (2-10)

$$P_{width} = \frac{1 - P_{length}}{2} \tag{2-11}$$

where e is the ellipticity, given by:

$$e^2 = 1 - \left(\frac{length}{width}\right)^2 \tag{2-12}$$

Plasmonic nanoparticles for optical applications are commonly embedded in a polymer/glass host material, resulting in nanocomposites which allow development of useful devices [42]. The host (or matrix) material houses the nanoparticles preventing agglomeration. The optical and photonic applications include communications, Raman scattering, waveguides, and many more.

Silver nanoparticles have been chosen over other noble metals due to its superior electrical and thermal conductive properties. It has the highest efficiency of plasmon excitation. "A single Ag nanoparticle interacts with light more efficiently than a particle

of the same dimension composed of any known organic or inorganic chromophore" [54]. Silver nanoparticles can capture increased amount of light (ten times their geometric cross-section). Also, silver is cheaper than gold. These properties of silver are the reason behind selection for this research project.

2.3 Synthesis of silver nanoparticles

2.3.1 Top-down & bottom-up methods

As discussed above, different types of Ag nanoparticles (AgNPs) with unique properties have been utilised for different applications. Various shapes and sizes have been developed for such applications. Therefore, it is critical to control their physical, chemical, and optical properties in order to optimise their performance. The following are important points to be considered when synthesising AgNPs: surface property, distribution of size, shape, reaction rate, reduction, and capping chemical (for chemical methods). The main methods for preparing AgNPs are distinguished by top-down & bottom-up techniques. In the top-down method, bulk materials are disintegrated to nano-sized particles, whereas in the bottom-up approach nanoparticles are assembled from single atoms [55]. Top-down approach normally involves energy, lasers and thermal methods. Some of the examples include arc discharge, laser ablation, evaporation and sputtering. [56]. In the bottom-up approach, there are following categories: gas, liquid and solid phases, and biosynthetic methods. Some of the examples include chemical vapour deposition, sol-gel, metal salt reduction, and template synthesis. [56]

The synthesis methods are categorised into physical, chemical, and biological approaches. The biological methods tend to be less labour intensive and offer high yield and stability compared to physical and chemical methods [57]. The following sections aim to explain the common methods used to synthesise silver nanoparticles, with a detailed review of chemical methods.

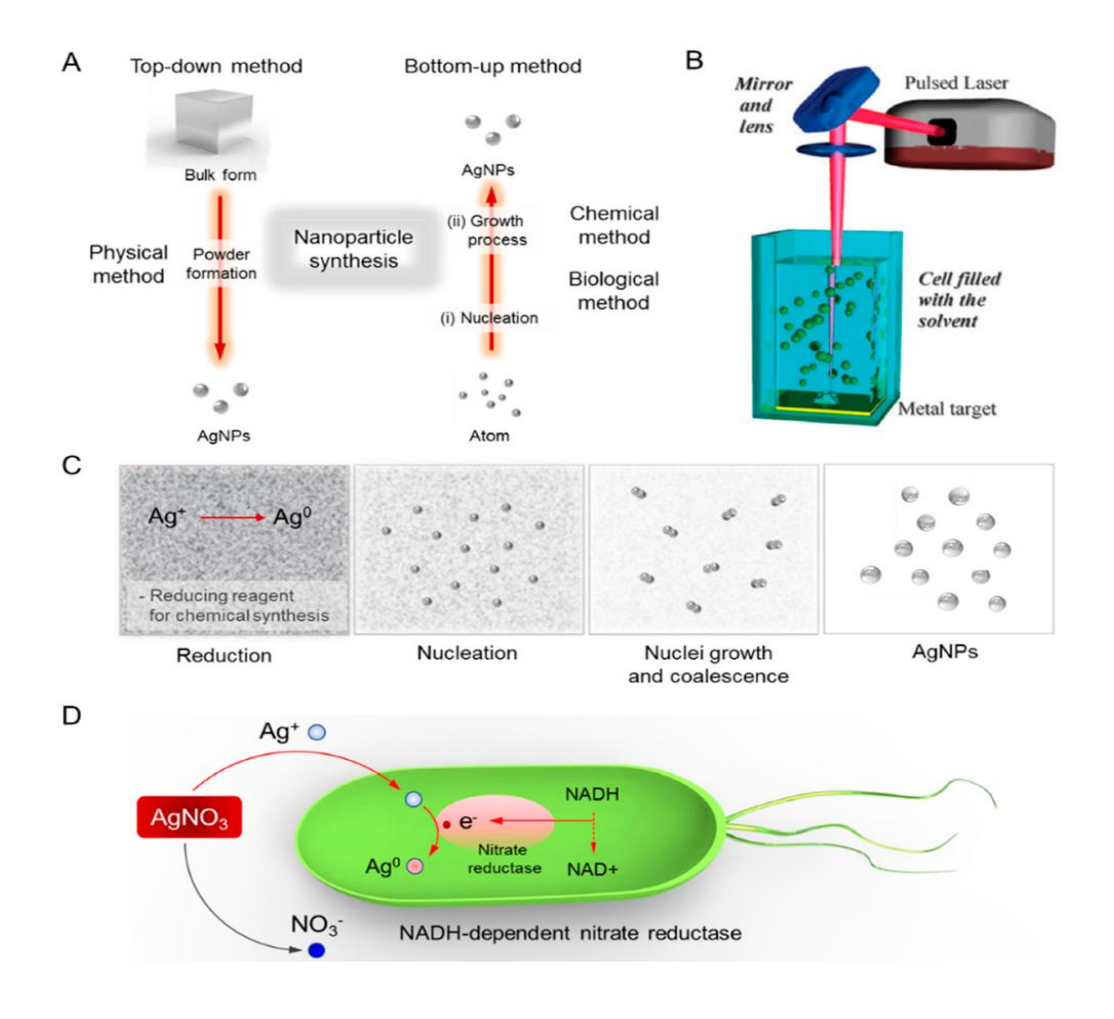


Figure 2.6. Various synthesis routes of silver nanoparticles. (A) Top-down and bottom-up methods. (B) Physical synthesis method. (C) Chemical synthesis method. (D) Plausible synthesis mechanisms of green chemistry. [58]

2.3.2 Chemical methods

Interest in metallic nanoparticles has grown hugely in recent decades, due to their unique properties that depend on size and shape [23]. It is no surprise then to see that there are numerous synthesis procedures to synthesise various shapes of nanoparticles including spheres, cubes, prisms, rods, wires and many more. Particularly, gold and silver nanorods are of great interest and thus different methods of synthesis to obtain gold and silver nanorods and nanorods have been reported. Concerning the fraction and aspect ratio of the nanorods, various synthesis parameters were analysed. A literature summary of synthesis processes for gold and silver nanorods and the influence of various synthesis parameters on the fraction and aspect ratio of gold and silver nanorods are given in the following section.

Chemical reduction is the most common method for AgNPs synthesis as its simple and doesn't require complex equipment and can produce a high yield at a low cost. The method requires three main constituents: metal precursor, reducing agent and stabilising agent. The commonly used precursors to produce AgNPs are silver nitrate (AgNO₃) [59], silver citrate (Ag₃C₆H₅O₇) [60] and silver acetate (AgC₂H₃O₂) [61]. Reducing agents include sodium citrate (Na₃C₆H₅O₇), sodium borohydride (NaBH₄), hydrogen (H) and many other copolymers. The reducing agents' role is to reduce silver ions (Ag⁺) to metallic silver (Ag⁰). Next, these are agglomerated into oligomeric clusters, which begins the colloidal AgNPs formation. It is necessary to use stabilisers to protect the nanoparticles and avoid them becoming agglomerated. [62]

Seed-mediated growth method

Murphy and coworkers first reported the synthesis of gold and silver nanorods using the seed-mediated method (see Figure 2.7) [63], [64]. First, small spherical seed particles were prepared in the presence of trisodium citrate by a reduction of sodium borohydride. These seeds were then added to a growth solution that contained hydrogen tetrachloroaurate (H[AuCl4]) and cetyltrimethylammonium bromide (CTAB) along with a weak reducing agent in ascorbic acid. This method produced nanorods with aspect ratios of 4.6±1. By employing a three-step seed technique, the aspect ratio was increased.

One of the important factors crucial to nanorod synthesis is the time interval between transferring solutions and this influences the aspect ratio. Another important factor is the pH control as it can be used to increase the yield. Increasing the pH resulted in nanorods increased aspect ratio. Increased aspect ratio led to an increase in polydispersity. A slight increase in the aspect ratio of was also reported by adding heptane to the growth solution [65]. This was reported to be due to the ability of alkanes to solubilise CTAB in water in a way that is dependent on the chain length, hence alkanes affect the CTAB adsorption onto gold nanoparticles. The influence of pH on silver nanorods was also reported [64]. The reduction potential of ascorbic acid has been reported to change with the pH value, thus resulting in different shapes and sizes of nanoparticles.

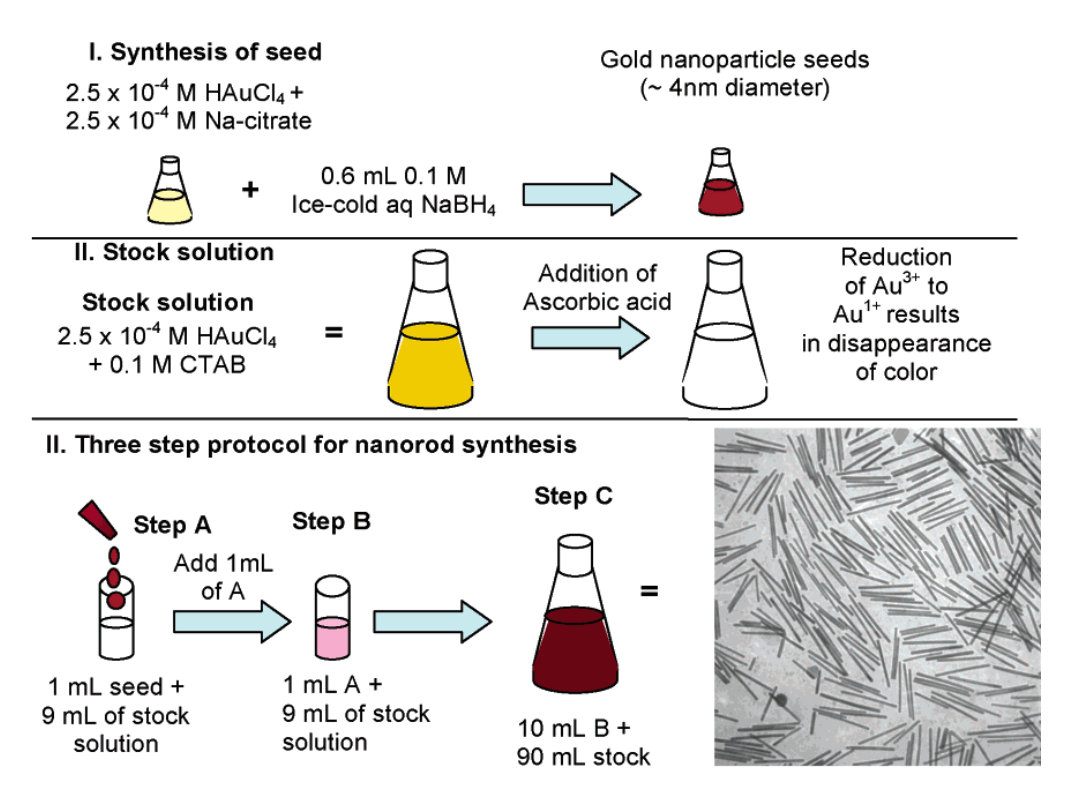


Figure 2.7. Seed-mediated growth approach used by Murphy and co-workers to synthesise gold and silver nanorods. (bottom right) Transmission electron micrograph of gold nanorods that are an average of 500 nm long. [66]

Many synthesis parameters, such as seed concentration, surfactants concentration, reaction temperature and size and nature of the seed particles, have also been reported to influence nanoparticle size and shape [37–40]. Murphy and coworkers reported the increase in the aspect ratio of gold nanorods with decreasing seed concentration [63]. The seed concentration was varied, and it was concluded that for the formation of rods, a lower amount of Au³⁺ ions per seed particle was available, leading to a reduced aspect ratio. In silver nanorod synthesis, the same effect was noticed [70]. For the growth of nanorods, the seed size and stabilising agent also have a great impact. Smaller seed particles apparently contribute to an increase in the fraction of gold nanorods and an increase in aspect ratio relative to larger seeds.

In the development of seed particles, the size can be influenced by the age of the seeds, as well as by the stabilising agent used. It is possible to achieve the growth of smaller seeds by further applying the growth solution and the reduction agent. In addition, the surfactant used in the growth solution also has an important effect on the rods' resulting aspect ratio. In the seed-mediated growth process, CTAB is an effective surfactant (see Figure 2.8 for its chemical structure). Neither a change in tail length nor varying the counter ion led to any change in the aspect ratio of

nanorods [68]. For different counter ions and shorter tail lengths, the cause was due to decreased adsorption of some crystal phases. In longer tail lengths, it was due to lower solubility. A certain amount of sodium bromide was applied to the solution to prove the first theory, and the concentrations of CTAB, cetyltrimethylammonium chloride (CTAC) and dodecyltrimethylammonium bromide (C₁₂TAB) were varied. Accordingly, gold nanorods were produced in the first two instances, but rod formation was not observed in the latter. It was therefore believed that Br⁻ ions adsorb on crystal faces, while the surfactant, due to the contribution of hydrocarbon interactions, helps stabilise the growing particles [71].

Figure 2.8. Molecular structure of Hexadecyltrimethylammonium bromide (CTAB), a cationic surfactant used in nanorod synthesis. [72]

Gold nanorods were also synthesised using binary surfactants, where benzyldimethylammonium chloride (BDAC) was applied to the solution, along with CTAB. This led to an increase in the aspect ratio, as compared to using CTAB only. The surfactant concentration was varied and found to affect the growth of the nanoparticle. An increased in the surfactant concentration led to enhanced aspect ratio [69]. The temperature also influenced the growth of gold and silver nanorods. Increasing temperature led to reduced aspect ratio, and increase in monodispersity [67]. Murphy and colleagues developed a new nanorod synthesis method based on the addition of silver nitrate [73]. The yield and aspect ratio of nanorods could be regulated with this technique by simply changing the concentration of seeds. They reported that Ag+ ions form AgBr and direct the growth of nanorods to adsorb on certain crystal faces. The yield of spherical particles, however, was between 40-50% and the other major shape was bipyramids.

Advantages and disadvantages of seed-mediated growth method of nanorods Advantages:

- Precise control over the size and shape of nanorods: Seed-mediated synthesis allows for the precise control over the size and shape of nanorods by varying the concentration of reactants, reaction time, and temperature.
 This results in a high degree of reproducibility and uniformity in the synthesised nanorods.
- High aspect ratios: This method can produce high aspect ratio nanorods with lengths up to hundreds of nanometers, making them suitable for various applications such as in nanoelectronics, biomedical imaging, and catalysis.
- Improved stability and homogeneity: The use of seed particles results in improved stability and homogeneity of the nanorod solution compared to other methods. Seed-mediated synthesis also enables the synthesis of monodisperse nanorods with uniform properties, which is essential for certain applications.

Disadvantages:

- Time-consuming: Seed-mediated synthesis can be a time-consuming process, as it requires the preparation of a seed solution before the growth of nanorods can be initiated. This can be a significant disadvantage for largescale production.
- Sensitivity to reaction conditions: The formation of nanorods in this method is highly sensitive to reaction conditions such as temperature, concentration, and pH. Any deviation from the optimal conditions can lead to the formation of unwanted morphologies or low yield of nanorods. The stability and reactivity of seed particles can change over time, affecting their efficiency in nanoparticle synthesis. As seed particles age, their surface chemistry may alter due to oxidation or aggregation, leading to inconsistencies in nanorod formation.
- High cost: The synthesis of seed particles can be expensive and timeconsuming. The use of specialised equipment such as ultrasonic probes and centrifuges may also add to the cost of the synthesis process.

Polyol method

A solution-phase approach, the so-called polyol synthesis, is the most studied

technique to synthesise silver nanorods [10-13]. A similar schematic process is shown in Figure 2.9. Silver nanorods were produced using this method by Jiu at al. [74]. First, AgNO₃ was reduced by ethylene glycol (EG) at approximately 150 °C to produce seed particles. Next, AgNO₃ and poly (vinyl pyrrolidone) (PVP) solutions were added to the seed solution drop by drop. Here, EG acts as a solvent and reducing agent. PVP acts as the surface modifier and controls the growth rate of certain crystal faces. Other parameters, such as temperature, seed conditions and AgNO₃ to PVP ratio were varied. The aspect ratio of nanorods decreased when temperature was increased. When the temperature was less than 100 °C, there were only a handful nanorods. Increasing the seed concentration resulted in decreased nanorod diameter. The PVP to AgNO₃ ratio greatly influences the size and shape of the nanoparticles [77]. When the PVP to AgNO₃ ratio was increased, spherical nanoparticles were produced. This was due to the high presence of PVP on all seeds' faces. A drop in the ratio of PVP to AgNO₃ resulted in increased nanorod diameter. In addition, the nanorods had rougher surfaces. It was suggested that reduced PVP to AgNO₃ ratio resulted in a reduction in coverage of all faces, including the side surfaces. Hence, the nanorods could then grow thicker due to this missing passivation of the side faces. Sun et al. concluded from their study that nanorods have a pentagonal cross section together with a pentatwinned crystal structure [78].

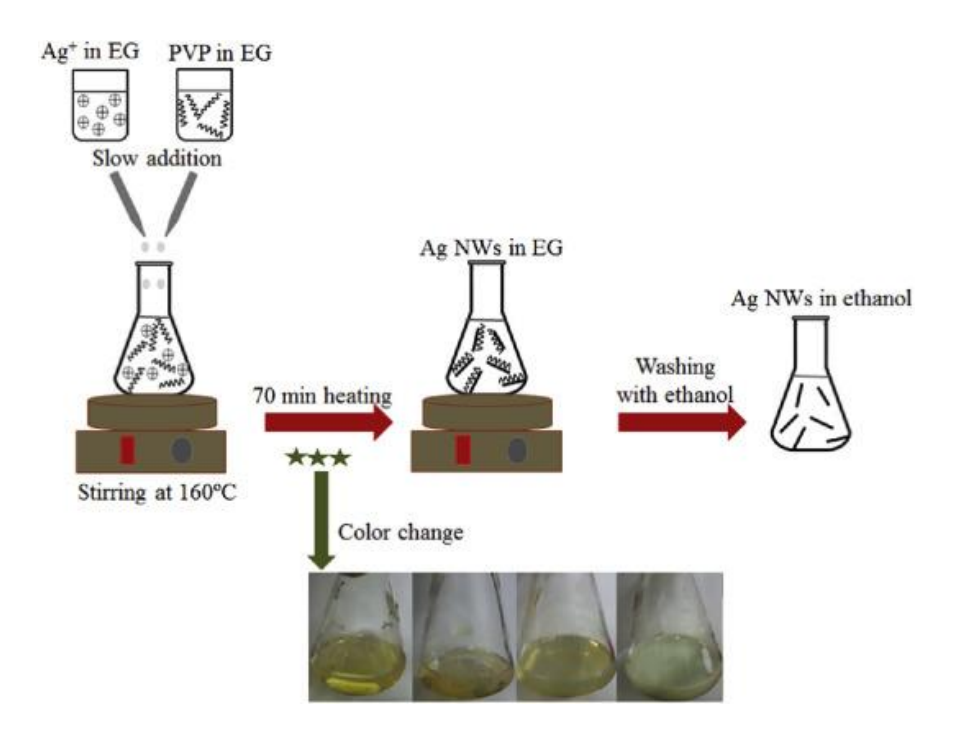


Figure 2.9. Schematic representation of the polyol synthesis of Ag nanowires [79]

Nanorods, nanowires, and microrods differ primarily in size and aspect ratio. Nanorods have diameters of a few to tens of nanometers and lengths up to a few hundred nanometers. Nanowires are significantly longer, often extending to several micrometers, with a high aspect ratio (>100:1). Microrods are larger in both diameter and length, typically in the micrometer range. A study by Wiley et al. used a shape-controlled polyol synthesis method to produce various shapes including cubes, bipyramids and nanowires [80]. The addition of NaCl in the reaction solution produced nanocubes. When NaCl was replaced by NaBr, bipyramids were formed, and combining NaCl with Fe produced nanowires. Li et al. concluded from their study that a low concentration of NaBr produced nanocubes and higher concentration yielded nanorods [81]. For the synthesis of silver nanowires, the use of inorganic salts of iron, copper, zinc and sodium resulted in higher amount of nanorod production. It has been concluded that this effect is caused by the accumulation of Cl- ions.

A seedless polyol synthesis of silver nanorods has been reported by Maiyalagan [82]. This technique doesn't require pre-synthesised seed particles as these are formed at the beginning of the synthesis, and these grow to become nanorods. Chen et al. introduced a three-step polyol method to synthesise silver microrods [83]. In the first step, silver seed particles were produced, from which nanowires

were formed. These silver nanowires were then further grown to microrods. The resultant length of microrods was same as nanowires. The aspect ratio between the two was ten times different. The cross section was different for both, with the nanowires being pentagonal and microrods polygonal. This was due to the adsorption of new particles on the (1 0 0) side surface than the (1 1 1) end surface.

Electrochemical method

For this procedure, two electrodes are immersed in the electrochemical cell in an electrolytic solution to synthesise gold and silver nanorods [84]. A cationic surfactant and a structure-directing cosurfactant comprise the electrolytic solution. As a cationic surfactant, Hexadecyltrimethylammonium bromide (CTAB) is frequently used, acting as a supporting electrolyte and stabilizing the particles. Tetradodecylammonium bromide (TC₁₂AB), a stronger hydrophobic cationic surfactant, is used as the rod-structure-directing cosurfactant. The experiment involves an anode, which is a gold metal plate, and a cathode, which is a platinum plate (as shown in Figure 2.10). Experiments are carried out in an ultrasonic bath at high temperatures. Small quantities of acetone and cyclohexane are added into the cell before electrolysis. Acetone loosens the micellar framework allowing TC₁₂AB into the CTAB micelles, and cyclohexane allows for enhanced formation of rod-like CTAB micelles [85]. Electrolysis current is regulated between 3 and 5 mA and varying electrolysis time is used in the process. The resulted gold nanorods have a wide distribution of aspect ratios [84]. Silver plates can be incorporated in the electrolytic solution to improve the nanorods' aspect ratio. The concentration and rate of release of silver ions is a major factor in controlling the aspect ratio of nanorods. Varying the silver plates in the electrolyte solution can allow the control of these parameters [86].

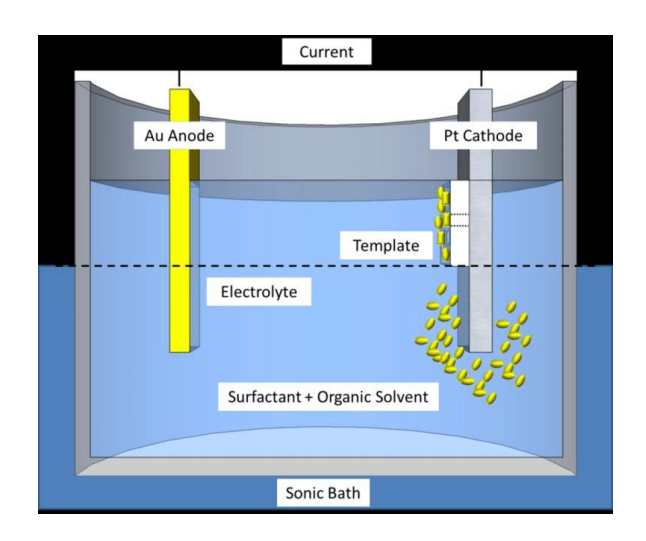


Figure 2.10. Electrochemical growth of gold nanorods [87]

Silver nanorods have also been prepared inside a two-electrode style cell [88]. A platinum sheet is used as the cathode, and the anode is a platinum wire. The electrolyte is made up of polyethylene glycol (PEG) and silver nitrate (AgNO₃). The nanorod formation is influenced by both of their concentrations. Rods are formed when PEG concentration is between 0.5-2 %, and higher concentration increased the viscosity thus producing no rods. It is suggested that PEG behaves as a stabiliser that can facilitate the formation of silver nanorods. The AgNO₃ concentration also needs to be in a certain range in order to produce silver nanorods [88].

Photochemical methods

For this procedure, an aqueous solution containing a surfactant and hydrogen tetrachloroaurate (HAuCl₄) was irradiated with UV light (wavelength 254 nm) to form gold nanorods [89]. The time of irradiation as well as the concentration of HAuCl₄ influenced the aspect ratios of the gold nanorods obtained. By adding silver nitrate to the solution, the amount of gold nanorods could be increased [90]. Silver nanorods have also been synthesised using the same procedure, and silver nitrate was used as the precursor [91]. Silver nitrate and surfactant (poly (vinyl alcohol) (PVA)) concentrations were varied and have been shown to affect the size and shape of resulting nanoparticle. Increasing AgNO₃ concentration led to an increase in the length and width of nanorods, when the PVA concentration was constant. When concentration of AgNO₃ increased further, it resulted in the formation of dendrites, this is explained due to the presence of excess silver in the

solution. This can support the aggregation and therefore result in development of dendrite shapes. Different PVA concentrations were used, whilst AgNO₃ concentration was kept constant. PVA concentration was found to control the size of the nanoparticles. Low concentrations produced irregular shapes. It was concluded that PVA acts like a surface modifier, and increasing its concentration leads to formation of different shaped nanoparticles [91].

Zhang et al. produced silver nanorods of different aspect ratios using photoinduced synthesis by varying the wavelength between 600 and 750 nm [92]. This approach is based on seed-mediated synthesis, where the seed particles are grown in a growth solution consisting of AgNO₃ and trisodium citrate (TSC). Nanorods with pentagonal cross sections, as well as uniform diameters and lengths, were produced from this method. These were penta-twinned along the longitudinal axis. Increasing the radiation wavelength resulted in increased nanorod length, and decreased width. The explanation for this was that reduction rate of Ag⁺ depends on the wavelength. This was explained by a wavelength-dependent reduction rate of Ag⁺, which at lower energy excitation wavelengths is slower and more kinetically regulated. Nanorods with higher aspect ratio were produced due to preferred reduction on the tips compared to the particle sides.

Microwave method

Gold nanorods were synthesised using a closed chamber microwave method [93]. HAuCl₄, trisodium citrate (TSC), acetone and tetradecylammonium bromide (TOAB) were rapidly heated in a microwave. An optical fiber was used to monitor and regulate the temperature. The study analysed the effect of TOAB concentration, and the reaction temperature rise rate, as both parameters play a major role in nanorod synthesis. Increasing TOAB concentration and reaction temperature rise rate resulted in increased aspect ratio of nanorods. Only spherical gold nanoparticles were produced without TOAB, while a concentration of 4.0 mM resulted in a significant amount of nanorods. Nanorods with aspect ratio of 25 and greater were formed when the reaction temperature rise rate was increased. The authors reported two possible explanations for this increase in aspect ratio: first explanation is that as the temperature rise rate is increased,

different micelles are formed. Secondly, it relates to formation of metal nanoparticles. Two phases are involved here, in the nucleation and the seed growth. Both phases are competing, and the nucleation of particles is highly temperature sensitive. A temperature increase could therefore lead to a change in the dimensions of the particles.

Tsuji et al. used a microwave-polyol method to synthesise silver nanofilms, nanorods and nanowires [94]. The reaction was carried out in a microwave oven containing a condenser, a thermocouple, and a Teflon coated magnetic stirrer (shown in Figure 2.11). A glass flask containing H₂PtCl₆·6H₂O solution, EG, AgNO₃ and PVP was placed in the oven. First, platinum seed particles are formed, which are then grown into silver nanorods. The group also studied the effects of various parameters such as concentration of different chemicals, heating time and microwave power. Also, the influence of seed particles and CI- ions on nanorod formation was analysed. It was understood that Pt seeds have no effect on the nucleation and nanorod formation. Rather, it's the CI ions that are responsible for nanorod formation [95].

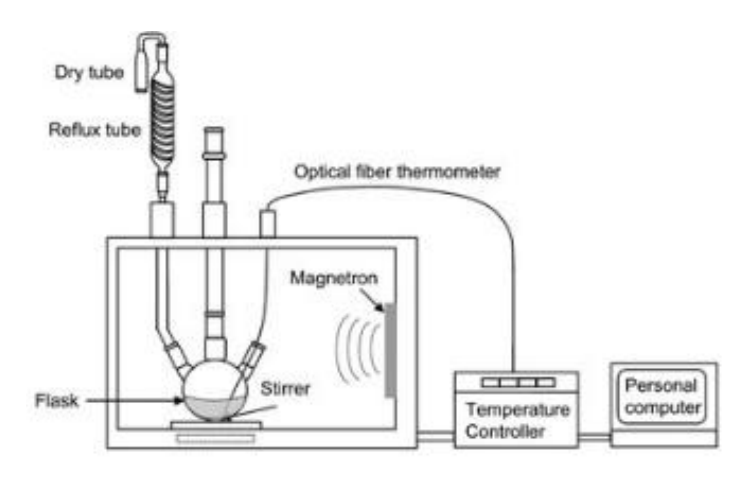


Figure 2.11. Apparatus used for the microwave-assisted synthesis of metallic nanostructures [94]

Gou et al. synthesised silver nanowires with using a microwave-assisted polyol synthesis [96]. Their approach varied the amount of NaCl to the solution, without using seed particles. Synthesis was performed at 300 W. At low NaCl to AgNO3 ratio, only nanospheres and nanocubes were formed. Varying the heating power and heating time did not have any effect. The formation of nanowires began when the ratio of NaCl to AgNO₃ was increased.

Template method

The template method for gold nanorod synthesis was introduced by Martin and colleagues [97]. A schematic of template-based synthesis is shown in Figure 2.12. They used electrochemically prepared alumina template membranes in their studies. These membranes contained cylindrical pores through which gold was deposited using an electrochemical deposition method. The resultant Au/Al composites were optically transparent in the near-infrared and in the visible region. In addition, the composite colour can be reproducibly changed by varying the size and shape of the particles.

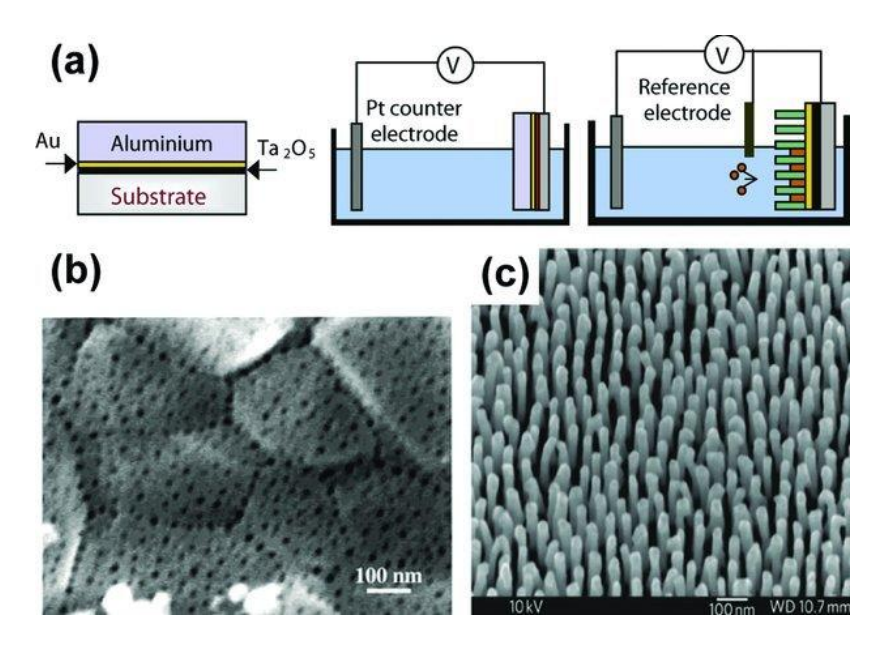


Figure 2.12. Porous membrane-templated synthesis of gold nanorods. (a) schematic of gold deposition, template membrane formation and nanorod (b) SEM image of porous alumina membrane. (c) SEM image of free-standing array of gold nanorods [98]

Van der Zande et al. synthesised gold particles by using electrodeposition of gold in nano-porous aluminium oxide [99]. Prior to depositing gold into the membrane pores, low amounts of copper were deposited. The copper can dissolve the membrane, allowing for release of nanorods from the support. Once the nanorods were released, they were dispersed in water and stabilised using PVP. The length of the resulting nanorods is determined by the amount of gold deposited into the pores. It is possible to control the diameter of the nanorods through the template's pore diameter [100].

Colloidal gold and silver nanorods were prepared electrochemically [101]. A

polycarbonate membrane filter was used as a template with one side covered with a thin film of silver. The membranes were dissolved after nanorod deposition. The nanorods were subsequently dispersed in an organic solvent. Ordered silver nanowire arrays were prepared by pulsed electrodeposition in porous alumina [102]. The templates were prepared through a two-step anodisation process. Applying a pulsed electrodeposition helped to overcome pore filling issues. Since there was no uniform barrier at bottom, pores didn't fill completely due to instabilities. Negative pulses were therefore used for pore-specific deposition of metal ions. Using low current, pores with a thicker barrier layer were then filled. The barrier layer capacitance was discharged by using positive pulse to allow for monocrystalline development.

An ethanol-thermal technique was used by Li et al. to synthesise uniform Ag nanorods [103]. Ethanol was employed as a solvent and reducer. An alumina membrane with different diameters was used as the template. Pore diameters were used to control the rod aspect ratio. Using capillary forces, the solution was distributed in the pores. AgNO₃ was reduced by ethanol during heating. Silver particles were deposited on the surface of the pores as they had active sites for nucleation and crystal growth. The reaction went further so long as there was enough reactant supply. This led to build up of particle clusters and thermal annealing was required was nanorod formation.

Hydrothermal method

There have been various studies of hydrothermal methods to synthesise silver nanorods and nanowires. Through a two-step heating procedure, silver nanorods were have been synthesised [104]. After dissolving all the compounds, the solution was first heated to 40°C for one hour, and then to 80 ° C for another 4 hours. This method produced nanorods with lengths of between 150 and 400 nm and a width of 30 nm. Zhou et al. reported a single-step heating procedure [105]. First, AgNO₃ and sodium dodecylbenzene sulfonic acid were dissolved in water using a three-necked flask. Next, ascorbic acid or trisodium citrate were added drop by drop. Finally, the solution was kept at 100°C for 60 min and 30 min to produce nanorods.

A surfactant-less and seedless nanorod synthesis was carried out by Murphy and

coworkers, using two separate silver solutions that were boiled for 60 minutes [106]. The two solutions contained varying fractions of water, AgNO₃ and NaOH. The volume was reduced to 75 mL and doubled by adding water. An autoclave for nanowires synthesis has been reported. A stainless-steel Teflon-lined autoclave was used to mix chemicals and heated in a surface. The reduction of silver chloride by glucose in a surfactant-less synthesis was reported by Wang et al [107]. They suggested that dissociated Ag+ ions are reduced by glucose to from silver nuclei for further grew. Due to the low solubility of silver chloride in water, silver chloride reduction and the generation of silver nuclei was very slow, leading to a low concentration of free Ag+ ions. Therefore, the nanowire growth was ideal for anisotropic growth.

A low temperature silver nanowire synthesis was achieved by Xu et al. using a gemini surfactant and methenamine reducing agent [108]. The AgBr formation was suggested to be obtained from a reaction between AgNO₃ and the gemini surfactant. A balance between AgBr and silver ions was established with the release of the reducing agent at the reaction temperature, which contributed to the production of silver nuclei. Due to the low solubility of AgBr in water and the presence of a surfactant, the formation of silver nanowires favoring anisotropic growth was slow.

Advantages and disadvantages of chemical synthesis of nanorods

Advantages:

- Precise manipulation of size and shape: Chemical synthesis enables accurate manipulation of the size and shape of nanorods, allowing for optimal customisation of their properties and uses.
- Attainment of high purity: Chemical synthesis facilitates the production of nanorods with high levels of purity, which holds significant importance in various fields, including medicine.
- Ease of scaling up: Chemical synthesis offers a scalable approach, simplifying the production of substantial quantities of nanorods with relative ease.
- Adaptability: Chemical synthesis possesses versatility, as it can be employed to generate diverse materials and can be tailored to meet specific application requirements.

Disadvantages:

- Challenging nature: The production of nanorods involves intricate procedures,
 necessitating specialised equipment and knowledge.
- Hazard potential: The utilisation of certain chemicals in the synthesis procedure can pose risks to both workers and the environment, necessitating safety precautions. The evaporation-condensation method poses several hazards, including high-temperature risks that can lead to burns or equipment failure, as well as inhalation of airborne nanoparticles, which may cause respiratory issues. Toxic gas emissions from precursor materials necessitate proper ventilation, while highly reactive substances increase the risk of uncontrolled reactions or explosions. Additionally, the method's high energy consumption contributes to environmental concerns, making it less sustainable.
- Financial considerations: Chemical synthesis can incur substantial costs,
 especially when aiming to produce nanorods of superior quality.
- Consistency concerns: Achieving consistent results through chemical synthesis can be problematic, especially during the scaling-up process. Minor deviations in the synthesis procedure can lead to noticeable variations in the properties of the produced nanorods. For example, Murphy et al. found that changes in seed concentration affected nanorod aspect ratio, with lower seed concentrations leading to longer nanorods [73].

2.3.3 Physical methods

There are various methods of synthesising Ag nanoparticles using biological, chemical, and physical methods. Scheibel and Porstendorfer developed an evaporation-condensation method to synthesise silver nanoparticles [109]. In this method, a small amount of bulk material is placed on crucibles which are placed on a boat inside the furnace. The material is vaporised at elevated temperatures and a gas carries the vapour out of the furnace. Typically, an inert gas such as Nitrogen is used. The rapid decrease in temperature condenses the vapour, leading nanoparticles to form. Despite being a simple method, the evaporation-condensation synthesis requires a lot of energy and is time-consuming. It is useful when synthesis [110]. The

evaporation/condensation method has been used to synthesise nanoparticles from materials including, silver, gold, and fullerene [111], [112].

Laser ablation is another type of physical method for AgNP synthesis. In this method, a bulk material plate is dipped in liquid solution and ablated. This generates a plume of plasma which is used to synthesise nanoparticles. Compared to reduction methods using chemicals, laser ablation is a reliable method. It is also a more environmentally friendly method. Laser ablation for the synthesis of Ag NPs has been used in numerous studies and some of earliest ones were conducted during 1990s [113], [114], [115]. The ablation efficiency and nanoparticle properties are dependent on the laser type used [116], [117]. The main advantage of using this method is it requires no chemical agents. Studies show that femtosecond laser pulses produce efficient nanoparticles then nanosecond laser pulses [118], [119]. According to Hamad [118], femtosecond lasers are superior to the nanosecond laser for precision material processing. Femtosecond lasers are more effective to produce nanoparticles than those with longer pulse durations.

Below is a table showing some of recent studies on silver nanoparticle synthesis using physical methods. The advantage of the method and the applications are also listed. There are numerous studies on the synthesis of silver nanoparticles using various physical methods. Of the physical synthesis methods not discussed in detailed, others include physical vapour deposition, and arc discharge.

Table 2-1 Some of the physical methods of AgNPs synthesis, along with their advantage and applications

Method overview	Advantage	Application	Reference
ZnO/Ag nanoparticle	Allows synthesis	Increase the	[120]
was synthesis by	without metal	catalytic activity in	
using pulsed laser	precursors and	ZnO	
ablation in liquid	reductant or	nanostructures	
	capping agents		
Synthesis of Au-Ag	Offers very high	Surface	[121]
core shell and	peak laser intensity	enhanced Raman	. ,
nanoalloy using	at lower pulse	scattering	
femtosecond laser	energy.		
ablation			
Ag@SiO2-Penicillin	Avoids toxicity	Enhance the	[122]
synthesised	related to impurities	bactericidal	[]
electromagnetic	from nanoparticle	efficacy and	
levitation gas	preparations. A	safety of	

condensation (ELGC)		Ag NPs against	
method		antimicrobial	
		resistant	
		organisms	
Polyindole stabilized	Reflux	Pigments, gas	[123]
silver-cobalt oxide	condensation	sensor, lithium ion	
(Pind/Ag-Co3O4)	prevents the solvent	batteries,	
nanocomposites	from boiling away.	electrochemical	
were synthesised by		devices, carrier	
reflux condensation		for the antibiotic	
method		delivery	
Silver/polymer	The γ doses boost	Organic	[124]
composite (Ag/PVA)	the electrical	electronics and	[]
films were irradiated	conductivity and	electrical devices	
with gamma (γ)	change its		
radiation	conduction		
	behaviour		
Ag-doped ZnO thin	Allows rapid effect	Solar energy in	[125]
films were deposited	of the surface areas	photovoltaic	
by pulsed laser	materials allowing	devices, as well	
deposition and	local diffusion of	as in	
subsequently laser	species, surface	photodetectors	
annealed	melting, ultra-rapid	and photo-	
	crystallisation	catalysis	
Laser ablation	Suitable for	Catalysts,	[126]
deposition was used	producing	electrical	
to synthesise silver-	multicomponent	contacts,	
nickel bimetallic	thin films has	switches, and	
nanoparticles	relatively low	conductor	
	substrate	material plating	
	temperature and		
	high deposition		
	rates		

Advantages and disadvantages of physical synthesis of nanorods

Advantages of physical synthesis of nanorods:

- Manipulation of size and shape: Physical synthesis techniques like vapour deposition and sputtering offer effective control over the dimensions and morphology of nanorods.
- Attainment of high purity: Physical synthesis methods enable the production of nanorods with exceptional levels of purity, a critical factor in various fields, including electronics.
- Consistency in characteristics: Physical synthesis methods generate nanorods with remarkable uniformity in size and shape, a crucial aspect for numerous applications.

Disadvantages of physical synthesis of nanorods:

- Equipment prerequisites: The utilisation of physical synthesis methods necessitates specialised and potentially costly equipment, posing challenges in terms of acquisition and operation, especially when scaling up.
- Material constraints: Physical synthesis methods generally have limitations regarding the range of materials that can be effectively deposited using the chosen technique.
- Intricacy: Physical synthesis methods can be intricate and demand proficient operators with the necessary expertise.
- Consistency concerns: The reproducibility of results may pose challenges in physical synthesis, especially during the scale-up process. Minor deviations in the synthesis procedure can lead to notable variations in the properties of the resulting nanorods.

2.3.4 Biological methods

As the understanding of nanoparticles properties and synthesis methods improved, new synthesis methods have been developed. These methods are based on using natural agents to produce nanoparticles. Namely, bacteria, fungi, plant extracts and other 'green' synthesis methods have received attention. These methods are useful for small batch synthesis and are ways to reduce harm to the environment. Commonly silver nitrate is reduced using biological sources.

	Biological synthesi	s of silver NPs	
Bacteria	Plants	Fungi	Algae
Aeromonas sp. SH10	Aloe vera leaf extract	Nitrate reductases	Spirulina platensis
(Bacterium)	(Plant)	(from Fusarium oxysporum)	(Alga)
Klebsiella pneumonia	Azadirachta indica	Phaeneroechaete	Oscillatoria willei
(Bacterium)	(Plant)	chrysosporium	(Alga)
Lactobacillus strains	Cinnamomum camphora	(Fungus)	Gelidiella acerosa
(Bacteria)	(Plant)	Verticillium sp.	(Alga)
Pseudomonas stutzeri AG259	Emblica Officinalis	(Fungi)	
(Bacterium)	(Plant)	Aspergillus flavus	
Corynebacterium sp. SH09	Pelargonium graveolens	(Fungus)	
(Bacterium)	leaves (Geranium)	Aspergillus	
Enterobacter cloacae	(Plant)	fumigatus	
(Enterobacteriacae)(Bacterium)	Pelargonium graveolens	(Fungus)	
	leaves (Geranium)	Fusarium oxysporium	
	(Plant)	(Fungus)	
	Pinus eldarica	Fusarium	
	(Plant)	semitectum	
		(Fungus)	

Figure 2.13. List of various bacteria, fungi, plants and algae used to synthesise AgNPs [127]

Microorganisms

In the bacterial synthesis, bacteria are used to synthesise nanoparticles, hence they are known as bio-factories. Specifically, these methods are used mostly for silver due to the biological properties it possesses. It is possible to synthesise nanoparticles with various shapes and sizes. Examples of bacteria used to synthesise silver nanoparticles include Lactobacillusfermentum [128], Bacillus flexus [129], Escherichia coli [130], Streptomyces hygroscopicus [131], and many more. These nanoparticles are affected by the pH, temperature, and silver nitrate concentration.

Numerous studies have shown that fungi can be used to produce nanoparticles. They can secrete nanoparticles as products using the metal ions and offer high yield and stability. The mechanism involved is that an metal ion is trapped by the fungal cell and reduction enzymes break it down [132].

Plants

Nanoparticles have been synthesised using plant extracts. It is economic and can be used to synthesis large scale production [133]. Tea extracts such as Camellia sinensis (green tea) and black tea have were used to produce silver nanoparticles [134], [135]. They produced stable nanoparticles with different shapes such as spheres, trapezoids, prisms, and rods. Polyphenols and flavonoids seemed to be responsible for the biosynthesis of these NPs.

There are lots of methods to produce nanoparticles. In this section, only a summary of some methods was discussed. Some other methods of nanoparticle synthesis include photosynthesis (using light), electrochemical, microwave, irradiation, etc.

Advantages and disadvantages of biological synthesis methods

Advantages of biological synthesis of nanorods:

- Sustainable approach: Biological synthesis methods employ natural materials and processes, offering an environmentally friendly alternative to chemical or physical methods.
- Economically viable: Biological synthesis methods prove to be cost-effective by utilising inexpensive materials and often eliminating the need for specialised equipment.

- Enhanced biocompatibility: Biological synthesis methods yield biocompatible nanorods, rendering them suitable for various medical applications.
- Ease and scalability: Biological synthesis methods are characterised by simplicity and scalability, facilitating large-scale production.

Disadvantages of biological synthesis of nanorods:

- Material constraints: Biological synthesis methods are commonly restricted to specific materials that can be synthesised through biological processes.
- Reduced precision in size and shape control: Biological synthesis methods generally yield nanorods with less meticulous control over their size and shape compared to chemical or physical methods.
- Consistency concerns: Reproducibility may pose challenges in biological synthesis methods, as the involved biological processes can be influenced by various factors, resulting in variations in the properties of the produced nanorods.
- Slower production: Biological synthesis methods can be time-consuming due to their reliance on biological processes, which inherently require a certain duration to complete.

2.3.5 Continuous flow synthesis of silver nanoparticles

Due to the rising popularity of nanotechnology, there is an increasing demand for inorganic nanoparticles such as metal oxides, metals, semiconductors, and other more complicated structures [136]. In the past, batch processes were employed in manufacturing nanoparticles. Although various techniques for nanomaterial synthesis have been described in numerous literature resources, large-scale production of nanomaterials remains limited. This gap arises from ineffective and costly production procedures. The flow processes might be a solution to address the limitations associated with the application of periodic processes. Advantages of using flow processes include enhanced operational efficiency of a plant that could be well-matched with increasing requests on nanomaterials and preservation of highly pure products possessing precisely determined physical and chemical properties. Certainly, in applications requiring accurate mixing, rapid heat transfer and fast

reactions as opposed to batch processing, the execution of reactions in intensified continuous flow reactors is highly advantageous [137]. In the use of continuous flow processes, processing benefits include waste minimisation by efficient use of reagents, improved handling of dangerous chemicals and improved yields of reactions. Reactants may be easily cooled or heated during the reaction phase due to the high surface-to-volume ratio in flow reactors [138]. In addition to the numerous advantages of heat transfer, kinetics and mixing, continuous flow synthesis allows spectroscopic techniques to characterise the product stream in-line without flow disturbance, thus enabling the monitoring, feedback and creation of self-optimisation techniques in real time [139]. From discovery to production of high yield reactions including pharmaceuticals, nanostructures and advanced organic materials, intensified reactors have found an ever growing number of applications in synthetic chemistry [140].

The main challenge in the synthesis of inorganic nanoparticles is to develop consistent processes and materials that produce particles with exact structural characteristics, such as size, shape, and distribution [141]. The synthesis method also needs to be commercially feasible. Even though they make up a small portion of a product, nanoparticles have a big impact on its cost and functional qualities later on [142]. Therefore, it is crucial to maintain high-quality nanoparticles regardless of changes in production volume. The physical and chemical characteristics of nanoparticles can be influenced by a number of variables related to the kinetics of the reaction and process.

2.3.5.1 Why continuous flow synthesis?

The synthesis of silver nanorods (AgNRs) has traditionally relied on batch methods, particularly seed-mediated growth protocols, due to their simplicity and high control over particle morphology. However, these batch processes suffer from critical limitations when scaling, including poor reproducibility, inefficient mixing, thermal gradients, and batch-to-batch variation [143]. These constraints present significant barriers for industrial applications where large quantities of uniform, shape-controlled nanostructures are required.

As an alternative, continuous flow synthesis—particularly in milli- or microfluidic systems—offers enhanced control over reaction conditions and scalability. In continuous flow reactors, parameters such as residence time, mixing efficiency,

reagent delivery, and heat transfer can be precisely tuned, allowing more reproducible control of nanoparticle nucleation and growth dynamics [144]. Additionally, flow systems offer a higher surface-area-to-volume ratio, facilitating rapid mixing and better control over reduction kinetics, which are especially important in the anisotropic growth of AgNRs.

Continuous flow methods also offer faster mixing of reagents, which reduces the likelihood of aggregation or formation of undesired by-products. Additionally, this method enables inline monitoring through techniques such as UV-Vis spectroscopy and dynamic light scattering, allowing real-time optimisation of synthesis parameters and immediate adjustments to reaction conditions [145]. These advantages make continuous flow synthesis particularly effective for the large-scale production of silver nanorods.

However, there are challenges associated with continuous flow synthesis, particularly when scaling up from laboratory to industrial levels. Maintaining precise control over flow rates, temperature, and mixing efficiency becomes more complex as system size increases [146]. Achieving consistent nucleation and growth for uniform particle size and shape remains a critical issue, as even small variations in reaction conditions can affect the final product [146]. Additionally, reactor design and material compatibility must be carefully considered, as the reagents used in nanoparticle synthesis may degrade or corrode certain reactor materials over time. Despite these challenges, the opportunities presented by continuous flow synthesis, such as real-time optimisation, high throughput, and improved nanoparticle quality, make it a compelling method for the large-scale production of silver nanorods.

2.3.5.2 Continuous flow synthesis using microfluidic and milli-fluidic devices

In recent years, the synthesis of mono-dispersed colloidal nanoparticles has become a significant research topic, as colloidal particles show specific optical, electronic and magnetic properties, making them ideal candidates for engineering applications. As discussed in the literature, colloidal nanoparticles find applications in different areas. The properties and thus applications of these nanoparticles rely on the nanoparticles' form, size and distribution [147]. Therefore, the synthesis of nanoparticles by microfluidic devices has gained considerable interest in recent years. In addition, batch synthesis requires the growth of atom-by-atom particles using the mechanism of

precipitation. Hence particle size and particle size distributions are typically large in case of batch synthesis. It is also necessary to note that downstream processing is required in such a batch process to extract the desired particle size. Due to improved mixing and mass transfer in microfluidic systems, the particle size obtained in microreactors has a smaller and narrower particle size distribution than the batch phase.

Microreactor systems provide higher surface to volume ratio compared to the batch reactors thus the removal of heat is effectively carried out for exothermic reactions. In addition to the synthesis of inorganic, organic and biological materials, microfluidics has been utilised in synthesis of polymeric nanoparticles and hybrid materials. Reaction takes place in small reaction volumes in microreactor systems, so there is less heat and mass transfer resistance that assists in the safe handling of exothermic reactions. Rapid reactant mixing and reagent concentration control can generate precise conditions that are needed for nanoparticle synthesis. The mixing of reactants in the microreactor takes place very quickly and reagent concentration control can create precise conditions that are needed for the synthesis of nanoparticles. Microreactor technology also synthesises hybrid nanoparticles, and at the fluid-fluid interfaces in microreactors, particle size can be manipulated [148].

Gold/silver metal nanorods have been synthesised in a flow reactor by Boleininger et al. using ascorbic acid, CTAB solution and au/ag precursors [149]. CTAB acts as a template, forming micelles for anisotropic growth of particles. The study found that original particles act as seeds in the process of batch synthesis, which increases the overall particle size. Although the seeding of particles is prevented in microreactor synthesis by maintaining short residence times in the microreactor. Lin et al. utilised a flow reactor to synthesise mono dispersed silver nanoparticles using single precursor pentafluoropropionate [150]. The effects of temperature, flow rates and reaction time were studied and the use of a single precursor for the preparation of monodisperse silver nanoparticles was reported. Reports on the synthesis of gold and silver metals and metal oxides and other nanoparticles using microreactor technology are published in numbers [151], [152], [153].

Synthesis of gold and silver nanoparticles in a polydimethylsiloxane (PDMS) microreactor by reducing reactions between metal salt solutions and borohydride with

tri-sodium citrate as the capping agent was performed by Singh et al [154]. Gold nanoparticles were synthesised by Wagner and Köhler through a microreactor citrate reduction reaction, using polyvinyl pyrrolidone as stabiliser [153]. The study found that the mean particle size increases with a decreasing flow rate, and also observed that particle growth is observed if the concentration of gold ions is equal to the concentration of seeds. In another article, Wagner et al. synthesised spherical AuNPs ranging in size from 5 to 50 nm using gold precursor and ascorbic acid at different flow rates [152]. They reported that compared to batch synthesis, a reduction in small size is achieved by doubling the flow rate. By responding to barium chloride and sodium sulphate solutions by precipitation reaction, Jeevarathinam et al. synthesised the barium sulphate nanoparticles [155]. They found that in such precipitation reactions carried out in a microreactor, mixing is a very critical parameter. Due to local mixing, the particle size is found to be decreased, giving higher local nucleation results in a reduction in the distribution of particle size. They have also observed that the particle size is found to be decreased by decreasing the flow rate of barium chloride.

2.3.5.3 Process parameters in continuous flow synthesis

Using exact control techniques is crucial for producing high-quality nanoparticles. The size, shape, and chemical characteristics of the nanoparticles as well as the effectiveness of the process can be affected by a number of variables, including residence time in the reactor, reactant flow rates, temperature, energy transfer technique, and reactor specifications [156], [157]. The ultimate properties of the nanomaterials can be altered by varying certain factors.

A chemical reaction's result in flow synthesis is greatly influenced by a number of important parameters [158], [159], [160]. Precise control of these variables is essential to getting the desired nanoparticles. The rate at which reactants pass through the flow reactor is one of these parameters [153]. The residence time of the reactants in the reactor and the size of the reaction are both impacted by this rate [161].

The concentration of reactants in the reaction mixture is another important consideration. The rate of reaction and the desired products' selectivity are directly impacted by this concentration. In addition, temperature is important because it influences the thermodynamics and kinetics of the reaction, which basically determines the direction and pace of the process.

Another important factor that affects the reaction's kinetics and thermodynamics as well as the solubility of the reactants and products is pressure. Additionally, the flow reactor's mixing efficiency is critical since it influences the reaction rate as well as the reactor's selectivity for particular products.

Since catalysts can significantly boost both the reaction rate and the selectivity towards desired products, their usage in the reaction mixture is essential. Moreover, the kinetics of the reaction and mixing can be greatly influenced by the injection procedures, which dictate how reactants are supplied into the flow reactor. Lastly, the kinetics and mixing of the reaction are affected by the physical parameters of the flow, such as its direction and velocity.

2.3.6 Summary

A number of synthesis methods for anisotropic nanoparticles have been discussed above, and each has its advantages and disadvantages. Generally, chemical synthesis methods are relative easier and allow better control of synthesis (in terms of nanoparticle morphology) compared to physical and biological methods. For the physical methods, the processes are energy-intensive and are expensive as they require more complex equipment. For the biological methods, it is quite difficult to control the process parameters such as pH, temperature, moisture, and result in high impurity. Even some chemical methods such as electrochemical and photochemical methods require special apparatus to carry out synthesis. The synthesis is fairly challenging in the aforementioned methods. Of all the methods, the seed-mediated synthesis is much easier as it can be carried out in a single reactor. This method allows precise control over nanoparticle dimensions, operational simplicity, and scalability. Unlike other synthesis methods, such as template-assisted or polyol-based approaches, seed-mediated synthesis enables fine-tuning of nanorod aspect ratios by adjusting seed concentration and growth conditions, ensuring reproducible and monodisperse anisotropic nanoparticles [162]. Additionally, this method operates at room temperature without the need for specialised equipment, making it cost-effective. The use of surfactants, such as cetyltrimethylammonium bromide (CTAB), further enhances the process by stabilising specific crystal facets, directing controlled anisotropic growth, and preventing aggregation [162].

Besides, this method requires no templates (which are expensive and complicated to fabricate) nor needs specialised laboratory equipment. Hence, it seems a prime candidate to explore for nanoparticle synthesis in this project. Although, studies using this method have been reported [64], [69], [70], none have targeted absorbance in the NIR regions, and there are problems with reproducibility. There are still unanswered questions for this method. For example, the influence of parameters on the morphology and absorbance has not been studied in detailed. Therefore, it is important to explore this method by systematically studying the effect of each parameter in the seed phase and growth phase to optimise the synthesis. This will allow an improved understanding of nanoparticle growth. By building on the information gained about the nanoparticle growth, the enhancement in the absorbance by controlling the growth would be feasible. Optimal parameters can then be selected for synthesis of nanoparticles that would result in absorption of higher wavelengths. This method also has the potential for scaling up the synthesis which will lead to higher fraction.

2.4 Applications

Anisotropic nanomaterials have been used for different applications due to size and shape-dependent physical and chemical properties. Below are a few of the key applications of various kinds of nanostructures. Where applicable, references to detailed reviews have been specified in the appropriate sections.

2.4.1 Antibacterial applications

Throughout the recent decades, the antibacterial properties of Ag nanoparticles have been growing and more and more antibacterial applications have been reported [163], [164]. Helmlinger and colleagues studied AgNPs in different shapes [165]. By observing the differences in the cytotoxicity and antibacterial effects of silver nanoparticles with different shapes, it can be established that silver nanoparticles have the same cytotoxicity, but they have different antibacterial effects. In the meantime, larger particles with a greater surface area are more toxic to bacteria than smaller particles. The rate of dissolution of particles with a large surface area is greater than the rate of dissolution of particles with a small surface area. The difference in the rate at which silver dissolves enables the synthesis of silver nanoparticles that are more

effective at killing bacteria but less cytotoxic to cells. However, their research did not examine the antibacterial effect of various sizes of AgNPs.

The function of silver nanoparticles was studied by Agnihotri et al [166]. It was reported that 5 nm particles had the highest antibiotic activity. It was discovered that smaller particles exhibited better antibacterial properties, as compared to larger particles. Figure 2.14 illustrates the antibacterial properties of silver nanoparticles of different sizes.

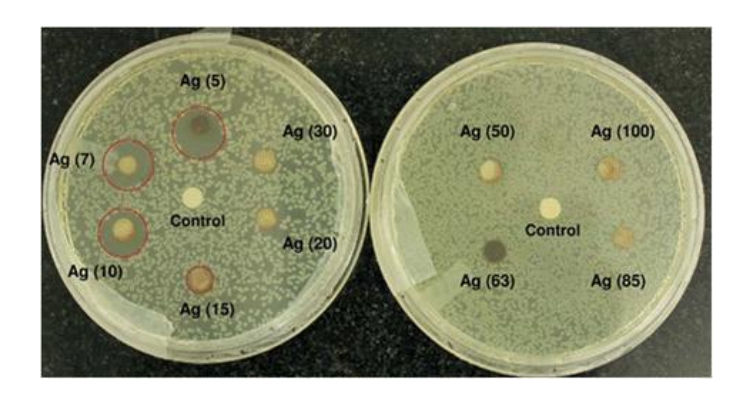


Figure 2.14. Different-sized silver nanoparticles tested in diffusion disks against E. coli MTCC 443 strain [166].

Silver results in enhanced antimicrobial properties when combined with other products. Research on combining various materials including SiO₂@Ag [167], Poly-L-lactic acid (PLLA) microcapsules combined with silver nanoparticles [168], Agdecorated polymeric micelles with curcumin, graphene quantum dot/silver nanoparticle [169] and so on.

The above-mentioned examples are about antibacterial activities. Some of the antimicrobial applications are discussed in the following. A study by Kujda et al. showed that silver nanoparticles can be used as an antimicrobial treatment [170]. The silver particles attach to the bacteria's surface via electrostatic interactions, which allows the bacteria to be ruptured apart by the silver particles. Future applications of silver nanoparticles include using their antibacterial properties while combined with other materials. For example, Meng et al. prepared silver nanoparticles by coating them with silk fibres [171]. The silk could effectively kill some of the existing bacteria and could inhibit the growth of new bacteria. Furthermore, the release of Ag⁺ for the modified silk results in lasting antimicrobial activity, affording the modified silk

sustainable. This research may create novel methods for producing antimicrobial silk for potential textile applications.

Silver nanoparticles coated with zirconia have been developed for use in antibacterial prosthesis [172]. In light of AgNPs' antimicrobial properties and their low toxicity, the biocompatible AgNPs-coated zirconia can be used in the treatment of dental cavities and periodontal diseases. The study will prove that wound healing could be inspired by these findings. The exceptional bactericidal properties of silver nanoparticles are revealed by this research. Additionally, this work will help someone interested in researching antibacterial bacteria.

2.4.2 Applications in catalysis

It has been demonstrated that silver nanoparticles can greatly boost the catalytic ability of chemical reactions. Nano catalysis of silver nanoparticles is a research field that has been growing rapidly these days. The fact that metals such as Ag, Au, Pt, and other metal ions catalyse the decomposition of H₂O₂ to O₂ is well-known. Guo et al. discovered that inserting the silver nanoparticles into the solution of luminol-H₂O₂ could greatly improve chemiluminescence (CL) emission from luminol-H₂O₂ [173]. AgNPs displayed the best catalytic performance of CL in the assays. One reaction that was catalysed by AgNPs was the decomposition of hydrogen peroxide to produce hydroxyl radicals and superoxide anions.

Silver has the highest reaction rate with oxygen, water, carbon dioxide, ethylene, and methanol [174]. Jiang et al. combined silver nanoparticles with silica for enhancing the catalytic properties of Ag, and then used that detect dye reduction [175]. By supporting silver particles on silica spheres, the flocculation of colloidal metal particles can be avoided, which contributes to the efficient catalytic dye reduction. Figure 2.15 shows that the absorbance spectrum of the dyes decreases as the dyes are reduced. Furthermore, silver possesses catalytic properties which are applicable in the fields of water treatments and fibre processing [176].

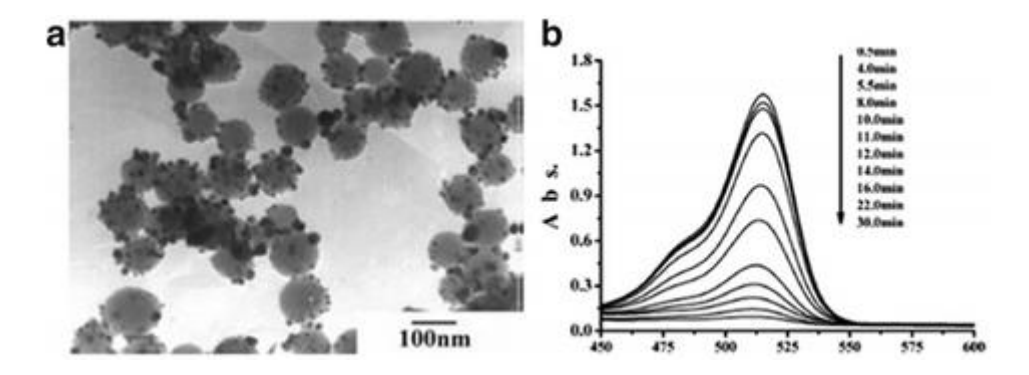


Figure 2.15 (a) Silver nanoparticles attached to silica spheres. (b) The absorbance spectrum of the dyes decreases as the dyes are reduced. [175]

2.4.3 Applications in bioconjugation

In the medical field, one of the most important applications for metallic nanoparticles is that they can be functionalised with biological molecules to target cancer cells [177]. Liao and Hafner studied gold nanorods by for biological applications [178]. They replaced the surfactant bilayer surrounding gold nanorods by ethylene glycol. Bioconjugation of the nanorods was achieved using a heterobifunctional cross-linker, and strip-plate assay confirmed the antibody activity. Conjugation of functionalised nanorods has also been achieved in murine macrophage cells [179]. Takahashi et al. used NIR radiation to conjugate gold nanorods with phosphatidylcholine to study the plasmid DNA release [180]. Metallic nanoparticles can be functionalised with various biomolecules including nucleic acids, antibodies, lipids, etc. which can be used in nanomedicine, cancer diagnostic and tumour therapy [177]. Figure 2.16 shows the schematic description of the protocol used by Chen et al. to conjugate the surface of Au nanocages with antibodies [181]. To examine the molecular binding of bioconjugated nanoparticles, a breast cancer cell line, SK-BR-3, was used. By incubating the SK-BR-3 cells into anti-HER2 antibodies, primary mice antibodies were immobilised on cancer cells. Next, gold nanocages were conjugated with a secondary antibody, and a buffer solution containing IgG-conjugated gold nanocages was added. Fluorescence imaging showed cells of uniform green colour, suggesting a homogeneous distribution on the cell surface.

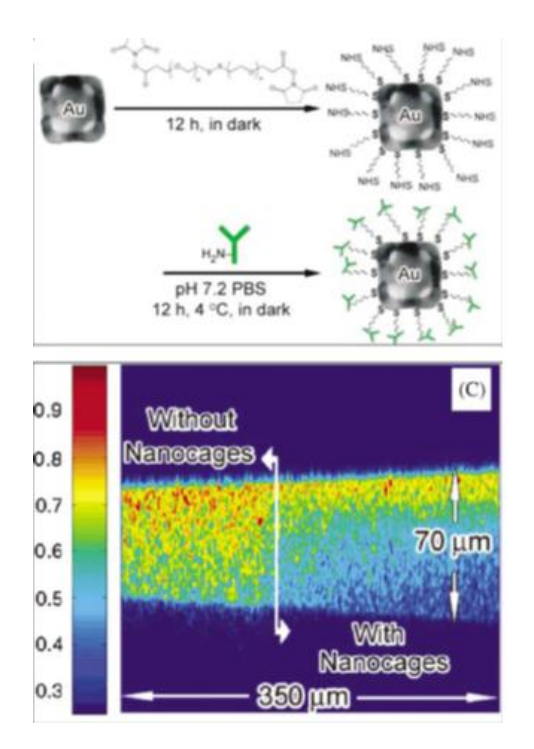


Figure 2.16. Schematic illustration of the protocol used to conjugate antibodies to the surface of Au nanocages. [181]

2.4.4 Photothermal applications

The cells of all living organisms are extremely sensitive to changes in temperature and increases in several degrees can cause cell death. The plasmonic nanoparticles' NIR absorption and associated photothermal effects are other important features of the material. Compared to non-metallic photothermal absorbers, the anisotropic nanoparticles have the additional benefits of in-vivo imaging and therapeutic action. It has been demonstrated that specific nanoparticles such as nanorods, nanocages, nano-shells and nano-stars have an absorptive capacity for NIR light, which can be used for photothermal therapy [145]–[146]. The Au nanocages are capable of producing a local heat that can be selectively applied to cancer cells leading to cell death [185]. Based on the absorption cross-section of Au nanocages, the absorbed photon energy is converted into phonons which raise the system's temperature.

It is shown that ultrafast laser epitaxial growth of Ag nanocages can produce extremely high lattice temperatures [186]. As a modern type of cancer treatment, such therapy is less invasive than chemotherapy or surgery and holds strong promise. A study by Skrabalak et al. demonstrated the photothermal destruction of breast cancer cells by using nanocages with an immune targeting agent [185]. An average nanocage size of

65 nm was conjugated with HER2 antibody to bind onto a breast cancer cell. In this way, the cancer cells were targeted with a NIR laser. By varying the power density and the exposure duration, it is possible to efficiently destroy cancer cells. Cells targeted with the immuno- Au nanocages showed immediate response to laser irradiation and irreversible damage was occurring at power densities greater than 1.6 W/cm² (see Figure 2.17). The level of dead cells increased as time increased following exposure.

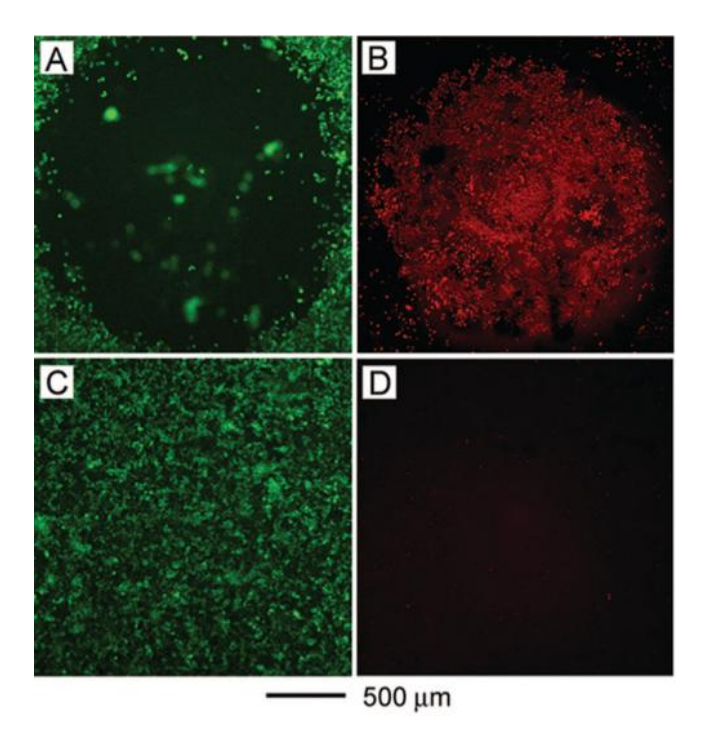


Figure 2.17. (A, B) SK-BR-3 breast cancer cells treated with immuno- Au nanocages, then irradiated with 810 nm light at a power density of 1.5 W/cm² for 5 min. (C, D) SK-BR-3 cells irradiated under the same conditions but without immuno-Au nanocage treatment. [185]

Salem et al. have shown a new non-viral gene therapy technique using multisegmented metal nanorods [183]. Nanotriangles offer another candidate for cancer treatment as a very effective compound. The large NIR light absorption of nanotriangles shows promise in hyperthermic treatment of cancerous cells. The nanotriangle's flat nature would enable it to interact with cancer cells in a more intimate manner, reducing the exposure time. Nanotriangles may also be used to target targeted transmission to the cancer cells, which decreases the risk of toxicity from the metal.

2.4.5 Cancer cell imaging

The high SPR of metallic nanoparticles facilitates imaging with microscopic techniques including dark-field optical microscopy and TPL microscopy. Gold nanoparticles are an outstanding choice for biomedical imaging, due to the much higher light-scattering capability compared to conventional fluorescent dye molecules [188]. Gold and silver nanorods are ideal cancer imaging agents since they possess strong absorption and scattering properties in the near infrared region. Huang and colleagues synthesised a gold nanorods and modified the surface by using PSS and mixing with an antibody solution in HEPES buffer [189]. The nanorods bound to anti-EGFR monoclonal antibodies were added to the cultured cells. Testing was carried out on two malignant cells, and one non-malignant cell. The nanorods bound to malignant cells strongly. Figure 2.18B shows the light-scattering results of nanorods bound to malignant and non-malignant cells. Nanorods exhibit an orange colour, which signifies surface plasmon resonance in the near infrared. The spectroscopic analysis showed that the chemical composition of the cancerous cells is around twice the non-cancerous cells.

A study by Wang et al. reported that a gold nanorod exhibiting LSPR peak of 820 nm, was able to generate photoluminescence signals 58 times stronger in comparison to rhodamine molecule [190]. There have been also been other studies on using gold nanorods as contrast agents for imaging of cancer cells [191], [192].

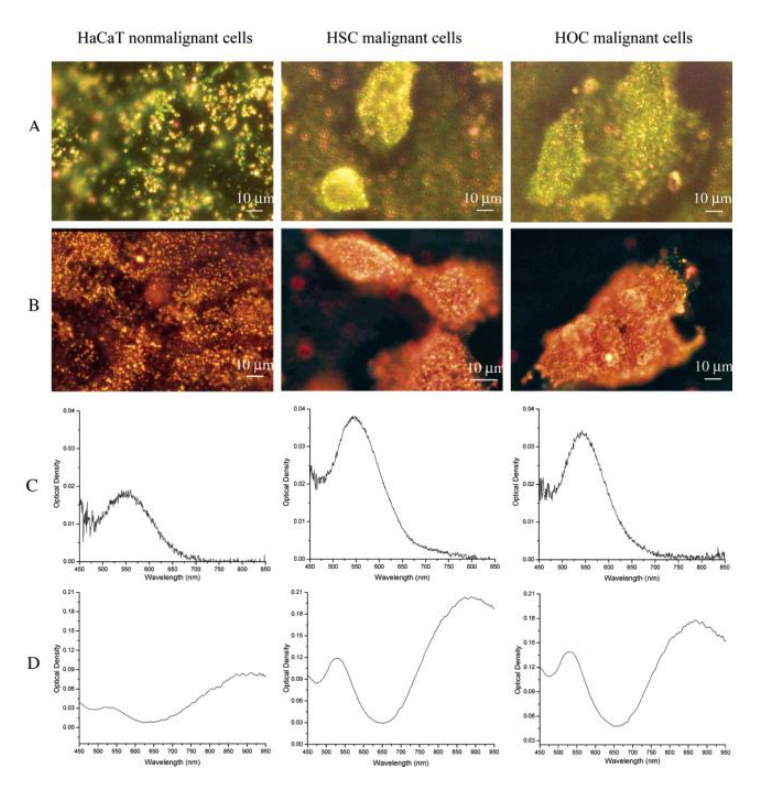


Figure 2.18. (A) Light scattering images of anti-EGFR/Au nanospheres; (B) Light scattering images of anti-EGFR/Au nanorods (C) Average extinction spectra of anti-EGFR/Au nanorods. [189]

2.4.6 Surface-enhanced Raman scattering (SERS) substrate

Surface-Enhanced Raman Spectroscopy (SERS) is an advanced analytical technique that significantly enhances the Raman scattering signal of molecules adsorbed onto nanostructured metallic surfaces, typically silver, gold, or copper. This enhancement occurs due to localised surface plasmon resonance (LSPR), where incident light excites collective oscillations of conduction electrons in the metal nanoparticles, creating intense electromagnetic fields. These fields amplify the Raman signal of nearby molecules, enabling highly sensitive molecular detection, even at single-molecule levels. Since the SERS technique is an accepted analytical method and a reliable measuring instrument, a number of research studies have been previously conducted on this topic [154–158]. The shape of nanoparticles is important as the sensitivity is strongly dependent on that. Mulvihill et al. used this technique to show that different kinds of Ag nanocrystals made by the polyol process are excellent for detecting arsenic and in water down to 1 part per billion [198]. The highly resonant dielectric response of dielectric arrays coated with a variety of organic species was determined. There is a need to develop a non-invasive way to detect arsenic in

drinking water in developing countries. There are some significant advantages that the SERS detection method has. It is also possible that gold nanoflower (AuNF) nanoparticles could be effective SERS substrates. The AuNF nanoparticles could be packaged with denatured proteins to become Raman-active tags.

SERS has also been utilised for real-time detection of molecules [199]. Yang & coworkers report higher SERS values for triangular plates owing to their sharp edges and corners [195]. The aggregate of silver nanoplates detect molecule with better enhancement than the single silver nanoplates as a result of high electromagnetic coupling between neighbouring nanoplates. The LSPR-active property and sharp edges in the surface of the nanoparticles are responsible for producing high SERS values.

2.4.7 Hydrophobic surfaces

Surface structure and morphology has an effect on the wetting properties of materials. Surface hydrophobicity can be increased by increasing surface roughness or size. Super-hydrophobic surfaces exhibit very high repellence to water. The water droplets arranged on a superhydrophobic surface form droplets that is nearly spherical in shape. Contaminants adhere to water droplets and are removed along with them. Anisotropic nanoparticles can be useful as superhydrophobic surfaces. The formed superhydrophobic film having a thickness of about 10 millimetres with n-decanethiol SAM produced surfaces showed a tilt angle of below 28 degrees and a contact angle of 154.591 degrees [200], [201]. The presence of Ag crystallites on a particular substrate improves its hydrophobicity, compared to other substrates without Ag crystallites (Figure 2.19). The Ag nanoplates were grown on GaAs materials that displayed the 'Lotus' pattern [201]. Ag nanoplates were made hydrophobic using 1-hexadecanethiol molecules. Ag nanoplate/GaAs composite surface can be varied depending on the size of individual nanoplate but also the extent of nanoscale surface roughness of said nanoplate.



Figure 2.19. Water droplets on the Ag dendritic film surface, Ni surface, and Cu surface. All surfaces were modified with n-dodecanethiol. [200]

2.4.8 Infrared absorbent material

It has been well known that Au-based NIR absorbing films are an alternative to reflective coatings for blocking IR radiation. The use of nanoparticles is highly efficient, and cost-competitive with other technologies. Nanoparticles of the NIR-IR absorbing materials have been used to develop infrared filters. A study demonstrated that gold nanofibres could absorb a significant amount of heat causing the temperature inside of the box to decrease when exposed to daylight [202]. Heat absorption experiments were conducted with a monolayer of mesoflowers (MF)-coated glass slides, and a blank glass substrate was used as the control. The resulting temperature in the MF-coated glass was 2 °C lower in comparison to the blank glass substrate. Metallic nanotriangles have an NIR and IR absorbing property, which can be used as heat-absorbing or window-reflective coating [202], [203].

2.5 Stealth

Stealth in the military field is the use of methods and tactics to counter active and passive measures; in order to avoid detection against radar, infrared, acoustic and other sensors for aircraft, equipment, vehicles and uniform [204]. Also known as low observable stealth and signature management, it's a way of achieving camouflage for military systems to avoid detection by various sensor equipment such as infrared, acoustic, radar, etc. Survivability of aircraft, ships and other military vehicles is critical to achieve success in wars. By camouflaging military vehicles and equipment, chances

of surviving can be increased. With developments in sensor technologies, signatures such as radar, infrared, acoustic can be detected easily and used to deploy surface to surface or surface-to-air missiles to destroy air, ground and naval vehicles.

Humans have always employed stealth methods through history. The advent of World War 1 brought about visual stealth methods, whereas World War 2 saw the invention of radar stealth. Since the development of reconnaissance technology, the goal for any country has been to operate without the knowledge of the enemy. That has also led to development of various detection methods. Therefore, to counter them, it is necessary to use special materials and designs to reduce signatures such as infrared, acoustic, radar.

2.5.1 Active stealth

Emphasis on stealth technologies began during World War II, as radar technology was developed to detect aircraft and naval ships [205]. Radar stands for Radio Detection and Ranging. The technology makes use of electromagnetic radiation to detect objects. It does so by sending out radio and microwave signals from a transmitter which are reflected from objects and picked by up a receiver (usually from the same antenna). The received signal is processed to determine the nature and distance of object; based on such information, appropriate action can be taken [206]. By using radar cross section (RCS), the size the of an object can be known. This mode of detection is known as active detection since the electromagnetic signals are transmitted from the detector and reflected signals are used to obtain necessary information.

To counter radar detection, aircraft are designed in a special way. By using flat geometries and sharp angles, the radar signals may be deflected and/or avoided. Another use is by using materials that absorb radar signals at frequencies used the detectors.

2.5.2 Passive stealth

Passive mode of detection involves detection of signals produced by aircraft, naval and ground vehicles. Infrared is the major passive signature used to detect objects. Any object with temperature over 0 K emits radiation in the infrared spectrum. According to Stefan–Boltzmann law [207], the radiation emitted from an object

increases with a fourth fold increase in temperature, and as the temperature increases the wavelength of the radiation becomes shorter. An object at room temperature emits radiation at a wavelength of 9.9 μ m, and the radiation emitted by an object at 1000 °C is at 2.3 μ m.

The infrared (IR) spectrum ranges between 770 nm to 1 mm, which corresponds to frequencies between 4.3×10^{14} Hz and 300×10^9 Hz. However, the common region in use has a range between 0.77 to 14 μ m. This range is separated into three sub-bands: near-IR (NIR) at 0.7-1.5 μ m; mid-wavelength (MWIR) at 1.5-6.0 μ m; and long-wavelength (LWIR) at 6-14 μ m.

2.5.3 Threat detectors

Advancements in technology and materials science has led to development of sensors with high degrees of accuracy. These allow detection of targets across a range of electromagnetic and acoustic spectrums. These sensors are highlighted below in *Table 2-2*.

Wavelength	Detector equipment	Range
UV to NIR	- Telescope	- Long
(0.4 to 1 um)	- Sight	- Short
	- CCDs	- Short
MWIR to LWIR	- Thermal	- Long
(3-5, 8-14 um)	- Photonic	- Long
Radar	- Doppler	- Long
(2.7 mm to 100 m)		
Acoustic	- Sonar	- Long

Table 2-2 Examples of sensors for detecting different electromagnetic wavelengths

IR detectors use materials that are sensitive to certain wavelengths in order to easily differentiate objects from background. To detect objects between 2-4 μ m wavelength (such as an aircraft shown in Figure 2.20), sensors with cooled or uncooled lead selenide (PbSe) are used. Mercury cadmium telluride (MCT) are used to detect 5 μ m and longer wavelengths and can be integrated with microbolometers and photodetectors. In addition, detection ranges have benefited from the integration of focal plane arrays, with increasing numbers of detectors for higher resolution. The

properties of materials also determine emissions. One such property is emissivity, which is defined as the ratio of radiation emitted from a material relative to a blackbody (that has an emissivity of 1).

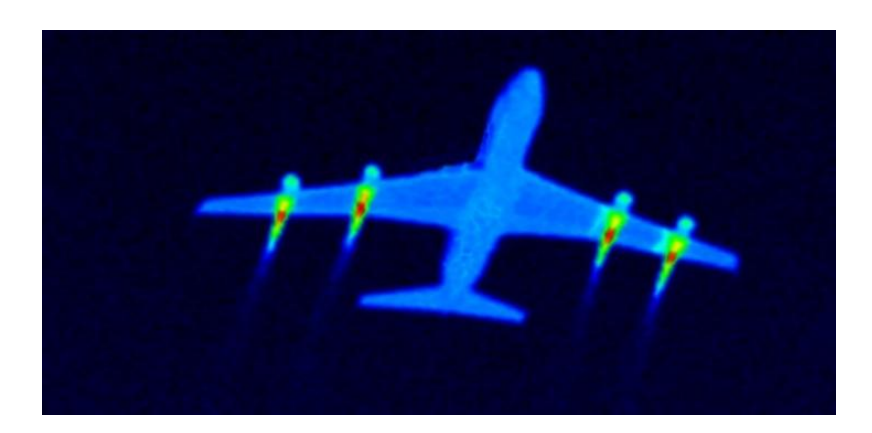


Figure 2.20. Mid-wavelength infrared signature of a commercial aircraft showing engine emissions – vulnerable to IR- seeking missiles [208]

The property of the 'radiance' (emissions for each unit area) of a material can be determined by its temperature and emissivity, whereas its 'intensity' (its signature-strength with regards to a sensor) is dependent upon the portrayed area at a sensor. This is as detectors respond to 'irradiance', the concentrations of the emission projecting on it. Thus, a material's infrared intensity is dependent upon the angle of view from which it is detected and due to the sensor being placed at a sphere's centre, a decrease in irradiance is proportional to the square of the distance.

Additionally, to thermal radiation emission, aircraft have the potential to reflect rays emitted by the Sun (sunshine), from the sky (sky shine) and from the ground (earthshine). Thus, both reflected and emitted forms of radiation must be considered if trying to determine the control of the IR signature. All rays of incident radiation must be reflected, absorbed, or transmitted, as to follow Mayer's law of conservation of energy. If emissivity is to decrease, then the reflectivity of a material must increase as absorptivity is directly proportional to its emissivity. Many materials are commonly too thick to allow transmission.

The sum IRSL (infrared signature level) of a target is the combined total signatures of its complete components. Each individual component has an individual signature which can be calculated through the difference between the radiance it produces and the background and path.

The following paper by K. E. Andersson and C. Åkerlind S [38], identifies six characteristics that would make an ideal spectral coating material. These are:

- spectrally selectively reflectance- this means the coating is reflected to required waveband such as UV-VIS-NIR (0.2-2), MWIR (3-5), LWIR (8-14), and Radar (>1 mm)
- 2. low gloss- this means less reflectance
- 3. low degree of polarisation
- 4. low infrared emissivity 0.4 to 0.6
- 5. non-destructive properties- to avoid damage to other
- 6. controllability- the ease of modifying the material

Identified coating designs include pigments, one-dimensional structures, multidimensional structures, bio-mimic and metamaterials. For pigments, the design consists of metal oxides embedded in a binder material.

Refere nce	Coating material (s)	Geometry	Preparation method	Substrate	Coating method	Result
[209]	PANI/CB	Powder	Sol-gel	Al	Spin	Absorption increased
[210]	Cu, EBDM	Spheres, flakes	Chemical	Ti	Sputter	Emissivity reduced due to leafiness
[211]	Cu, PU	Powder	Chemical	Ti	Doctor blade, spray	Emissivity reduced with higher Cu
[212]	C-Al ₂ O ₃	Powder	Chemical	Ti		-
[213]	AI/PU	Powder		Ti	Spray	ε of 0.06 achieved 8-14 μm
[214]	Cs _x WO ₃	Nano-rods	Chemical	Quartz	Spray	-

Table 2-3 Some studies showing combination of materials used for IR stealth purposes

2.5.4 Summary

Low observable materials are desirable in defence applications to reduce radiation signatures. Metal/polymer composites offer solutions for certain applications in signature management. By developing composite coatings that can absorb selective radiation signatures, platforms such as vehicles and military equipment can be protected from being detected and targeted. From Table 2-2, it can be seen that certain sensors detect radiation signatures between 0.4 to 1 µm wavelengths. It is possible to synthesise silver nanomaterials that can absorb selective wavelengths between 400

- 1200 nm. By developing a nanocomposite coating, detection of aforementioned radiation wavelengths can be countered. This is an area to be explored using the nanomaterials in this research project.

2.6 Conclusions

In the literature, the theory behind surface plasmon resonance was discussed. Also, various synthesis methods nanoparticles along with their applications have been discussed. The following key points can be concluded. Gold and silver nanoparticles offer unique optical and electronic properties, making them attractive for numerous applications. The absorbance of these nanoparticles can be tuned by changing their morphology. Spherical nanoparticles exhibit LSPR absorbance in the ultraviolet-visible wavelengths, whereas anisotropic nanoparticles are capable of absorbing wavelengths in the near-infrared. It is possible to customise nanoparticles for an intended application.

A number of synthesis methods for anisotropic nanoparticles were discussed. The seed-mediated method is relatively easy as it can be carried out in a single container at room temperature. It was therefore selected for further exploration by systematically studying the effect of each parameter to optimise the synthesis. This allows an improved understanding of nanoparticle growth. By building on the information gained about the nanoparticle growth, the enhancement in the absorbance by controlling the growth would be feasible. Optimal parameters can then be selected for synthesis of nanoparticles that would result in absorption of higher wavelengths. This method also has the potential for scaling up the synthesis which can lead to larger production. By developing a flow reactor, continuous synthesis can be achieved to enable controllable synthesis.

Chapter 3 Batch Synthesis of Silver Nanoparticles

3.1 Introduction

This chapter describes the batch synthesis methods and analytical techniques used to synthesise and characterise silver nanoparticles. In this project, seed-mediated approach was used to synthesise nanoparticles. Two methods from the literature were selected, namely, 'Rekha method' and 'Murphy method'. Reaction conditions and parameters were varied to study their effect on the optical properties and morphology of nanoparticles. Investigating the effect of these parameters was carried out to identify the optimal parameters for higher absorbance, and to provide useful information for design and operation of continuous flow production.

In most chemical methods, initial work involved synthesis of Ag seed particles, which were achieved by reducing silver nitrate (AgNO₃). These seeds were then grown into nanorods. The reason for selecting this method was the ease of synthesis as it required non-special equipment and was also relatively quick as well as cost-effective. The reactions were carried out at room temperature using chemicals bought from well-known chemical suppliers (Sigma Aldrich and Fischer). It was vital to use a chemical method as one of the objectives of the project was to produce these nanorods continuously. This can be achieved through the development of micro/milli flow reactors once optimal parameters for AgNR synthesis are identified.

3.2 Synthesis of silver nanoparticles

This section introduces the synthesis methods used in this project to produce anisotropic silver nanoparticles using the seed-mediated approach. Two methods using different capping agents for seed solutions and different concentrations of chemicals were used, as detailed in the following sections.

3.2.1 Chemicals

Silver nitrate (AgNO₃, 99.995%), cetyltrimethylammonium bromide (CTAB, 99%), sodium borohydride (NaBH₄, 99%), L-ascorbic acid (AA, 99%), trisodium citrate (TSC) and sodium hydroxide (NaOH, 99%) were purchased from Fisher Scientific and Sigma Aldrich and used without further purification. Millipore water was used for the

synthesis. All glassware was washed with detergent, thoroughly rinsed with double distilled water, and dried prior to usage.

3.2.2 General seed-mediated synthesis procedure

For the preparation of silver nanorods, seed-mediated growth method was used. It was a two-step process as shown in Figure 3.1. In principle, it included the mixing of two main components. The first component was the seed solution containing silver nanoparticles in the nucleation stage. In the second component, a surfactant, hexadecyltrimethylammonium bromide (CTAB), was used for providing the anisotropic growth of silver rods. The Ag seed was prepared by chemical reduction of AgNO₃ with NaBH₄ in the presence of two different capping agents to stabilise the nanoparticles. In growth solution silver was reduced by ascorbic acid in the presence of seed.

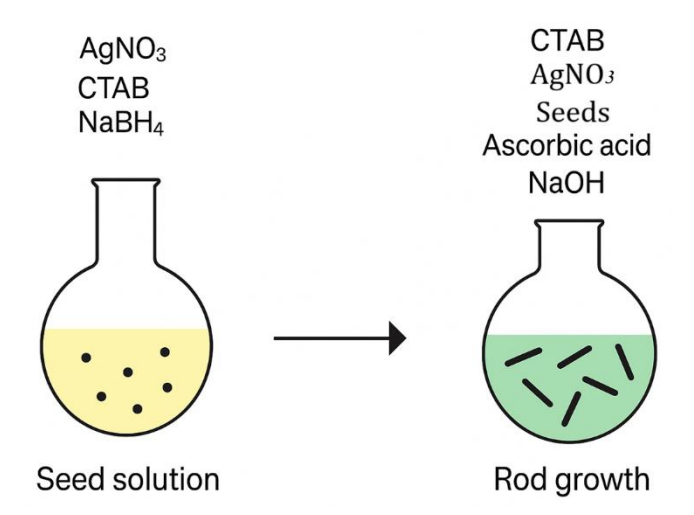


Figure 3.1. The Schematic illustration of the seed-mediated synthesis of silver nanorods. The seed solution includes silver nitrate (AgNO₃), sodium borohydride (NaBH₄), and CTAB. The growth solution comprises CTAB, AgNO₃, ascorbic acid (AA), NaOH, and seed solution.

Preparation of seed particles

To prepare silver seed particles, an aqueous solution containing AgNO₃, and a capping agent were mixed in a 50 mL round-bottom flask (Figure 3.2). Next, NaBH₄ (reducing agent) solution was injected into the solution all at once while stirring at high speed (600 rpm). The colour of solution changed to light yellow, as shown in Figure 3.2. This solution was used as a stock silver seed solution.



Figure 3.2. Colloidal solution of Ag seeds

Procedure of silver nanorod growth

For the growth solution, first an aqueous solution containing CTAB was prepared. This solution was heated to 35 °C while stirring to dissolve the CTAB and used after cooling to room temperature. CTAB solution was added to glass vial (15 mL). Next, AgNO₃ and freshly prepared ascorbic acid were added, and varied amount seed solution was added. Finally, NaOH was added. Within 2 minutes, the solution colour changed depending on the seed concentration (see Figure 3.3 for different colours of solutions in cuvettes).

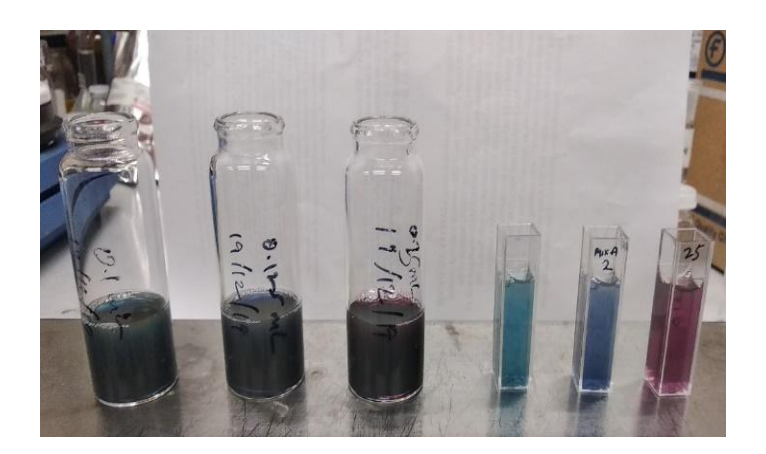


Figure 3.3. Ag nanorod solutions prepared using varied seed volume

3.2.3 Method 1 – Rekha method

In this method, silver nanorods were prepared according to a seed mediated synthesis used by Rekha et al. [48]. The seed solution was prepared by mixing 5 mL of 0.01M AgNO₃ and 80 µL of 0.1 M CTAB stock solution in a 50 mL round-bottom flask. This was made up to 20 mL with Millipore water and to this 0.6 mL of 0.01 M NaBH₄ was added and stirred for 2 minutes. The solution was kept undisturbed for 1 hour, before adding to it the growth solution. To produce silver nanorods with varying aspect ratios, 10 mL of a growth solution consisting of 0.01M CTAB, 0.25 mL 0.02 M AgNO₃ and 0.5 mL 0.1 M ascorbic acid was taken. To this, a varied amount of seed solution (between 0.02 - 1.0 mL) was added. Finally, 0.10 mL of 1 M NaOH was added to each set and shaken gently. The colour of the solution was seen to change gradually depending upon the concentration of the seed solution added. The above concentrations were used as reference and were each varied individually to study their effect on the optical properties on the nanoparticles (see Figure 3.4 for reference spectra). The table below shows the concentrations used for each solution.

Chemical	Reference	Varied
	concentration	concentrations
AgNO ₃ in seed solution	10 mM	1, 5, 20 mM
CTAB in seed solution	100 mM	N/a
NaBH₄ in seed solution	10 mM	1, 5, 20 mM
AgNO ₃ in growth solution	20 mM	10, 40, 50 mM
CTAB in growth solution	10 mM	5, 20, 50 mM
AA in growth solution	100 mM	50, 200, 300 mM
NaOH in growth solution	1 M	0.5, 2.0 M

Table 3-1 Parameters for Method 1

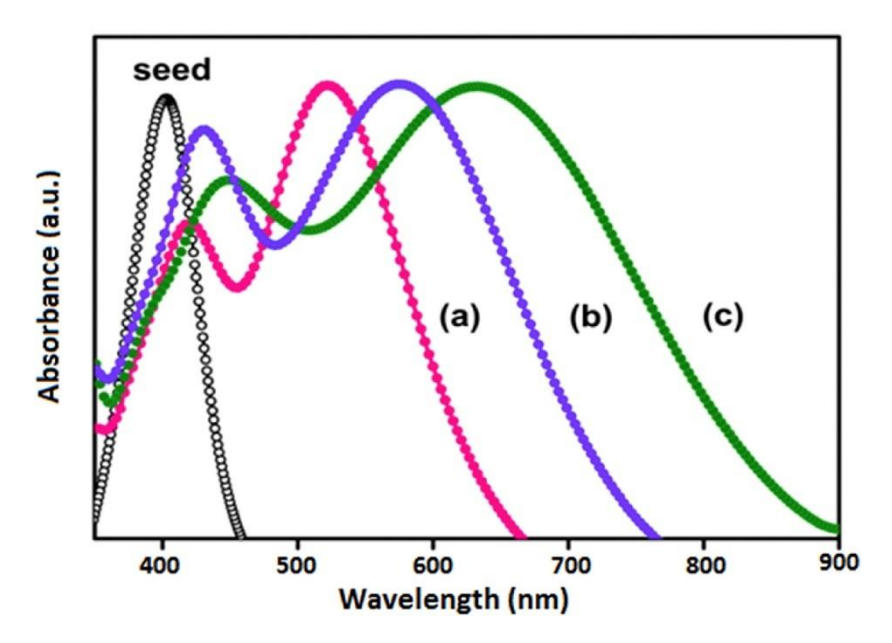


Figure 3.4. Absorption spectra of silver nanorods prepared with different concentrations of seed particles: (a) 0.25 mL, (b) 0.125 mL, and (c) 0.1 mL The three spectra correspond to aspect ratios of (a) 6 ± 0.86 , (b) 11 ± 0.43 and (c) 15 ± 2.87 [48].

3.2.4 Method 2 - Murphy method

This method was referenced from experimental work carried by the infamous Murphy group [64]. This method is different from the above method in the preparation of seed particles, as well as using different concentrations for other chemicals. For the preparation of seed solution: a 20 mL solution with a final concentration of 0.25 mM AgNO₃ and 0.25 mM trisodium citrate in water was prepared in a round bottom flask (50 mL). While stirring vigorously (600 rpm), 0.6 mL of 10 mM NaBH₄ was added all at once. Stirring was stopped after 30 s. The seed solution was left for 2 hours before being used. The resulted solution was brownish yellow in colour.

For the preparation of Ag rods: first, a set of solutions were prepared containing 0.25 mL of 10 mM AgNO3, 0.50 mL of 100 mM ascorbic acid, and 10 mL of 80 mM CTAB. Next, a varied amount of seed solution (between 0.02 – 1 mL) was added. Finally, 0.10 mL of 1 M NaOH was added to each set. NaOH is added last to obtain the desired nanorods in decent yield. After adding the NaOH, the solution was gently shaken just enough to mix the NaOH with the rest of the solution. Within a few minutes a colour change occurred depending on seed concentration. The above concentrations were used as reference and were each varied individually to study their effect on the optical

properties on the nanoparticles (see Figure 3.5 for reference spectra). The table below shows the concentrations used for each solution.

Chemical	Reference	Varied
	concentration	concentrations
AgNO ₃ in seed solution	0.25 mM	0.5, 1, 2 mM
TSC in seed solution	0.25 mM	N/a
NaBH₄ in seed solution	10 mM	N/a
AgNO ₃ in growth solution	10 mM	20, 40 mM
CTAB in growth solution	80 mM	50, 100 mM
AA in growth solution	100 mM	50, 200 mM
NaOH in growth solution	1 M	0.5, 2.0 M

Table 3-2 Parameters for Method 2

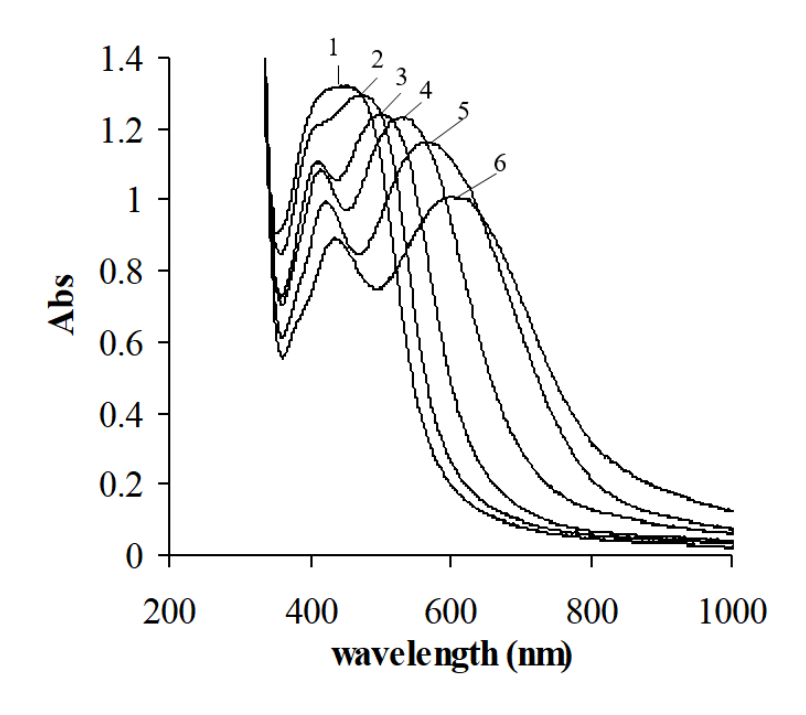


Figure 3.5. UV-vis spectra of silver nanorods: Effect of changing amount of seed. (1) = 2.0 mL, (2) = 1.0 mL, (3) = 0.5 mL, (4) = 0.25 mL, (5) = 0.125 mL and (6) = 0.06 mL of seed solution [64].

The seed-mediated synthesis method was selected for this project due to its superior control over particle shape and aspect ratio, which are critical parameters in tuning the optical properties of silver nanorods [162], [215]. Compared to other chemical

approaches, such as the polyol method or photochemical synthesis, seed-mediated growth offers a higher degree of reproducibility and yields nanorods with narrower size distributions and more uniform morphologies. This level of precision is essential for producing AgNRs with specific absorption characteristics in the near-infrared (NIR) region, a key requirement for the intended applications in IR stealth and optical filtering.

The rationale for selecting these two specific seed-mediated methods, namely the Rekha and Murphy methods, stems from their reported efficacy in producing anisotropic nanoparticles and their differing strategies in reagent concentration and growth kinetics, which provided a valuable comparison framework [162], [48]. The Murphy method is one of the most established protocols in the literature and forms the basis of many subsequent adaptations. It involves well-defined seed preparation and growth solution composition using CTAB as the surfactant and ascorbic acid as the mild reducing agent. In contrast, the Rekha method introduces variations in reagent ratios and reaction sequence, offering potential improvements in yield and particle uniformity under specific conditions.

The main differences between these methods lie in their treatment of silver nitrate concentrations, seed aging protocols, and the balance between reducing and stabilising agents. These variations directly affect the kinetics of silver ion reduction and crystal facet stabilisation, which in turn influence the final nanorod length, diameter, and aspect ratio. By trialling both methods under controlled conditions, this project aimed to evaluate their suitability for consistent production of AgNRs with targeted NIR absorption, ultimately selecting the more scalable and stable synthesis route for nanocomposite integration and flow synthesis development.

3.2.5 Purification method

The nanoparticles were purified using two methods: static precipitation and centrifugation, as described below.

The Ag nanoparticles in Method 1 were mostly purified through static precipitation, which was an effective and easy separation process without using centrifugation or filtration. When left for an hour or more, bigger nanoparticles such as rods naturally precipitated at the bottom of glass tubes due to electrostatic aggregation. Smaller particles and by-products remained in the supernatant. The precipitate was re-

dispersed in Millipore water and used to measure its absorbance and carry out TEM analysis.

Samples in Method 2 were purified by centrifugation. An Eppendorf centrifuge was used at 6000 rpm for 15 minutes to remove smaller particles and excess chemicals. The supernatant was disposed of, and precipitated nanoparticles were dispersed in Millipore water for further characterisation.

3.3 Characterisation

The prepared colloidal samples were analysed for their absorbance of light, and the morphology of nanoparticles was examined using transmission electron microscopy (TEM).

3.3.1 Optical Spectrometry

The localised surface plasmon resonance (LSPR) of silver nanoparticles was studied by measuring their absorbance corresponding to the shape and size the nanoparticles. For example, the recorded LSPR of silver nanoparticles of different sizes exhibited a red shift in maximum absorbance of the silver particles indicating bigger particles.

UV-visible-NIR spectroscopy analysis employed a Perkin Elmer Lambda 750S UV-visible-IR spectrophotometer (Figure 3.6) over a wavelength of 300 to 1100 nm with a scan rate of 480 nm/min and a step of 2 nm per data point. A 10 mm quartz cuvette was employed. All samples were measured for absorbance against Millipore water.



Figure 3.6. Perkin Elmer Lambda 750S UV-VIS-IR spectrophotometer

3.3.2 Transmission Electron Microscopy

Transmission electron microscope (TEM) analysis utilised an FEI Tecnai T12 TEM (Figure 3.7). This TEM has an operating voltage range of 20 to 120 kV, with magnification capability of thin samples (<200 nm) up to 700,000 times. It also has an energy-dispersive X-ray spectroscopy (EDS) system, a Gatan MSC794 CCD camera for digital image acquisition, and a video camera for video-rate recording at moderate magnifications. Samples were prepared by drop-casting the prepared nanoparticle solution onto carbon and Formvar coated Cu/Pd 200 mesh grids with subsequent base-fluid evaporation. Further TEM picture analysis was carried out using ImageJ image analysis software. The scale bar on the TEM image was used to calibrate the line length employed in the ImageJ image analysis software and the size of the individual nanoparticles was then measured.



Figure 3.7. FEI Tecnai T12 transmission electron microscope

Batch synthesis results

Below, the outcomes related to silver nanoparticles synthesised through two seed-mediated techniques, as detailed above, are elucidated. The primary emphasis of this segment pertains to the optical characteristics and structural morphology of the nanoparticles. The implications of both synthesis techniques are deliberated upon, with a sequential analysis of the impact of each parameter examined.

3.4 Batch synthesis using method 1

In this method, CTAB capped silver seed particles were used to produce anisotropic nanoparticles. The concentrations of reagents in the seed phase as well as growth phase were varied separately to study their effects on optical properties of silver nanoparticles.

The seed particles were prepared by reducing AgNO₃, mixed with an aqueous solution of CTAB, using NaBH₄ as the reducing agent to ensure the complete reduction of Ag⁺. A colour change was observed within 1 minute from a clear solution to yellowish, indicating the formation of spherical silver nanoparticles. The colloidal solution was covered with aluminium foil and kept out of light for 1 hour before being used.

This seed solution was then further used without any purification to produce secondary nanoparticles. For each seed solution, five sets of growth solutions were made. Each set contained the surfactant CTAB, $AgNO_3$ and ascorbic acid. Then seed solution was added in amounts of 0.01 - 0.2 mL. Lastly, a solution of NaOH was added. Within a few minutes, the colour of each set changed according to the seed amount.

3.4.1 Effects of silver nitrate added during seed particles formation

The effect of concentration of silver nitrate in seed solution was investigated. Seed particles were synthesised at four different concentrations of silver nitrate: 1, 5, 10 and 20 mM. The selection of four specific silver nitrate concentrations (1 mM, 5 mM, 10 mM, and 20 mM) was based on the need to systematically investigate the influence of precursor concentration on the formation, size distribution, and optical properties of silver nanoparticles. These concentrations were chosen to cover a broad range, from low (1 mM) to high (20 mM), allowing for a comprehensive analysis of how varying silver ion availability impacts the nucleation and growth processes. Lower concentrations are expected to produce fewer nucleation sites, leading to the

formation of larger but more uniform seed particles. Conversely, higher concentrations can promote rapid nucleation, potentially resulting in a broader size distribution. The concentrations of other reagents were kept constant. Below, the effect on seed particles and final particle growth is discussed.

Effect on seed particles formation

Spectrophotometry serves as an instrumental method for analysing the optical characteristics and structural morphology of nanoparticles. This is because varying nanoparticles manifest surface plasmon resonance at distinct frequencies, contingent upon their shape and dimensions [23]. As depicted in Figure 3.8, the UV-Vis absorption spectra of silver seed nanoparticles show a dependence on silver nitrate (AgNO₃) concentration. The absorption peaks are located within the 400–420 nm wavelength range, consistent with the surface plasmon resonance (SPR) of spherical silver nanoparticles [216]. As the AgNO₃ concentration increases, the SPR peak exhibits a slight red shift, from approximately 405 nm at 1 mM to 414 nm at 20 mM. This shift suggests a change in nanoparticle size or local dielectric environment, which can be attributed to variations in nucleation and growth dynamics.

The full-width at half-maximum (FWHM) values provide a quantitative measure of peak broadness, reflecting the size distribution of the nanoparticles. At 1 mM AgNO₃, the FWHM is approximately 52 nm, indicating a relatively narrow peak and suggesting a more uniform particle size distribution. However, as the concentration increases, the FWHM values increase to 72 nm (5 mM), 80 nm (10 mM), and 77 nm (20 mM), respectively. This trend indicates that increasing the silver nitrate concentration results in a broader absorption peak, which is typically associated with a higher degree of polydispersity in nanoparticle size.

The broadening of the SPR peak at higher AgNO₃ concentrations suggests that while a greater availability of silver ions facilitates more nucleation events, it also leads to variations in the growth rates of different particles, producing a wider range of sizes. This effect is particularly pronounced at 10 mM AgNO₃, where the FWHM reaches its maximum (80 nm), indicating the highest size polydispersity. A slight decrease in FWHM at 20 mM (77 nm) suggests a marginal reduction in size variation, possibly due to saturation effects in the precursor concentration. This aligns with literature reports that correlate increased FWHM with polydispersity in nanoparticle synthesis [217].

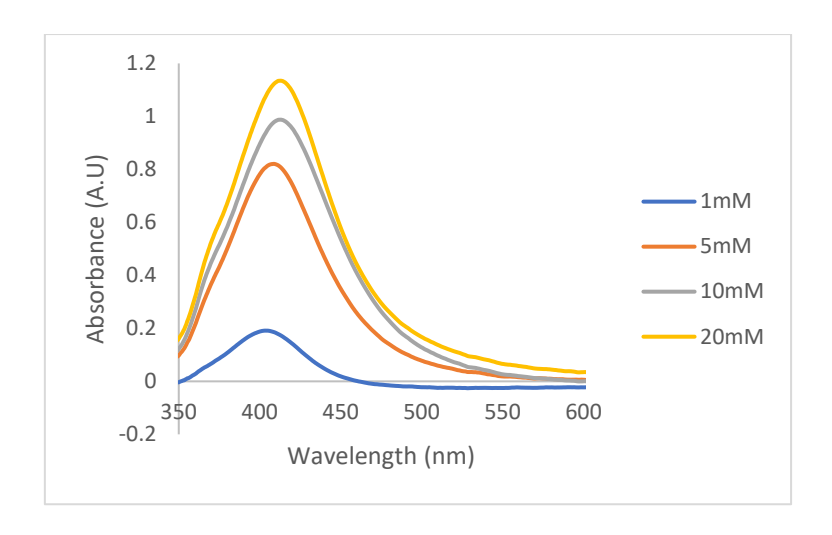


Figure 3.8. UV-Vis spectra of silver seed particles obtained at 1, 5, 10 and 20 mM of silver nitrate

Figure 3.9 shows exemplar TEM images of nanoparticles synthesised at the lowest and highest (1 and 20 mM, respectively) concentrations of silver nitrate. As evident from Figure 3.9A, the 1 mM sample showed nanoparticles of various diameters (ranging between 4-40 nm), with some quasi-spherical shaped particles. The nanoparticles showed a high polydispersity. When AgNO₃ was increased to 20 mM, the average diameter of nanoparticles was 5.9 ± 1 nm, with a better monodispersity. It can be concluded that a relatively high amount of AgNO₃ was favourable for producing uniform seed particles.

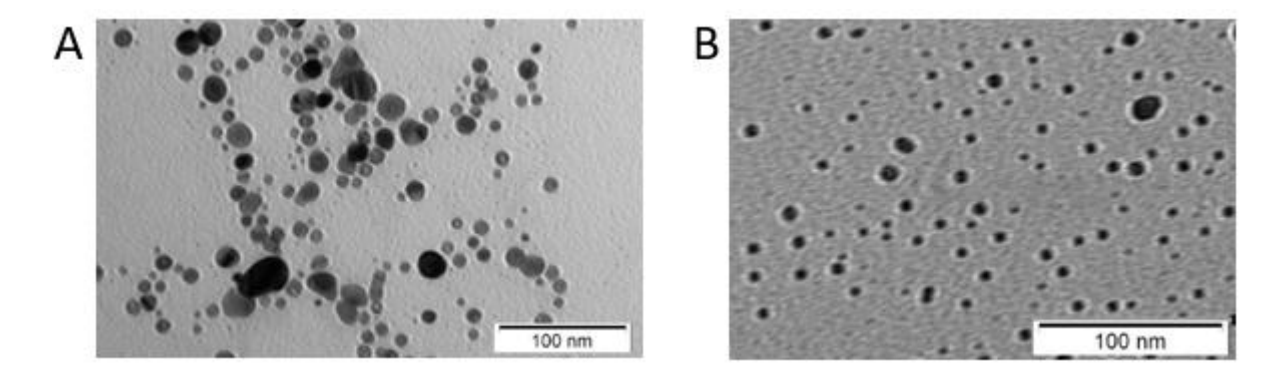


Figure 3.9. TEM images of Ag nanoparticles synthesised at lowest and high AgNO3 concentrations: (A) 1 mM; (B) 20 mM.

Effect on final particle growth

Figure 3.10 illustrates the optical absorption spectra corresponding to nanoparticles synthesised utilising four distinct concentrations of silver nitrate in the seed particles. Various amounts of seed in the growth solution were employed to produce these

nanoparticles. Analysis revealed that every sample displayed two plasmon peaks, signifying the development of anisotropic nanoparticles. The surface plasmon resonance (SPR) characteristics of these nanoparticles were intrinsically linked to the seed concentration. A notable red shift in the absorption peak's position was discernible with diminishing seed concentration, suggesting a concomitant increase in the nanoparticle dimensions. Specifically, for a seed solution with a silver nitrate concentration of 1 mM, incorporating 0.01 mL of seed into the growth solution facilitated the formation of nanoprisms and hexagonally structured nanoparticles, as delineated in Figure 3.11A. The SPR characteristic manifested two distinct peaks: one proximate to 400 nm and another situated between 950 and 1000 nm. The dimensions of these nanoparticles ranged from approximately 300 to 400 nm, gauged from one edge to the other. It is imperative to highlight that at an AgNO₃ concentration of 1 mM, the samples presented two peaks. The initial, subdued peak proximate to 400 nm could be attributed to the existence of spherical nanoparticles. In contrast, the subsequent expansive peak was associated with the in-plane dipole resonance mode, indicative of the presence of nano triangular structures.

The formation of these anisotropic shapes can be attributed to the characteristics of the seed particles. As previously explained, upon synthesising seed particles with a concentration of 1 mM AgNO₃, there was the formation of comparatively sizable and non-homogeneous particles. This scenario provided an abundance of nucleation sites on the seed particles, facilitating silver atoms from the growth solution to adhere and cultivate these distinct shapes. With an increase in seed concentration, there was a discernible shift of the peaks toward reduced wavelengths, signifying a diminution in the size of the nanoparticles. Furthermore, the spectral peaks corresponding to elevated seed concentrations exhibited reduced breadth, signifying a more consistent size distribution among the nanoparticles.

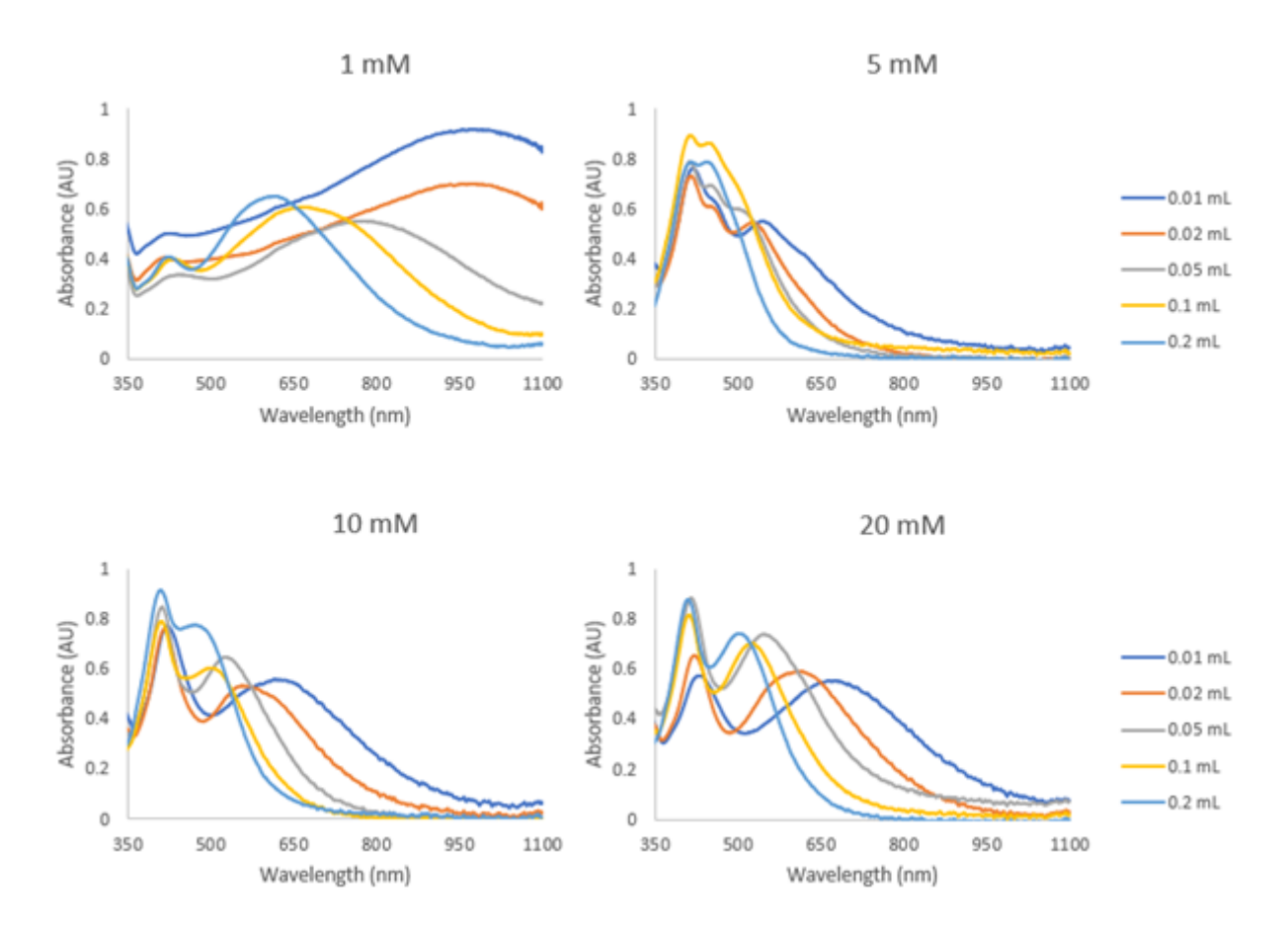


Figure 3.10. UV-Vis spectra of the final nanoparticle growth at different concentrations of silver nitrate in the seed solution. For each concentration, the seed amount was varied between 0.01 to 0.2 mL.

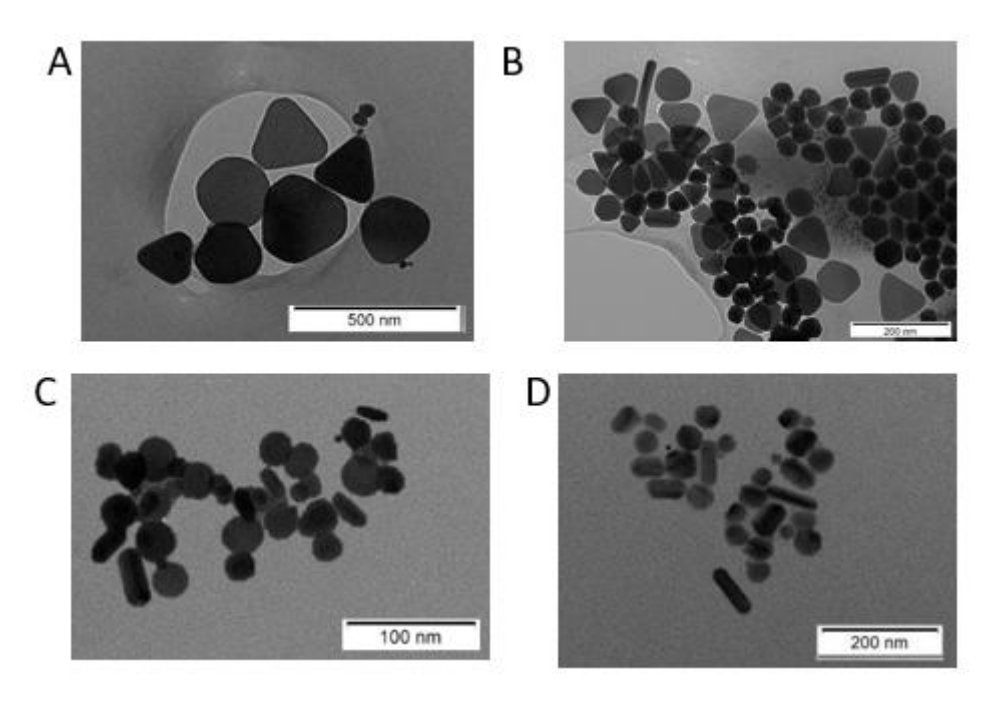


Figure 3.11. TEM images of nanoparticles produced using different amount of AgNO3 in seed solution: (A) 1 mM AgNO3, 0.01 mL seed; (B) 5 mM AgNO3, 0.01 mL seed; (C) 10 mM AgNO3, 0.01 mL seed; (D) 20 mM AgNO3, 0.01 mL seed

When the AgNO₃ concentration in the seed was increased from 1 to 5 mM, the absorption peaks observed for all specimens transitioned to shorter wavelengths. Nevertheless, the morphology of the nanoparticles varied considerably, encompassing forms such as truncated nanoprisms, nanocubes, quasi-spherical configurations, and abbreviated nanorods, as illustrated in Figure 3.11B. With a further increment in the AgNO₃ concentration in the seed to 10 and 20 mM, there was a discernible shift in the absorption spectra toward extended wavelengths. Transmission Electron Microscopy (TEM) imagery of the samples with a 0.01 mL seed depicted elongated nanorods, along with more expansive spherical and triangular particulates, in contrast to the ones synthesised using a 5 mM AgNO₃ concentration.

The two distinct absorption peaks in nanorods were due to absorption in the transverse and longitudinal axis of the nanorods. Lower concentration of seed resulted in absorbance of higher wavelengths, indicating that the size of nanoparticles increased as the seed amount was decreased. The growth of nanoparticles in solutions with higher silver nitrate in seed solution was related to the seed particles. When AgNO₃ concentration in the seed was high, small particles with a uniform diameter were formed. Smaller particles had less nucleation sites for silver atoms to attach to, and form longer particles, in this case nanorods. Also, as the seed concentration was decreased, the number of nucleation sites overall was relatively smaller compared to those in larger seed amount. Hence, the frequency of silver atoms to attach to one particular site increased, leading to growth in that particular direction [48].

The UV-Vis and TEM data were compared against reference spectra (Figure 2.4) for silver nanorods and nanoprisms to evaluate morphological influence on plasmonic response. A summary of results in present in Table 3-3. For nanoprisms (1mM, 0.01 mL sample), a large edge length of ~250 nm resulted in an LSPR peak at 990 nm. Compared to literature spectra, which show LSPR peaks from 500-700 nm for 35-64 nm prisms, this redshift confirms the expected spectral behaviour of larger planar structures with greater dipolar oscillation pathways. In comparison to the equivalent sample synthesised using Rekha's method, the nanoparticle morphology in this experiment was notably different. Despite the morphological variation, the LSPR peak in the current sample was significantly redshifted, centred at 990 nm, whereas Rekha's method produced a peak around 650 nm.

Nanorods produced in 10 mM and 20 mM samples exhibited aspect ratios of 2.5 and 3.2, with corresponding longitudinal LSPR peaks at 632 nm and 685 nm, respectively. These values differ to the literature's aspect ratio range (AR 6-15), but follow a consistent redshift trend as aspect ratio increases, in line with Rekha's method.

AgNO ₃ (mM)	Seed Volume	LSPR λ (nm)	Morphology	Size / Aspect
	(mL)			Ratio
1	0.01	990	Nanoprisms	~250 nm edge length
5	0.01	560	Mix: prisms, spheres, rods	~60 nm average size
10	0.01	632	Mix: quasispheres and rods	Rods AR = 2.5; spheres ~30 nm
20	0.01	685	Mix: quasispheres and mostly rods	Rods AR = 3.2; spheres ~40 nm

Table 3-3 Summary of morphological and optical characteristics of silver nanoparticles synthesised using Method 1 under varying AgNO₃ concentrations. The table includes seed volume, observed longitudinal surface plasmon resonance (LSPR) peak wavelengths from UV-Vis spectra, corresponding nanoparticle morphology, and particle size or aspect ratio as determined from TEM analysis.

3.4.2 Effects of reducing agent during seed particles formation

The effect of changing concentration of reducing agent in seed solution was investigated. Seed particles were synthesised at four different concentrations of sodium borohydride: 1, 5, 10 and 20 mM. The concentrations of other reagents were kept constant. Below the effect on seed particles and final particle growth is discussed.

Effect on seed particles formation

Figure 3.12 shows the UV-Vis absorption spectra of seed particles prepared at different concentrations of sodium borohydride. The results showed that all four peaks were around 420 nm wavelength, indicating synthesis of spherical silver nanoparticles. However, differences in peak intensity and full width at half maximum (FWHM) were observed across the samples, indicating changes in nanoparticle size and dispersity. When concentration of NaBH₄ was 1 mM, the UV-Vis spectrum exhibited a relatively broad absorption peak with a FWHM of 90 nm and low intensity, suggesting low

particle concentration and high polydispersity. TEM image analysis showed relatively larger non-uniform particles of up to 50 nm in diameter (as shown in Figure 3.13A).

Increasing the NaBH₄ concentration to 5 mM resulted in a narrower absorption peak (FWHM = 84 nm) and significantly increased intensity. The particles produced were smaller (average diameter: 5.9 ± 1.1 nm) and more uniform in size. At 10 mM, the peak width remained consistent (FWHM = 85 nm), while the average particle size slightly increased. Interestingly, further increasing the concentration to 20 mM did not lead to further peak narrowing; instead, the FWHM returned to 90 nm, correlating with a moderate increase in particle size (8.7 \pm 1.2 nm, Figure 3.13B.). These results suggest that while NaBH₄ concentration influences nanoparticle size and number, the assumption that higher NaBH₄ always leads to sharper peaks is not valid.

The data demonstrate that moderate NaBH₄ concentrations (5–10 mM) are optimal for generating relatively monodisperse and small silver nanoparticles. At lower concentrations, fewer nuclei form, allowing larger particle growth and broad size distribution. At excessively high concentrations (e.g. 20 mM), rapid nucleation may increase particle number, but size uniformity may be compromised due to uncontrolled growth kinetics or aggregation. This trend aligns with findings reported by Liu et al. [218]., who also observed non-linear relationships between reductant concentration and nanoparticle monodispersity.

In summary, NaBH₄ not only contributes to nanoparticle generation but also serves a pivotal role in stabilising the synthesis process by thwarting nanoparticle agglomeration.

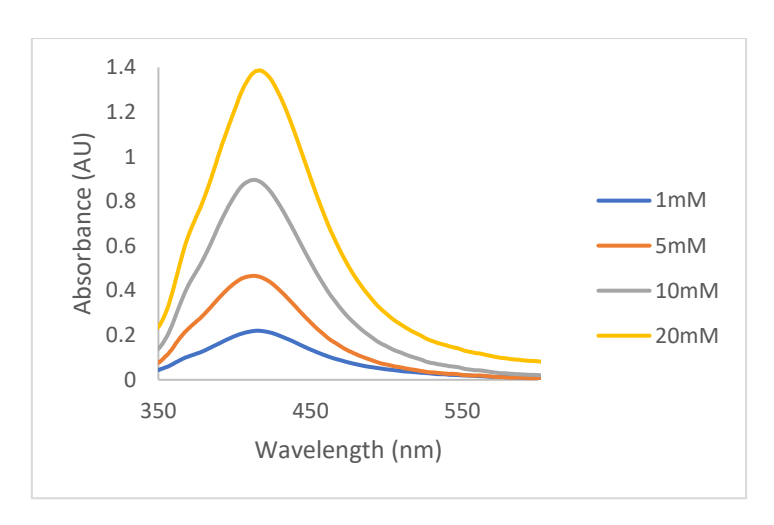


Figure 3.12. UV-Vis spectra of silver seed particles obtained at 1, 5, 10 and 20 mM of sodium borohydride

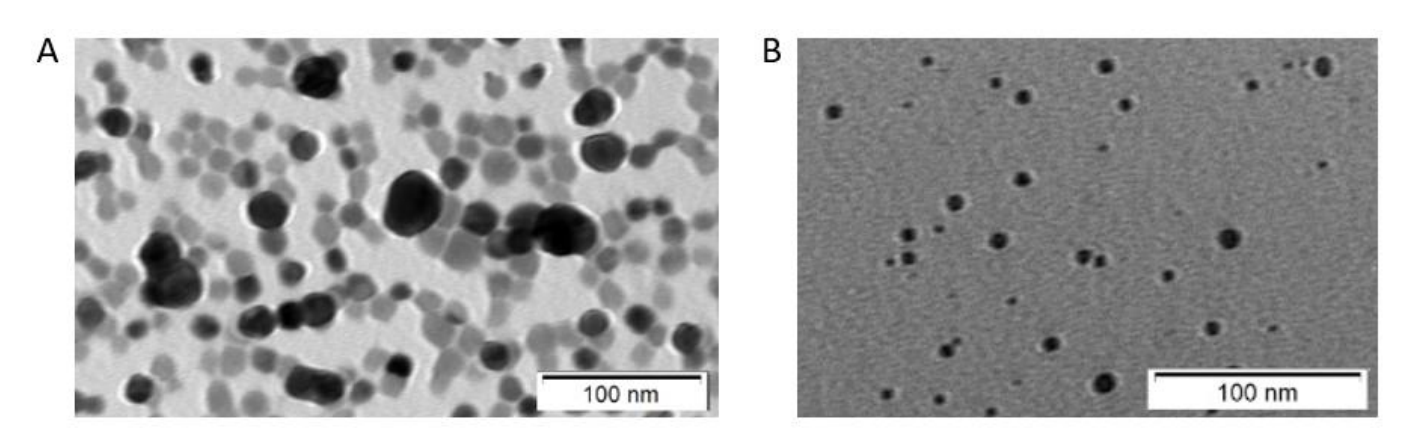


Figure 3.13. TEM image of Ag nanoparticles synthesised at lowest and high sodium borohydride concentrations: (A) 1 mM; (B) 20 mM.

Effect on nanoparticle growth

Figure 3.14 shows the optical absorption spectra of the colloidal nanoparticles prepared using three different concentrations of sodium borohydride in seed phase. For each concentration, seed volumes of 0.01 – 0.20 mL were used to synthesise nanoparticles. When the concentration of sodium borohydride was 1 mM, the resulting nanoparticles showed only one peak between 420 and 450 nm, indicating they were spherical in shape. As the seed concentration was reduced, the peak shifted to longer wavelengths, indicating increase in nanoparticle size. As discussed above, when a smaller amount of sodium borohydride in seed solution was used, larger spherical particles were formed. Due to the large seed particles, their addition in the growth solution only resulted in formation of spherical nanoparticles. Hence, they exhibited only one absorption peak.

Nanoparticles produced at 5 mM of NaBH₄ in seed phase exhibited two absorption peaks, consistent with nanorod formation. All samples exhibited an initial peak at around 400 nm due to absorption in the transverse axis, and a secondary peak due to absorption along the longitudinal axis. As the seed concentration was reduced, the secondary peak shifted to higher wavelengths, indicating increase in the nanorod length. Nanoparticles made with 0.01 mL seed concentration showed the highest absorbed wavelength centred at around 660 nm.

When the concentration of NaBH₄ in the initial seed phase was increased to 10 mM, a discernible shift towards lower wavelengths in the absorption peaks was observed across all samples, in contrast to the 5 mM samples. Upon further amplification to 20 mM, the absorption within the nanoparticles substantially diminished in comparison to the 5 mM samples. Notably, when the seed sample volume was maintained at 0.20 mL, a solitary absorption peak manifested, signifying the formation of spherical nanoparticles. This phenomenon can be rationalised by the substantial abundance of silver seed particles, which reduced the likelihood of silver atoms binding to specific growth sites or crystal facets, consequently yielding spherical or quasi-spherical nanoparticle configurations.

As the seed concentration was decreased, two peaks emerged, with the second peak exhibiting an elongation in wavelength, indicative of nanorod formation. The maximum LSPR peak for the 0.01 mL sample was situated at 580 nm. In comparison to the 5 mM and 10 mM samples, the absorption at 20 mM was measurably lower. This outcome was attributed to the heightened conversion of AgNO₃ into seed particles at elevated NaBH₄ concentrations. The augmented presence of seed particles corresponded to an increased number of nucleation sites for silver ions within the growth solution to adhere to, thereby producing smaller anisotropic nanoparticles and, consequently, lower wavelength absorption.

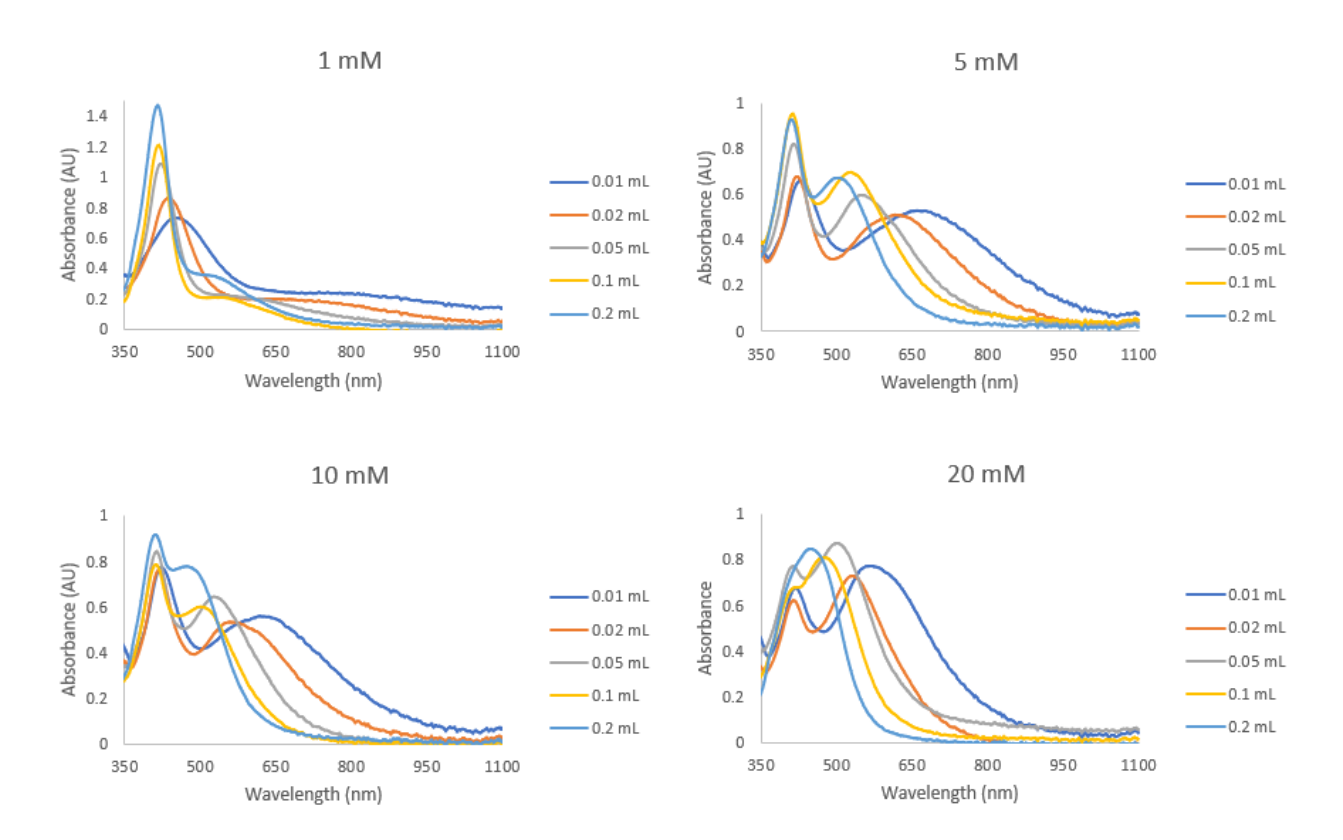


Figure 3.14. UV-Vis spectra of the final nanoparticle growth at different concentrations of sodium borohydride in the seed solution. For each concentration, the seed amount was varied between 0.01 to 0.2 mL.

3.4.3 Effects of silver nitrate added in growth solution

The effect of concentration of silver nitrate added into growth solution was investigated. Particles were synthesised at four different concentrations of silver nitrate: 10, 20, 40, and 50 mM. The concentrations of other reagents were kept constant.

Figure 3.15 shows the optical absorption spectra of the nanoparticles prepared using four different concentrations of silver nitrate in growth solution. When the concentration was 10 mM, it can be seen that for 0.20- and 0.10-mL seed samples, there was only one peak, indicating formation of spherical nanoparticles. The concentration of AgNO₃ in growth solution relative to the seed concentration was lower. Hence when high seed concentrations of 0.20 and 0.10 mL were used, there were fewer silver atoms to attach to the nucleation sites on seed particles. As the seed concentration was reduced, two peaks were observed: the second peak increasing in wavelength, indicating nanorod formation. Here, the AgNO₃ in growth solution to seed concentration ratio was higher, which meant there were enough silver atoms to attach to growth sites on the seed

particles and nanorods to form. The highest LSPR peak for 0.01 mL sample was centred at 540 nm. Increasing AgNO₃ to 20 mM led to a red shift in the absorption for all samples.

When the AgNO₃ concentration in growth solution was increased to 40 mM, all the samples exhibited two separate peaks. A noteworthy observation was the progressive shift of the second peaks toward longer wavelengths as the seed concentration decreased, signifying an augmentation in the aspect ratio of the nanorods. Further increasing the AgNO₃ concentration in the growth solution to 50 mM yielded analogous outcomes to those observed in the 40 mM samples. The escalation in AgNO₃ concentration within the growth solution ensured a surplus of silver ions available for binding to seed particles, thereby facilitating the formation of lengthier nanorods. This, in turn, translated into an enhanced aspect ratio and, consequently, heightened absorption at longer wavelengths. Comparing the 0.01 mL seed samples derived from growth solutions with 40 mM and 50 mM AgNO₃ concentrations, it was evident that the LSPR peaks were centred at 660 nm and 680 nm, respectively. From these observations, it can be deduced that a higher AgNO₃ concentration in the growth solution has the capacity to yield nanorods with greater aspect ratios, provided that the seed concentration remains diminished, and all other experimental parameters are held constant.

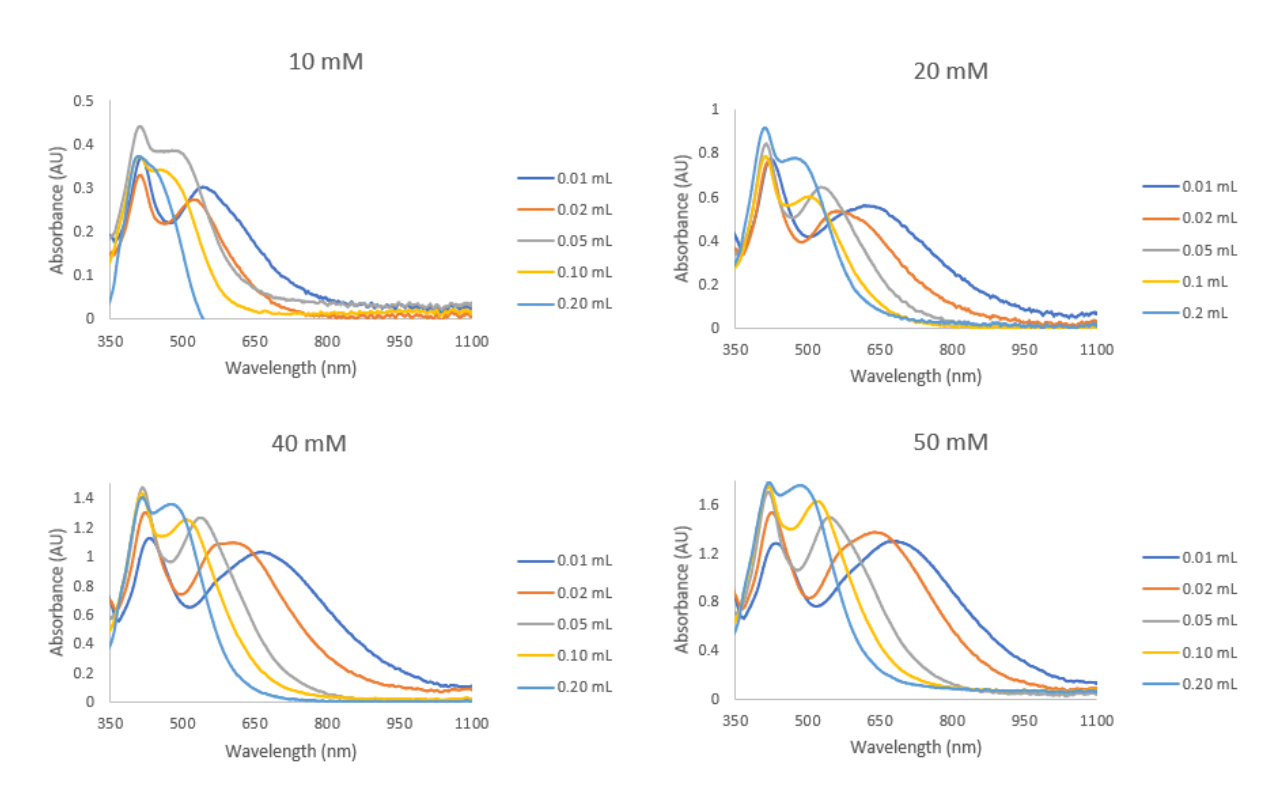


Figure 3.15. UV-Vis spectra of the final nanoparticle growth at different concentrations of AgNO3 in the growth solution. For each concentration, the seed amount was varied between 0.01 to 0.2 mL.

3.4.4 Effects of surfactant added in growth solution

The effect of concentration of CTAB in growth solution was investigated. Particles were synthesised at four different concentrations of CTAB: 5, 10, 20 and 50 mM. The concentrations of other reagents were kept constant.

CTAB is a surfactant used to direct the growth of silver nanorods in the longitudinal axis by forming stable, elongated micelles. In principle, Ag^+ in the growth solution reacts with Br^- (bromine) in CTAB to form AgBr, which adsorbs to the growth sites on seed particles [73]. This allows preferential growth in one direction. Figure 3.16 shows the optical absorption spectra of the nanoparticles prepared using four different concentrations of CTAB in growth solution. For each CTAB concentration, the seed concentration was varied between 0.01 - 0.20 mL.

At a CTAB concentration of 5 mM, the 0.2 mL seed sample exhibited a solitary absorption peak, signifying the exclusive presence of spherical nanoparticles. This outcome likely stemmed from the elevated seed-to-CTAB ratio, which hindered the formation of anisotropic particles. As the seed concentration diminished, two peaks

emerged, indicative of the synthesis of nanorods. Among these, the 0.01 mL seed sample demonstrated the most significant wavelength absorption, with the LSPR peak centred around 650 nm. Elevating the CTAB concentration within the growth solution to 10 mM and 20 mM resulted in the absorption of longer wavelengths compared to the 5 mM concentration. However, it's worth noting that the secondary peaks were broader, suggesting the presence of nanoparticles of varying sizes or shape. It is noteworthy that when the CTAB concentration reached 20 mM, both the 0.01 mL and 0.02 mL samples displayed three peaks: a weak initial peak around 400 nm attributed to spherical nanoparticles, a second peak around 540 nm linked to the in-plane quadrupole resonance mode, and a third broad peak associated with the in-plane dipole resonance mode, indicative of the presence of nanotriangles [219]. Further increasing the CTAB concentration within the growth solution to 50 mM resulted in the absorption of shorter wavelengths compared to the 5 mM concentration. The LSPR peaks were centred around 500 nm, indicating the synthesis of shorter nanorods.

It was found that 20 mM concentration of CTAB in growth produced longer nanorods. The seed concentration to CTAB ratio appeared critical in controlling the nanoparticle growth. Another factor that could be co-related alongside the CTAB concentration was the existence of AgNO₃ in the growth solution. CTAB capped the silver atoms when they were reduced by addition of ascorbic acid (AA) and sodium hydroxide. If the concentration of CTAB was increased, perhaps the concentration of AgNO₃ should also be increased to synthesise longer nanorods.

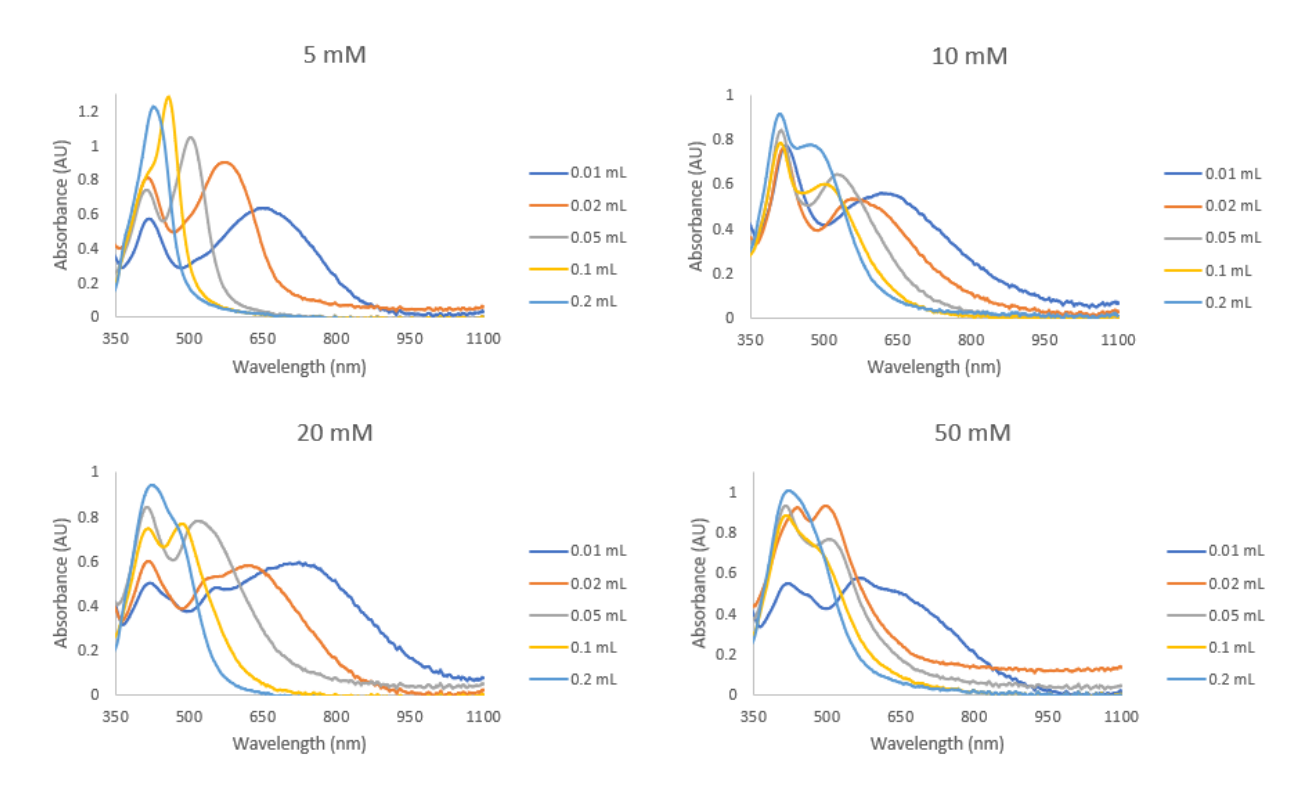


Figure 3.16. UV-Vis spectra of nanoparticles synthesised at different concentrations of CTAB in the growth solution. For each concentration, the seed amount was varied between 0.01 to 0.2 mL.

3.4.5 Effects of ascorbic acid (AA) in growth solution

The effect of concentration of AA in growth solution was investigated. Particles were synthesised at four different concentrations: 50, 100, 200, and 300 mM. The concentrations of other reagents were kept constant.

AA is a weak reducing agent which cannot reduce AgNO₃ in growth solution without the presence of seeds and NaOH [105]. Figure 3.17 shows the optical absorption spectra of the nanoparticles prepared using four different concentrations of ascorbic acid in growth solution. When the concentration was 50 mM, there were two peaks for all seed concentrations, and the second shifted to higher wavelengths with decreasing seed concentration. When the concentration was increased to 100 mM, the secondary peaks for all samples shifted to lower wavelengths. This indicated that the nanoparticles became smaller. When the size of anisotropic nanoparticles reduced, the absorption shifted to lower wavelengths. When the concentration was 200 mM, only 0.02 mL seed sample showed two peaks, indicating that there was no growth of anisotropic particles in other samples. Increasing the concentration further to 300 mM

led to diminishing of the secondary peaks, indicating that most of nanoparticles in all samples were isotropic.

As the concentration of AA in the growth was increased from 50 to 300 mM, the general trend in the maximum absorption wavelength band showed a blue shift. This may be related to the ratio of AA to NaOH in the growth solution. As the AA concentration was increased, so was the AA to NaOH ratio. Due to relatively less NaOH concentration, this limited the reduction power of AA to reduce AgNO₃ in the growth solution to silver ions to form anisotropic nanoparticles [220]. When a higher amount of AA was used, NaOH concentration must be also increased to produce nanorods.

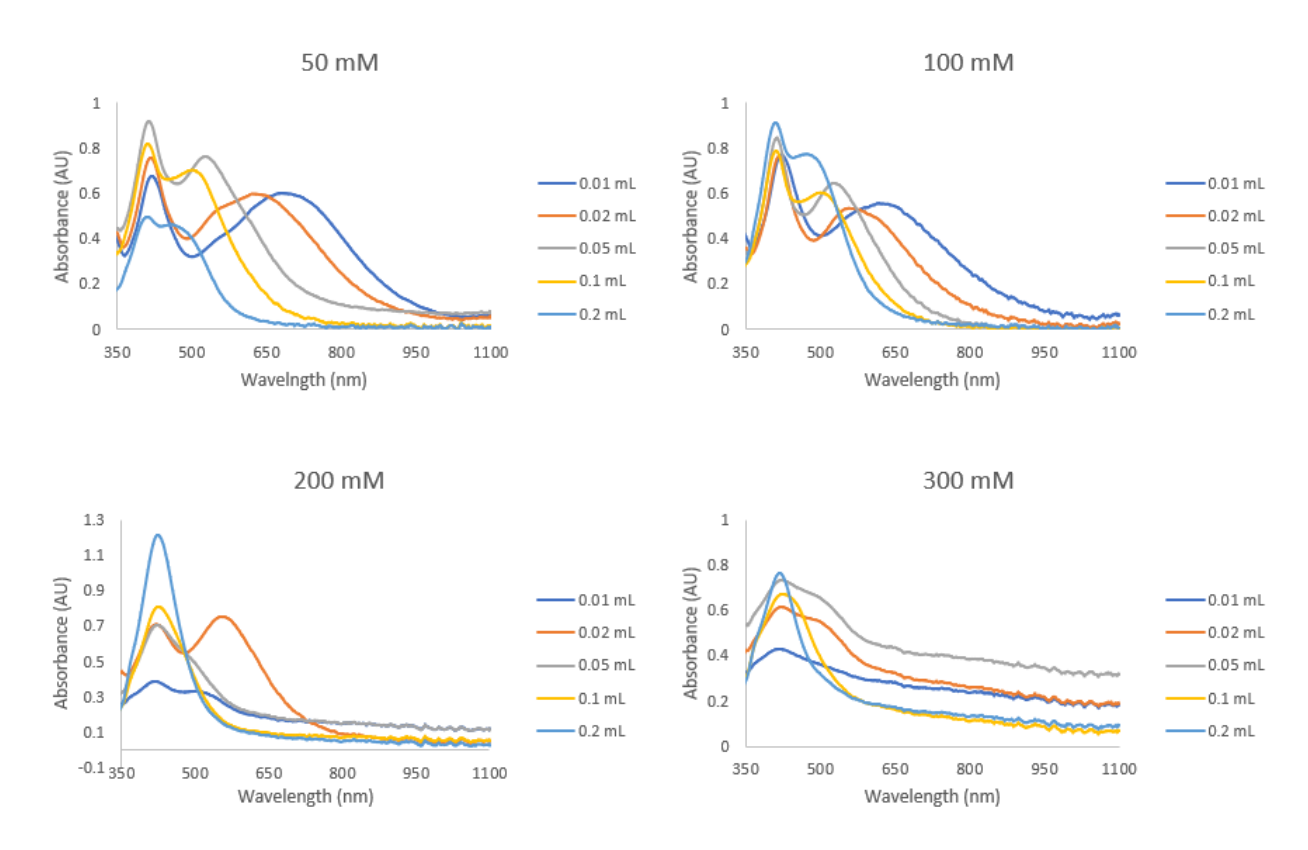


Figure 3.17. UV-Vis spectra of nanoparticles synthesised at different concentrations of ascorbic acid in the growth solution. For each concentration, the seed amount was varied between 0.01 to 0.2 mL.

3.4.6 Effects of sodium hydroxide added in growth solution

The effect of concentration of sodium hydroxide in growth solution was investigated. Particles were synthesised at three different concentrations: 0.5, 1 and 2 M. The concentrations of other reagents were kept constant.

Figure 3.18 shows the optical absorption spectra of the nanoparticles prepared using three different concentrations of NaOH added in growth solution. When the concentration of NaOH was 0.5 M, all the samples showed only single peaks. This indicated that the nanoparticles were spherical in shapes. It was largely due to the fact that the pH of the growth solution was relatively low with a value of 6. This meant the reduction power of ascorbic acid was rendered, hence no silver ions in growth solution were converted to form bigger nanoparticles on to seed particles. Zhong et al. concluded from their research on the influence of pH in silver nanoparticle synthesis that when the growth solution was acidic, the reduction rate of Ag⁺ by ascorbic acid was too slow to form nanoparticles [221]. The results obtained in the present work aligned well with the hypothesis by Zhong et al.

When the NaOH concentration was elevated to 1 M, all test samples displayed two absorption peaks, signifying the formation of nanorods. As the seed volume decreased, the secondary peaks exhibited a shift towards longer wavelengths, with the most pronounced absorption peak occurring at 650 nm in the case of the 0.01 mL sample. The augmentation of NaOH concentration induced a rise in the pH level within the growth solution, reaching a pH of 9. This, in turn, enhanced the reducing capacity of ascorbic acid, resulting in an increased production of silver ions that subsequently attached to the seed particles. Consequently, the aspect ratios of the nanorods varied depending on the seed volume.

Raising the NaOH concentration to 2 M led to a shorter maximum absorption wavelength, and the secondary peaks shifted towards shorter wavelengths compared to the 1 M concentration. At this higher concentration of 2 M, the pH of the growth solution was notably elevated, thereby amplifying the reducing capability of ascorbic acid. Consequently, AgNO₃ was converted at an accelerated rate, leading to the aggregation of nanoparticles and, consequently, a reduction in the aspect ratio of the nanorods. These outcomes underscore the significance of manipulating the reducing potential of ascorbic acid, modulated by variations in pH within the growth solution, as a pivotal determinant in governing the morphology of AgNPs.

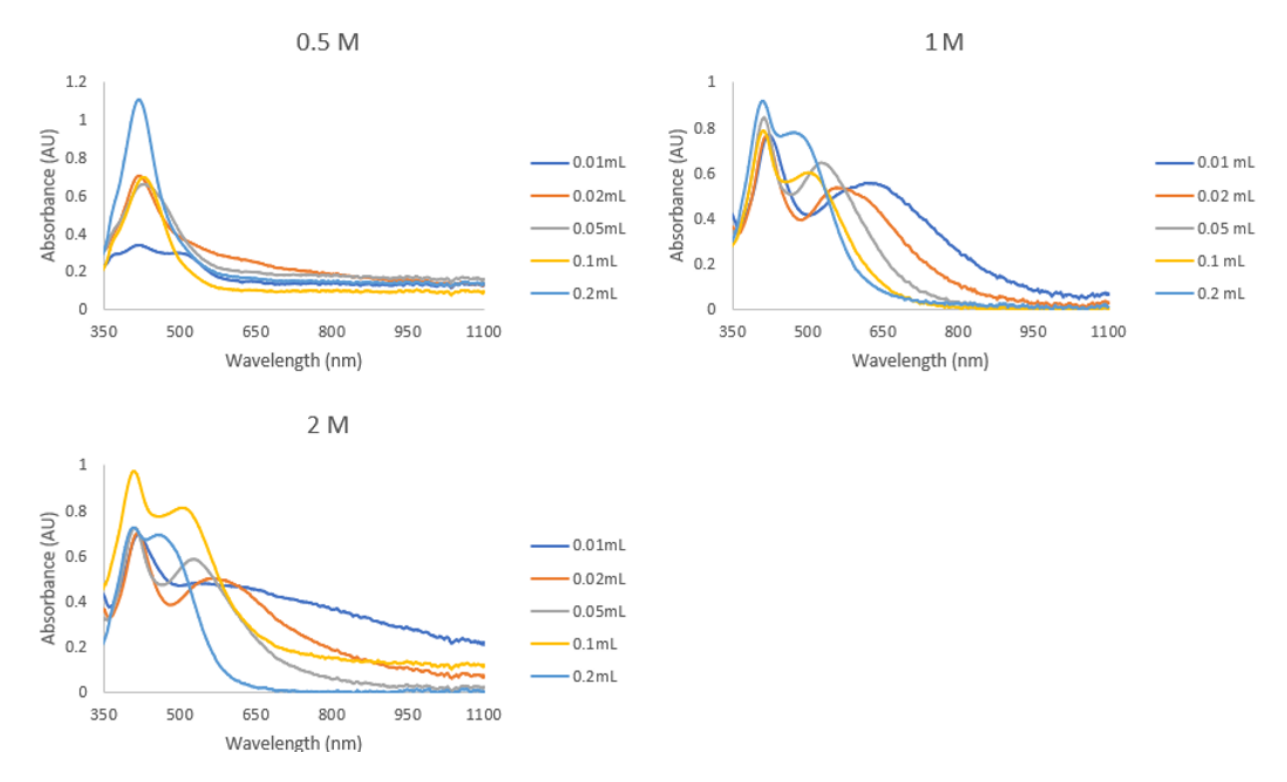


Figure 3.18. UV-Vis spectra of nanoparticles synthesised at different concentrations of NaOH in the growth solution. For each concentration, the seed amount was varied between 0.01 to 0.2 mL.

3.4.7 Optimisation of reaction conditions in method 1

From the above experiments, optimal parameters for maximum absorption wavelength bands were identified. Three trials were conducted to further identify the optimal concentration of each reagent.

First trial

Table 3-4 shows the parameters which produced maximum absorption wavelength bands in the previous experiments. Nanoparticles were synthesised using these parameters and their optical properties were measured. The seed volume was varied between 0.01 - 0.2 mL, and two different volumes of NaOH were used.

Reagent	Concentration
AgNO ₃ in seed solution	1 mM, 5 mL
CTAB in seed solution	100 mM, 0.08 mL
NaBH₄ in seed solution	5 mM, 0.6 mL
CTAB in growth solution	20 mM, 10 mL
AgNO ₃ in growth solution	50 mM, 0.25 mL

AA in growth solution	100 mM, 0.25 mL
NaOH in growth solution	1 M, 0.10, or 0.15 mL

Table 3-4 Parameters used to synthesise nanoparticles in trial 1

Figure 3.19 shows the absorption spectra of nanoparticles synthesised using parameters from the Table 4-1. When the NaOH volume was 0.1 mL, all samples showed broad peaks in the near-infrared region. The 0.02 mL seed sample showed the maximum absorption band around 1000 nm wavelength. The highest absorption exhibited with the 0.05 mL seed samples, having an absorption peak centred around 950 nm wavelength. As the peaks were broad, it suggested that there were different sized nanoparticles in each sample. Where the absorption peak wavelength was longer, there were bigger sized nanoparticles in that sample, as observed in previous studies [222].

When the NaOH volume was set at 0.15 mL, it was observed that the peaks in all the samples were well-defined, albeit exhibiting a slight shift towards longer wavelengths when compared to samples containing 0.1 mL of NaOH. Notably, the peaks for the 0.01 mL and 0.02 mL samples exhibited considerable broadening, indicative of a significant variance in the sizes and shape of the nanoparticles. As the seed volume was reduced from 0.2 mL to 0.05 mL, there was a noticeable trend of the peaks shifting towards higher wavelengths. These distinct peaks observed in the 0.2 mL, 0.1 mL, and 0.05 mL samples suggested a uniformity in the size of the nanoparticles. The experimental conditions employed in this study thus validated the feasibility of synthesising silver nanoparticles capable of absorbing light at near-infrared wavelengths. Specifically, the optimal volume of NaOH for achieving these outcomes was determined to be 0.15 mL, exhibiting a maximum absorption peak at around 1000 nm.

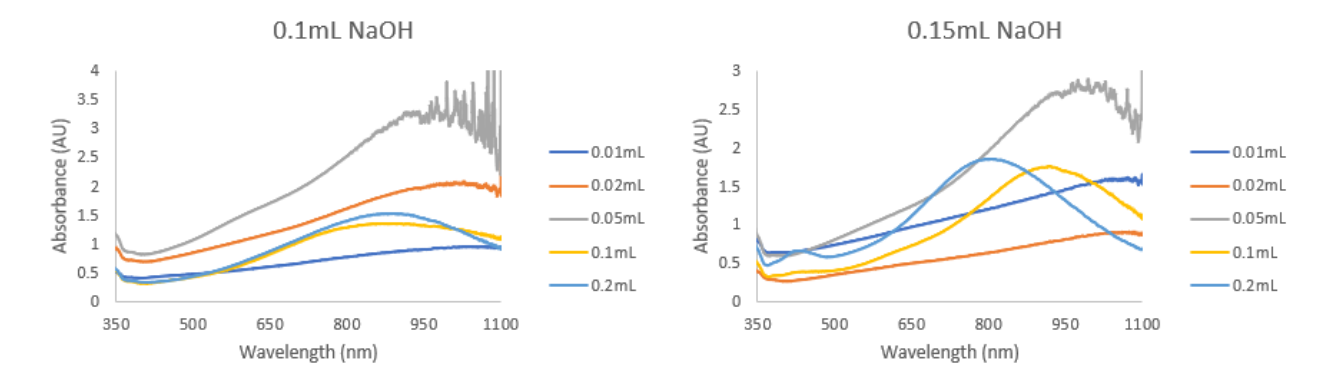


Figure 3.19. Absorption spectra of nanoparticles synthesised using parameters in Trial 1

Second trial

A second trial was conducted where the concentrations of CTAB and $AgNO_3$ in the growth solution were varied in order to investigate their influence on nanoparticle morphology and yield. The volume of CTAB was increased from 10 mL to 15 mL, and the concentration of $AgNO_3$ was reduced from 50 mM to 20 mM. The seed volume was varied between 0.01 - 0.2 mL. The parameters are given in Table 3-5.

Reagent	Concentration
AgNO ₃ in seed solution	1 mM, 5mL
CTAB in seed solution	100 mM, 0.08 mL
NaBH ₄ in seed solution	5 mM, 0.6 mL
CTAB in growth solution	10 mM, 15 mL
AgNO ₃ in growth solution	20 mM, 0.5 mL
AA in growth solution	100 mM, 0.25 mL
NaOH in growth solution	1 M, 0.10 mL

Table 3-5 Parameters used to synthesise nanoparticles in trial 2

Figure 3.20 shows the absorption spectra of nanoparticles synthesised using parameters from table above. All samples exhibited two separate peaks. The first weak peaks around 400 nm wavelength were due to presence of spherical nanoparticles. The second peaks were due to in-plane dipole resonance mode of nanotriangles [219]. The absorption peak's wavelength increased with decreasing seed volume. For the lower seed volumes of 0.01 mL and 0.02 mL, the maximum absorption peak was around 1100 nm, albeit the peaks were quite broad. For the highest seed volume, the maximum absorption peak was at around 760 nm.

Figure 3.21 shows the resulting morphologies of nanoparticles at the two highest and two lowest seed volumes. At low seed concentrations, very large triangular and non-spherical nanoplates were produced, with edges of up to 500 nm long. This explained the broad peaks in the absorbance measurement. As the concentration was increased, the resulting morphologies were different. As seen from Figure 3.21C, there were small spherical nanoparticles, with large triangular nanoparticles, as well as long nanorods. When the seed volume was 0.2 mL, nanorods were produced (see Figure 3.21D) that were shorter than those in the 0.01 mL seed sample.

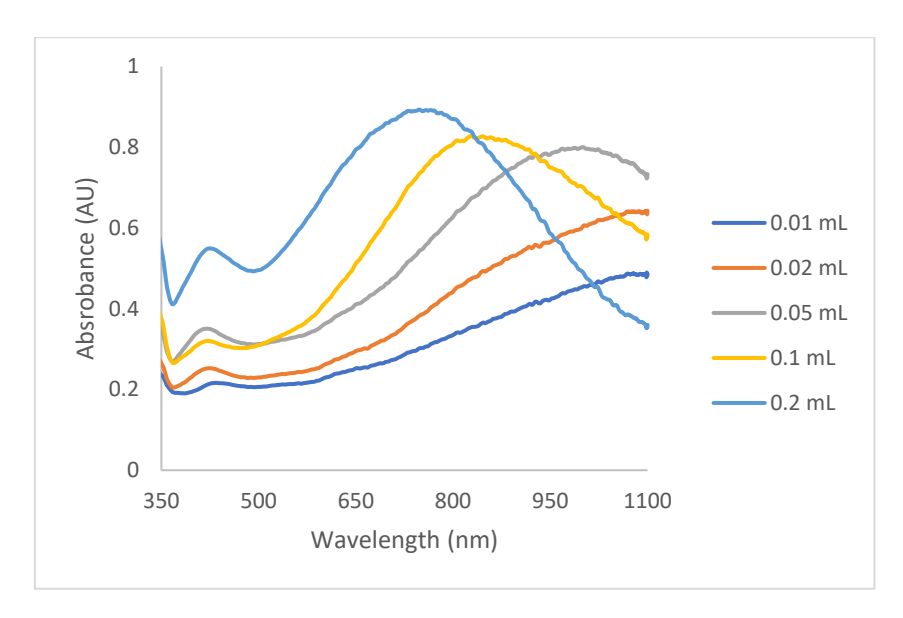


Figure 3.20. Absorption spectra of nanoparticles synthesised using parameters in Trial 2

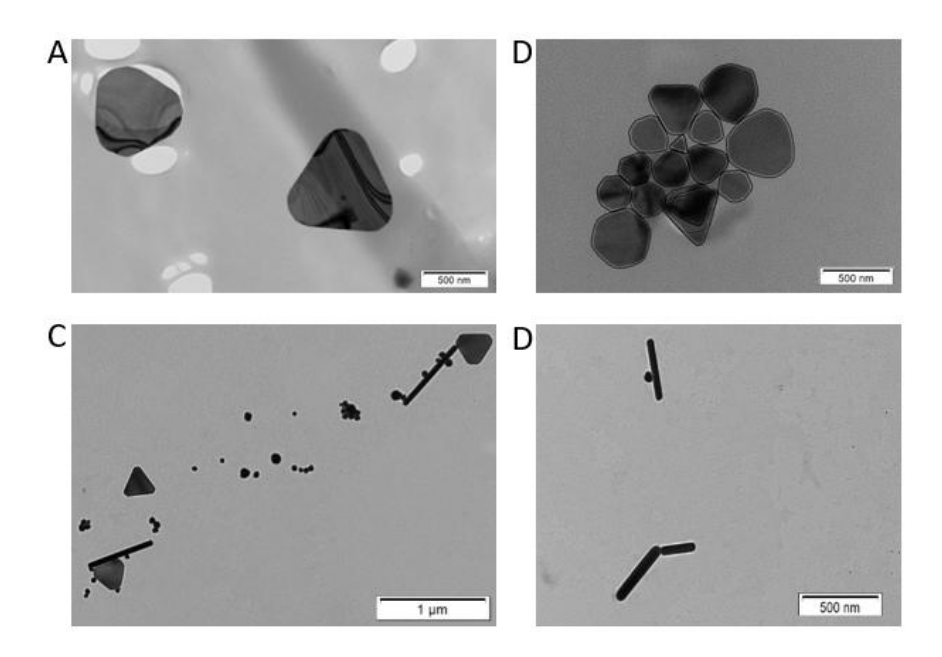


Figure 3.21. TEM images of nanoparticles synthesised using parameters in Trial 2. (A) 0.01 mL seed sample; (B) 0.02 mL seed sample; (C) 0.1 mL seed sample; (D) 0.2 mL seed sample

Analysis of trial 2 results in context of reference spectra

Table 3-6 presents the evolution of nanoparticle morphology and LSPR peak position as a function of seed volume in Method 1 – trial 2. A clear relationship is observed between seed volume, particle shape, and optical properties, which aligns well with reference spectra for silver nanoprisms and nanorods.

Seed volume	LSPR λ (nm)	Dominant	Size / Aspect
(mL)		Morphology	Ratio
0.01	>1100	Nanoprisms	~650 nm edge
			length
0.02	1095	Nanoprisms,	~340 nm
		quasi-shapes	average size
0.10	846	Rods,	Prisms
		nanoprisms,	~300 nm; Rods
		spheres	AR ≈ 9
0.20	760	Nanorods	Rods AR ≈ 5.5

Table 3-6 Summary of morphological and optical characteristics from Method 1 – Trial 2, showing the effect of seed volume on LSPR peak position and nanoparticle shape.

At low seed volumes (0.01–0.02 mL), the UV-Vis spectra exhibited strong LSPR peaks beyond 1100 nm, corresponding to large triangular nanoprisms with edge lengths up to 650 nm. These results are consistent with the reference spectra (Figure 2.4a), which show progressive red-shifting from ~500 to 700 nm as prism size increases from 35 to 64 nm. The above data extends this trend, confirming that LSPR continues to redshift well into the near-infrared with further increases in lateral dimension.

As the seed volume increased to 0.1 and 0.2 mL, the morphology shifted to rod-dominant structures, with aspect ratios of 9 and 5.5, and corresponding LSPR peaks of 845 nm and 760 nm, respectively. These values align with the reference nanorod spectra (Figure 2.4b), where LSPR peaks shift from ~540 to ~650 nm as aspect ratio increases from 6 to 15.

Third trial

A third trial was conducted where the CTAB in the growth solution was varied. The volume of CTAB was increased from 10 mL to 15 mL, and the concentration of AgNO₃

was reduced from 50 mM to 20 mM. The seed volume was varied between 0.01 - 0.2 mL. The synthesis parameters are given in Table 3-7.

Reagent	Concentration
AgNO ₃ in seed solution	1 mM, 5mL
CTAB in seed solution	100 mM, 0.08 mL
NaBH₄ in seed solution	5 mM, 0.6 mL
CTAB in growth solution	100 mM, 10 mL
AgNO ₃ in growth solution	20 mM, 0.25 mL
AA in growth solution	100 mM, 0.5 mL
NaOH in growth solution	1 M, 0.10 mL

Table 3-7 Parameters used to synthesise nanoparticles in trial 3

Figure 3.22 shows the absorption spectra of nanoparticles synthesised using parameters from the table above. Again, the peaks showed that the surface plasmon response of nanoparticles depended on the seed volume. The maximum absorption band was red-shifted as the seed concentration was reduced. For the lowest seed concentrations of 0.01 and 0.02 mL, the peaks were broad and centred around 950 nm wavelength.

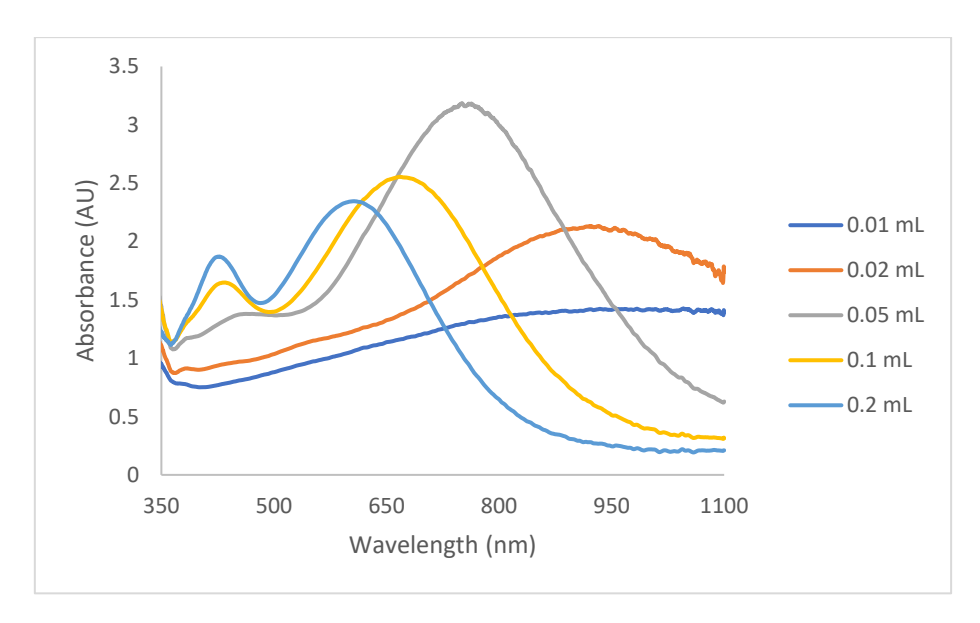


Figure 3.22. Absorption spectra of nanoparticles synthesised using parameters in Trial 3

Figure 3.23 shows the corresponding nanoparticle morphologies for these two samples. The nanoparticle shapes ranged from very large hexagonal to smaller

triangular nanoplates, and smaller nanorods. The variations in size and shape were the main cause for the peaks to be broad for these two samples.

The three samples, each prepared with seed volumes of 0.05 mL, 0.1 mL, and 0.2 mL, exhibited the presence of two discernible peaks, indicative of nanorod growth. Among these samples, the 0.05 mL sample displayed the highest absorption peak, with the peak centring at 770 nm. As the seed volume was increased to 0.1 mL and 0.2 mL, a noticeable reduction in the height of the absorption peaks was observed, concomitant with a significant broadening of the two peaks. This reduction was directly proportional to the decrease in the aspect ratio of the nanorods. Figure 3.23C and D depict TEM images of the nanoparticles in these two samples. These images reveal the presence of nanorods in both samples, along with smaller non-spherical nanoparticles. In the case of the 0.1 mL sample, the nanorods exhibited a length ranging between 300 to 400 nm, while in the 0.2 mL sample, they were notably shorter. This observation substantiates the redshift of the absorption band in the 0.1 mL sample when compared to the 0.2 mL sample.

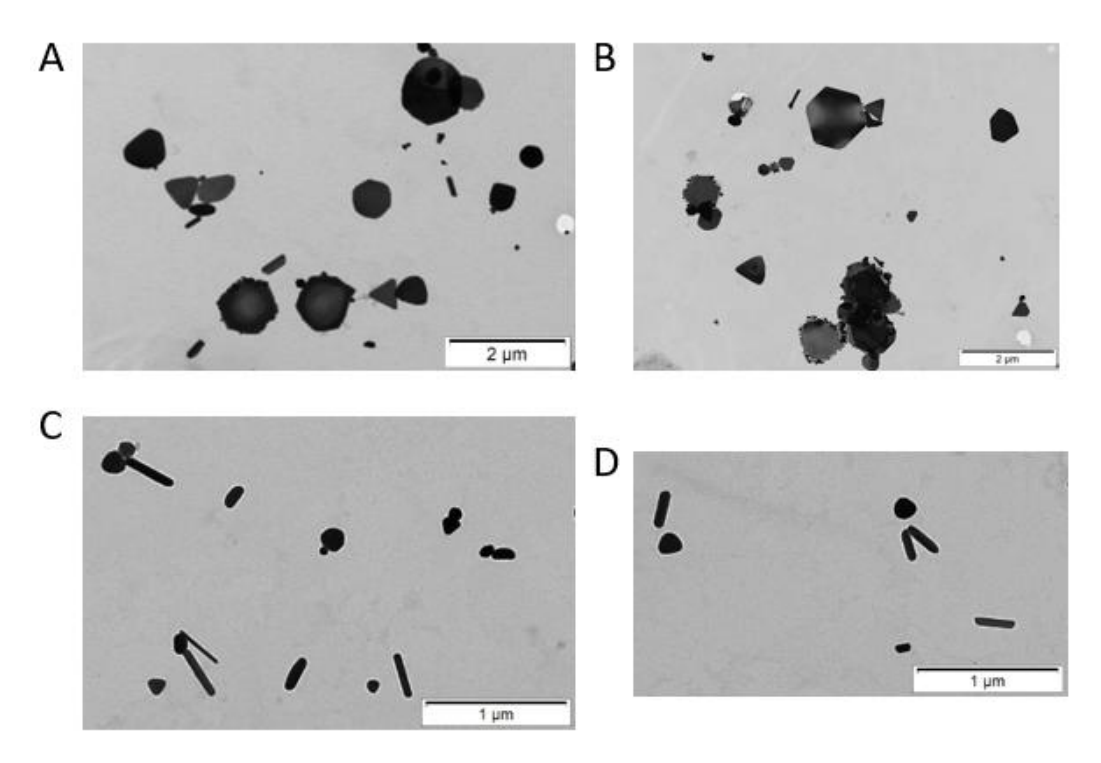


Figure 3.23. TEM images of nanoparticles synthesised using parameters in trial 3. (A) 0.01 mL seed sample; (B) 0.02 mL seed sample; (C) 0.1 mL seed sample; (D) 0.2 mL seed sample

Comparison of method 1 with reference spectra

In order to assess how seed volume influences nanoparticle shape and optical properties, three trials from Method 1 using 0.1 mL of seed solution were compared with a literature reference (Figure 3.4 in which silver nanorods with an aspect ratio of approximately 15 produced a longitudinal LSPR peak at 650 nm. This reference provides a baseline for understanding how variations in morphology and size affect plasmonic behaviour. Please see table below for the comparison:

Source	LSPR λ (nm)	Morphology	Aspect Ratio / Size
Literature (ref)	650	Nanorods	AR ≈ 15
Trial 1	870	Not determined	Unknown
Trial 2	846	Rods, prisms, Spheres	Rods AR ≈ 9; Prisms ~300 nm
Trial 3	675	Rods, quasispheres	Rods AR ≈ 5

Table 3-8 Comparison of UV-Vis LSPR peak positions and nanoparticle morphologies obtained using 0.1 mL seed volume in three experimental trials (Method 1), against a reference silver nanorod sample reported in literature.

In Trial 1, the LSPR peak was observed at 870 nm, notably redshifted relative to the reference. Although the morphology was not explicitly determined by TEM for this sample, the significant shift suggests the presence of either higher-aspect-ratio rods or large planar structures such as nanoprisms, both of which are known to drive LSPR features into the near-infrared. The broad, high-wavelength response is characteristic of anisotropic and potentially mixed particle populations.

Trial 2 confirmed a heterogeneous morphology, consisting of nanorods (AR ~9), triangular nanoprisms (~300 nm edge length), and smaller spherical particles. The resulting LSPR peak at 846 nm supports a composite plasmonic response, where the longer-wavelength contributions from nanoprisms dominate the spectrum, with additional influence from nanorods and scattering from spheres. This result is consistent with both experimental literature and theoretical models that predict strong redshifts in the presence of large planar nanostructures.

In contrast, Trial 3 yielded a cleaner nanorod-dominant morphology, with rods having an average aspect ratio of ~5, accompanied by a small fraction of quasispherical particles. The LSPR peak for this trial, 675 nm, is the closest match to the literature reference of 650 nm, although the observed aspect ratio is significantly lower. This apparent discrepancy is likely due to variations in synthesis conditions, dielectric environment, and particle distribution—all factors that can subtly shift the resonance.

3.4.8 Stability testing

To assess the durability of the nanoparticles over time, a specimen underwent an absorption assessment following a 12-week storage period, juxtaposed with the initial measurement of a freshly prepared sample. During this 12-week duration, the sample was stored at room temperature, shielded from exposure to light. In Figure 3.24, the absorption spectra for both measurements are presented. The findings revealed a subtle adjustment towards a marginally shorter wavelength (from 806 nm to 804 nm), accompanied by a slight elevation in the absorption peak height (from 1.3 to 1.4). These observations suggest that the nanoparticles exhibited a reasonably stable behaviour under standard ambient conditions.

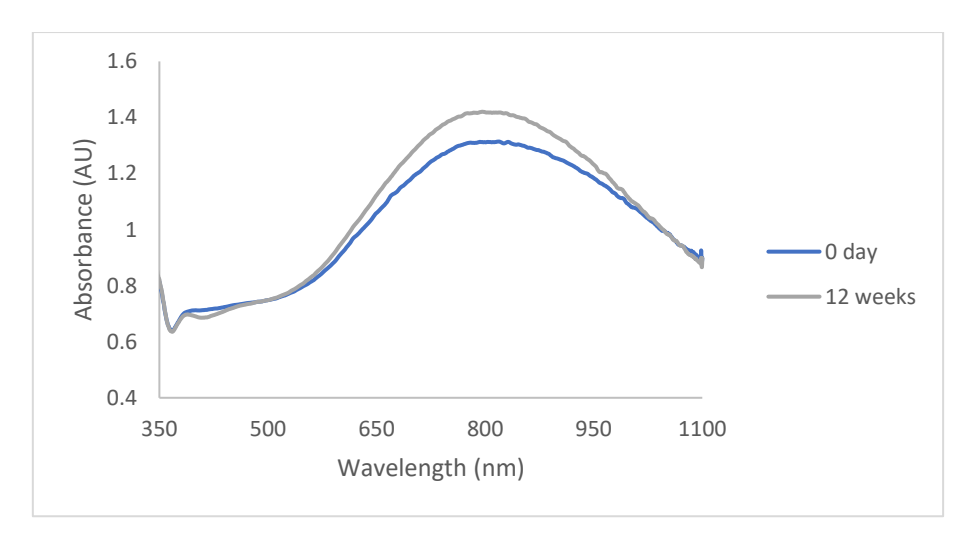


Figure 3.24. UV-vis absorption spectra of nanoparticles measured 12 weeks apart

3.5 Batch synthesis using method 2

In this method, trisodium citrate (TSC) capped silver seed particles were used to produce anisotropic nanoparticles. This method was initially developed by Jana et el., part of the Murphy group [64]. The concentrations of reagents in the seed phase as well as growth phase were varied separately to study the optical properties of silver nanoparticles.

The seed particles were prepared by reducing AgNO₃, mixed with an aqueous solution of TSC, using NaBH₄ as the reducing agent to ensure the complete reduction of Ag⁺. A colour change was observed within 1 minute from a clear solution to yellow, indicating the formation of spherical silver nanoparticles. The colloidal solution was covered with aluminium foil and kept out of light for 2 hours before being used.

This seed solution was then further used without any purification to produce secondary nanoparticles. For each seed solution, five sets of growth solutions were made. Each set contained the surfactant CTAB, AgNO₃ and ascorbic acid. Then the seed solution was added in varied amounts. Lastly, a solution of NaOH was added. Within a few minutes, the colour of each set changed according to the seed amount. All the samples were purified using centrifugation due to high amount of CTAB.

3.5.1 Influence of silver nitrate added in seed solution

The effect of concentration of silver nitrate in seed solution was investigated. Seed particles were synthesised at four different concentrations of silver nitrate: 0.25, 0.5, 1.0 and 2.0 mM. The concentrations of other reagents were kept constant. Below, the effect on seed particles and final particle growth is discussed.

Effect on seed particles

Figure 3.25 shows the UV-Vis absorption spectra of seed particles prepared at different concentrations of silver nitrate. The absorbance peak increased as the concentration of silver nitrate increased. The results showed that the positions of all the four peaks were between wavelengths of 380 - 400 nm. It was observed that at a concentration of 0.5 mM (blue curve), the absorbance was around 0.13, whereas increasing the concentration to 2 mM (yellow curve) led to increased absorbance.

Generally, the LSPR peak shifted to lower wavelength with increasing silver nitrate concentration and became narrow. At 2 mM concentration of AgNO₃ the LSPR peak was at 380 nm. This indicated a change in the size of nanoparticles, suggesting that they became smaller in size. The narrowing of the peak implied a better degree of the size distribution, whereas a broader peak implied that there were different sized nanoparticles. The exact size of these seed particles was difficult to be measured as it was limited by the available TEM resolution. However, based on the previous study by Jana et al. [64], it was still possible to estimate that these seed particles were about 4-5 nm in diameter.

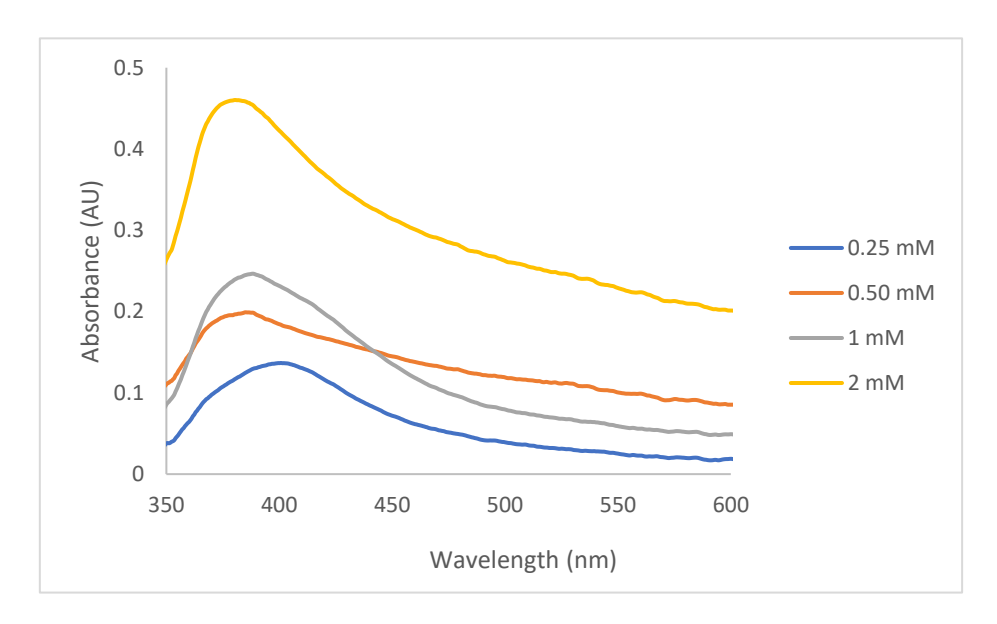


Figure 3.25. UV-Vis spectra of silver seed particles obtained at 0.25, 0.50, 1.0 and 2.0 mM of silver nitrate

Influence silver nitrate added in seed solution on final particle growth

Figure 3.26 shows the optical absorption spectra of the nanoparticles prepared using four different concentrations of silver nitrate added in seed solution. Different seed amounts in the growth solution were used to prepare nanoparticles.

All samples for each concentration showed very broad absorption peaks. For the 0.25 mM concentration, the 0.1 mL and 0.2 mL showed broad absorbance peaks, indicating presence of various sized anisotropic nanoparticles. When the concentration of AgNO₃ in seed solution was increased to 0.50 mM, the highest seed volume of 0.5 mL showed a narrow second peak centred at 740 nm. This indicated the presence of uniform sizes anisotropic nanoparticles. The peaks for 0.2 mL, 0.1 mL and 0.05 mL samples were

very broad, indicating nanoparticles of varying sizes. Increasing the concentration of AgNO₃ in seed solution further to 1 mM led to similar results to the 0.50 mM samples.

At the highest concentration of AgNO₃ in seed solution of 2 mM, all samples showed clear peaks around 400 nm, without clear second peaks, except for the 0.5 mL sample. This indicated that no anisotropic nanoparticles were formed. The 0.5 mL sample showed a weak second peak around 780 nm, indicating the presence of some nanorods. From these results, it is concluded that concentrations of 0.5 and 1 mM AgNO₃ in seed solution produce nanoparticles with higher absorbance compared to the other two concentrations. The seed volume should be 0.2 mL and higher to produce anisotropic nanoparticles.

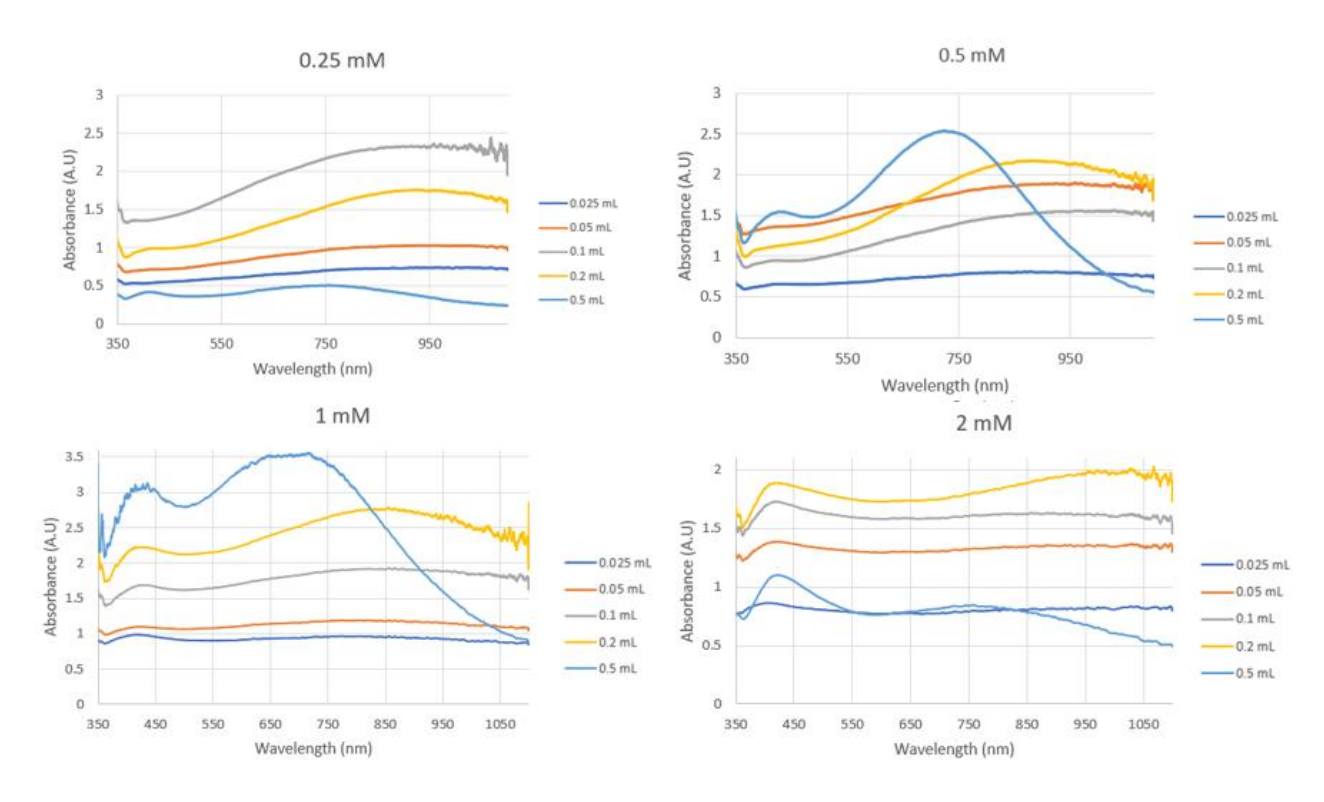


Figure 3.26. UV-Vis spectra of the final nanoparticle growth at different concentrations of silver nitrate in the seed solution. For each concentration, the seed amount was varied between 0.025 to 0.5 mL.

3.5.2 Effects of silver nitrate added in growth solution

The effect of concentration of silver nitrate in growth solution was investigated. Particles were synthesised at three different concentrations of silver nitrate: 10, 20, and 40 mM. The concentrations of other reagents were kept constant. Below, the effect on particle growth is discussed.

Figure 3.27 shows the optical absorption spectra of the nanoparticles prepared using three different concentrations of silver nitrate in growth solution. When the concentration was 10 mM, for 0.50- and 1.0-mL seed samples, there was a main peak around 540 nm with a shouldered peak. This indicated that nanoparticles were not fully isotropic, which could be very short nanorods or non-spheroids. For the 0.25 mL and 0.1 mL samples, two weak peaks were observed: one around 400 nm and the other 600 nm, indicating the presence of some nanorods.

Elevating the AgNO₃ concentration to 20 mM resulted in an augmentation of absorbance in comparison to the 10 mM samples, accompanied by a noticeable redshift in the positions of the absorption peaks. The 0.5 mL sample distinctly displayed a second peak centred at 720 nm, while the lower three seed samples exhibited broad peaks extending into the near-infrared region. The 0.25 mL sample (denoted by the grey peak) featured a broad peak spanning from 950 to 1000 nm, signifying the presence of some anisotropic nanoparticles.

Upon further increasing the AgNO₃ concentration in the growth solution to 40 mM, both the 0.5 mL and 1.0 mL samples exhibited dual, separate peaks. These secondary peaks exhibited a lengthening of wavelengths with diminishing seed concentration, indicative of an increase in the aspect ratio of the nanorods. Notably, the absorption peak shifted towards shorter wavelengths in comparison to the 20 mM samples, while the absorption peak itself intensified. The second peak in the 0.5 mL sample appeared relatively narrow, suggesting the presence of monodispersed nanorods. However, the 0.05 mL sample failed to exhibit a distinct peak, implying the absence of nanoparticle formation.

The escalation in AgNO₃ concentration within the growth solution translated to a surplus of silver ions available for attachment to seed particles, fostering the formation of elongated nanorods with heightened aspect ratios and, consequently, absorption of longer wavelengths. It is evident that higher AgNO₃ concentrations in the growth solution have the potential to yield nanorods with greater aspect ratios, provided the seed concentration is reduced and other experimental parameters remain constant. Additionally, a seed concentration greater than 0.25 mL is necessary to produce anisotropic nanoparticles using this method.

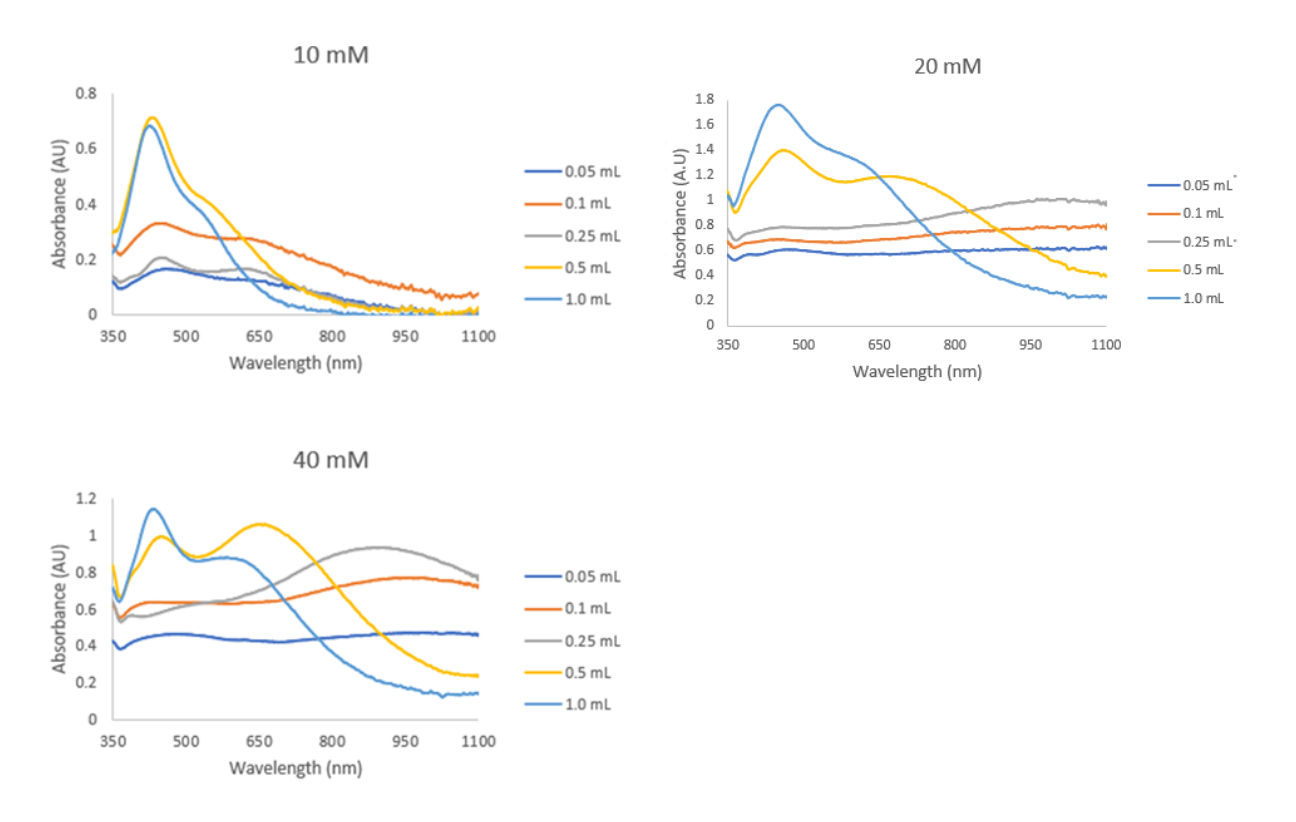


Figure 3.27. UV-Vis spectra of the final nanoparticle growth at different concentrations of AgNO3 in the growth solution. For each concentration, the seed amount was varied between 0.05 to 1.0 mL.

3.5.3 Effects of CTAB added in growth solution

The effect of CTAB concentration of in growth solution was investigated. Particles were synthesised at three different concentrations of CTAB: 50, 80 and 100 mM. The concentrations of other reagents were kept constant. Below, the effect on particle growth is discussed.

Figure 3.28 displays the optical absorption spectra of nanoparticles synthesised using varying concentrations of CTAB within the growth solution. In each case of CTAB concentration, the seed concentration was adjusted within the range of 0.05 mL to 1.0 mL. In instances where a 50 mM CTAB concentration was employed, all samples exhibited a predominant absorption peak within the wavelength range of 400 to 450 nm, accompanied by a secondary, somewhat subdued peak. Notably, the lowest seed sample of 0.05 mL exhibited a sole absorption peak at approximately 500 nm, indicative of the nanoparticles assuming a spherical morphology. This occurrence suggests that the CTAB concentration was sufficiently high to inhibit the formation of anisotropic particles. As the seed concentration was progressively increased, the

absorption spectra displayed two peaks, signifying the initiation of nanorod formation. The second peak demonstrated a trend towards shorter wavelengths with the incremental increase of seed volume, ranging from 0.1 mL to 1 mL. Remarkably, the 0.2 mL seed sample manifested the most extensive absorption in terms of wavelength, with the LSPR peak centring around 670 nm.

Upon elevating the CTAB concentration within the growth solution to 80 mM, the highest seed samples demonstrated an increase in the peak with the highest absorbance in comparison to the 50 mM CTAB concentration. Specifically, when scrutinising the 0.5 mL samples under both 50 mM and 80 mM CTAB concentrations, it becomes evident that the secondary peak exhibited a redshift, transitioning from 640 nm to 700 nm. This observation signifies the extension of nanorods when the CTAB concentration was heightened. In contrast, for the 0.05 mL and 0.1 mL samples, no distinct peaks were discernible, suggesting the absence of nanoparticle formation. Meanwhile, the 0.25 mL sample exhibited a broad peak spanning the range of 950 to 1000 nm, indicative of the presence of certain anisotropic nanoparticles.

Increasing the concentration of CTAB in growth solution further to 100 mM resulted in shorter wavelengths being absorbed compared to the 80 mM concentration. However, all samples showed (weak) second peaks. The 0.5 mL sample had an LSPR peak centred around 600 nm, indicating synthesis of short nanorods. Since the three concentrations of CTAB in growth solution in this method produced much lower number of nanoparticles, it was recommended that lower concentrations of CTAB might be favourable for nanoparticle growth.

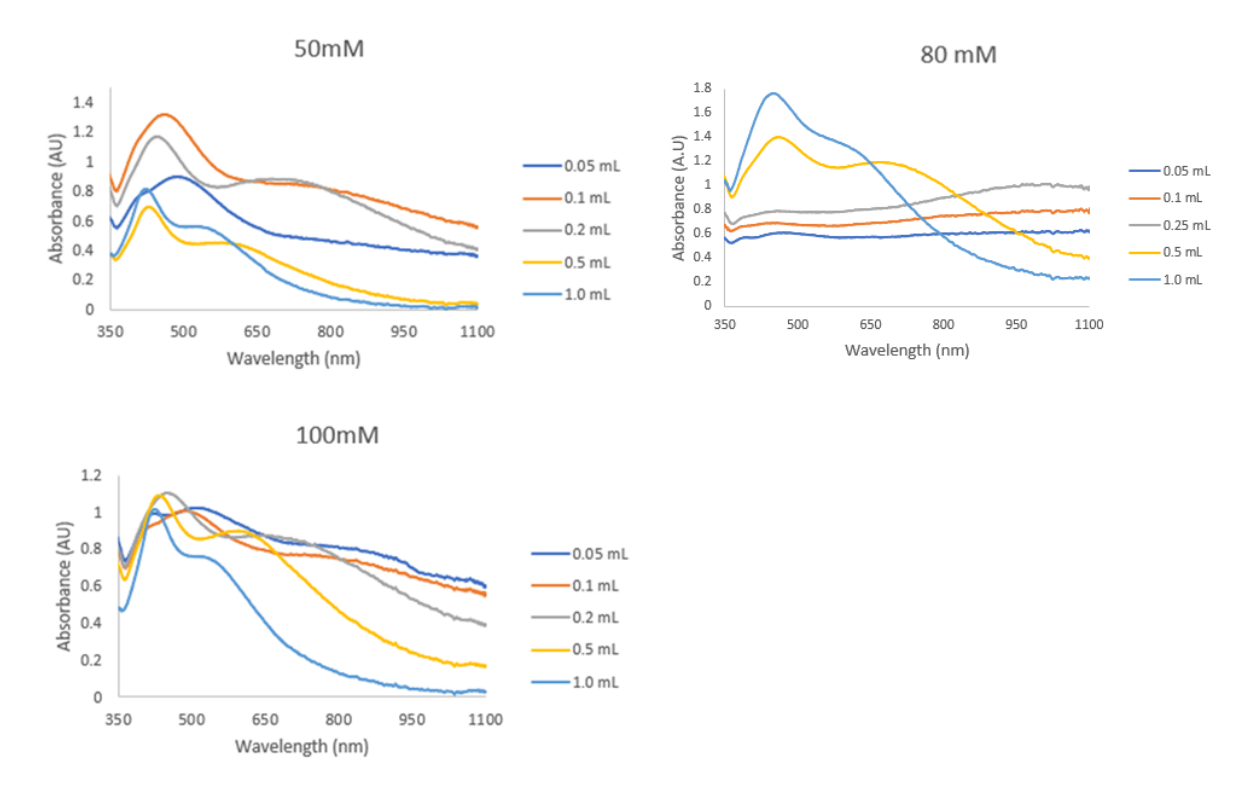


Figure 3.28. UV-Vis spectra of nanoparticles synthesised at different concentrations of CTAB added in the growth solution. For each concentration, the seed amount was varied between 0.05 to 1.0 mL.

3.5.4 Effects of ascorbic acid (AA) added in growth solution

The effect of concentration of AA in growth solution was investigated. Particles were synthesised at three different concentrations: 50, 100, and 200 mM. The concentrations of other reagents were kept constant.

Figure 3.29 shows the optical absorption spectra of nanoparticles synthesised employing three distinct concentrations of ascorbic acid (AA) introduced into the growth solution. At a 50 mM AA concentration, all seed concentrations exhibited two peaks, with the second peak shifting towards longer wavelengths as the seed concentration decreased. Upon elevating the AA concentration to 100 mM, the secondary peaks in all samples underwent a shift towards shorter wavelengths, signifying a reduction in nanoparticle size. This alteration in size was attributed to a decrease in nanorod length, consequently diminishing the aspect ratio and causing absorption to shift towards shorter wavelengths. Upon further amplifying the AA concentration to 200 mM, only the 0.02 mL seed sample displayed dual peaks, indicating the absence of anisotropic particle growth in the other samples. A subsequent increase in concentration to 300 mM resulted in a diminishing of the

secondary peaks, suggesting that most nanoparticles in all samples assumed an isotropic configuration.

As the concentration of AA in the growth was increased from 50 to 200 mM, the general trend in the position of absorption bands showed a blue-shift. As mentioned in Method 1, this may be related to the ratio of AA to NaOH in the growth solution. As the AA concentration was increased, so was the AA to NaOH ratio. Due to relatively less NaOH concentration, this limited the reduction power of AA to reduce AgNO₃ in the growth solution to silver ions to form anisotropic nanoparticles [220]. When a higher amount of AA was used, NaOH concentration needed to be also increased to produce nanorods.

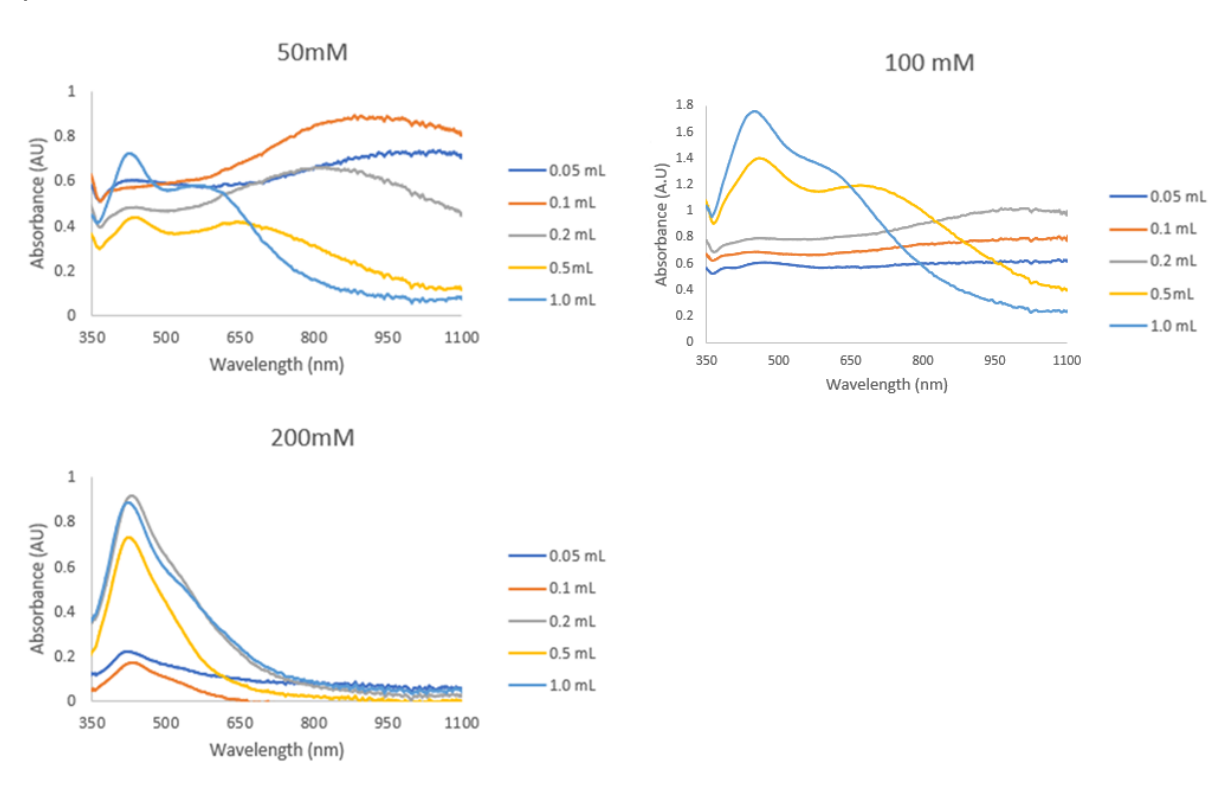


Figure 3.29. UV-Vis spectra of nanoparticles synthesised at different concentrations of ascorbic acid in the growth solution. For each concentration, the seed amount was varied between 0.05 to 1.0 mL.

3.5.5 Effects of sodium hydroxide added in growth solution

The effect of concentration of sodium hydroxide in growth solution was investigated. Particles were synthesised at three different concentrations: 0.5, 1 and 2 M. The concentrations of other reagents were kept constant.

Figure 3.30 shows the optical absorption spectra of the nanoparticles prepared using three different concentrations of NaOH added in growth solution. When the concentration of NaOH was 0.5 M, the lowest two seed samples showed no clear peaks. This indicated that there less nanoparticles formed. It may also result from the nanoparticles agglomerated. The 0.25 mL and 0.5 mL samples showed peaks at around 400 nm, indicating the presence of spherical nanoparticles. The results from this experiment were similar to that from Method 1. When the growth solution had a low pH (around 6), the reducing ability of ascorbic acid was diminished. As a result, no silver ions in growth solution were converted to form bigger nanoparticles on to seed particles.

Upon elevating the NaOH concentration to 1 M, there was a notable increase in the LSPR effect across all samples. The most extensive absorption wavelength, measuring ~1000 nm, was observed in the 0.25 mL sample. However, the peak displayed significant breadth, suggesting the presence of nanoparticles with varying sizes. Additionally, the 0.50 mL and 1.0 mL samples exhibited secondary peaks at 620 nm and 700 nm, respectively. The increase in NaOH concentration resulted in an elevated pH level within the growth solution, which, in turn, amplified the reducing capacity of ascorbic acid (AA). Consequently, this increase in reducing power led to the generation of more silver ions, which subsequently attached to the seed particles, yielding nanoparticles of differing sizes contingent upon the seed volume. Further raising the NaOH concentration to 2 M led to a reduction in absorption. Moreover, the secondary peaks shifted towards shorter wavelengths in contrast to the 1 M concentration. At this heightened concentration of 2 M, the pH within the growth solution reached notably elevated levels, thereby elevating the reduction capability of AA. This, in turn, accelerated the conversion of AgNO₃ and resulted in nanoparticle aggregation, ultimately culminating in a reduction in nanoparticle size.

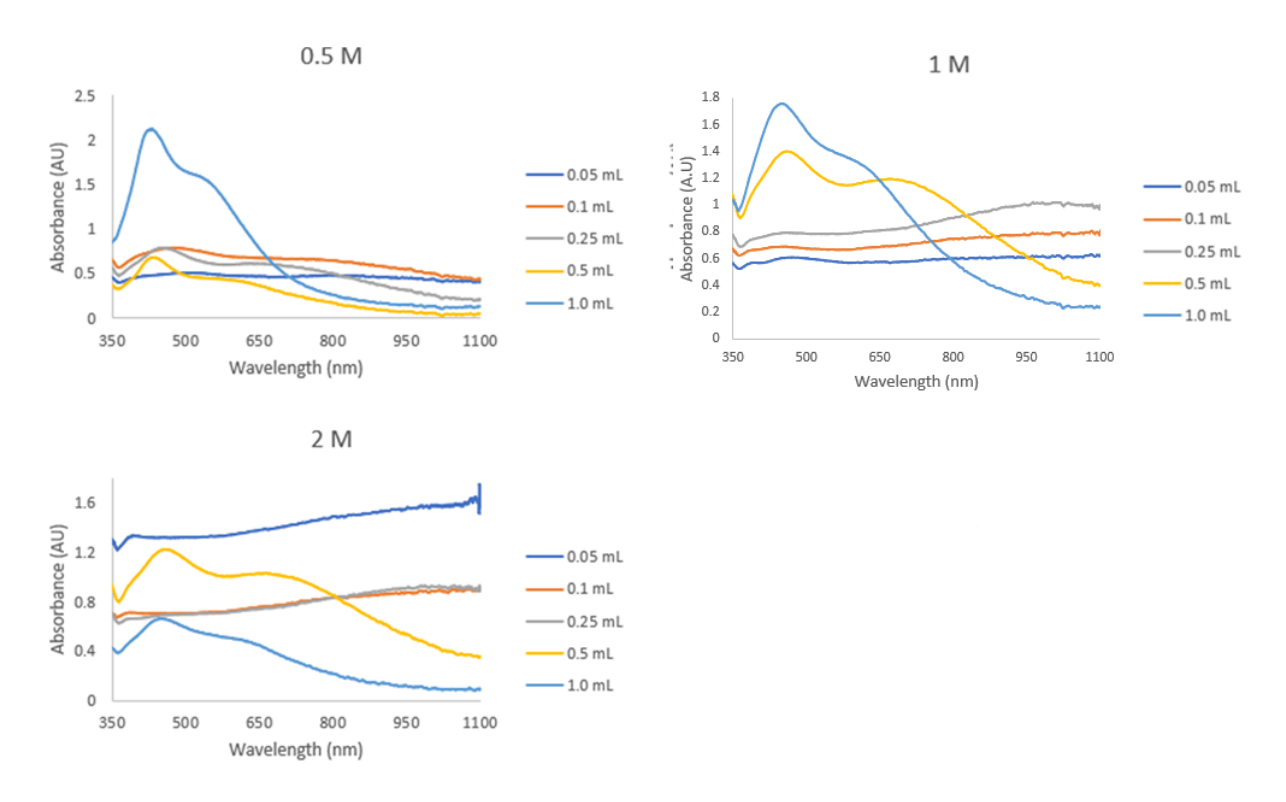


Figure 3.30. UV-Vis spectra of nanoparticles synthesised at different concentrations of NaOH in the growth solution. For each concentration, the seed amount was varied between 0.05 to 1.0 mL.

3.5.6 Trialling optimal parameters in method 2

From the above experiments, optimal reaction conditions and parameters for longest absorption wavelength bands were identified. Three trials were conducted to further identify the optimal concentration of each reagent.

Table 3-9 shows the parameters which produced maximum absorption wavelength bands in the previous experiments. Nanoparticles were synthesised using these parameters and their optical properties were measured. The seed volume was varied between 0.01 - 0.2 mL.

Reagent	Concentration
AgNO ₃ in seed solution	1 mM
TSC in seed solution	1 mM
NaBH₄ in seed solution	10 mM, 0.6 mL
CTAB in growth solution	100 mM, 10 mL
AgNO ₃ in growth solution	20 mM, 0.25 mL
AA in growth solution	100 mM, 0.25 mL
NaOH in growth solution	1 M, 0.10, 0.15 mL

Table 3-9 Optimal parameters used to synthesis nanoparticles in Method 2

Figure 3.31 shows the absorption spectra of nanoparticles synthesised using the parameters from Table 44. All samples, apart from 0.2 mL, exhibited broad peaks, indicating polydisperse nanoparticles. The maximum absorption wavelength band redshifted with decreasing seed volume. For the lower seed volumes of 0.01 mL and 0.02 mL, the maximum absorption wavelength band was around 1100 nm. Figure 3.32 shows the resulting morphologies of nanoparticles for the 0.01 mL sample. The shapes were mainly large hexagonal nanoparticles with some windmill-shaped nanoparticles, as shown in Figure 3.32B.

For 0.05 mL and 0.1 mL samples, the maximum absorption wavelength band was located between 1000 -1100 nm. For the highest seed volume of 0.2 mL, the maximum absorption wavelength band was around 780 nm. Figure 3.32D shows the formation of nanorods, ranging between 300 – 600 nm in length. For seed concentrations between 0.01 – 0.05 mL, very large hexagonal and non-spherical nanoplates in varying sizes were produced. This was the main reason to cause the broad absorbance peaks in the optical measurement. The LSPR peak for the 0.2 mL sample was narrow, indicating relatively lower polydispersity. For this method, high seed concentrations were favourable to synthesise nanorods that can absorb light between 700-800 nm wavelengths.

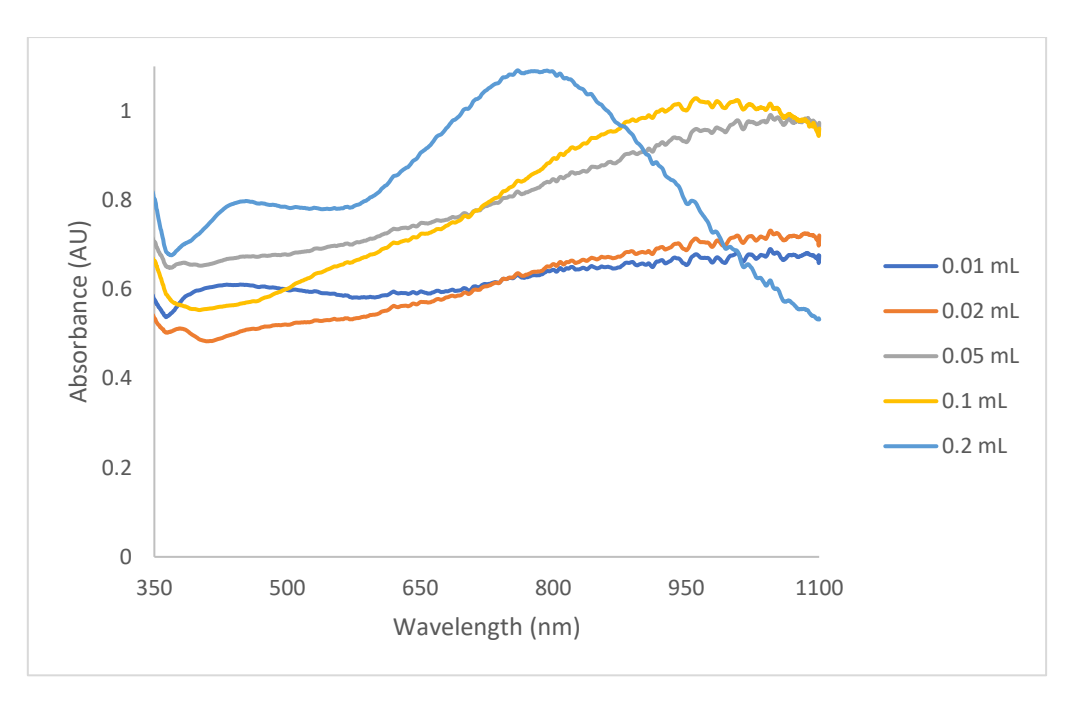


Figure 3.31. Absorption spectra of nanoparticles synthesised using optimal parameters in Method 2

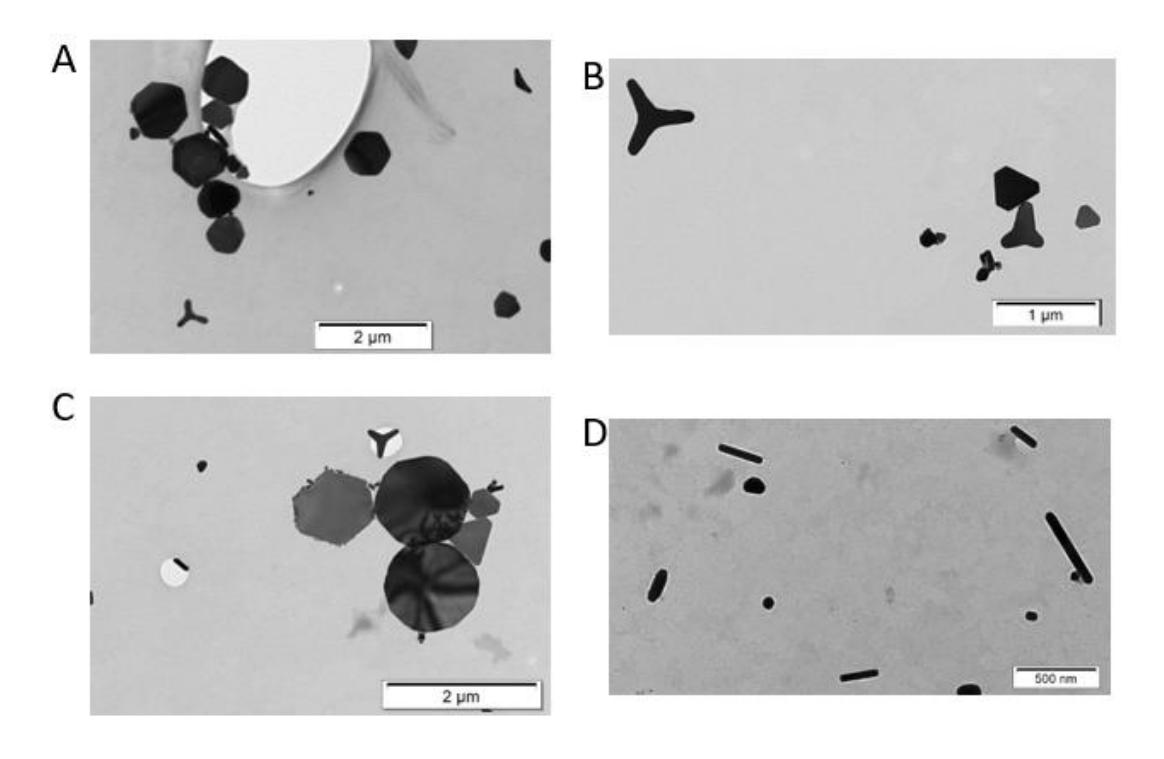


Figure 3.32. TEM images of nanoparticles synthesised using parameters in Method 2. (A) & (B) 0.01 mL seed sample; (C) 0.05 mL seed sample; (D) 0.2 mL seed sample

Analysis of Method 2 results in context of reference spectra

To evaluate the evolution of particle morphology and plasmonic response under different seeding conditions, the results of Optimised Method 2 were compared with the well-established work of Murphy et al., who used a seed-mediated growth method with varying seed volumes. These are summarised below. In Murphy's study, the LSPR peak progressively redshifted from 525 nm to 610 nm as seed volume decreased from 0.25 mL to 0.06 mL, with a corresponding change in rod aspect ratio (Figure 3.5). Although exact AR values were not given for most data points, an AR of approximately 3.5 was reported for the lowest seed volume, correlating with the 610 nm peak.

Source	Seed Volume	LSPR λ (nm)	Morphology	Size / Aspect Ratio
	(mL)			
Murphy et al.	0.25	525	Rods	AR: not specified
Murphy et al.	0.125	580	Rods	AR: not specified
Murphy et al.	0.06	610	Rods	AR ≈ 3.5
Optimised	0.2	785	Rods	AR ≈ 4.5
Method 2				
Optimised	0.05	1100	Hexagons	~1200 nm diameter
Method 2				
Optimised	0.01	1100	Hexagons and	Hexagons
Method 2			Nanowindmills	~1200 nm; Windmills
				~800 nm

Table 3-10 Comparison between LSPR responses and morphologies of silver nanoparticles synthesised using Optimised Method 2 and the reference method by Murphy et al. [64]. Both methods varied seed volume while maintaining similar growth conditions. Observed LSPR wavelengths and particle morphologies are presented along with known size or aspect ratio data where available.

In contrast, Optimised Method 2 produced a significantly more pronounced redshift in LSPR wavelength with decreasing seed volume. At 0.2 mL, the LSPR was observed at 785 nm, associated with well-defined nanorods having an aspect ratio of ~4.5—already significantly higher than the 610 nm peak in Murphy's method for a comparable morphology. This indicates that the modified growth conditions in Optimised Method 2 result in more anisotropic rod formation, or alternatively, produce rods with larger diameters that shift the LSPR more strongly into the NIR.

Strikingly, at even lower seed volumes (0.05 and 0.01 mL), the morphology shifted entirely from rods to non-rod anisotropic structures—notably hexagonal plates (~1200 nm) and nanowindmills (~800 nm). The observed LSPR peaks at 1100 nm in

both cases are consistent with such high-aspect-ratio planar geometries, and lie well beyond the range reported in Murphy's original rod-focused experiments [195].

3.6 Comparison of batch synthesis methods: method 1 vs method 2

A comparative analysis of the results from Method 1 (Rekha) and Method 2 (Murphy) offers valuable insight into how differences in seed preparation and growth solution chemistry influence the morphology and optical behaviour of silver nanoparticles. Both methods are rooted in seed-mediated synthesis but diverge significantly in reagent composition, seed capping agents (CTAB vs TSC), and final particle outcomes.

In Method 1, CTAB-capped silver seeds and a growth solution containing CTAB, AgNO₃, AA, and NaOH produced a diverse range of anisotropic nanostructures. Varying seed and silver nitrate concentrations led to the formation of nanoprisms, rods, and quasispherical nanoparticles, with LSPR peaks ranging from 560 nm to over 1100 nm. Notably, low seed volumes and low AgNO₃ concentrations promoted large triangular prisms, while higher concentrations of silver nitrate and seed volumes produced shorter nanorods with lower LSPR peaks (e.g., 685 nm for rods with AR \approx 3.2 at 20 mM AgNO₃). The highest LSPR peak (~1100 nm) was achieved using just 0.01 mL seed and large planar structures, confirming that large lateral dimensions and reduced nucleation densities favour longer-wavelength plasmon modes.

In contrast, Method 2, which used TSC-capped seeds and growth solutions rich in CTAB (up to 100 mM), generally produced less diverse morphologies, favouring nanorods and hexagonal plates. At higher seed volumes (0.2 mL), LSPR peaks were observed around 780-785 nm, corresponding to nanorods with AR ≈ 4.5 . However, at lower seed volumes (0.05–0.01 mL), very large hexagonal and windmill-shaped nanoplates formed, yielding broad LSPR peaks centred near 1100 nm. These structures are rare in the Murphy framework and suggest that under certain modified conditions, even TSC-capped seeds can support the formation of planar geometries. However, overall, Method 2 demonstrated greater sensitivity to reagent balance, often producing polydisperse or aggregated nanoparticles at lower CTAB or NaOH levels.

Comparing both methods, Method 1 provided superior morphological tunability and clearer structure-to-spectra correlations. The presence of well-defined prisms and

high-aspect-ratio rods allowed controlled tuning of LSPR between 500 and 1100 nm. Method 2, while capable of reaching similar LSPR values, showed greater variability and lower reproducibility, especially at low seed concentrations. Additionally, the use of static precipitation in Method 1 facilitated the isolation of specific morphologies, whereas Method 2 relied on centrifugation, which may have contributed to sample variability.

3.7 Conclusions

In this Chapter, two seed-mediated techniques were employed to synthesise silver nanoparticles with the objective of enabling absorption of near-infrared light wavelengths. A systematic modulation of parameters within both the seed phase and growth phase was undertaken. Subsequently, the nanoparticles were meticulously characterised through the utilisation of optical spectroscopy and transmission electron microscopy.

The outcomes derived from both methodologies revealed that the concentration of each reagent played a pivotal role in governing the synthesis of nanoparticles. The modulation of reagent concentrations within the seed phase had a discernible impact on the characteristics of the seed particles themselves. Consequently, the subsequent nanoparticle morphologies exhibited pronounced diversity contingent upon the nature of these initial seed particles. The size of the nanoparticles was found to exhibit a substantial reliance on the quantity of seed material introduced into the growth solution. In instances where the seed concentration was exceptionally low, nanoparticles with varied shapes such as triangles and hexagons, along with other non-spherical forms, emerged. These particular nanoparticles displayed absorption peaks of notable breadth, situated within the wavelength range of 900 to 1100 nm. Conversely, when the seed concentration was heightened, nanorods were the predominant configuration. The absorption spectra of these nanorods encompassed wavelengths spanning from 550 to 950 nm, with the specific range being contingent upon the aspect ratio.

In the growth medium, an increase in the concentration of silver nitrate was found to promote the generation of nanorods with higher aspect ratios, consequently resulting in the absorption of longer wavelengths. Moreover, the concentration of CTAB played a significant role in influencing the development of anisotropic nanoparticles. The utilisation of exceedingly high CTAB concentrations in the second method led to less nanoparticle synthesis as evidenced from the absorbance spectra. Ascorbic acid, although a relatively weak agent, exerted an influence on nanoparticle growth. Furthermore, its reduction potential was contingent upon the concentration of NaOH. In instances where NaOH concentrations were lower, corresponding to a lower pH, the reduction capacity of ascorbic acid was impeded, leading to the absence of anisotropic nanoparticles. Conversely, in situations involving markedly higher NaOH concentrations, associated with a higher pH, the reduction potency of ascorbic acid was augmented.

The most favourable parameters for both methodologies were determined and subsequently employed for nanoparticle synthesis. In summary, Method 1 yielded nanoparticles with enhanced absorption characteristics, particularly in the longer wavelengths within the near-infrared spectrum. Building upon these optimised parameters, a continuous flow system, could be devised for the continuous and efficient production of nanoparticles.

Chapter 4 Flow Synthesis Experiments

Chapter overview

This chapter focused on the flow synthesis of silver nanoparticles, highlighting the shift from traditional batch production methods to more efficient continuous flow systems. This transition was driven by the need for scalable production that can meet the rising demand in fields like nanotechnology. Flow synthesis offers several advantages over batch processes, including enhanced operational efficiency, minimal waste, and more controlled reaction conditions. Four different designs and configurations were studied using standard and 3D-printed components. Following testing of the different designs, the optimal synthesis was carried out using two designs.

4.1 Justification of reactor design choices and iterative development strategy

The selected size regime for continuous flow synthesis significantly influences mixing efficiency, reaction kinetics, and scalability. Microfluidic systems (≤100 µm channels) provide precise reaction control but suffer from clogging when handling metallic nanoparticles, limiting their long-term feasibility [223]. Additionally, their low throughput makes industrial scaling difficult. On the other hand, cm-scale batch reactors often result in poor mixing, broad particle size distributions, and reduced reproducibility due to concentration gradients [224].

Milli-fluidic systems (100 µm–1 mm channels) offer a balance between reaction control and scalability [225]. They enable higher flow rates while maintaining monodispersity and reduce clogging risks. Furthermore, milli-fluidic reactors facilitate continuous production, improving nanoparticle uniformity and ensuring efficient material usage. Due to these advantages, milli-fluidic systems were chosen as the optimal regime for continuous flow synthesis of silver nanorods. [224]

The use of tubular systems was chosen over on-chip microfluidics to allow modularity, ease of prototyping with 3D-printed components, and flexibility in modifying parameters such as flow path length, internal volume, and residence time [226]. Tubular reactors are also more adaptable to high-throughput synthesis and scaling without introducing complex fabrication constraints. Moreover, this architecture allows integration of commercial connectors and fittings, reducing system costs and

complexity during iterative development. Additionally, modular tubular reactor designs facilitate inline monitoring, allowing real-time process adjustments to improve reaction efficiency. Conversely, on-chip microfluidic systems provide high control over reaction kinetics but are difficult to scale due to their low throughput [224]. Given these limitations, a tubular milli-fluidic reactor was selected to balance controlled synthesis and scalability.

Each subsequent iteration of the flow reactor design was guided by systematic evaluation of synthesis outcomes – primarily nanoparticle size, shape uniformity, and NIR absorption characteristics. Modifications included changes to the number of inlets, geometry of mixing regions (e.g., Y vs. T junctions), use of 3D-printed static mixers, and varying residence time through tubing length or flow rate. These refinements were informed by performance metrics obtained in prior designs, with the goal of enhancing nanorod yield and stability. The iterative nature of design allowed for rapid feedback between experimental results and reactor tuning, essential for optimisation of anisotropic silver nanorod synthesis under continuous flow .

4.2 Materials and reagent preparation steps used in all flow synthesis experiments

4.2.1 List of the components:

- Syringe Pumps: syringe pumps were employed to control the flow rates of the different reagents. Syringe pumps were selected for their ability to deliver precise and consistent flow rates, ensuring accurate mixing and reaction control. Syringe pumps included WPI (AL-1010) and Harvard Apparatus Pump33.
- 2. Syringes: two sizes of syringes were used to contain the reagents. Syringes included: 1. Disposable2-norm-ject ® parts 20ml (24ml) luer lock needle-free sterile syringe; 2. Disposable2-norm-ject ® parts 10ml (12ml) luer lock needle-free sterile syringe. The 20 mL syringe was used to hold growth solutions and 10 mL to hold seed and NaOH solutions. These were purchased from VWR.
- 3. PTFE Tubing: PTFE (Polytetrafluoroethylene) tubing was used for its excellent chemical resistance and minimal reactivity with a wide range of substances. The tubing connects the syringe pumps to connectors and facilitates the

- transport of reagents from the pumps to the mixing point. Tubing was purchased from Merck. Tubing diameters were 0.2 mm and 0.5 mm.
- 4. Reactors: reactors were used to merge the flows of different reagents into a single stream, enabling efficient mixing within the reactor. Standard y-type (Idex P-512) and t-type (IDEX P-632) reactors were purchased from Cole Parmer. Others were designed and 3D-printed on campus.
- 5. Luer lock connectors: connectors to join tubing to syringes and reactors. These included Idex P-628 threaded luer adapter, Idex P-678 threaded luer adapter and Idex XP-218X flangeless fitting. All connectors had UNF 1/4-28 thread size. These were purchased from Cole Parmer.

4.2.2 List of reagents used in all flow synthesis experiments

Silver nitrate (AgNO₃, 99.995%), cetyltrimethylammonium bromide (CTAB, 99%), sodium borohydride (NaBH₄, 99%), L-ascorbic acid (AA, 99%) and sodium hydroxide (NaOH, 99%) were purchased from Fisher Scientific and Sigma Aldrich and used without further purification. Millipore water was used for the synthesis. All glassware was washed with detergent, thoroughly rinsed with double distilled water, and dried prior to usage.

Preparations of reagents

Reagent concentrations were selected from optimised method 1 parameters in batch synthesis (Table 3-4). These are given below:

Reagent	Concentration
AgNO ₃ in seed solution	1 mM, 5 mL
CTAB in seed solution	100 mM, 0.08 mL
NaBH₄ in seed solution	5 mM, 0.6 mL
CTAB in growth solution	20 mM, 10 mL
AgNO ₃ in growth solution	50 mM, 0.25 mL
AA in growth solution	100 mM, 0.25 mL
NaOH in growth solution	1 M, 0.10,

Table 4-1. Reagent concentrations used in the flow synthesis experiments

To prepare silver seed particles, an aqueous solution containing AgNO₃ and CTAB were mixed in a 50 mL round-bottom flask. Next, NaBH₄ (reducing agent) solution was

injected into the solution all at once while stirring at high speed (600 rpm). The colour of solution changed to light yellow. This solution was only used between 2-5 hours after synthesis.

For the growth solution, first an aqueous solution containing CTAB was prepared. This solution was heated to 35 °C while stirring to dissolve the CTAB and used after cooling to room temperature. CTAB solution was added to a glass vial (15 mL). Next, AgNO₃ and freshly prepared ascorbic acid were added. For designs 1-4, an equivalent seed amount of 0.1 mL was tested. NaOH solution was prepared separately. Syringes were filled with reagents using new needle for each experiment to avoid cross contamination of reagents.

4.2.3 Flow synthesis steps

The flow synthesis was carried out in the following steps:

- 1. Flow reactor set-up: first, place the syringe pumps on a stable surface, and securely attach the PTFE tubing at the outlets. Also, when installing the pumps, the tubing was arranged in such a way that it ran from the pumps to the reactors located at the merging point of all the tubes.
- 2. Preparation of the reagents: silver seed nanoparticles were prepared in batches on the basis of the optimised parameters in batch synthesis. Growth, seed, and NaOH solutions were prepared at concentrations shown in Table 4-1 above. The prepared solution was then delivered into its respective syringe pump.
- 3. Starting the reaction: activate the syringe pumps to start the flow of reagents.
- 4. Mixing and reaction: mixed solution flowed through the tubing and mixed in the connectors and tubing, where it initiated reaction. It further flowed in the direction of the area of reaction.
- 5. Monitoring and collection: reaction monitored visually; samples were collected in a glass vial (15 mL) from the outlet and analysed for absorption and size.
- 6. Shutdown and cleanup: after the reaction, stop the pumps, disconnect the tubing, and dispose of waste. Syringes were only used once and discarded. All

tubing and connectors were washed with soap, purged three times with milli Q water and flushed with nitrogen prior to each experiment run. New tubing and connectors were utilised for each design type.

UV-visible-near-infrared (UV-vis-NIR) spectra ranging from 300 to 1400 nm were recorded using Avantes Avaspec 2048 (range 200 – 1100 nm) and Avaspec NIR 1.7 (range 900 – 1700 nm) fibre-optic spectrophotometers equipped with a quartz cell (10 mm optical path).

Transmission electron microscope (TEM) images were captured using an FEI Technai12 TEM, employing an electron acceleration of 120 kV and a tungsten filament source. TEM grids (Carbon on Cu, 400 mesh) were procured from Agar Scientific (UK).

4.2.4 Flow regime in the flow reactors

To understand the impact of hydrodynamics on nanoparticle morphology and synthesis consistency, the flow profiles at the junctions—where reactant streams merge—were characterised using Reynolds number (Re) calculations. The Reynolds number is given by [227]:

$$Re = \frac{\rho uD}{\mu}$$
 where $u = \frac{Q}{A}$

Where:

- ρ is the fluid density (1000 kg/m³ for water-based solutions)
- μ is the dynamic viscosity (0.89×10⁻³ Pa·s for water)
- u is the mean velocity (m/s),
- D is the inner diameter of the tubing (m)
- Q is the volumetric flow rate (m³/s)
- A is the tubing cross-sectional area (m²)

For the milli-fluidic systems used in this study, the Reynolds number ranged from 5 to 510, confirming that the flow remained well within the laminar regime (Re < 2000). This is consistent with findings from continuous-flow nanoparticle synthesis literature, where laminar flow dominates in low Reynolds number systems and has a significant influence on mixing-dependent nucleation and growth kinetics.

At Y- and T-junctions, laminar flow leads to diffusion-limited mixing between the reagent streams, which is a critical factor in the shape-controlled growth of nanorods. Variations in mixing geometry and inlet angle were therefore introduced across reactor iterations to enhance interfacial contact between streams and reduce mixing time. In later prototypes, static mixers were introduced to induce secondary flows, increasing radial mixing without transitioning into turbulence, maintaining process stability while improving particle uniformity.

4.2.5 Residence time and post-synthesis handling

To ensure reliable interpretation of nanoparticle synthesis outcomes, both residence time within the flow reactor and the duration between collection and analysis were quantified. The residence time (τ) was calculated using the relation:

$$\tau = \frac{V}{O}$$

V is the internal volume (m³) of the coiled tubing and Q is the total volumetric flow rate (m³/s).

The delay between synthesis and analysis was minimised and consistently maintained at under 10 minutes. All samples were stored at room temperature and protected from light during this short interim. This handling protocol ensured that the reported characterisation data accurately reflected the products as they emerged from the flow reactor.

4.3 Flow synthesis using design 1

4.3.1 Design 1 details

Figure 4.1 illustrates the apparatus configuration adopted for flow synthesis of silver nanorods within the context of Design 1. This design utilised a series of syringe pumps that precisely control the delivery of reagent solutions into the system. The solutions consisted of silver nanoparticle seeds, sodium hydroxide (NaOH), and a growth solution containing cetyltrimethylammonium bromide (CTAB), silver nitrate (AgNO₃), and ascorbic acid, which acts as a reducing agent. The objective of the design was to use the silver seed nanoparticles to grow silver nanorods, similar to the batch synthesis, where seed nanoparticles were used as nucleation points for the nanorod growth.

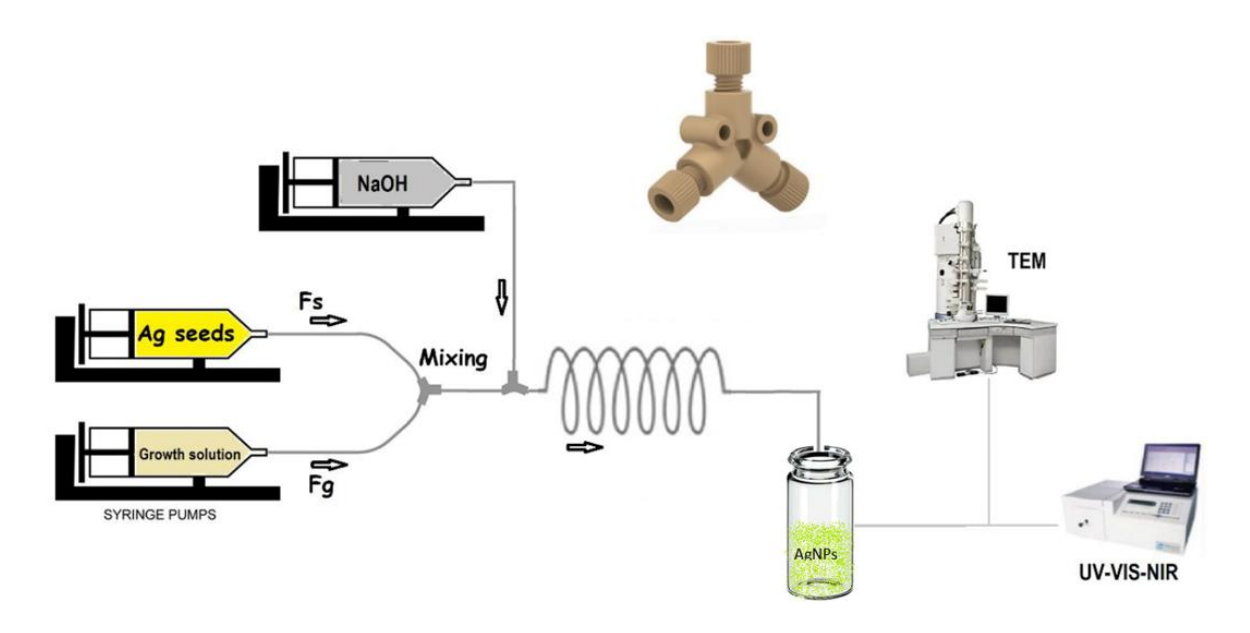


Figure 4.1. Flow synthesis apparatus for silver nanorods utilising syringe pumps, y-type fittings, and PTFE tubing

In this particular design, a y-type reactor (Idex P-512 from Cole Parmer) was utilised for the mixing of reactants. The reactor facilitated the merging of reactants at the 'Y' junction, thereby enabling efficient and swift chemical reactions. Y-type fittings were sourced from Cole-Parmer. These fittings are integral to the mixing zone, enabling the controlled mixing of the silver seed solution with the growth solution and the sodium hydroxide (NaOH). The use of such fittings ensured a streamlined flow that promotes the efficient combination of reagents. See appendix A for reactor details.

Each of the reactants was dispensed with precision by syringe pumps, which meter the silver seed solution and the growth solution at specified flow rates. The combined solution then proceeded through a coiled section of Polytetrafluoroethylene (PTFE) tubing, where the silver nanoparticles underwent growth. The coiled configuration of the tubing is designed to extend the reaction time, allowing for a more complete development of the nanoparticles. Post-reaction, the silver nanoparticles were directed to a collection vial for subsequent characterisation such as UV-VIS-NIR spectroscopy and Transmission Electron Microscopy (TEM).

The table below shows the tubing details in the design set up:

Tubing	Dimensions		
	Internal diameter (mm) Length (m)		
Seed to y-reactor	0.50	0.25	

Growth to y-reactor	0.50	0.25
NaOH to y-reactor	0.50	0.25
Y-reactor to y-reactor	0.50	0.30
Coiled tubing	0.50	5.0

Table 4-2 Tubing details for flow synthesis using design 1

4.3.2 Flow rates for design 1

The table below shows the flow rates of three different solutions used in a series of four distinct flow synthesis experiments aimed at creating silver nanorods. These experiments were labelled from D1_1 to D1_4, and for each, there were corresponding flow rates for the growth solution (G), seed solution, and sodium hydroxide (NaOH) solution. The flow rate for the growth solution was based on its constituents in the batch synthesis: 10 mL CTAB, 0.25 mL ascorbic acid and 0.25 mL silver nitrate. For each experiment, a stock growth solution was prepared and added to syringe. The flow rates are critical parameters that influence the reaction kinetics and the final properties of the synthesised nanorods. Reynolds numbers clearly show that all iterations in design 1 operate within the laminar flow regime (Re < 2000). Notably, the highest Reynolds number (510 in D1_1) still reflects stable, ordered flow.

Experiment	G flow rate (mL/min)	Seed flow rate (mL/min)	NaOH Flow rate (mL/min)	Residence time (s)	Reynolds number
D1_1	10.5	0.1	0.1	6	510
D1_2	2.1	0.02	0.02	28	102
D1_3	1.05	0.01	0.01	55	51
D1_4	0.105	0.001	0.001	551	5

Table 4-3 Flow rates utilised in design 1

The objective of this design was to establish a foundational understanding of the flow synthesis process and its impact on the growth of silver nanorods. The primary goal was to optimise the synthesis of silver nanorods with a specific focus on controlling their size, aspect ratio, and uniformity.

The hypothesis driving the initial design was that the controlled flow rates of the reactant and seed solutions, along with the pH adjustment by NaOH, would allow for the precise manipulation of the nanorods' nucleation and growth stages, leading to a uniform production of nanorods with desired optical characteristics. Experiment D1_1 implemented the highest flow rates to explore the effects of rapid reaction conditions on nanorod synthesis. The flow rates were reduced in subsequent experiments to further examine the influence of slowed kinetics and prolonged reaction times on the growth of nanorods.

4.3.3 Results for design 1

Figure 4.2 displays the optical absorption spectra of silver nanoparticles synthesised using varying flow rates as outlined in Table 4-3. Absorption was only detected in D1_2 and D1_3, each showing two absorption peaks. These two distinct peaks of absorption in nanorods were due to the absorption in the transverse and longitudinal axis of the rod. Evidently, these anisotropic nanoparticles manifested LSPR properties influenced by the flow rates of the solutions used during synthesis.

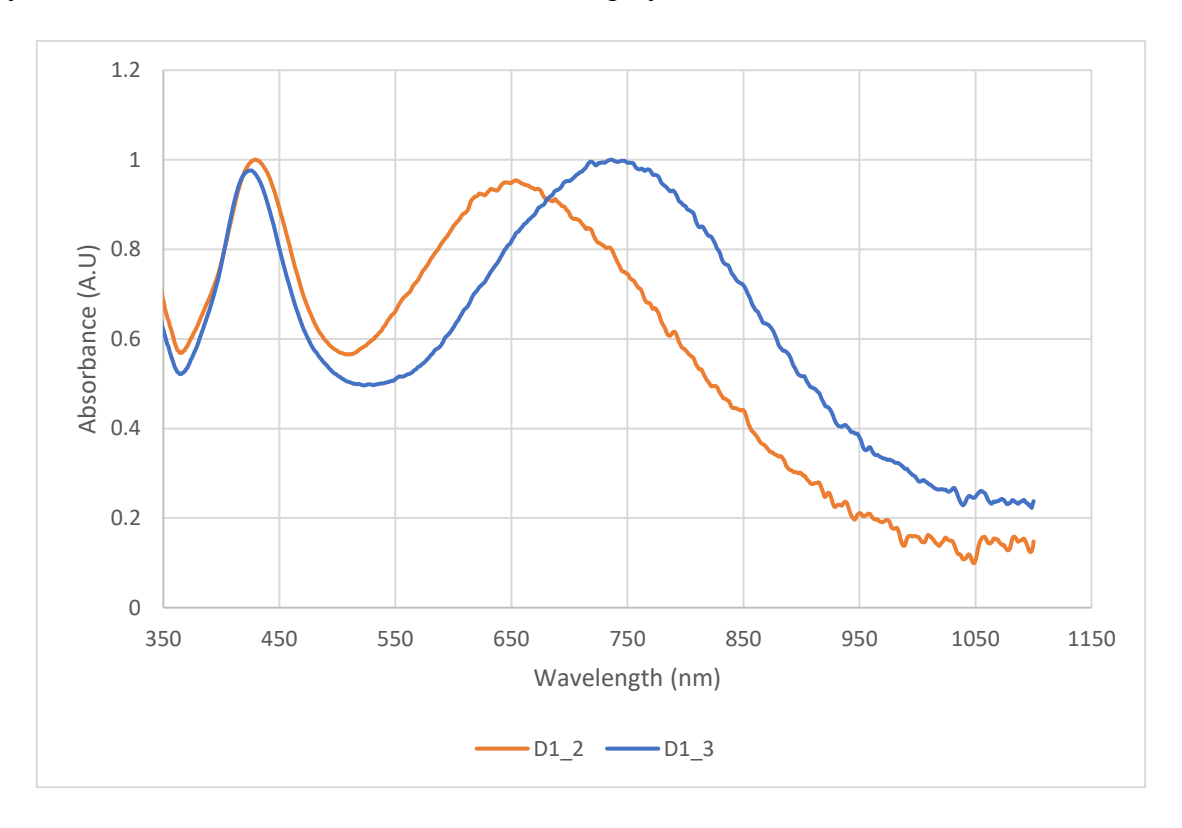


Figure 4.2. Absorption spectra for D1 2 and D1 3

There was no absorption in nanoparticles synthesised in D1_1. It was assumed that due to higher flow rates, there was not enough time for the solutions to mix and grow

into nanorods. For D1_2 (orange curve), the LSPR peak was centred around 650 nm. The flow rates were reduced x10 in D1_3, and the longitudinal LSPR absorption peak was centred around 740 nm, resulting in a red-shift of about 90 nm. TEM results showed nanorods measuring 90-110 nm in length for D1_2 and over 200 nm in length for D1_3. There were also some quasi-spherical shaped nanoparticles present in the samples. A further reduction in flow rates was tested in D1_4, but there was also no absorption detected. The cause for non-absorption could be due to very low flow rates of seed and NaOH solutions. The D1_3 experiment, showed the highest longitudinal LSPR absorption peak where the flow rates were not too higher or low. This allowed for extended growth periods for the nanoparticles, leading to larger sizes and potentially more elongated shapes, as can be seen from the significant absorption in the near-infrared region.

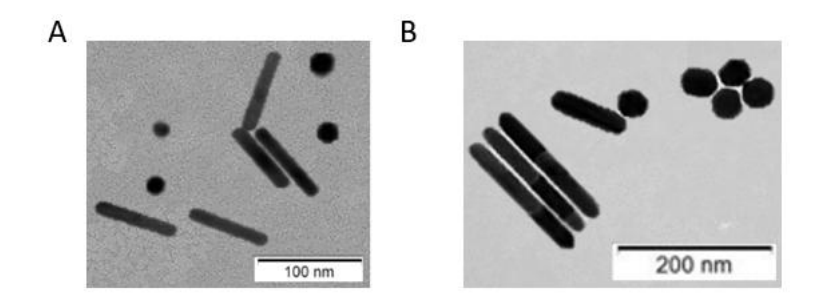


Figure 4.3. TEM images of nanoparticles produced using design 1: (A) D1 2; (B) D1 3

From these experiments, it was concluded that the optical properties of the silver nanoparticles, as determined by the SPR peaks in the absorption spectra, are significantly affected by the flow rates used during their synthesis. The precise tuning of the flow rates in the synthesis process enables the manipulation of nanoparticle characteristics, offering a controllable method for tailoring nanomaterials for specific applications.

4.3.4 Modification of flow synthesis using design 1

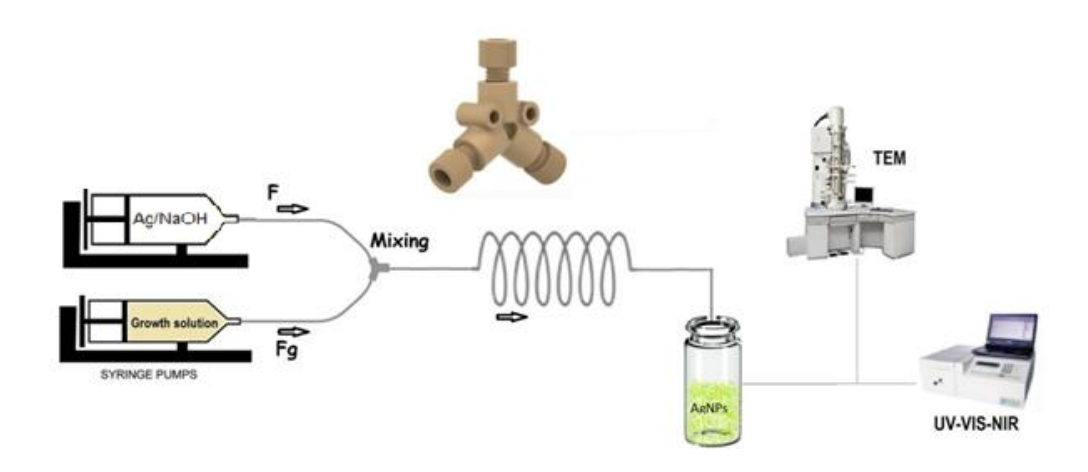


Figure 4.4. Schematic of modified design 1 for synthesis of silver nanorods

The above schematic depicts a modified flow synthesis design for the production of silver nanorods, presenting a simplified version of the design 1 system. This design was refined to integrate the seed solution with the sodium hydroxide (NaOH) solution prior to the introduction to the growth solution - a slight modification from the previous approach where the seed and NaOH solutions were introduced separately. The reason for this change was to allow for usage of higher flow rates by combining the seed and NaOH solutions. For example, when both of these solutions were pumped separately such as in D1_3, each required a flow rate of 0.01 mL/min. By mixing seed and NaOH, the flow rate can be increased to 0.02 mL/min.

In this modified setup, the two solutions were stored in individual syringe pumps that carefully controlled their flow into the reactor. Upon combining the seed/NaOH and the growth solution, the reagents converge at a singular Y-type reactor. This was followed by reaction mixture flow through coiled PTFE tubing to extend the reaction path and, hence, provide residence time conditions that would be controlled for the synthesis of the nanorod. The synthesised silver nanorods were eventually collected in a glass vial, ready for characterisation.

The table below shows the tubing details in the design set up:

Tubing	Dimensions	
	Internal diameter (mm) Length (m)	
Seed/NaOH to y-reactor	0.50	0.25

Growth to y-reactor	0.50	0.25
Coiled tubing	0.50	5.0

Table 4-4 Tubing details for modified design 1

4.3.4.1 Flow rates for modified design 1

The table below shows the flow rates of three different solutions utilised in the modified design 1. These experiments were labelled from D1_5 to D1_7, and for each, there were corresponding flow rates for the growth solution (G), and seed/sodium hydroxide (NaOH) solution.

Experiment	G flow rate (mL/min)	Seed/NaOH flow rate (mL/min)	Residence time (s)	Reynolds number
D1_5	1.05	0.02	55	51
D1_6	0.525	0.01	110	25.5
D1_7	0.105	0.002	551	5.1

Table 4-5 Flow rates used in modified design 1 flow synthesis

4.3.4.2 Results for modified design 1

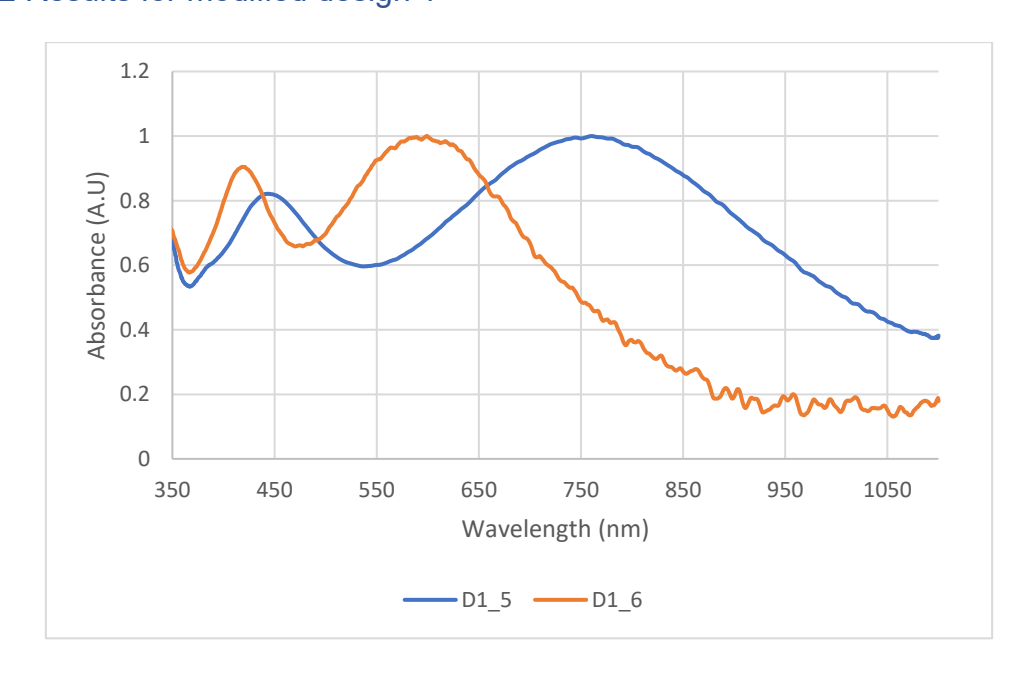


Figure 4.5. Absorption spectra for D1_5 and D1_6

Figure 4.5 shows the optical absorption spectra of silver nanoparticles produced under the modified flow synthesis design. There was no absorption in experiment D1_7, possibly due to low seed/NaOH flow rate. The results for D1_5 and D1_6 showed two peaks each, with a red shift in the longitudinal LSPR peak as the flow rates were reduced. The secondary LSPR maximum absorption peaks for D1_5 and D1_6 were 595 nm and 765 nm respectively .This shift suggests larger or more elongated silver nanorods due to longer residence times in the reactor, which facilitates more extensive growth.

Comparing the results for D1_5 and D1_6 with earlier experiments D1_1 to D1_4, where flow rates ranged from high to very low, a clear trend is observable. In the initial design, decreasing flow rates also led to a red-shift in the longitudinal LSPR peaks, with each decrease in flow rate leading to a slight further red-shift and increase in size. This is indicative of the modified design's potential for fine-tuning nanoparticle characteristics by adjusting residence times and reaction dynamics.

The comparison between the two designs shows the fine control that can be achieved via the flow chemistry in nanoparticle synthesis. In the original Design 1, it is easy to manipulate the size of the nanoparticles by a change in the flow rate. In contrast, the modified Design 1 variation incorporates premixing of the seed and base solutions, which most likely leads to a more homogeneous reaction environment and finer control, evidenced by the optical properties that are more pronounced in all cases. Both designs confirm the fundamental role of flow rates in dictating nanoparticle morphologies and optical properties, with the modified design providing higher capabilities in fine-tuning.

4.3.5 Modifying reagent concentrations for modified design 1

In the subsequent phase of the experimental design 1, an alteration was introduced to the concentration of the reactants. This modification involved diluting both the seed and NaOH solutions by a ratio of 1:5 with water. The objective of this design change was to investigate the influence of reactant concentration on the nucleation and growth processes of silver nanorods. This would also allow higher flow rates to use for the seed/NaOH solution.

4.3.5.1 Flow rates for modified design 1

The table below shows the flow rates used for the modified design 1:

Experiment	G flow rate (mL/min)	Seed/NaOH flow rate (mL/min)	Residence time (s)	Reynolds number
D1_8	2.1	0.2	26	109.7
D1_9	1.05	0.1	51	54.8
D1_10	0.525	0.05	102	27.4

Table 4-6 Flow rates used in the modified design 1

4.3.5.2 Results for modified design 1

Figure 4.6 shows the optical absorption spectra of silver nanoparticles synthesised in three different sets of conditions, designated as D1_8, D1_9, and D1_10. Each of the three spectra exhibited two absorption peaks, consistent with the SPR effect observed in silver nanorods.

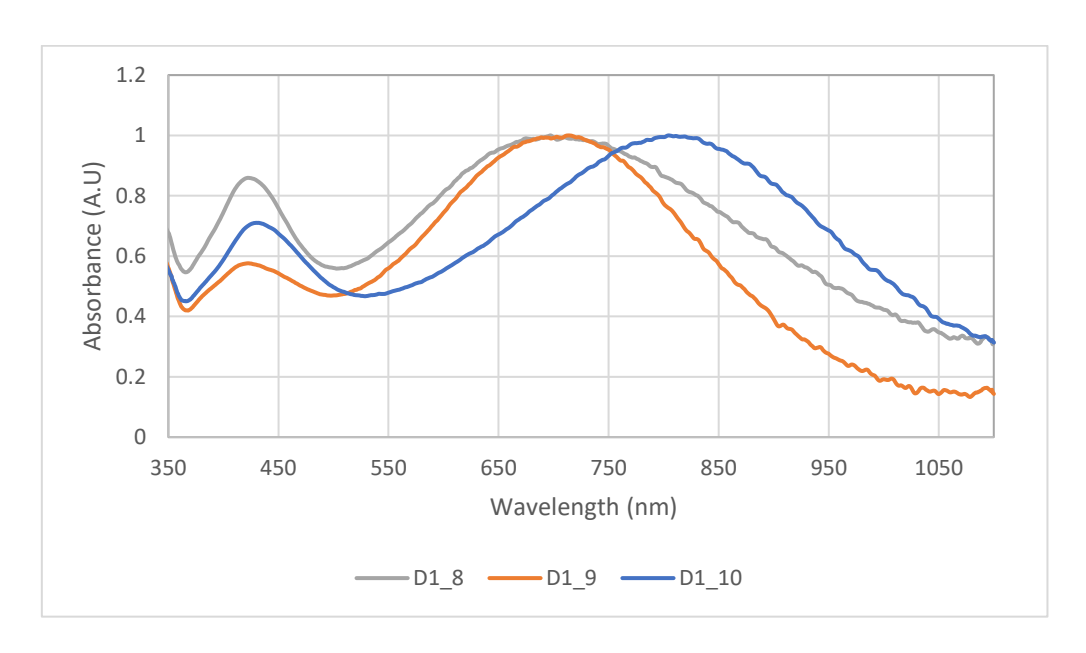
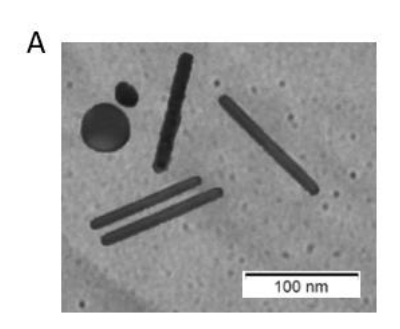


Figure 4.6. Absorption spectra for D1_8, D1_9 and D1_10

D1_8 spectrum, shown in grey, showed a secondary peak occurring at approximately 700 nm. For D1_9, the longitudinal absorption peak was also centred around 700 nm, although it was slightly sharper compared to D1_7, which could be interpreted as a more uniform size distribution of the anisotropic particles. The D1_10 spectrum,

showed a more substantial redshift compared to D1_8 and D1_9. The secondary peak, centred around 810 nm, implied the presence of larger or more elongated structures. TEM results showed nanorods measuring between 120 – 150 nm in length for D1_9 and around 250 nm long for D1_10 (Figure 4.7). The presence of other shaped nanoparticles explained the peaks being slightly broader.



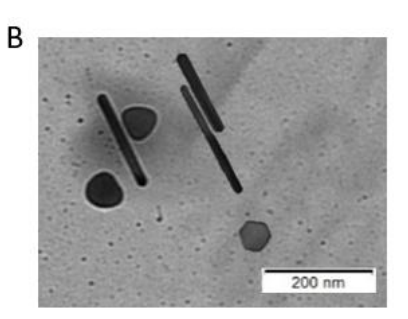


Figure 4.7 TEM images of nanoparticles produced using modified design 1 : (A) D1_9; (B) D1_10

In all three cases, the position of the peaks reflects the size, shape, and distribution of the silver nanoparticles within the samples. The trend of redshift from D1_8 to D1_10 could be associated with changes in the flow rates during synthesis, which are known to influence the nanoparticle size. As the flow rates were reduced, the absorption peaks shifted to higher wavelengths. The absorption spectra indicated complex interchanges between the nanoparticle synthesis conditions and the resulting optical characteristics. D1_10 showed the optimal flow rates using the modified design 1 set up and other parameters.

A comparison between batch and Design 1 experiments reveals the effect of flow conditions and reactor configuration on nanorod formation. In Trial 1, an LSPR peak of 870 nm was observed, though the morphology was not determined. In contrast, flow experiments under similar reagent conditions but varied flow rates produced more defined outcomes:

D1_3 (moderate flow rate): LSPR = 745 nm, nanorods with AR \approx 11, and minor quasispherical content.

D1_6 (lower flow rate): LSPR = 765 nm, morphology not captured but spectral shift suggests anisotropic growth.

D1_10 (lowest flow rate): LSPR = 810 nm, with rods (AR \approx 12), along with prisms and hexagonal structures.

These results confirm that decreasing the flow rate in Design 1 increased the residence time, favouring the growth of higher aspect ratio nanorods and extending the LSPR toward the NIR region. The incorporation of Y-mixers and extended tubing also contributed to improved reagent mixing and elongation kinetics. Compared to the less-defined batch Trial 1 outcome, flow conditions in Design 1 enabled more controlled and morphologically resolved synthesis.

Within Design 1, the transition from early experiments (e.g., D1_1-D1_4) to later modified versions (e.g., D1_9 and D1_10) showed a distinct enhancement in absorbance.

4.4 Flow synthesis using design 2

4.4.1 Design 2 details

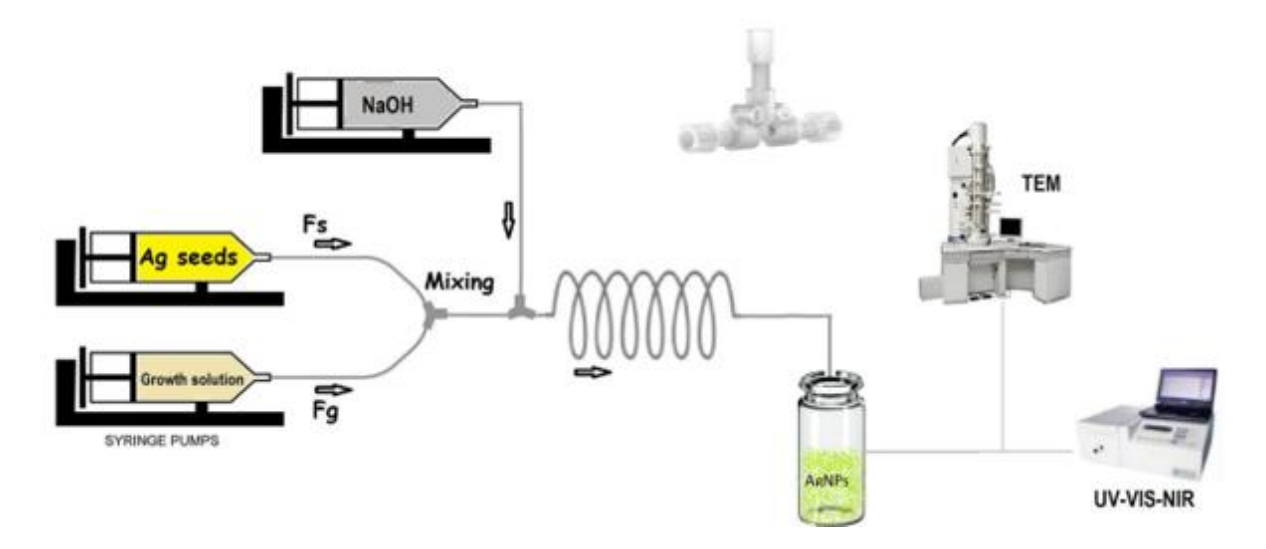


Figure 4.8. Flow synthesis apparatus for silver nanorods utilising syringe pumps, t-type fittings, and PTFE tubing

Figure 4.8 above presents the configuration used for the flow synthesis of silver nanorods as per design 2. Design 2 differs by incorporating a t-type reactor instead of the y-type used in Design 1. The t-type reactor (Idex P-632 from Cole Parmer) simplifies the confluence of reactants, where the two streams merge at a single point, promoting a quick and efficient synthesis process. The silver seed solution and the growth solution were both precisely metered by the syringe pumps at predetermined flow rates, leading to their convergence in the t-type reactor. Subsequent to mixing, the solution travels through a coiled section of PTFE tubing which functions as a

microreactor. Once the reaction had concluded, the resultant silver nanoparticles were then collected in a glass vial, where they underwent analysis through Transmission Electron Microscopy (TEM) and UV-VIS-NIR spectroscopy.

The table shows the tubing details in the design set up:

Tubing	Dimensions		
	Internal diameter (mm)	Length (m)	
Seed to t-reactor	0.50	0.25	
Growth to t-reactor	0.50	0.25	
NaOH to t-reactor	0.50	0.25	
Y-reactor to t-reactor	0.50	0.30	
Coiled tubing	0.50	5.0	

Table 4-7 Tubing details for design 2

4.4.2 Flow rates for design 2

The table below shows the flow rates of three different solutions used in a series of four distinct flow synthesis experiments aimed at creating silver nanorods. These experiments are labelled from D2_1 to D2_3, and for each, there are corresponding flow rates for the growth solution (G), seed solution, and sodium hydroxide (NaOH) solution.

Experiment	G flow rate (mL/min)	Seed flow rate (mL/min)	NaOH Flow rate (mL/min)	Residence time (s)	Reynolds number
D2_1	2.1	0.02	0.02	28	102
D2_2	1.05	0.01	0.01	55	51
D2_3	0.1	0.001	0.001	577	4.8

Table 4-8 Flow rates used in flow synthesis using design 2

4.4.3 Results for flow synthesis using design 2

Figure 4.9 the optical absorption spectra of synthesis in design 2. There was no absorption for D2_3. This might have been due to low flow rates resulting in no synthesis of nanoparticles. D2_1 and D2_2 showed two weak absorption peaks each. There was an initial absorption peak at around 430 nm, and a broad weak peak centred around 600 nm.

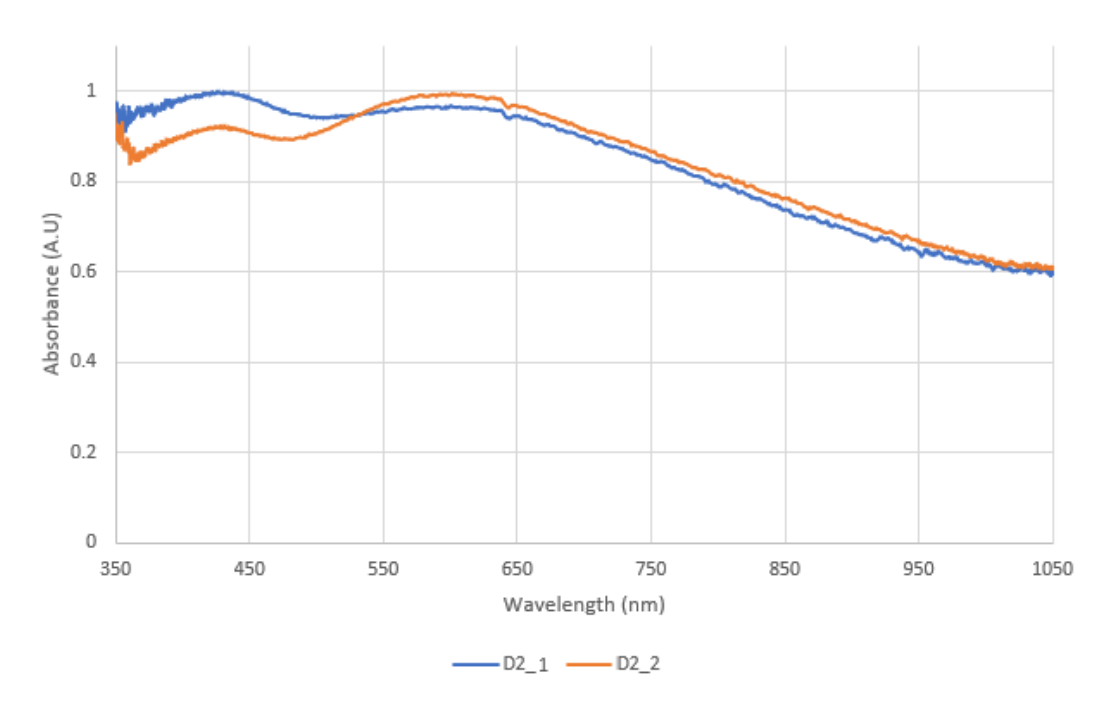


Figure 4.9. Absorption spectra for D2_1, and D2_2

D2_1 showed a gradual decrease in absorption as the wavelength increased. The peak appeared to be broad, suggesting a distribution of particle sizes or a range of nanoparticle shapes within the sample. This indicated that the overall concentration of nanoparticles may be lower or that the nanoparticles had a reduced capacity for light absorption. D2_2 followed a similar trend but with a slightly higher secondary absorption peak. Comparing these results to design 1, there was a significant difference in results between the two designs. For example, the flow rates for D1_3 and D2_2 were same, however the two experiments showed different absorption results. D1_3 showed a pronounced secondary LSPR absorption maximum of 740 nm, whereas D2_2 showed a weak secondary LSPR absorption maximum of 600 nm.

4.4.4 Modified design 2 flow synthesis

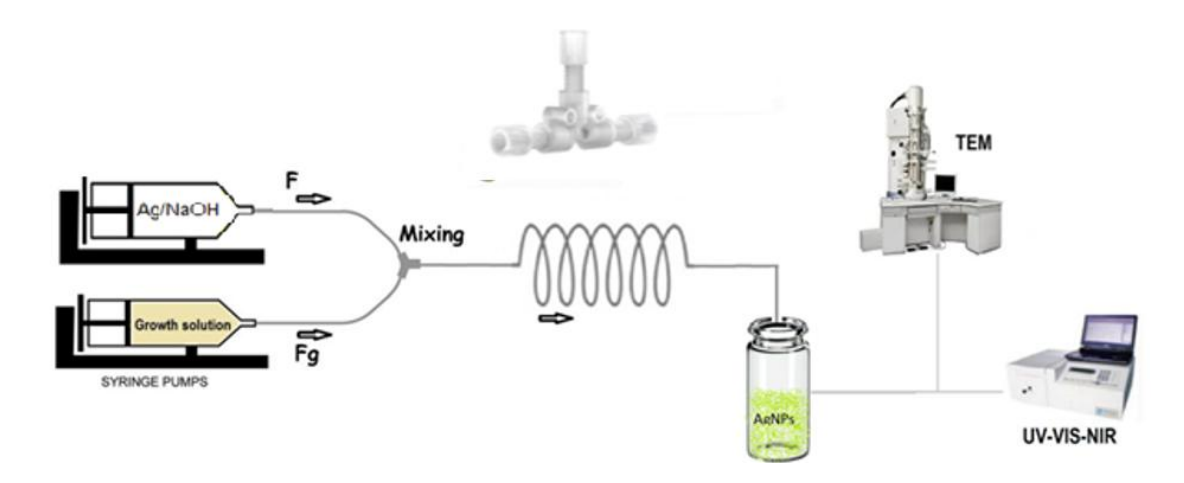


Figure 4.10. Schematic of modified design 2

Figure 4.10 shows the modified configuration for the production of silver nanoparticles. The designed was similar to the modified design 1. Design 2 differs by incorporating a t-type reactor instead of the y-type used in Design 1 Two syringe pumps were utilised to deliver precise volumes of two different solutions: one containing silver seeds mixed with sodium hydroxide (NaOH), and another containing the growth solution. Following the mixing chamber, the reaction mixture is passed through coiled tubing, which is often used in flow chemistry to enhance heat and mass transfer, promoting a more uniform reaction environment. The coiled configuration provides a longer pathway for the reactants, enabling better control over reaction time and temperature, factors that are critical for determining the final properties of the nanoparticles. After the reaction has taken place in the coiled tubing, the synthesized nanoparticles are collected in a glass vial. The collected suspension of AgNPs is then subject to characterisation using two analytical techniques

The table below shows the tubing details in the modified design 2 set up:

Tubing	Dimensions	
	Internal diameter (mm)	Length (m)
Seed/NaOH to t-reactor	0.50	0.25
Growth to t-reactor	0.50	0.25
Coiled tubing	0.50	5.0

Table 4-9 Tubing details in the modified design 2 set up

The table below shows the flow rates of three different solutions used in a series of four distinct flow synthesis experiments aimed at creating silver nanorods. These experiments are labelled from D2_4 to D2_6, and for each, there are corresponding flow rates for the growth solution (G) and seed/sodium hydroxide (NaOH) solution.

Experiment	G flow rate (mL/min)	Seed/NaOH flow rate (mL/min)	Residence time (s)	Reynolds number
D2_4	2.1	0.02	28	101.1
D2_5	1.05	0.01	56	50.5
D2_6	0.1	0.001	583	4.8

Table 4-10 Flow rates used in modified design 2

4.4.5 Results for modified design 2 flow synthesis

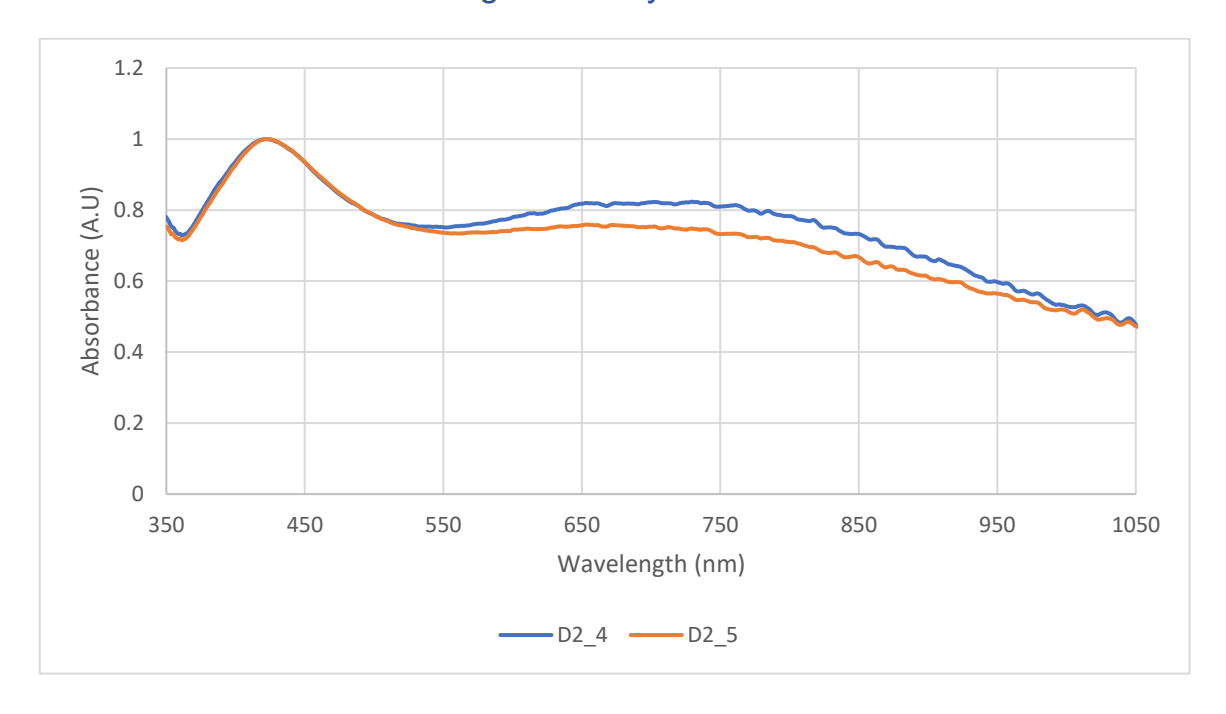


Figure 4.11. Absorption spectra for D2_4 and D2_5

Figure 4.11 provides the optical absorption spectra for modified design 2. D2_6 showed no absorption, possibly due to low flow rates. Both D2_4 and D2_5 exhibited a strong absorption peak centre at around 425 nm. After reaching their respective maxima, both curves gradually decreased in absorbance as the wavelength increased,

with no significant secondary peaks observed. The longitudinal LSPR peaks very broad, indicating synthesis of some anisotropic nanoparticles of various sizes.

Compared to the previous design 2 results, there was a somewhat red-shift in the absorption, however the peaks not very pronounced. The absorbance curves for D2_4 and D2_5 converge and closely follow each other, which might indicate that the nanoparticles in these samples shared similar properties.

In conclusion, the differences in the peak intensities and the shapes of the absorbance spectra suggested variations in the concentration, size, and the shape distribution of the nanoparticles produced under the different conditions corresponding to D2_2, D2_3, D2_4, and D2_4. The results in design 2 showed that synthesis of anisotropic silver nanoparticles is possible, although further research should be conducted to refine the synthesis process.

A comparison of Design 2 flow results with batch method further highlights the effect of flow parameters on spectral outcomes. In Trial 1, an LSPR peak of 870 nm was recorded, although the particle morphology was not determined. In the continuous flow Design 2, D2_2 exhibited a much lower LSPR peak at 600 nm, while D2_5 showed a broader peak at 718 nm, again with undetermined morphology. The significantly lower LSPR values in Design 2 suggest the formation of smaller or less anisotropic particles compared to those in batch.

This deviation may be attributed to the use of T-junction connectors in Design 2, which provided suboptimal mixing and thus less efficient anisotropic growth. Furthermore, the flow rates used in D2_2 and D2_5 were higher than those in later optimised designs, reducing residence time and limiting the elongation process. As supported by literature (e.g., Wagner et al., 2005), poor mixing dynamics in T-configured systems can hinder the uniformity and aspect ratio of nanorods [153]. Consequently, Design 2's performance under these parameters did not replicate the morphological and optical outcomes achieved under static batch conditions.

4.5 Flow synthesis using design 3

4.5.1 Design 3 details

Conventional flow synthesis reactor designs often encounter challenges with adaptability and scaling up. The emergence of additive manufacturing, also known as 3D printing, presents a promising alternative, enabling the creation of reactors with intricate designs, customised fluid dynamics, and integrated features. Compared to traditional methods of reactor production, 3D printing enables quicker and more adaptable prototyping, enhanced reaction rates, and greater efficiency in processes.

Okafor et al. (2017) demonstrated the application of small-scale continuous flow oscillatory baffled reactors (mCOBR), fabricated using 3D printing, for generating almost uniform silver nanoparticles [228]. These reactors displayed enhanced mixing capabilities and superior particle size distribution control compared to standard tubular flow reactors.

Singh (2020) presented a 3D-printed apparatus for producing various types of nanoparticles, such as iron oxide and metallic nanoparticles. This study highlighted the cost efficiency and multipurpose nature of 3D-printed microfluidic devices in the field of nanoparticle production [229].

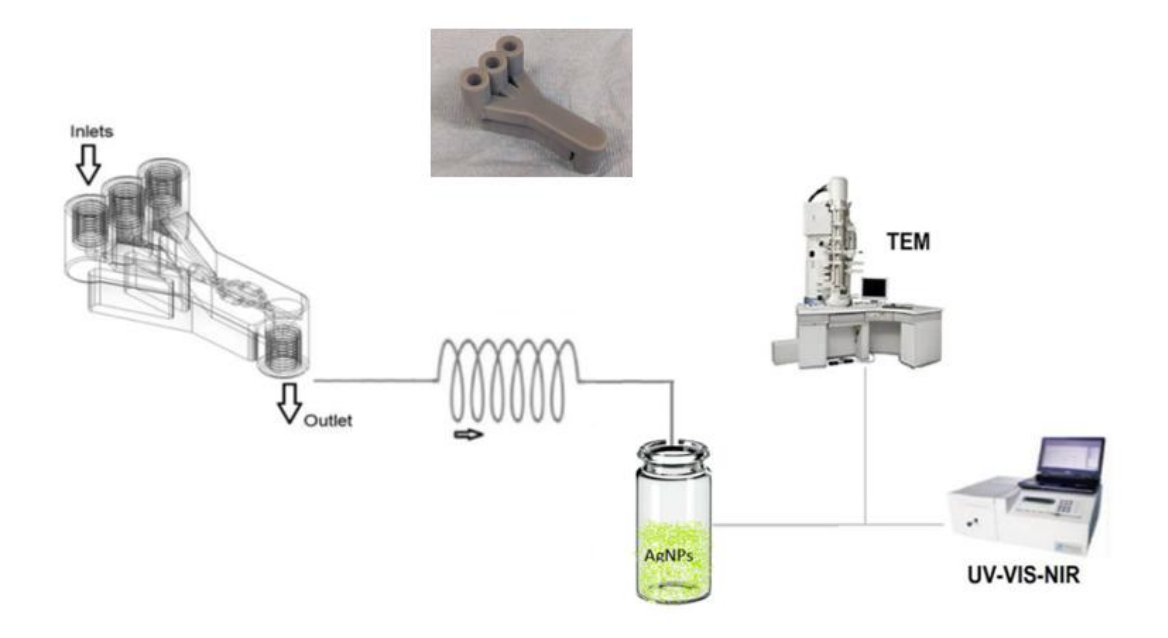


Figure 4.12. Flow synthesis apparatus for silver nanorods utilising syringe pumps, 3D-printed three-inlet reactor, and PTFE tubing

The above schematic describes the flow synthesis process of silver nanorods using a 3D printed flow reactor. The reactor features three parallel inlet ports, each with 1/4-28 UNF threads, spaced 10 mm apart. These ports are compatible with standard microfluidic fittings and allow precise, modular delivery of reagent streams. Internally, each inlet is connected to a 2.00 mm diameter straight channel, which converges toward a central mixing junction. The internal channels are angled and directed inward to promote convergence at the mixing zone. The converging channel architecture leads to a central tapered mixing chamber, where all three streams collide. This geometry is designed to enhance passive mixing by forcing fluid streams together at a sharp angle, thereby promoting laminar breakdown and chaotic advection, particularly important at moderate flow rates [230]. The model was created in Autodesk Inventor CAD software and printed using Elegoo Mars SLA printer at the campus. The threads were created on the model, and several prototypes were printed in order get the correct thread size, i.e., the thread pitch, diameters, angle, etc. This was done until a final prototype without leakage was acquired. See appendix A for more details.

There were three inlets connected to syringe pumps holding seed nanoparticles, NaOH, and a growth solution containing AgNO₃, ascorbic acid, and CTAB. The inlet solutions were passed through internal channels that enhanced the mixing process. After the reactants had mixed and reacted, the solution from the outlet was passed through PTFE tubing for transmission from the reactor to a glass vial where AgNRs are collected. The characterisation of the synthesised nanoparticles was carried out using UV-Vis-IR spectrophotometry and TEM.

The table below shows the tubing details in the design set up:

Tubing	Dimensions		
	Internal diameter (mm)	Length (m)	
Seed to reactor	0.50	0.25	
Growth to reactor	0.50	0.25	
NaOH to reactor	0.50	0.25	
Coiled tubing	0.50	5.0	

Table 4-11 Tubing details for design 3

4.5.2 Flow rates for design 3

The table below shows the flow rates of three different solutions used in the three-inlet 3D-printed flow reactor. These experiments were labelled from D3_1 to D3_3, and for each, there were corresponding flow rates for the growth solution (G), seed solution, and sodium hydroxide (NaOH) solution. Experiment D3_1 implemented the highest flow rates to explore the effects of rapid reaction conditions on nanorod synthesis. Experiment D3_3 utilised the lowest flow rates of the series to further examine the influence of slowed kinetics and prolonged reaction times on the growth of nanorods.

Experiment	G flow rate (mL/min)	Seed flow rate (mL/min)	NaOH Flow rate (mL/min)	Residence time (s)	Reynolds number
D3_1	5.25	0.05	0.05	11	63.8
D3_2	1.05	0.01	0.01	55	12.8
D3_3	0.525	0.005	0.005	110	6.4

Table 4-12 Flow rates used in flow synthesis design 3

4.5.3 Design 3 flow synthesis results

The results of the experiments are illustrated in the UV-Vis-NIR absorption spectra for D3_2 and D3_3 (Figure 4.13). The spectrum for D3_1 is reported as inadequate due to low absorption. A higher flow rate in D3_1 may have led to a faster reaction, possibly resulting in a less controlled growth environment. From the absorption spectra provided, D3_2 and D3_3 only showed single peaks in the UV-Vis region, which correspond to the SPR of spherical silver nanoparticles. D3_3 experiment showed a high SPR peak at 430nm compared to D3_2, which suggested synthesis of larger sized nanoparticles. From the spectra, it is evident that there were no anisotropic nanoparticles, therefore this particular design and reaction parameters may not be suitable for nanorod synthesis.

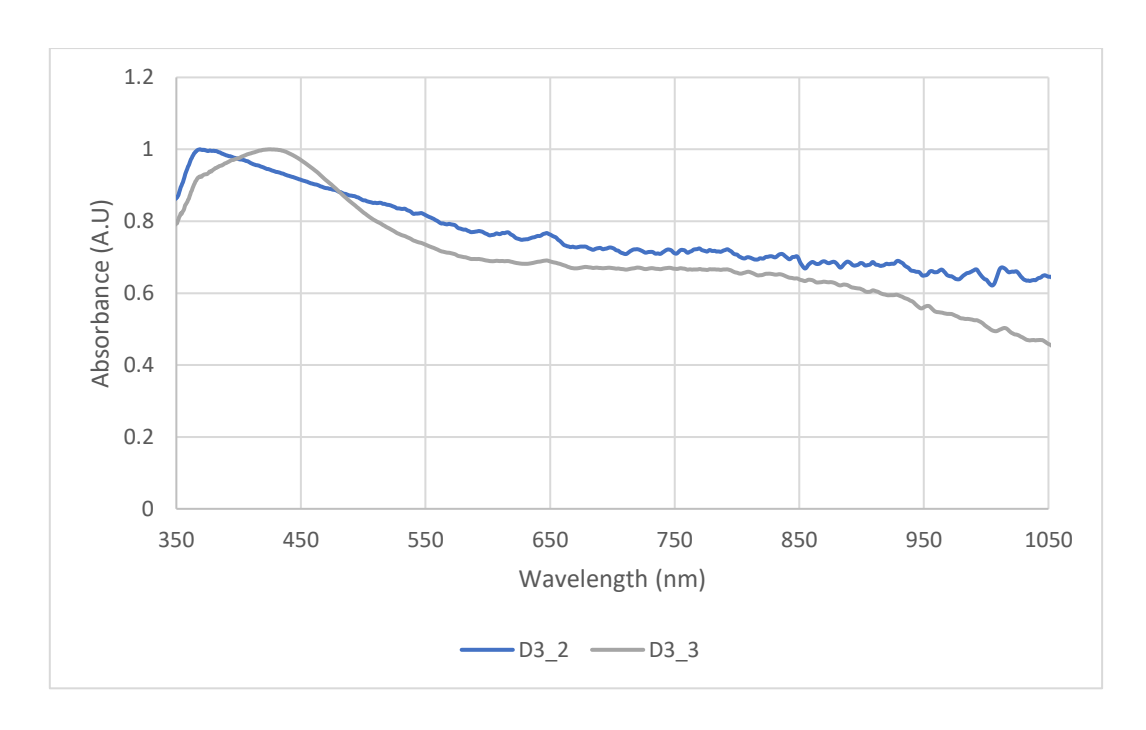


Figure 4.13. Absorption spectra for D3_2 and D3_3

4.5.4 Modifying design 3 parameters

In the subsequent phase of the experimental design 3, an alteration was introduced to the concentration of the reactants. This modification involved diluting both the seed and NaOH solutions by a ratio of 1:5 with water.

Experiment D3_4 had a moderate flow rate for the diluted solutions, aiming to determine if the reduced concentration still permitted the formation of nanorods with uniform properties. Experiment D3_5 tested a lower flow rate for the diluted solutions to investigate the impact of a reduced reactant delivery rate on the synthesis, challenging the kinetics and thermodynamics of nanorod formation further.

Experiment	G flow rate (mL/min)	Seed flow rate (mL/min)	NaOH Flow rate (mL/min)	Residence time (s)	Reynolds number
D3_4	1.05	0.01	0.01	55	12.8
D3_5	0.525	0.005	0.005	110	6.4

Table 4-13 Flow rates used in the modified design 3

4.5.5. Flow synthesis results for modified design 3

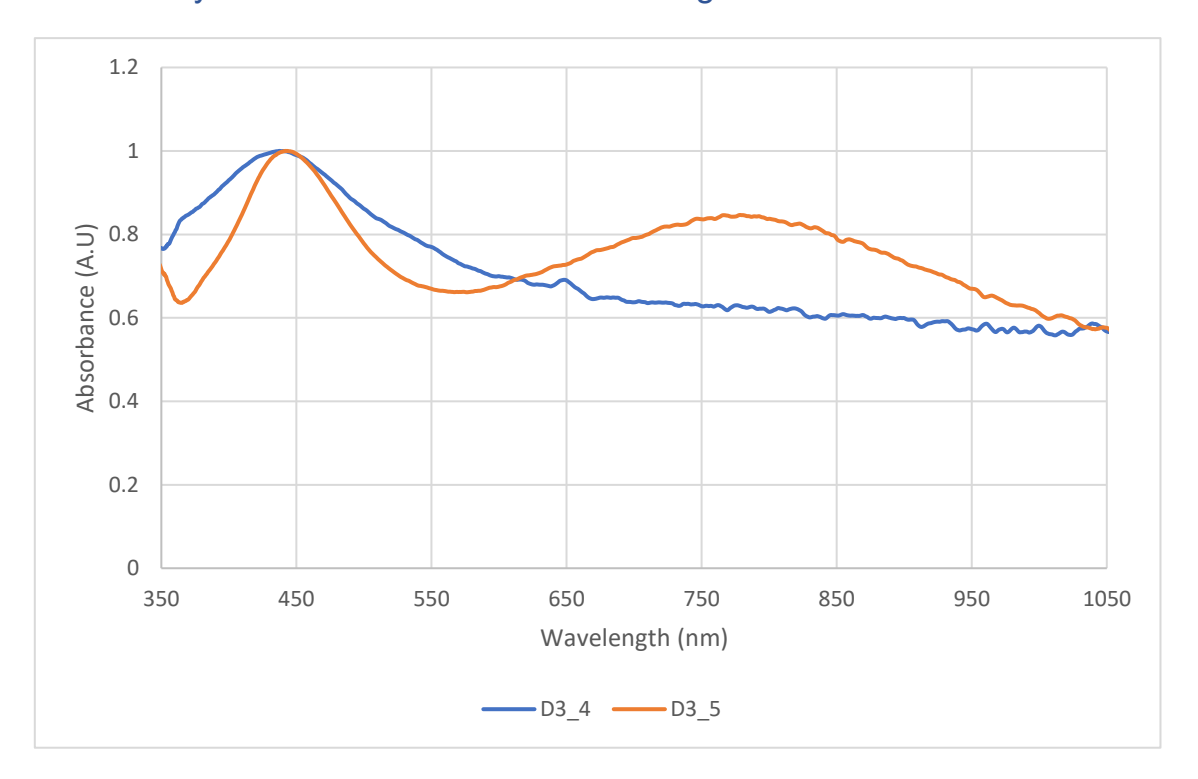


Figure 4.14. Absorption spectra for 3 4 and D3 5

Figure 4.14 shows absorption spectra for D3_4 and D3_5. In D3_4, there was only one SPR peak, which means only spherical nanoparticles were present in the synthesis. Due to the higher flow rates, there might have been less time for the growth of nanorods, resulting in only one absorption peak. On the other hand, D3_5, with a lower flow rate, showed two LSPR peaks, which suggests presence of anisotropic nanoparticles. The reduced flow rates may have led to more effective nucleation and elongation processes, culminating in the production of anisotropic nanoparticles.

It is important to consider the effect of the dilution of the seed and NaOH solutions. The 1:5 dilution may have significantly decreased the number of nucleation sites and moderated the pH increase, respectively, affecting the rate of nanorod formation and the kinetic control over the synthesis process. The diluted conditions in D3_5, combined with the lowest flow rate, appear to be more optimal for the formation of uniform nanorods, as evidenced by the secondary LSPR peak.

In conclusion, the experimental data imply that both the flow rates and the concentration of reactants are critical parameters in the flow synthesis of silver nanorods. Experiment D3 5 suggests that a certain threshold of flow rate and reactant

concentration is necessary to achieve a synthesis of nanorods. These findings underscore the importance of carefully balancing the reactant concentrations and flow rates to achieve precise control over the nanostructure synthesis in a flow chemistry setup, and further, they serve as a valuable reference for optimising the flow synthesis protocol for silver nanorods.

In Design 3, lower flow rates (e.g., D3_5) produced clearer longitudinal LSPR peaks around 780 nm, indicative of rod formation. The spectral and morphological features closely resemble batch method, where lower seed volume and slower kinetics favoured longer rod development. While the yield was lower, the higher absorbance peak under optimised flow conditions (e.g., diluted seed and NaOH) showed advantages over batch synthesis.

4.6 Flow synthesis using design 4



Figure 4.15. Flow synthesis apparatus for silver nanorods utilising syringe pumps, 3D-printed y-type reactor, and PTFE tubing

Figure 4.15 shows the design for the synthesis of silver nanorods employing another 3D printed y-shaped flow reactor. This approach utilised a dual inlet system, enabling the precise control of reagent delivery to the reactor's internal mixing channels. The inlet channels have a diameter of 2.00 mm. Internally, the two inlets taper gradually and symmetrically into a mixing chamber, designed to promote the interfacial contact of reagent streams. The internal channel merging length is approximately 30.00 mm, with each angled inlet contributing to early convergence within the mixing zone. The

gentle angular offset improves the uniform distribution of flow velocities, which in turn enhances mixing efficiency even under laminar flow regimes. Following the merging region, the reactor transitions into a single 2.00 mm diameter outlet channel, directing the mixed stream into downstream components. The reactor was designed using Autodesk Inventor and printed using the Elegoo Mars 3D printer, with multiple iterations of print settings to achieve the correct internal features such the threads and channels, i.e., with thread sizes that are compatible with UNF 1/4-28 thread size luer lock fittings, ensuring a seamless and secure connection for the flow of solutions. See appendix A for more details about the design.

This reactor was equipped with two inlets, specifically configured to different diameters. The internal channel diameter was 1.25 mm for the seed/NaOH solution and 2.50 mm for the growth solution. The solutions converged in a well to allow mixing before exiting the reactor. This design feature addressed a critical aspect of flow dynamics: it allowed a higher flow rate through one inlet for the growth solution - thereby mitigating the potential for backflow at the other inlet, which was reserved for the seed/NaOH solution. After the reaction occurred, the solution left the reactor and flowed through coiled PTFE tubing for further mixing. Finally, it was collected in a glass vial and characterised using UV-VIS-NIR spectroscopy and TEM.

The table below shows the tubing details in the design set up:

Tubing	Dimensions			
	Internal diameter (mm)	Length (m)		
Seed/NaOH to reactor	0.20	0.25		
Growth to reactor	0.50	0.25		
Coiled tubing	0.50	5.0		

Table 4-14 Tubing details for design 4

4.6.1 Flow rates for design 4

The table below shows the flow rates of the solutions used in design 4 flow synthesis experiments aimed at creating silver nanorods. These experiments were labelled from

D4_1 to D4_3, and for each, there are corresponding flow rates for the growth solution (G) and seed / NaOH solution.

For D4_1, the flow rate of the growth solution was the highest among the three at 5.25 mL/min, while the seed/NaOH solution was introduced at a flow rate of 1 mL/min. For D4_2, both the growth solution and the seed/NaOH solution flow rates were decreased by a factor of five compared to D4_1, with values of 1.05 mL/min and 0.01 mL/min, respectively. For D4_3, the flow rates were further reduced to half from D4_2, setting them to 0.525 mL/min for the growth solution and 0.005 mL/min for the seed/NaOH solution.

Experiment	G flow rate (mL /min)	Seed/NaOH flow rate (mL/min)	Residence time (s)	Reynolds number
D4_1	5.25	0.05	11	63.2
D4_2	1.05	0.01	56	12.6
D4_3	0.525	0.005	111	6.3

Table 4-15 Flow rates for flow synthesis using design 4

4.6.2 Results for design 4

Figure 4.16 shows the absorption spectra for experiments using design 4. The D4_1 experiment was unsuccessful due to the flow rates that did not result in the formation of nanoparticles. The absorption spectra for D4_2 and D4_3 showed two peaks in each. They both showed initial peaks at the lower wavelength of around 420 nm due to the transverse mode of the plasmon resonance. D_2 showed a secondary peak at 540 nm and D4_3 at 550 nm. Such plasmonic resonances represent the anisotropic shape of the nanoparticles and, thus an indication that the synthesis approach has was successful. The shift in peak wavelengths and could be indicative of changes in the nanorod dimensions or aspect ratios, which are influenced by the kinetics of the reaction dictated by the flow rates of the reagents.

The dual peak characteristic of the absorption spectra proved that anisotropic silver nanoparticle synthesis is possible using this design, although the absorption for LSPR was not as high as desired. It appears that the flow synthesis parameters, as well as reagent concentrations are important factors in nanorod synthesis.

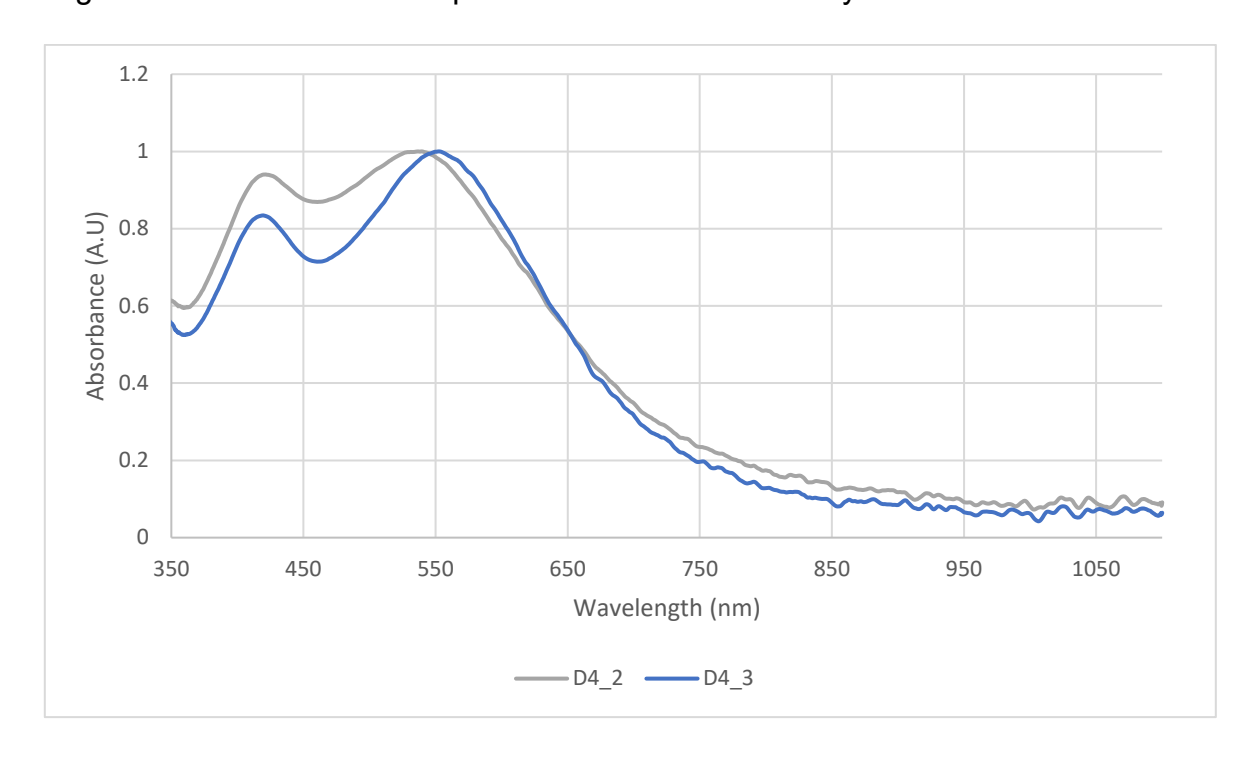


Figure 4.16. Absorption spectra for D4_2 and D4_3

4.6.3 Modifying reagent concentration in design 4 flow synthesis

Following on from previous flow synthesis experiments, the flow rates and reagent parameters were modified to enhance the synthesis. The seed and NaOH solutions were diluted to one-fifth (1:5) of their original concentrations. The table below shows data for three additional experimental runs, labelled D4_4, D4_5, and D4_6, which were part of a series of experiments conducted in this design.

In experiment D4_4, the growth and seed/NaOH solutions were administered at higher flow rates. In D4_6, the flow rates were reduced to lower than in D4_3. At this low flow rate, it was hypothesised that the reaction kinetics would be significantly slower, providing a more controlled environment for the nanorod growth.

Experiment	G flow rate (mL/min)	Seed/NaOH flow rate (mL/min)	Residence time (s)	Reynolds number
D4_4	2.1	0.2	26	27.4

D4_5	1.05	0.1	51	13.7
D4_6	0.105	0.01	512	1.4

Table 4-16 Flow rates for flow synthesis using modified design 4

4.6.4 Results for modified design 4

The absorption spectra for experiments D4_4, D4_5, and D4_6 is shown in figure below. All three spectra exhibited two prominent peaks corresponding to the transverse and longitudinal surface plasmon resonances, which are distinctive optical signatures of anisotropic silver nanoparticles.

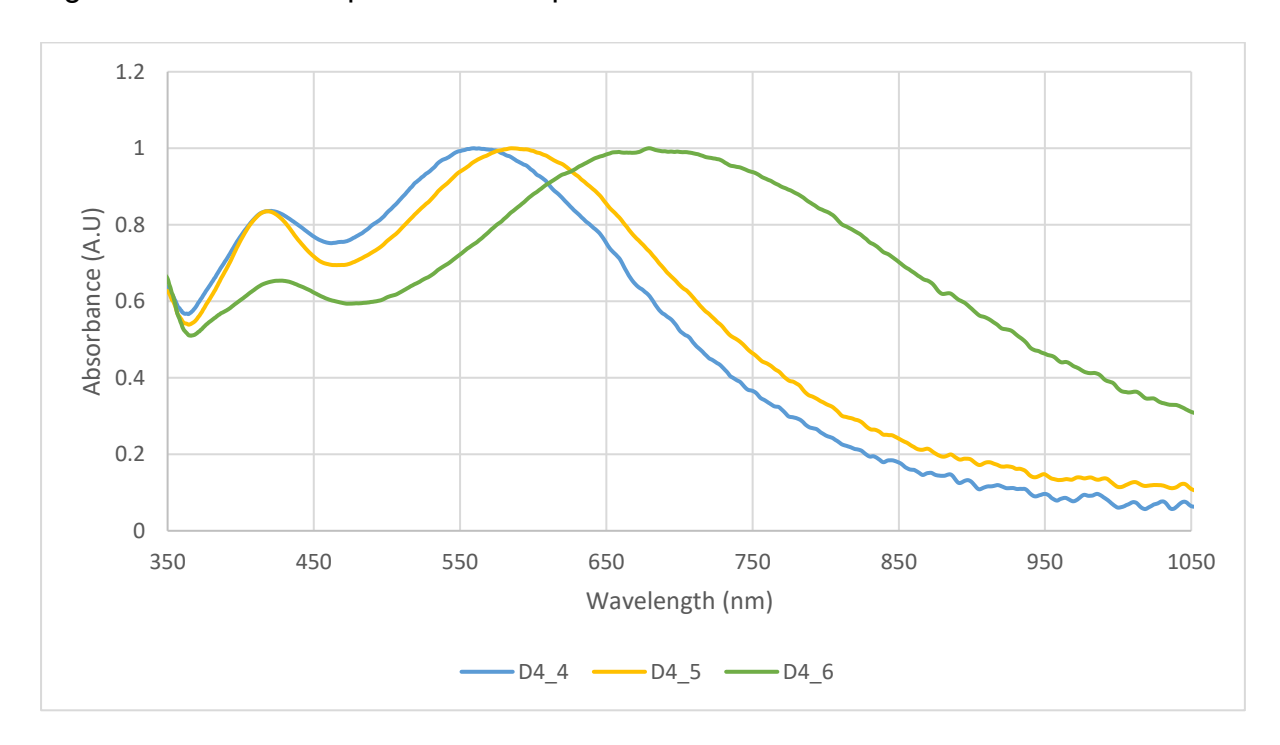


Figure 4.17. Absorption spectra for D4_4, D4_5 and D4_6

D4_4 absorption peaks showed that both transverse and longitudinal modes were pronounced, indicating the formation of silver nanorods. The longitudinal LSPR peak for this experiment was the lowest of the three centred at around 560 nm. The higher flow rates in D4_4, as compared to the subsequent experiments, suggested a faster reaction environment which may have led to shorter nanorods.

D4_5 showed a noticeable shift in the longitudinal LSPR absorption towards higher wavelength with the peak centred around 590 nm. This could be interpreted as a result of a slower reaction rate due to the reduced flow rates, allowing for more controlled

growth and leading to nanorods with a larger aspect ratio and more uniformity compared to D4 4.

In D4_6, the trend continued with a further shift of the longitudinal absorption peak towards higher wavelength at around 690 nm, though there is a change in the overall shape of the spectrum. The lowest flow rates in D4_6 would have slowed the kinetics considerably, resulting in nanorods with the largest aspect ratios among the three experiments. TEM results in Figure 4.18B showed presence of nanorods measuring around 170-180 nm in length, along with other shaped nanoparticles which explained the broader peak.

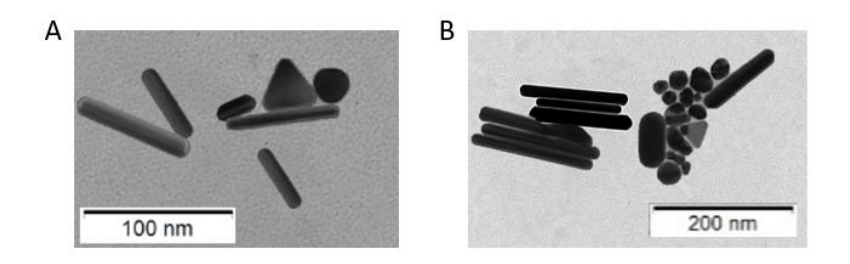


Figure 4.18. TEM images of nanoparticles produced using modified design 4 : (A) D4_5; (B) D4_6

When comparing these results to D4_2 and D4_3, where the seed/NaOH solutions were diluted 1 in 10 parts in water, there is a general trend where the longitudinal absorption wavelengths increase with decreasing flow rates and dilution of the seed/NaOH solutions. The D4_2 and D4_3 spectra indicated the formation of shorter silver nanorods than D4_4 to D6_6, suggested by their shorter-wavelength absorption peaks. The lower longitudinal absorption wavelength of the D4_3 spectrum as compared to D4_2 could be a result of the reduced concentration of nanorods or smaller nanorods formed at the relatively higher flow rates.

A systematic modification in the concentration of the seed/NaOH solutions in the experiments, followed by further variation of the flow rates, clearly showed a trend where, under slower reaction conditions, long silver nanorods were formed. The absorption spectra were good optical characterisations for these nanorods and shifts in plasmon resonance peaks across the experiments were found to correlate to changes in nanorod size. The results indicated the delicate balance that must be struck when placing the flow chemistry parameters against the control of morphologies of nanoscale materials in order to tune their plasmonic properties.

A comparison between batch Method 1 (Trial 1) and Design 4 reveals interesting differences driven by flow rate and design geometry. In batch Trial 1, an LSPR peak of 870 nm was observed, but particle morphology was not recorded. In contrast, flow experiments in Design 4 showed:

D4 3 (higher flow rate): LSPR = 550 nm, morphology unknown.

D4_6 (lower flow rate): LSPR = 690 nm (very broad), with nanorods of AR \approx 10 and a mixture of other shapes.

These results suggest that reducing the flow rate in Design 4 enhanced nanorod formation, increasing the longitudinal plasmon resonance. However, the presence of other shapes in D4_6 indicates some instability in particle uniformity, likely due to design constraints in the mixing region or inlet asymmetry. Compared to batch Trial 1, Design 4's flow conditions favoured shorter nanorods or mixed populations, resulting in lower and broader LSPR peaks.

4.7 Optimised flow synthesis experiments

From the above experiments, design 1 and design 4 were selected for further optimisation due to their superior performance in terms of plasmonic tuning, nanoparticle morphology, and reproducibility. Both designs demonstrated a clear correlation between flow rate, residence time, and the resulting aspect ratio of silver nanorods, aligning well with batch synthesis results and reference literature.

- Design 1 produced well-defined nanorods with aspect ratios up to ~12 (e.g., D1_10) and LSPR peaks reaching 810 nm, showing excellent agreement with batch Trial 1. The incorporation of a Y-mixer and extended coiled tubing contributed to improved residence time control and mixing efficiency, making it a strong candidate for fine-tuned synthesis.
- Design 4, despite a simpler inlet configuration, also yielded nanorods with high aspect ratios (~10 in D4_6) and an LSPR peak at 690 nm. Its compact Y-mixer design supported consistent reagent flow and was more modular, making it easier to prototype and adapt for future scaling.

The decision to further improve these designs was informed by their ability to reproducibly generate anisotropic nanoparticles with desirable near-infrared (NIR) optical properties. However, it was also observed that even in these successful designs, mixing at the junctions remained a limiting factor—especially at moderate flow rates where laminar flow dominates. To address this, a final improvement was introduced in the form of a modular in-line mixing unit, enabling enhanced mixing via turbulence or induced shear, leading to better control over particle uniformity and size distribution. This optimisation phase was therefore a direct evolution of the insights gained from the earlier design iterations, merging the best-performing configurations with enhanced fluid dynamic control.

A modular 3D printed mixer, shown in Figure 4.19, was developed to improve mixing of reagents. The reactor consisted of two parts: a base with a chamber into which the solution flowed and mixed using a magnetic bar; a top lid that screwed on to the base. The chamber in the base had holes that allowed the solution to flow out into a cavity and then exit out. Both of the parts had protrusions with internal 1/4 - 28 threads to

connect luer connectors, this allowed for connections of the PTFE tubing. A magnet stirrer bar, 1 cm long, was placed in the reactor prior to each synthesis and the lid was screwed on to the base. The thread size was M-25, i.e., 25 mm outer diameter on the base and 25 mm inner diameter on the lid. PTFE tape was wrapped around the external thread of the base to ensure a good seal and there was no leakage. The reactor was placed on a magnetic stirrer and fixed with a clamp to ensure there was no movement of the reactor during synthesis. Further details about the reactor design are presented in the appendix A.



Figure 4.19. Schematic and set up of 3D-printed mixing reactor used in optimised flow synthesis experiments. Top two figures show the actual reactor. Below are cad models, with the image in bottom right showing a magnet bar in the base part.

4.7.1 Optimised synthesis using design 1

Figure 4.20 shows the schematic of design 1 flow synthesis system with the mixing reactor added after the coiled tubing. The set up of the design was same as the modified design 1, apart from the addition of the 3D-printed mixing reactor added after the coiled tubing. The stirring speed in the mixer was 200 rpm. The synthesis was carried out using two syringe pumps: one for the growth solution and one for the seed/NaOH solution.

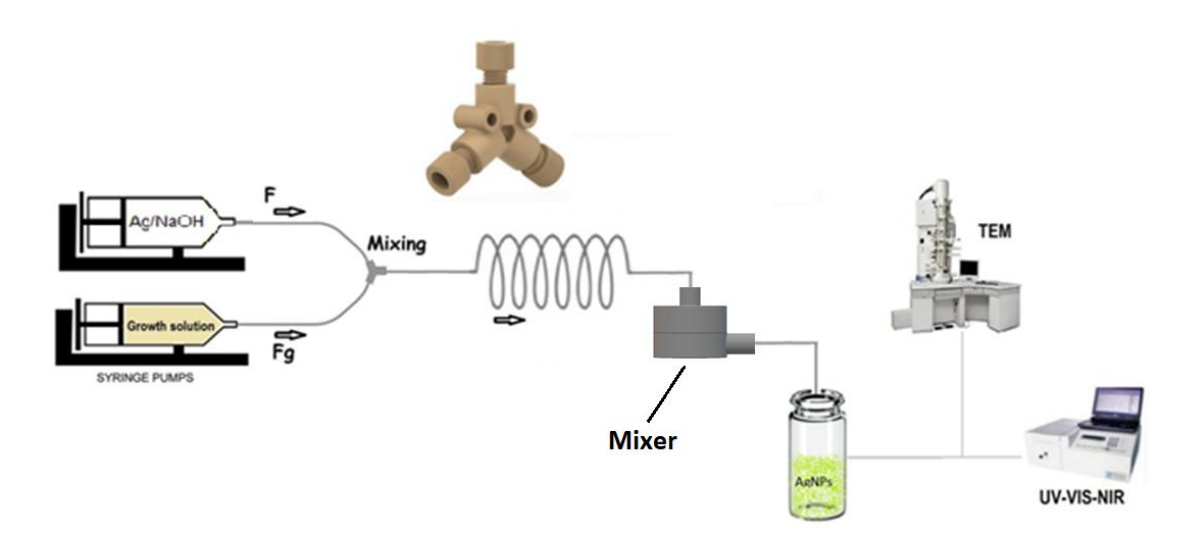


Figure 4.20. Flow synthesis apparatus for silver nanorods utilising syringe pumps, y-type fittings, PTFE tubing, and 3D-printed mixing reactor

The table shows the tubing details used in the above design:

Tubing	Dimensions			
	Internal diameter (mm)	Length (m)		
Seed/NaOH to y-reactor	0.20	0.25		
Growth to y-reactor	0.50	0.25		
Coiled tubing	0.50	5.0		
Mixer reactor to glass vial	0.50	0.30		

Table 4-17 Tubing details for optimised design 1 flow synthesis

4.7.1.1 Flow rates and reagent concentrations

The table below shows the flow rates of the different solutions utilised in the optimised design 1. These experiments were labelled from D5_1 to D5_6, and for each, there are corresponding flow rates for the growth solution (G), and seed/sodium hydroxide (NaOH) solution. The seed and NaOH solutions were diluted 1:5 parts in water. The seed concentration, equivalent to batch synthesis, was varied to study its effect on the synthesis of nanoparticles. In the previous designs, the equivalent seed volume was 0.10 mL, whereas herein it was varied between 0.02 to 0.10 mL. The seed volume was varied between 0.02 mL and 0.10 mL to systematically investigate its effect on nanoparticle morphology, particularly the formation and elongation of anisotropic silver nanorods. This decision was informed by observations from both batch and earlier flow synthesis experiments, which demonstrated that seed concentration plays a

critical role in determining the nucleation density, growth kinetics, and final particle shape. In previous flow designs (e.g., Design 1), a seed volume equivalent to 0.10 mL was consistently used. While this produced elongated nanorods with favourable LSPR responses, the morphology distribution was relatively broad, and it was unclear whether the seed concentration was optimal for controlling aspect ratio or reducing byproduct formation. By varying the seed volume in this optimised setup, while keeping other parameters constant, the study aimed to:

- Assess the extent to which seed availability influences particle elongation,
- Determine whether lower seed volumes result in higher aspect ratio rods or alternative shapes (e.g., nanoprisms or plates),
- Evaluate the reproducibility and spectral sharpness of nanorods under different nucleation conditions.

This variation allows a more refined control over nanorod aspect ratio tuning via seed-limited growth, supporting the goal of producing monodisperse particles with tailored plasmonic properties. The findings also align with established batch synthesis results, where reducing seed input has been linked to more anisotropic growth due to fewer competing nucleation sites.

Experiment	G flow rate (mL/min)	Seed/NaOH flow rate (mL/min)	Eqv. seed volume (mL)	Residence time (s)	Reynolds number
D5_1	0.525	0.05	0.10	102	27.4
D5_2	0.525	0.0375	0.05	105	26.8
D5_3	0.525	0.03	0.02	106	26.5

Table 4-18 Flow rates and seed concentrations used in optimised design 1 flow synthesis

4.7.1.2 Optimised design 1 flow synthesis results

Figure below shows the optical absorption spectra of silver nanoparticles synthesised in the above design. D5_1 and D5_2 both showed primary LSPR absorption peaks below 450 nm and broad secondary peaks centred at around 830 nm, although the maximum absorption peak for D5_2 was at a slightly higher wavelength. D5_3 didn't

exhibit a pronounced primary peak but had a secondary LSPR absorption peak centred at around 960 nm.

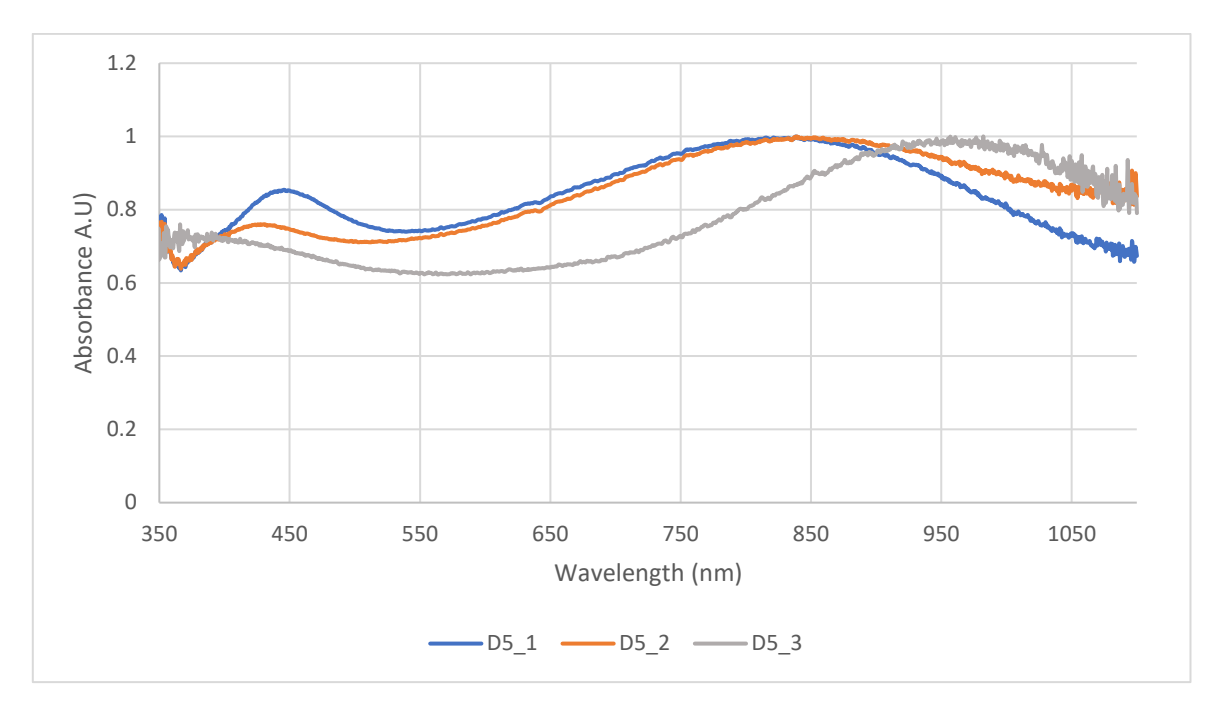


Figure 4.21. Absorption spectra for D5_1, D5_2 and D5_3

The results showed a red-shift in the maximum absorption as the amount of the seed solution was reduced. This correlated well with the batch synthesis, where reducing the volume of seed nanoparticles resulted in larger nanoparticle synthesis and higher absorption. TEM results showed the presence of various shapes of anisotropic nanoparticles including rods, prisms, and spheres. D5_2 showed nanorods measuring 200-220 nm in length, whereas for D5_3 the nanorods were much longer measuring between 350-400 nm in length. This corresponded well with the red-shift in the absorption, as the increased aspect ratio of nanorods results in absorption of higher wavelengths.

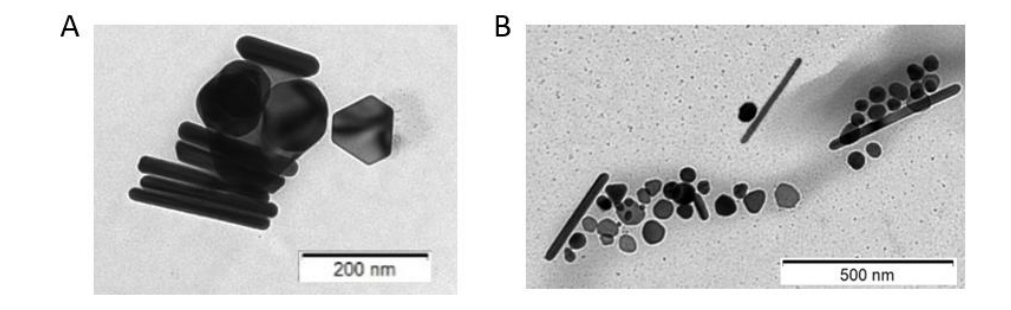


Figure 4.22. TEM images of nanoparticles produced using optimised design 1 : (A) D5_2; (B) D5_3

Comparing the absorption in D5_1 to all previous designs showed an improvement in the maximum secondary LSPR absorption. For example, the secondary LSPR absorption maximum in design 1 was 810 nm, whereas in D5_1 it was 830nm. The results showed that this design set up is suitable to synthesise nanoparticles for absorption of near-infrared wavelengths.

Comparison of optimised design 1 with batch Method 1

To assess the performance of Optimised Design 1 in comparison to batch synthesis, a comparison was carried out between the Optimised Design 1 flow experiments (D5_1 to D5_3) and equivalent batch synthesis results from Method 1, where the seed volume was varied from 0.02 mL to 0.1 mL. This analysis provides insight into how the seed concentration affects the plasmonic response and morphology under both synthesis regimes.

Sample	LSPR λ (nm)	Morphology
0.1 mL batch	870	Unknown
0.05 mL batch	950	Unknown
0.02 mL batch	1000	Unknown
D5_1/2 (0.1 and	830	Rods (AR ≈ 13), prisms
0.05 mL)		(~200 nm), spheres
D5_3 (0.02 mL)	960	Rods (AR ≈ 16),
		quasispheres (~80 nm)

Table 4-19 Comparison of LSPR peak positions and nanoparticle morphologies between batch synthesis (Method 1) and Optimised Design 1 flow experiments across matched seed volumes of 0.1, 0.05, and 0.02 mL. While both methods demonstrate increasing LSPR redshift with decreasing seed volume, the flow synthesis yielded more uniform rod growth and narrower spectral features, reflecting enhanced control over aspect ratio and particle uniformity.

In batch synthesis, a 0.1 mL seed volume (Trial 1) produced an LSPR peak at 870 nm, though the particle shape was not characterised. At 0.05 mL, the LSPR peak increased to 1000 nm, and at 0.02 mL, it reached 950 nm, both indicative of elongated rods or large planar nanostructures. These redshifts suggest that lower seed concentrations reduce nucleation density, enabling the growth of highly anisotropic particles.

In the flow experiments, the LSPR peaks followed a similar trend. D5_1, using 0.1 mL seed, produced a peak at 830 nm, with TEM showing a mixture of nanorods (AR ≈ 13),

nanoprisms (~200 nm), and spherical nanoparticles. This slightly blue-shifted spectrum relative to the batch suggests more uniform rod growth and fewer high-NIR contributing structures.

In D5_2 (0.05 mL seed), the LSPR remained at 830 nm, but with improved rod elongation and similar structural diversity. In D5_3 (0.02 mL seed), the LSPR shifted further to 960 nm, with rods of AR \approx 16 and minor spherical by-products (\sim 80 nm). These results highlight that the flow setup replicates the batch redshift trend, though the absolute LSPR values are slightly lower, likely due to tighter particle distributions and reduced formation of large planar morphologies in flow.

4.7.2 Optimised synthesis using design 4

Figure 4.23 shows the schematic of design 4 flow synthesis system with the mixing reactor added after the coiled tubing. The set up of the design is same as the modified design 4, apart from the addition of the 3D-printed mixing reactor added after the coiled tubing. The stirring speed in the mixer was 200 rpm. The synthesis was carried out using two syringe pumps: one for the growth solution and one for the seed/NaOH solution. The tubing details were same as optimised design 1.

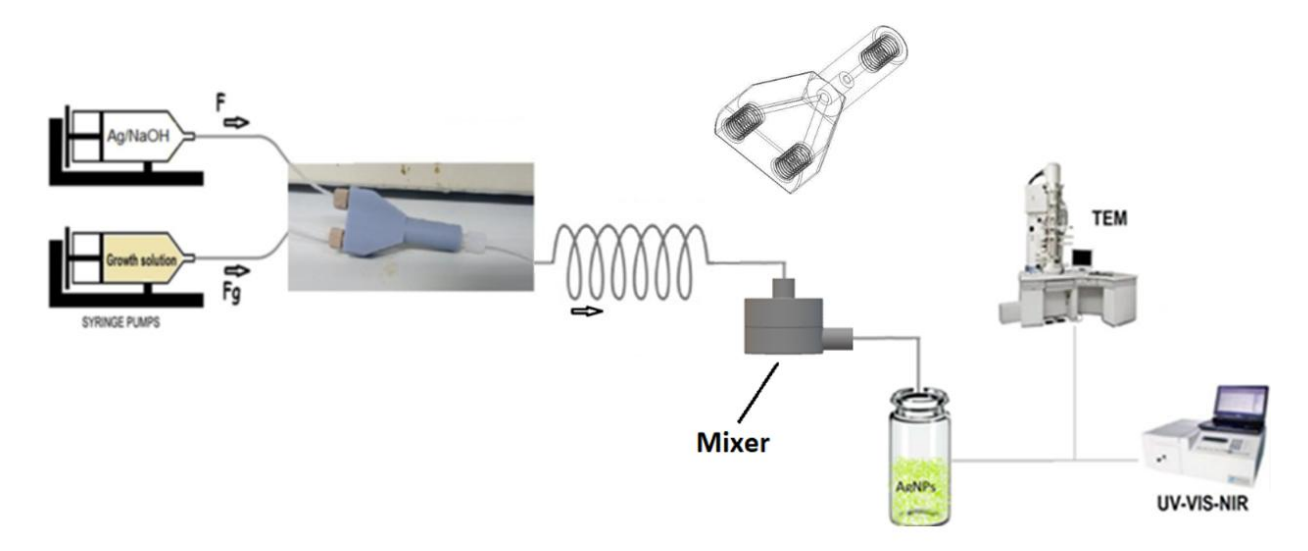


Figure 4.23. Flow synthesis apparatus for silver nanorods utilising syringe pumps, 3D-printed y-type reactor, PTFE tubing, and 3D-printed mixing reactor

4.7.2.1 Flow rates and reagent concentrations

The table below shows the flow rates of three different solutions utilised in the optimised design 1. These experiments were labelled from D6_1 to D6_6, and for each, there are corresponding flow rates for the growth solution (G), and seed/sodium hydroxide (NaOH) solution. The seed and NaOH solutions were diluted 1:5 parts in water. The seed concentration, equivalent to batch synthesis, was varied to study its effect on the synthesis of nanoparticles. In the previous designs, the equivalent seed volume was 0.10 mL, whereas here it was varied between 0.02 to 0.10 mL.

Experiment	G flow rate (mL/min)	Seed/NaOH flow rate (mL/min)	Eqv. seed volume (mL)	Residence time (s)	Reynolds number
D6_1	0.525	0.05	0.10	102	27.4
D6_2	0.525	0.0375	0.05	105	26.8
D6_3	0.525	0.03	0.02	106	26.5

Table 4-20 Flow rates for flow synthesis using optimised design 4

4.7.2.2 Results for optimised design 4 flow synthesis

Figure 4.24 displays the optical absorption spectra of silver nanoparticles synthesised in design 6. All three samples showed primary weak absorption peaks at around 430 nm, with D6_3 showing a very slight peak at around 410 nm.

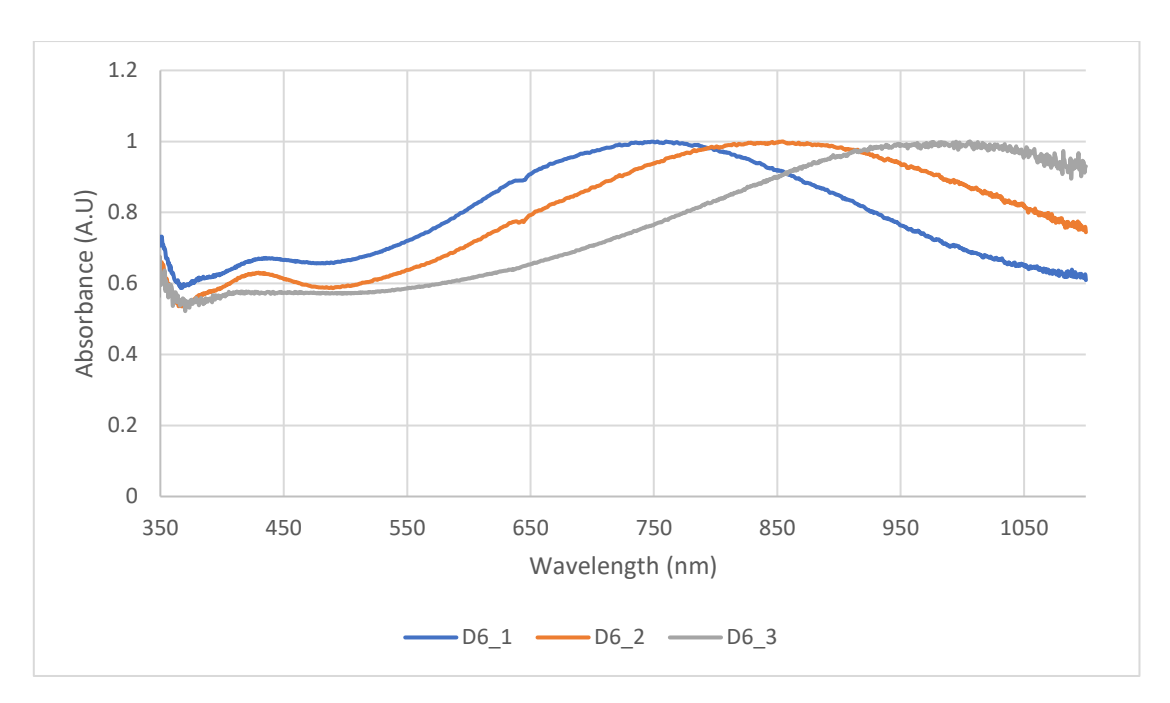


Figure 4.24. Absorption spectra for D6_1, D6_2 and D6_3

D6_1 showed a secondary, broader absorption peak centred roughly at around 750 nm, which suggested the presence of larger or elongated particles that have a longitudinal SPR band. Figure 4.25A showed presence of nanorods measuring 150-180 nm in length, along with other quasi-spherical nanoparticles.

D6_2 showed a secondary longitudinal LSPR peak centred at around 850nm. This showed a red-shift compared to D6_1. TEM results as shown in Figure 4.25B showed presence of nanorods measuring 220-250 nm in length, along with other quasi-spherical nanoparticles.

D6_3 exhibited a secondary broader LSPR absorption peak centred at around 1000 nm. This experiment showed the absorption of the highest wavelengths. The lower seed concentration allowed the nanoparticles to grow larger in comparison to earlier experiments. TEM results as shown in Figure 4.25C showed presence of nanorods measuring 380-420 nm in length, along with other large quasi-spherical nanoparticles.

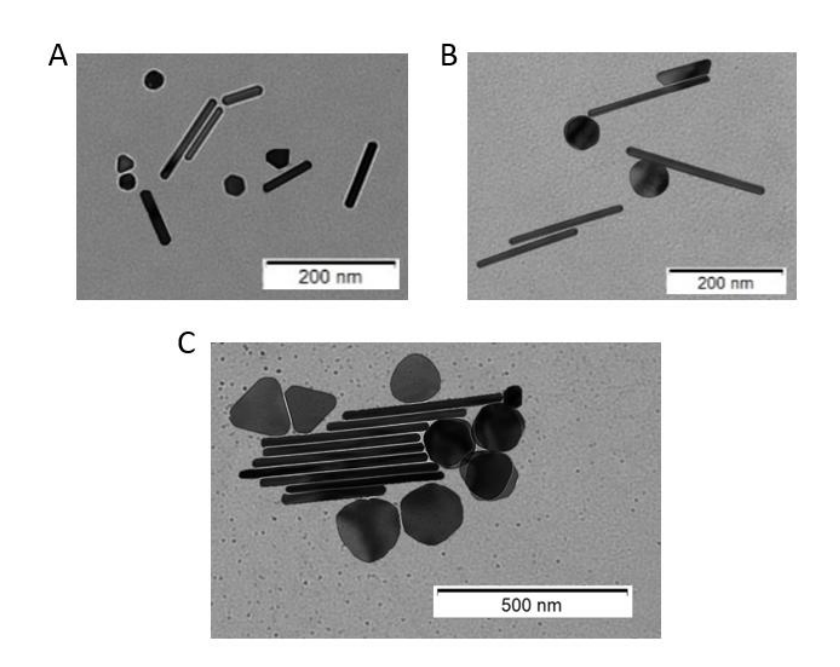


Figure 4.25. TEM images of nanoparticles produced using optimised design 4 : (A) D6_1; (B) D6_2; (C) D6_3

Compared to D5_1, D5_2, and D5_3, the samples D6_2 and D6_3 showed absorption of higher wavelengths, indicating presence of larger anisotropic particles. D6_3 displayed the highest absorption across the spectrum compared to the D5 series, pointing to concentration of largest nanoparticles.

The results from optimised synthesis experiments showed that by varying the flow rates and reagent concentrations, synthesis of silver nanorods absorbing in NIR wavelengths is achievable. Future experiments should alter the reagent concentrations further in order to synthesise larger nanorods that would absorb even higher wavelengths.

Comparison of optimised design 4 with batch Method 1

A comparison between Optimised Design 4 (D6 series) and batch Method 1 trials was conducted to evaluate the influence of seed volume on nanoparticle morphology and plasmonic response under continuous flow versus batch conditions. See summary of the results below.

Sample	LSPR λ (nm)	Morphology
0.1 mL batch	870	Unknown
0.05 mL batch	950	Unknown

0.02 mL batch	1000	Unknown
D6_1 (0.1 mL)	750	Rods + quasispheres Rods
		AR ≈ 9
D6_2 (0.05 mL)	850	Rods AR ≈ 19; quasispheres
		≈ 65 nm
D6_3 (0.02 mL)	1000	Rods AR ≈ 17;
		prisms/hexagons ≈ 160 nm

Table 4-21 Comparison of LSPR peak positions and nanoparticle morphologies between batch synthesis (Method 1) and Optimised Design 4 (D6_1 to D6_3) across seed volumes of 0.1 mL, 0.05 mL, and 0.02 mL.

In batch synthesis, a 0.1 mL seed volume (Trial 1) resulted in an LSPR peak at 870 nm, though no morphological data were available. Reducing the seed volume led to progressive redshifts: 950 nm at 0.02 mL and 1000 nm at 0.05 mL. These values are consistent with increased anisotropy and suggest the formation of longer nanorods or larger anisotropic structures (e.g., nanoprisms or hexagonal plates).

In the flow experiments, a similar redshift trend was observed across D6_1 to D6_3. At the highest seed volume of 0.1 mL (D6_1), the LSPR peak was broad and centred around 750 nm, with particles composed of nanorods (AR \approx 9) and quasispheres. Compared to batch, the lower LSPR position may reflect more uniform rod growth and the presence of spherical by-products, resulting in spectral broadening and dilution of NIR-specific features.

Reducing the seed volume to $0.05 \, \text{mL}$ (D6_2) produced a broader LSPR peak centred around $850 \, \text{nm}$, with a mixture of nanorods (AR ≈ 19) and quasispherical particles ($\sim 65 \, \text{nm}$). This shows enhanced elongation compared to D6_1 and reflects a higher anisotropic population contributing to the redshift. The morphology closely mirrors that of batch samples at this seed level, although with more defined rod populations.

In D6_3 (0.02 mL seed), the LSPR peak further redshifted to 1000 nm, consistent with the batch equivalent. Morphological analysis revealed nanorods (AR \approx 17) alongside nanoprisms and hexagonal plates (\sim 160 nm). These complex planar and elongated shapes are known to produce strong NIR absorption, and their co-existence in flow confirms that low seed concentration promotes diverse anisotropic growth. Despite the broadness of the spectrum, this experiment most closely matched the batch sample

at 0.05 mL, indicating that Optimised Design 4 can replicate batch-like outcomes while maintaining modularity and scalability.

4.8 Overall discussion

Chapter 4 presents a comprehensive analysis of several designs and an optimised version for the flow synthesis of silver nanoparticles, each assessed based on absorption morphology.

The initial designs (Designs 1 through 4) explored various configurations and parameters, providing a foundational understanding of how different variables impact nanoparticle synthesis. Design 1 and its modifications demonstrated that varying flow rates and reactant concentrations can substantially alter nanoparticle morphology. For example, reduced flow rates often result in larger or more elongated nanoparticles, suggesting that extended residence times within the reactor promote growth. Modifications to Design 1, like pre-mixing reactants, have shown to refine the homogeneity of the reaction mix, leading to more consistent nanoparticle characteristics.

Design 2, featuring a t-type reactor, and its subsequent modifications highlight the importance of reactor configuration on nanoparticle properties. Design 3 incorporated a 3D-printed reactor, allowing an innovative approach to test how slight changes in reactor geometry can influence synthesis outcomes. These adjustments have shown that even minor tweaks can lead to significant differences in the final product.

Design 4 took a unique approach by integrating a 3D-printed dual inlet system and manipulating dilution levels of seed and NaOH. This design focused on how changes in the kinetics of the growth process can be leveraged to produce nanoparticles with specific aspect ratios and properties, showcasing the nuanced control offered by flow chemistry techniques.

The optimised design built upon these initial models, incorporating advanced adjustments to further refine the synthesis process. Key modifications included precise control on flow rates and reagent concentrations, aiming to enhance the absorption properties and achieve a more desirable particle size distribution. This design employed a 3D-printed mixing reactor to improve mixing efficiency, ensuring more uniform conditions throughout the synthesis process. The results from the optimised

design, particularly in terms of optical absorption spectra and TEM imaging, show marked improvements in the LSPR absorption peaks and more controlled particle morphology compared to earlier designs.

In summary, the progression from initial designs to the optimised setup in Chapter 4 demonstrates the evolution of flow synthesis in nanoparticle production. Each design iteration has contributed to a deeper understanding of the critical factors influencing nanoparticle characteristics, culminating in an optimised design that exemplifies the potential of flow chemistry to control nanoparticle synthesis efficiently and precisely on a scalable level. This series of designs not only illustrates the adaptability and versatility of flow synthesis methods but also underscores their importance in the continuous development of nanomaterials for advanced applications.

4.9 Conclusions

The continuous flow synthesis designs explored in this chapter offer a scalable and controlled environment for silver nanorod synthesis. Standard and 3D printed y-type reactors offered promising results. The flow rates and reagent concentrations can be tuned to achieve nanorods that absorb NIR wavelengths. Overall, this chapter effectively outlines the transformative impact of flow synthesis on nanoparticle production, providing a blueprint for future research and development in the field of nanotechnology.

Chapter 5 Development of Silver/polymer Nanocomposite

This chapter is dedicated to the investigation into the formulation and assessment of a nanocomposite coating comprising silver nanoparticles and polymer materials. The chapter's outset encompasses a concise introduction to the domain of silver-polymer nanocomposites. Subsequently, it transitions into an exploration of the synthesis procedures, followed by an exposition of the outcomes and a comprehensive discourse on the characteristics of the resultant nanocomposite. In a nutshell, the methodology entailed the production of nanoparticles through the optimisation of the batch synthesis process, subsequent coating with silica, and integration into a polymethyl methacrylate (PMMA) matrix. The assessment of this nanocomposite encompassed spectrophotometric characterisation and electron microscopy imaging.

5.1 Introduction to metal-polymer nanocomposites

The introduction of inorganic nanoparticles into a polymer framework can exert a notable influence on the characteristics of the matrix [231], [232], [233]. These resultant nanocomposite materials have the potential to manifest enhanced attributes encompassing optical, thermal, mechanical, electrical, magnetic, and flammability properties. The specific attributes of polymer composites are contingent upon a variety of factors, including the nature of the integrated nanoparticles, their dimensions and morphology, their concentration within the matrix, and their interactions with the polymer matrix. Polymers are widely recognised as exceptional host materials for metallic nanoparticles. When these nanoparticles are introduced into the polymer matrix, the polymer serves as a proficient surface-coating agent. Consequently, the resulting nanocomposites have the potential to exhibit enhanced optical characteristics.

Due to their diverse array of attributes, polymer nanocomposites have garnered significant attention. These attributes include exceptional performance, enhanced properties relative to their constituent elements, versatile design options, and reduced life cycle costs. These nanocomposites employ organic or inorganic nanoparticles embedded within polymer matrices, yielding novel materials with potential utility in catalysis, bioengineering, photonics, electronics, and antibacterial applications [234].

The synthesis of silver-polymer nanocomposites entails the amalgamation of a nanoparticle solution with the polymerisation mixture. These versatile materials find application in a wide spectrum of fields, including biomedicine, textiles, water treatment, food storage containers, household appliances, and medical devices [235].

PMMA, classified as an amorphous polymer within the acrylate group, possesses superior optical characteristics and demonstrates significant compatibility with human tissue [236]. Owing to its pronounced biocompatibility, PMMA is frequently utilised in the fabrication of biomedical equipment. Additionally, this polymer can associate with metallic nanoparticles, such as silver, leading to an enhancement in their inherent features, including mechanical resilience, solubility, and optical attributes.

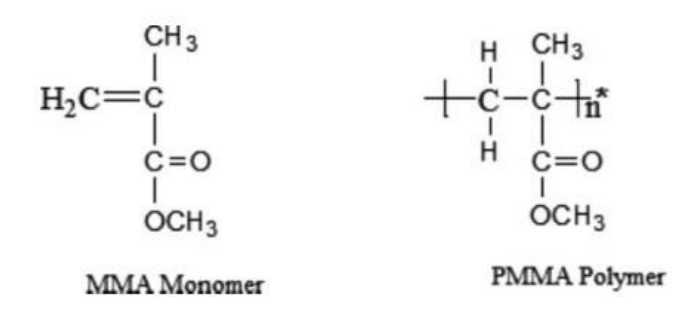


Figure 5.1. Structures of MMA and PMMA.[237]

The characteristics of these polymer composites are influenced by the specific nanoparticles integrated, in addition to their dimensions, morphology, density, and synergy with the polymer framework. Within the realm of polymer substances, PMMA is renowned for its role as a polymeric glass, boasting a diverse array of uses [237]. Employing PMMA often introduces carboxylate functional groups, potentially aiding in the chemical linkage with metal ions. Furthermore, PMMA's pronounced solubility in solvents such as DMF aids in the potential reduction of silver nitrate when required.

Silver nanoparticles exhibit distinct optical, electrical, and thermal characteristics as discussed in above chapters, leading to their integration into a diverse array of products, spanning from photovoltaic systems to bio-chemical sensors. They are employed in materials such as conductive inks, pastes, and fillers due to their notable electrical conductivity, stability, and reduced sintering temperatures. Furthermore, their unique optical attributes are leveraged in molecular diagnostic tools and photonic instruments. A growing trend is the deployment of silver nanoparticles in antimicrobial coatings. Consequently, numerous items, including textiles, keyboards, wound care

products, and biomedical equipment, have been embedded with silver nanoparticles that perpetually emit a minimal quantity of silver ions, offering antibacterial protection. Silver nanoparticles (AgNPs) have demonstrated the capability to create hybrid materials in conjunction with various polymers, including but not limited to polyvinyl alcohol, polypyrrole, polyvinylidene fluoride, chitosan, and cellulose [238]. The synthesis of polymer-silver nanocomposites necessitates precise control over the nanoparticle size within the polymer matrix, as well as the attainment of a uniform distribution of these nanoparticles throughout the polymer matrix.

Numerous endeavours have been made to formulate silver nanoparticles incorporated within PMMA. Typically, in these approaches, silver ions are introduced to the polymer framework and are then transitioned to a zero-valence state either through thermal processing or by employing a reducing agent [239], [240]. Agents utilised for the reduction of silver ions within the polymer structure encompass hazardous chemicals such as dimethylformamide (DMF), hydrazine, and sodium borohydride [241], [242].

Noble metal particles embedded within an insulating matrix, whether composed of oxides or polymers, hold broad applicability. Beyond their optical use as bandpass filters, there is a notable focus on achieving an optical absorber that spans from the visible to the far-infrared (far-IR) region for diverse applications, particularly in the realm of solar energy absorption [243].

When nanoparticles are embedded within a dielectric matrix and exposed to light, the electric vector of the electromagnetic wave triggers oscillations in charge density corresponding to the plasmon frequency (vp) of the metal particles. This phenomenon results in the potent absorption of light at a specific wavelength ($\lambda p = c/vp$, where 'c' represents the speed of light) [244]. This light absorption, coupled with ensuing surface plasmon oscillations, engenders a significantly amplified electric field (up to approximately 50 times greater than the externally applied field) within the nanoparticles and the interparticle gaps [245]. Particularly, elongated particles are anticipated to exhibit notably enhanced electric field amplification compared to spherical nanoparticles.

In cases where the metal volume fraction forms a fractal-percolating network due to the amalgamation of metal particles, the surface plasmon resonance can extend into the far-IR region [239]. It is technologically pivotal to attain light absorption across a broad spectrum, spanning from the visible to the infrared region. This holds significance for applications like high-efficiency solar cells with absorption capabilities ranging from 330 to 2500 nm, infrared photodetectors, sensors, and solar control glazing windows [246], [247].

5.2 Materials and methods

5.2.1 Materials

For the synthesis of silver nanoparticles, silver nitrate (AgNO₃, 99.995%), cetyltrimethylammonium bromide (CTAB, 99%), sodium borohydride (NaBH₄, 99%), L-ascorbic acid (AA, 99%), and sodium hydroxide (NaOH, 99%) were procured from reputable suppliers, specifically Fisher Scientific and Sigma Aldrich, and were employed without the need for additional purification steps. Millipore water was utilised in the synthesis process. All glassware utilised in the experiments was subjected to a rigorous cleaning protocol involving treatment with aqua regia, thorough rinsing with double-distilled water, and subsequent drying before their utilisation in the synthetic procedures. Silver nitrate and silver nanoparticle containers were covered with aluminium foil throughout the experiments to reduce photo-oxidation.

For the subsequent steps to develop the nanocomposite, various reagents were acquired from trusted sources. These reagents encompassed tetraethyl orthosilicate (TEOS), 6-Mercaptohexanoic acid (MHA), methyl methacrylate (MMA) with a minimal quantity of monomethyl ether of hydroquinone (MEHQ) as an inhibitor (present at concentrations below 30 ppm), and a 40 wt.% solution of dimethylamine in H₂O (DMA), all of which were obtained from Sigma-Aldrich (Merck, UK). Azobisisobutyronitrile (AIBN) was procured from Molekula (UK). Additionally, Polydimethylsiloxane (PDMS) monomer and its corresponding curing agent (bought as SYLGARD ™ 184 Silicone Elastomer Kit), were sourced from Dow Corning (USA). These chemicals were utilised in their original, unaltered form, except for MMA, which underwent purification to eliminate the inhibitor prior to its utilisation in the polymerisation process. Solvents employed in the experimental procedures included chloroform (CHCl₃), ethanol (EtOH), methanol and toluene.

Methyl methacrylate (MMA) underwent polymerisation utilising the UVP Black-Ray B-100 AP High Intensity UV Lamp (Analytik Jena US). Strict precautions were taken during the lamp's operation, and the irradiation process was conducted under a large enclosure to prevent the escape of UV radiation.

Transmission electron microscope (TEM) images were captured using an FEI Technai12 TEM, employing an electron acceleration of 120 kV and a tungsten filament source. TEM grids (Carbon on Cu, 400 mesh) were procured from Agar Scientific (UK).

UV-visible-near-infrared (UV-vis-NIR) spectra ranging from 300 to 1400 nm were recorded using Avantes Avaspec 2048 (range 200 – 1100 nm) and Avaspec NIR 1.7 (range 900 – 1700 nm) fibre-optic spectrophotometers equipped with a quartz cell (10 mm optical path).

Infrared (IR) spectroscopy was conducted using a Nicolet iS5 FTIR instrument equipped with an iD7 ATR diamond crystal Smart Orbit for attenuated total reflection (ATR) experiments.

5.2.2 Synthesis of silver nanorods

In this method, silver nanorods were prepared according to the seed mediated synthesis which was optimised in the batch synthesis. The seed solution was prepared by mixing 0.01M AgNO₃ and 80 µL of 0.1 M CTAB stock solution. This was made up to 20 mL with Millipore water and to this 0.6 mL of 0.01 M NaBH₄ was added and stirred for 2 minutes. The solution was kept undisturbed for 1 hour, before adding to the growth solution. To produce silver larger nanorods, 10 mL of a growth solution consisting of 0.01M CTAB, 0.25 mL 0.02 M AgNO₃ and 0.5 mL 0.1 M ascorbic acid was taken. To this, a 0.01 mL of seed solution was added. Finally, 0.10 mL of 1 M NaOH was added and shaken gently. The colour of the solution was seen to change gradually from yellow to orange, red, blue, and finally to light hay-green (characteristic of silver nanorods). The 10 mL colloid was centrifuged at 12000 rpm for 6 minutes to remove excess chemicals and smaller nanoparticles. After discarding the supernatant, Millipore water was added to achieve a total volume of 10 mL.

5.2.3 Coating of silver nanorods with silica

To prevent the aggregation within the polymeric host, silver nanoparticles were enveloped in a silica shell, which serves as an optically transparent protective layer. To achieve a sustained dispersion of silica-coated nanorods (AgNR@SiO2) within a polymethyl methacrylate (PMMA) matrix, these particles were additionally functionalised with allyl groups and underwent polymerisation with methyl methacrylate, resulting in the formation of covalent AgNR@SiO2/PMMA composite materials. This represents a pivotal advancement in the creation of robust inclusion coatings that are both stable and optically transparent. The procedural details for the surface coating stages are depicted in Figure 5.2. The successful encapsulation of silver nanoparticles with silica has been previously documented in the works of Carboni and Kimpton, respectively [247], [248]. In the present investigation, this method has been adopted with slight modifications following multiple experimental iterations aimed at attaining optimised coating characteristics.



Figure 5.2. A simple depiction of the steps to modify the silver nanorod surface

To the 10 mL AgNR solution obtained in the preceding step, 0.5 mL of a 1 mM ethanolic solution of 6-mercaptohexanoic acid (MHA) was introduced and agitated using a vortex mixer at a frequency of 10 Hz for a duration of 2 minutes. Subsequently, the AgNR/MHA solution underwent centrifugation at 5000 rpm for a period of 10 minutes to eliminate any excess MHA. The resulting supernatant was meticulously decanted, and 1.5 mL of Millipore water was introduced into the mixture. To this aqueous phase, 0.034 mL of tetraethyl orthosilicate (TEOS) was carefully injected.

An ethanolic solution of dimethylamine (DMA@EtOH) was prepared by combining 1 mL of dimethylamine with 10 mL of ethanol. The AgNR/TEOS composite was then introduced into the DMA@EtOH solution and subjected to stirring at 600 rpm for a duration of 15 minutes. An additional 5 mL of ethanol was subsequently incorporated into the solution, which was then subjected to centrifugation at 5000 rpm for 7 minutes.

The supernatant was discarded, and the resulting residue was subjected to sonication in 10 mL of ethanol for a period of 5 minutes. Following this, the solution was subjected to centrifugation once more, this time at 3000 rpm for 6 minutes. After discarding the supernatant, 1.5 mL of ethanol was added to the remaining precipitate, which was subsequently subjected to sonication for a period of 5 minutes. The AgNR@SiO₂ was ready for the next step.

5.2.4 Development of AgNR@SiO₂/PMMA nanocomposite

MMA underwent a purification process involving sequential washing steps (5-6) with a 0.5 M sodium hydroxide (NaOH) solution, followed by desiccation with sodium sulphate (Na₂SO₄). The resultant MMA was subsequently filtered and stored at a temperature of +4 °C.

In the initial phase, 0.028 g of azobisisobutyronitrile (AIBN) was meticulously weighed in a glass vial, and 0.75 mL each of MMA and toluene were combined. Notably, the amount of AIBN utilised, specifically 0.028 grams, corresponded to a 4% weight-to-weight (w/w) ratio concerning MMA (in 0.75 mL, there is 0.702g of MMA). This proportion was found to be optimal following an assessment of a range spanning from 1% to 10%.

Subsequently, varying volumes of the silver nanorod solution were incorporated, ranging from 1% to 20% v/v, where, for instance, a 10% inclusion would translate to 0.075 mL of the as prepared AgNR@SiO₂ solution from silica coating step. To mitigate oxygen interference, the solutions were subjected to a 5-minute argon degassing process. Following this, the solutions were exposed to ultraviolet (UV) irradiation emanating from a 100W UV lamp operating at a wavelength of 365 nm. An irradiation duration of 2 hours proved sufficient for the polymerisation of MMA.

To illustrate the surface functionalisation pathway employed in this study, Figure 5.3 presents the stepwise mechanism for modifying silver nanorods (AgNRs) to enable silica coating and integration into a PMMA matrix. The process begins with the displacement of the native CTAB surfactant layer using 11-mercaptoundecanoic acid (MHA), followed by the deposition of a silica shell via tetraethyl orthosilicate (TEOS) condensation, and final dispersion within poly(methyl methacrylate) (PMMA).

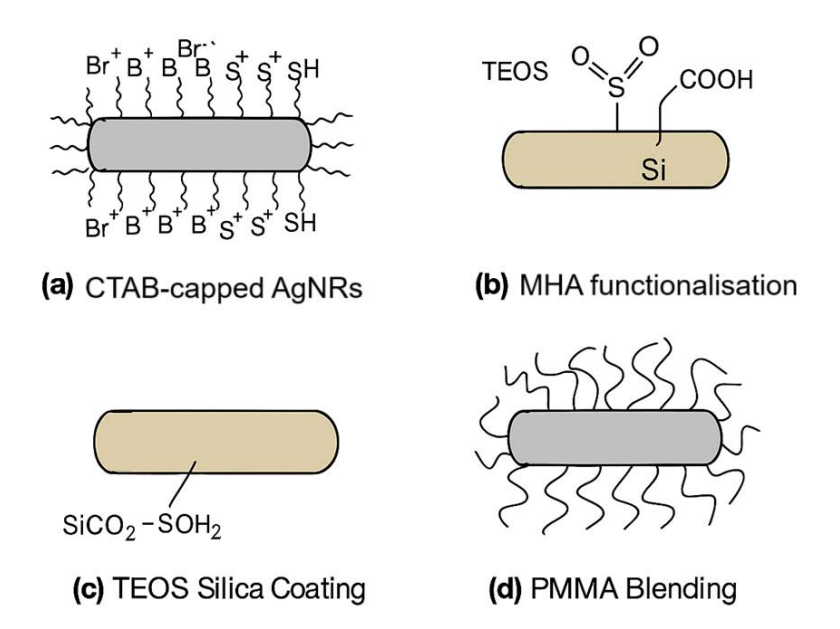


Figure 5.3. Schematic representation of surface modification of silver nanorods. The process involves thiol-based ligand exchange with MHA, silica coating through TEOS hydrolysis and condensation, and final dispersion in PMMA.

The surface modification proceeds in four stages:

- CTAB capping: As-synthesised nanorods are stabilised by a bilayer of (CTAB),
 which binds to the silver surface through electrostatic interactions (Figure 5.3a).
- MHA Functionalisation: To enable further surface chemistry, CTAB is replaced
 with 11-mercaptoundecanoic acid (MHA), a bifunctional molecule possessing a
 thiol (-SH) group and a terminal carboxyl (-COOH) group. The thiol moiety
 forms a strong covalent bond with the Ag surface, displacing CTAB through
 ligand exchange (Figure 5.3b).
- Silica coating via TEOS: Using the carboxyl-rich MHA surface as a scaffold, tetraethyl orthosilicate (TEOS) is hydrolysed in situ to initiate silica (SiO₂) shell formation via condensation reactions (Figure 5.3c). This step enhances particle stability, optical tunability, and compatibility with a wide range of solvents and polymers. Silica shells also provide a physical barrier against aggregation or reshaping.
- Embedding in PMMA: The silica-coated nanorods are physically dispersed in a PMMA solution (Figure 5.3d).

5.2.5 Preparation of PDMS mould and nanocomposite film

Thin films of the AgNR@SiO₂/PMMA nanocomposite were prepared by casting the polymer solution into a mould comprising a PDMS-glass slide assembly. PDMS sheet of approximately 2mm thickness featuring square/rectangle sections precisely cut into it was firmly pressed against a glass slide to make the moulds, and the slide was cleaned and dried prior to pouring the polymer solution (see example shown in Figure 5.4). The solutions were formulated by dispersing the composite solution in chloroform.

To enhance the homogeneity of the films, the mould orifices were covered with watch glasses to retard the chloroform's evaporation process. Films that were allowed to evaporate without the watch glasses exhibited a fractured and undulating surface. The polymer solution was left undisturbed overnight. Next day, the PDMS sheet could be gently peeled away, leaving the nanocomposite film on the slide. Polymer films were synthesised using a 10-30% v/v ratio (in reference to chloroform) solution of AgNR@SiO2/PMMA containing varying quantities of silver nanoparticles (2%, 5%, and 10%). Employing more diluted mixtures led to the delamination of the PDMS film due to penetration at the juncture between the glass slide and the PDMS. Conversely, a polymer concentration exceeding 30% culminated in a film exhibiting an exceptionally dark hue, akin to deep black.

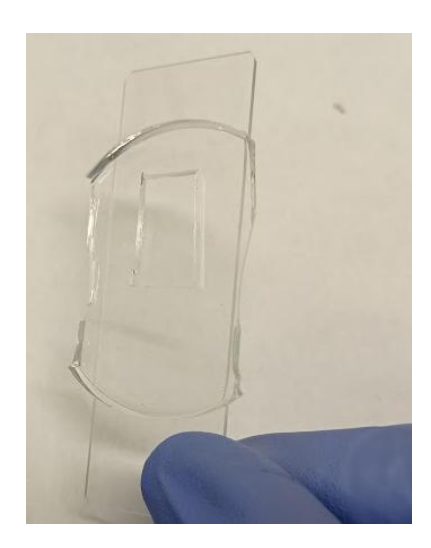


Figure 5.4. Example of a glass slide-PDMS mould

5.3 Results and discussion

5.3.1 AgNR synthesis

The characterisation of the fabricated silver nanorods using spectrophotometry, taken at three distinct coating phases, is depicted in Figure 5.5. These nanoparticles display a pronounced SPR peak (indicated by the continuous blue line) approximately at 1060 nm. Results derived from TEM imaging reveal elongated nanorods with dimensions ranging from 350 to 400 nm in length and possessing an aspect ratio of about 7.6. Additionally, the synthesis also contained nanoparticles that deviated from the typical rod-like shape. The pronounced dimensions of the nanorods contribute to the observed absorbance within the NIR spectrum. These findings align with anticipations based on prior synthesis experiments documented in chapter 3.

Addition of MHA resulted in a slight blue-shift of absorbance. MHA molecules have a thiol (-SH) functional group that can bind strongly to the silver nanoparticle surface. This can lead to the displacement or exchange of the original capping agents or ligands on the nanoparticle surface. The exchange of ligands alters the surface chemistry of the silver nanoparticles. MHA molecules have a longer and more flexible structure compared to many other ligands, and they can effectively passivate the nanoparticle surface. This change in surface chemistry can affect the electron density and distribution on the nanoparticle's surface. The surface plasmon resonance of silver nanoparticles is highly sensitive to the local environment and the electron density on the nanoparticle's surface. When MHA replaces other ligands, it can lead to changes in the electron density distribution on the nanoparticle's surface, which in turn affects the plasmon resonance. The interaction of MHA with the silver nanoparticles resulted in a blue-shift of the absorbance maximum peak. This blue-shift is indicative of changes in the resonance conditions, which can be attributed to the altered surface properties caused by MHA.

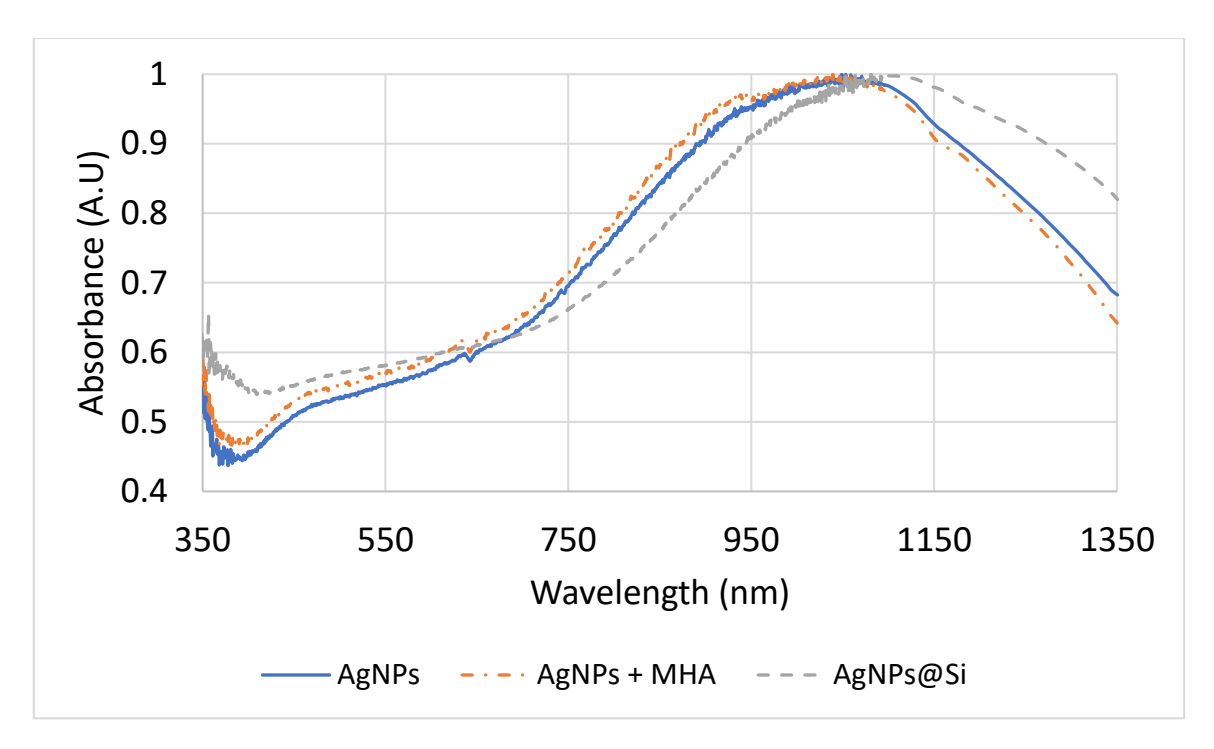


Figure 5.5. Normalised absorbance spectra for silver nanoparticles

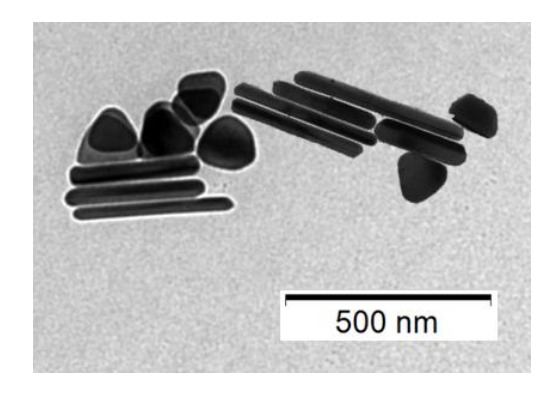


Figure 5.6. TEM image of silver nanoparticles prepared for AgNR/PMMA synthesis

5.3.2 AgNR coating with silica

The encapsulation of nanoparticles with silica shells has been successfully demonstrated with various metallic nanoparticles, including silver. Coating these nanoparticles with silica offers several compelling advantages. Firstly, the silica shell provides enhanced stability, safeguarding the metallic core from external environmental factors and possible degradation. Secondly, the transparency of the silica shell allows for accurate optical measurements without significant interference. Lastly, a silica surface presents opportunities for further functionalisation through solgel chemistry, broadening the potential applications and adaptability of these nanoparticles.

The methodology for coating adopted in this study draws inspiration from the works of Carboni and Kimpton, albeit with a few modifications [247], [248]. To ensure the effective growth of the silica shell, the silver nanorods (AgNRs) were first stabilised using a surface functionalisation process with mercaptohexanoic acid. This was followed by introducing the nanoparticles into a TEOS solution, where dimethylamine (DMA) acted as a catalyst, resulting in the formation of AgNR@SiO₂. A distinction in the current approach from that of Carboni's was the exclusion of allyl-triethoxysilane (ATES).

Upon examining the absorbance spectrum of the AgNR@SiO₂, as depicted in Figure 5.5 (gray dashed curve), a distinct red-shift in absorbance was observed. This phenomenon, consistent with previous studies, indicates the influence of the silica coating, which shifted the peak position by approximately 65 nm. This additionally shifts the absorbance towards longer wavelengths, suggesting that these nanomaterials hold potential for applications in near-infrared nanocomposites intended for signature suppression objectives.

The effective creation of the silica shell on the nanoparticles is further evidenced by TEM images (shown in Figure 5.7). These images not only displayed a uniform thickness of the silica coating on the AgNRs but also revealed the presence of some silica nanoparticles devoid of the silver core, suggesting a potential versatility in the synthesis process that could be harnessed for varied applications in the future.

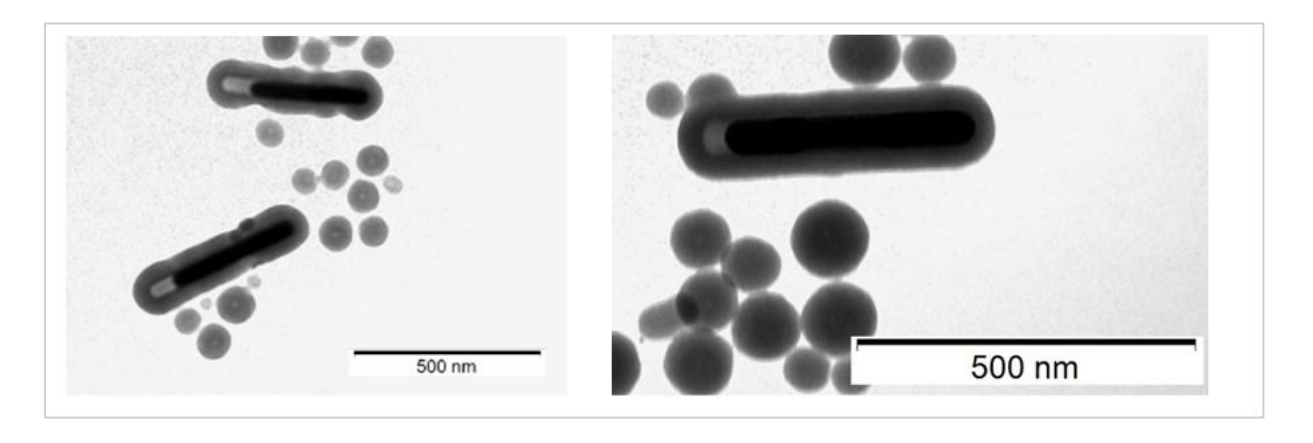


Figure 5.7. TEM results showing silver nanorods coated in a silica shell.

5.3.3 AgNR@SiO₂-PMMA nanocomposite

Integrating allyl-groups to AgNR@SiO₂ is imperative for the generation of robust polymer inclusion frameworks. This is achieved through the covalent bonding of the AgNRs to the polymer lattice, which also augments the distribution of AgNRs within the matrix. The AgNR@SiO₂/PMMA composite was formulated by developing the polymer while incorporating diverse quantities of AgNR@SiO₂. An ideal concentration was determined to be between 10-25%(vol) for the composites, yielding films characterised by consistent thickness and commendable transparency in the visible range.

Optical assessment of the AgNR@SiO₂/PMMA nanocomposites was executed in their solution state. The absorbance spectra, shown in Figure 5.8, illustrate a correlation between enhanced absorbance intensity and the increase in the content of AgNR@SiO₂. A composite with 10% loading exhibited pronounced absorbance at extended wavelengths (around 1150 nm). This absorbance intensity witnessed a decline with decreased loadings at 5% and 2%. The absorbance properties of PMMA were also analysed (indicated by the blue curve) and served as a reference for evaluating absorbance in AgNR@SiO₂/PMMA nanocomposites.

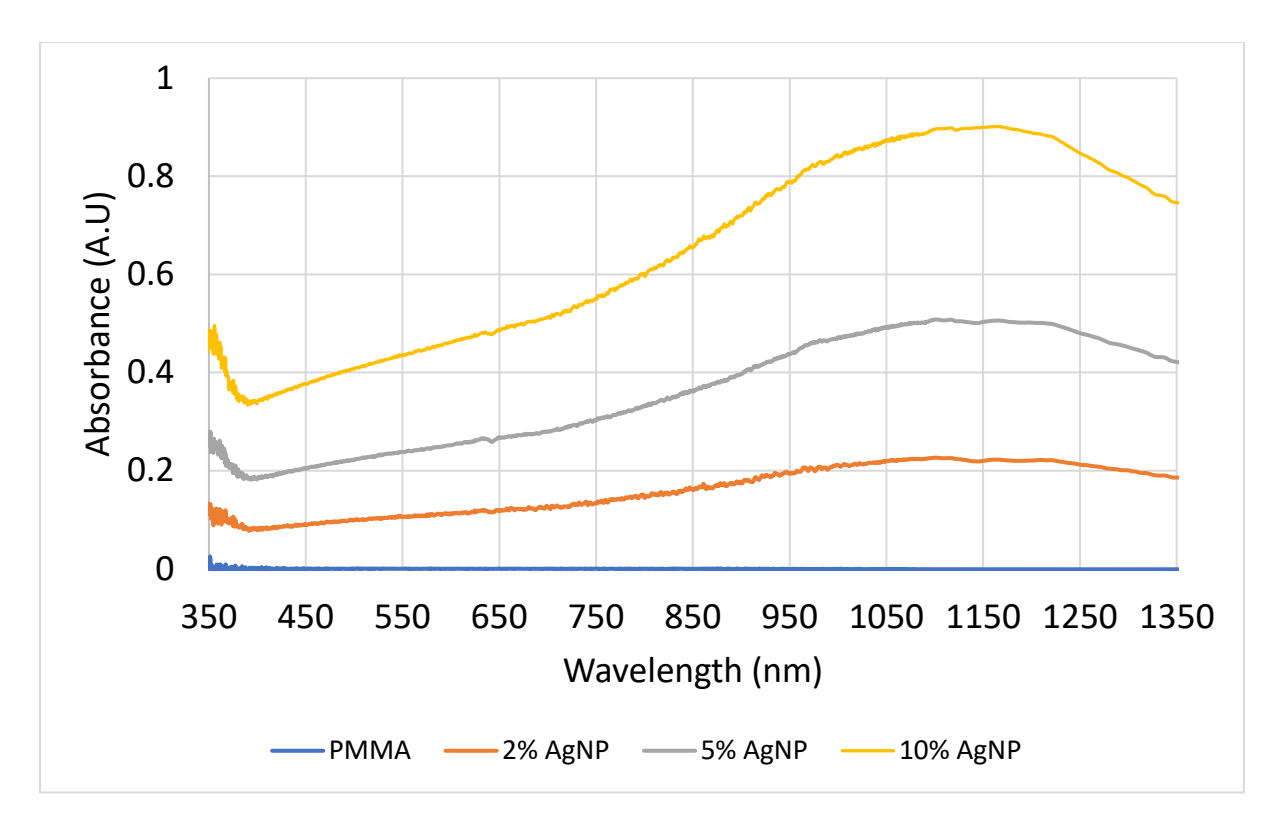


Figure 5.8. Absorbance spectra AgNR/PMMA nanocomposites

5.3.4 AgNR@SiO₂-PMMA nanocomposite FTIR

Poly (methyl methacrylate) (PMMA) is a widely used polymer with myriad applications ranging from optical devices to biomedical implants. The incorporation of nanoparticles, like silver, can potentially augment the material properties of PMMA. Fourier Transform Infrared Spectroscopy (FTIR) was conducted to elucidate the structural ramifications of incorporating silver nanorods into a PMMA matrix. The FTIR spectra of prepared PMMA, PMMA with 5% AgNRs, and PMMA with 10% AgNRs were meticulously compared to discern the molecular interactions and structural nuances induced by the AgNRs. Figure 5.9, Figure 5.10 and Figure 5.11 show the FTIR results for the PMMA and AgNR/PMMA nanocomposites.

Across all spectra, peaks around ~2950 cm⁻¹ and ~2995 cm⁻¹ were consistently observed. These are indicative of C-H stretching vibrations from the methyl (CH₃) and methylene (CH₂) groups inherent to PMMA. The consistent manifestation of these peaks across the samples underscores that the aliphatic hydrocarbon structure in PMMA remains largely unscathed by the integration of AgNRs.

A pronounced peak, emblematic of the carbonyl (C=O) stretching vibration, was identified at ~1722 cm⁻¹ in all the spectra, underscoring the preservation of the ester functionality in PMMA, irrespective of nanoparticle incorporation.

Peaks situated at ~1434 cm⁻¹ and ~1386 cm⁻¹, attributed to the C-H bending vibrations of the methyl group in PMMA, manifested consistently across the samples.

The presence of a peak at ~1239 cm⁻¹, typically resonating with the C-O stretching vibration of ester groups, was uniformly identified across the spectra.

Peaks discerned at ~1143 cm⁻¹ and ~1061 cm⁻¹, potentially attributable to the C-C stretching of the polymer backbone and the C-O-C stretching vibrations, respectively, were evident in all spectra.

A unique peak at ~1506.89 cm⁻¹, absent in the pure PMMA spectrum but conspicuous in both the 5% and 10% AgNRs spectra, suggests an interaction or molecular motif attributable to the silver nanoparticles.

Peaks residing below 1000 cm⁻¹ in the spectra remained analogous across the samples, affirming that the foundational structure of PMMA remains intact upon nanoparticle inclusion.

The FTIR spectral analysis divulged that PMMA's intrinsic chemical structure remains predominantly unaltered with the introduction of silver nanoparticles, albeit the appearance of new peaks suggestive of interactions or associated molecular structures from the nanoparticles. A more granular study, especially focusing on peak intensities and widths, could provide further insights into the concentration-dependent effects of the nanoparticles.

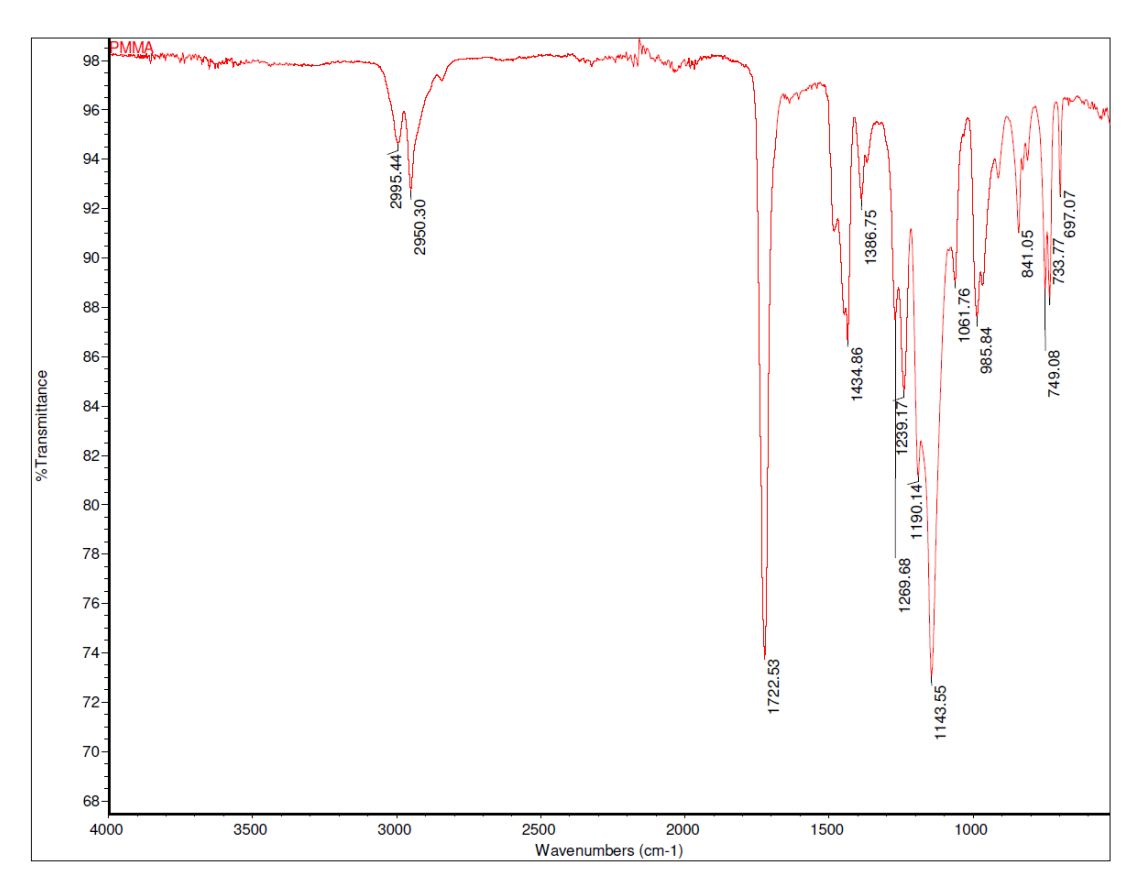


Figure 5.9. FTIR spectrum of PMMA

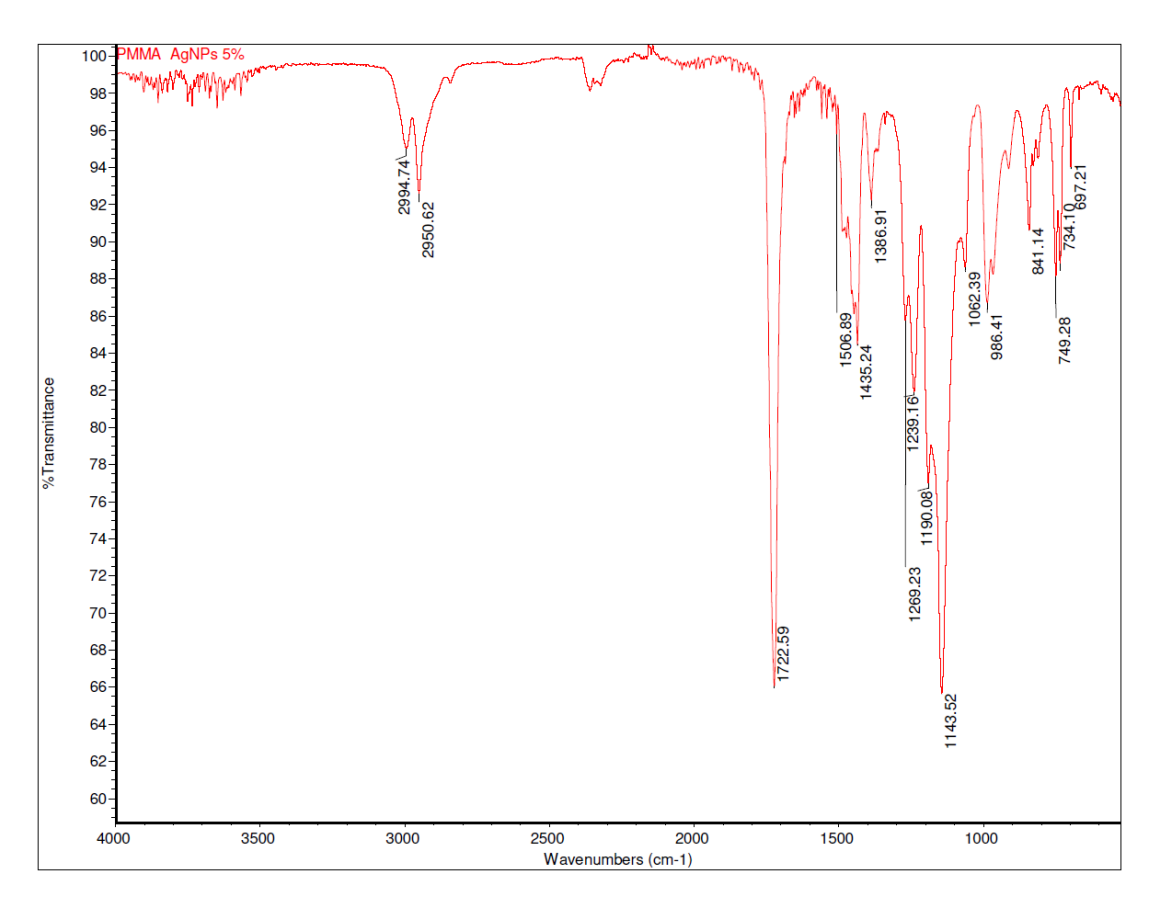


Figure 5.10. FTIR spectrum of AgNR/PMMA nanocomposite containing 5% AgNRs

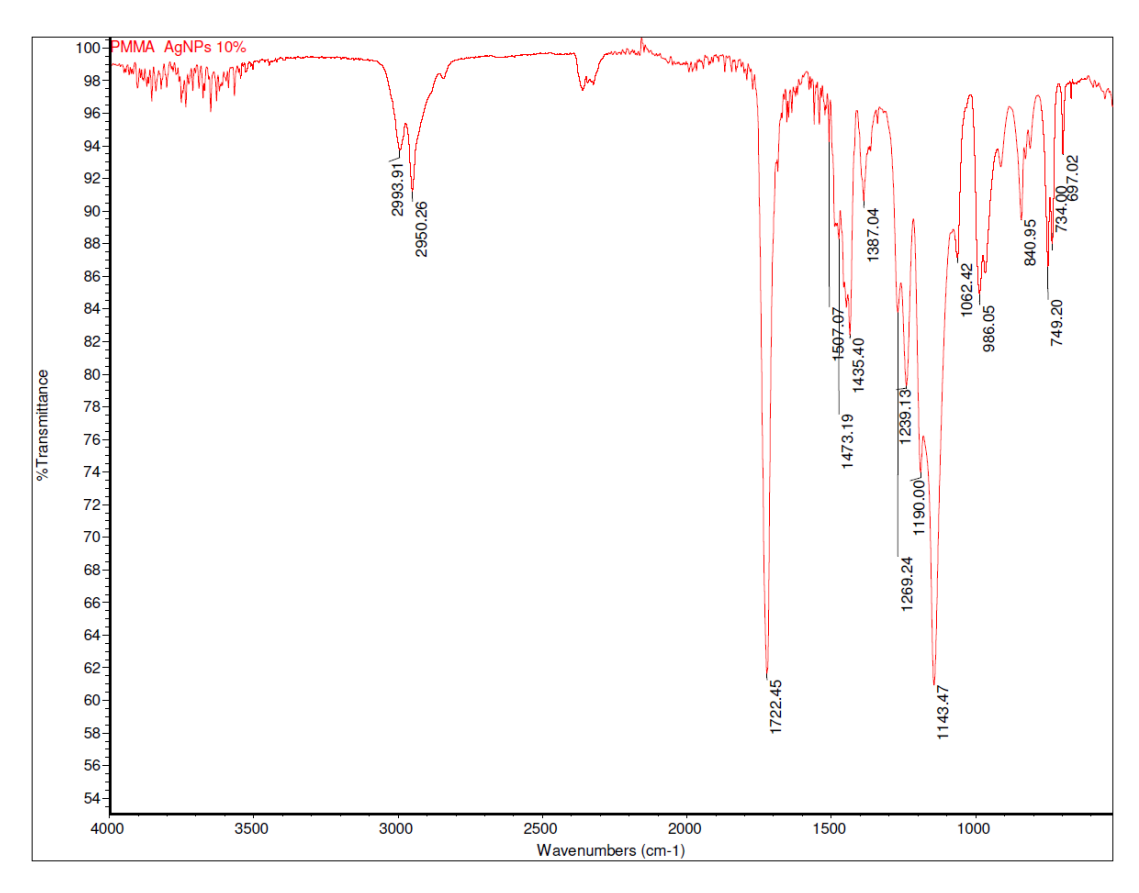


Figure 5.11. FTIR spectrum of AgNR/PMMA nanocomposite containing 10% AgNRs

5.3.5 Novelty and contribution of the work

The work presented in Chapter 5 introduces a novel multi-stage integration strategy for silver nanorods into a polymeric matrix, demonstrating several key innovations over conventional approaches. Firstly, rather than relying on in situ reduction of silver ions within the polymer (which often yields polydisperse spherical particles), this study utilised pre-synthesised, highly anisotropic silver nanorods, optimised under controlled seed-mediated growth [249]. These nanorods were then successfully encapsulated with uniform silica shells, enhancing both their colloidal stability and compatibility with PMMA.

Secondly, the surface modification pathway employed – involving thiol-based ligand exchange using MHA, followed by TEOS-driven silica deposition, and final dispersion within a UV-polymerised PMMA matrix – enabled strong interfacial integration while preserving the plasmonic properties of the nanorods. This approach avoids the use of hazardous reducing agents like hydrazine or DMF and provides an optically

transparent matrix suitable for flexible applications in NIR filtering, sensors, and optical coatings.

Finally, the study introduced systematic control of nanorod loading (2%–10% v/v) within the PMMA, supported by quantitative absorbance and FTIR analyses. The resulting composites demonstrated tuneable NIR absorbance up to 1150 nm, which surpasses values typically reported for random in situ nanoparticle formation in polymers. This combination of morphological control, scalable surface chemistry, and matrix compatibility represents a distinct advancement in the fabrication of metal-polymer nanocomposites, offering a reproducible and safe route to functional NIR-active materials.

5.4 Conclusions and future research directions

The pursuit of developing a nanocomposite comprising silver nanoparticles and polymer materials has yielded a substantial body of knowledge regarding the intricacies of nanoparticle synthesis, surface modification, and their integration into a polymer matrix. The foundational comprehension of metal-polymer nanocomposites, expounded upon in Section 6.1, lays the groundwork for the comprehensive examination of silver nanorod synthesis. Utilising a seed-mediated approach, the study successfully synthesised silver nanorods characterised by distinctive dimensions, which in turn exhibited unique absorbance properties within the near-infrared (NIR) spectrum.

Furthermore, the process of coating these nanorods with silica, as elucidated in Section 6.2.3, marked a pivotal advancement. This encapsulation not only prevented the aggregation of nanoparticles but also facilitated their seamless incorporation into the polymethyl methacrylate (PMMA) matrix. The subsequent creation of the AgNR@SiO₂/PMMA nanocomposite material and its thorough characterisation underscored the potential utility of this nanocomposite in diverse applications.

Optical assessments provided valuable insights into the correlation between the AgNR@SiO₂ content and absorbance intensity. The notable absorbance observed at extended wavelengths, particularly in the case of the 10% loading, accentuates the

applicability of these nanocomposites in specialised domains where such optical characteristics are desired.

In summary, the exploration and discoveries outlined in this chapter demonstrate the capability and potential of silver/polymer nanocomposites within the realm of advanced materials. The meticulous synthesis process, coupled with comprehensive characterisation, opens up promising avenues for future research and potential applications in fields that necessitate enhanced optical, thermal, and mechanical properties. The adaptability of these nanocomposites, combined with opportunities for further refinement, positions them at the forefront of next-generation material development.

The successful development and characterisation of the silver/polymer nanocomposite have laid a solid foundation for numerous avenues of future research and applications. Here are some proposed directions for continued exploration:

- Optimisation of synthesis protocols: While the current synthesis approach has
 yielded promising results, there is always room for refinement. Future works
 could focus on optimising the synthesis conditions to produce silver nanorods
 with even more uniform dimensions, higher yields, and improved stability.
- Exploration of different polymers: While PMMA served as an excellent matrix
 for the current nanocomposite, the exploration of other polymer matrices might
 lead to nanocomposites with distinct and potentially enhanced properties.
 Polymers with different mechanical, thermal, or optical attributes could be
 investigated.
- Functionalisation of nanorods: The current work employed MHA for surface modification. Future research could delve into the use of other functional groups or molecules to modify the surface of the nanorods. This could lead to nanocomposites with tailored properties, catering to specific applications.

Chapter 6 Conclusions

The comprehensive research on the synthesis of silver nanoparticles (AgNPs), with a special emphasis on silver nanorods (AgNRs), presented in this thesis, encapsulates significant advancements in nanoparticle technology through both batch and flow synthesis methods, along with the innovative development of silver/polymer nanocomposites. Each synthesis technique has been meticulously studied to optimise the properties of AgNPs for varied applications, reflecting substantial contributions to the field of nanotechnology.

1. Batch synthesis of silver nanoparticles

The batch synthesis of AgNPs, primarily focusing on the seed-mediated growth approach, was explored extensively. This method involved the nucleation of initial seed particles followed by their growth through the gradual addition of AgNO₃, and a reducing agent in the presence cetyltrimethylammonium bromide (CTAB). The research has effectively demonstrated that the morphology, specifically the aspect ratio and size of AgNRs, can be finely tuned by adjusting the concentration ratios of reagents in the growth solution. Key results have shown that higher aspect ratios, desirable for applications such as plasmonic sensors and optical devices, can be achieved under controlled pH level and concentrations of the capping agent. These findings highlight the critical influence of synthesis conditions on the quality and functionality of nanoparticles. Both methods employed in the batch synthesis were optimised for synthesis of silver nanorods that absorb NIR wavelengths.

Furthermore, the optimal parameters offered the basis for tackling the scalability issues providing a transition into the exploration of continuous flow synthesis as a means to address these challenges.

2. Continuous flow synthesis

The development and optimisation of a continuous flow synthesis method for AgNPs represent a significant advancement in this research. By employing microreactor technology, this method facilitates a more controlled reaction environment, which enhances the reproducibility and scalability of nanoparticle production. Experimental

results from the continuous flow synthesis indicated that anisotropic silver nanoparticles can be synthesised using the reactor designs employed in this project. The ability to maintain constant reaction conditions mitigated the common discrepancies observed in batch reactions, leading to a more consistent quality of nanoparticles. Moreover, the continuous flow methods can offer enhanced efficiency in material usage and energy consumption, aligning with the principles of green chemistry by minimising waste and reducing the environmental footprint of nanoparticle synthesis.

3. Development of silver-polymer nanocomposites

Building on the synthesised AgNRs, the research also explored nanocomposite development, specifically integrating AgNRs into polymethyl methacrylate (PMMA) matrices. This approach aimed to harness the unique properties of AgNRs, including their enhanced optical properties, to improve the functionality of the polymer matrix. The nanocomposites were prepared by embedding silica-coated AgNRs into the PMMA matrix, which provided a stable and dispersed phase of nanoparticles within the polymer. Characterisation of the AgNR/PMMA nanocomposites revealed significant enhancements in their optical absorption properties, particularly in the near-infrared (NIR) region. This is crucial for applications such as NIR shielding materials and advanced photonic devices.

4. Overall project conclusions and comparative evaluation

This project systematically addressed the synthesis of anisotropic silver nanostructures with NIR absorption capabilities, aligning with the demands for spectrally selective materials in defence and photonic applications. A comprehensive comparison between batch and continuous flow synthesis methods revealed distinct advantages and limitations inherent to each approach. Batch synthesis (Chapter 3), while accessible and versatile for parameter screening, was limited by poor reproducibility, batch-to-batch variability, and challenges in scaling. In contrast, continuous flow synthesis (Chapter 4) offered improved control over reaction kinetics, precise tuning of residence time, and scalability — essential for translating laboratory protocols to industrial-level manufacturing. These advantages were particularly

evident in the later optimised flow designs (Designs 5 and 6), where high aspect ratio nanorods with LSPR values exceeding 900 nm were synthesised with reproducibility and control exceeding their batch equivalents.

This research has demonstrated novelty in several aspects: (i) the development of bespoke 3D-printed reactors enabling modular mixing and inline monitoring; (ii) the correlation between reactor geometry, flow regime, and nanoparticle anisotropy; and (iii) the integration of silica-coated Ag nanorods into PMMA to create NIR-absorbing nanocomposites. The early-stage challenges identified in Chapter 1—namely, the difficulty of controlling nanorod aspect ratio, reproducibility of synthesis, and scalability—have been to an extent addressed through this dual-pronged approach. Furthermore, this work provides one of the few detailed comparisons of UV-vis spectra with TEM-derived morphologies for both batch and flow methods, validating LSPR as a reliable proxy for nanoparticle shape control. The integration of flow-synthesised AgNRs into polymers further extends the applicability of the platform, demonstrating the readiness of these materials for advanced infrared absorption applications.

Chapter 7 Future Recommendations

Based on the comprehensive analysis and results obtained from the synthesis of silver nanoparticles (AgNPs), particularly silver nanorods (AgNRs), using both batch and continuous flow methods, as well as the development of silver/polymer nanocomposites, several recommendations can be suggested for future research in this promising area of nanotechnology.

1. Advanced control and optimisation of synthesis parameters

Future studies should be directed towards refining control over the synthesis parameters which influence morphology and functional properties of AgNPs. Much development in the control of these parameters has been achieved, but the subtle interplay of such factors as reactant concentration, , pH, and reaction kinetics provides vast area for exploration. Further research includes exploring the effects of varying the concentrations of silver nitrate, reducing agents, and capping agents in both batch and continuous flow methods.

2. Exploration of new reducing and capping agents

The impact of reducing and capping agents on the quality and functionality of AgNRs has been highlighted in the current research. Exploring new and cost-effective reagents could not only enhance the chemistry aspects of nanoparticle synthesis but also open up new pathways for the synthesis of nanoparticles with unique properties. It would be useful to study green reagents that are environmentally friendly. Bio-based agents derived from plant extracts or biopolymers could offer sustainable alternatives to conventional chemical agents, potentially introducing new functionalities to the nanoparticles.

3. Scale-up considerations for flow synthesis systems

If additional time and resources were available, a major area of future development would focus on designing a continuous flow system capable of true scale-up for industrial production of anisotropic silver nanoparticles. While the modular systems

developed in this study demonstrated reproducibility and tunability on the laboratory scale, further optimisation is needed for larger-scale manufacturing.

A key consideration for scale-up is the transition from millifluidic reactors to mesofluidic or parallelised systems, which maintain the advantages of laminar flow and high surface area-to-volume ratios, while increasing overall throughput. This could involve the parallel integration of multiple modular units, allowing uniform product formation while avoiding the clogging and complexity associated with microfluidic scaling.

Future systems should also incorporate automated feedback control using real-time UV-Vis or inline spectroscopic monitoring to dynamically adjust flow rates and reagent concentrations. This would support consistent product quality under continuous production and allow for real-time process corrections.

Finally, integration with downstream processing, such as inline silica coating, purification, or direct casting into polymer matrices, would represent a significant step toward scalable nanocomposite production. This vision aligns with current trends in flow chemistry for nanomaterials and would enable the translation of lab-scale precision into commercially viable processes.

4. Long-term stability and storage of nanoparticles

The stability of AgNPs, especially in various environmental conditions and over long periods, is critical for their commercial use. Research into the mechanisms of nanoparticle aggregation and sedimentation can lead to better preservation techniques and formulations. Encapsulation or surface modification strategies could be explored to enhance the stability and extend the shelf life of nanoparticle suspensions.

5. Development and testing of AgNP/polymer nanocomposites

While the initial results from the development of AgNR/PMMA nanocomposites are promising, comprehensive testing of these materials under real-world conditions is needed. Future studies should assess the durability, functionality, and environmental impact of these composites. Additionally, exploring a wider range of polymer matrices

and nanoparticle loadings could yield materials with tailored properties for specific applications, such as flexible electronics, or optically active coatings.

6. Environmental and health impact studies

As the application fields for AgNPs expand, so does the need to understand their environmental and health impacts. Future research should include detailed toxicological studies and environmental impact assessments, especially for applications that might lead to direct or indirect human exposure to nanoparticles. Developing guidelines for the safe production, handling, and disposal of nanoparticles is imperative to ensure that the benefits of nanotechnology do not come at an unacceptable cost to health and the environment.

These recommendations aim to build on the current findings and push the boundaries of what is possible with AgNPs, ensuring their safe, effective, and sustainable use across various domains.

Appendix A Details of Flow Synthesis Designs



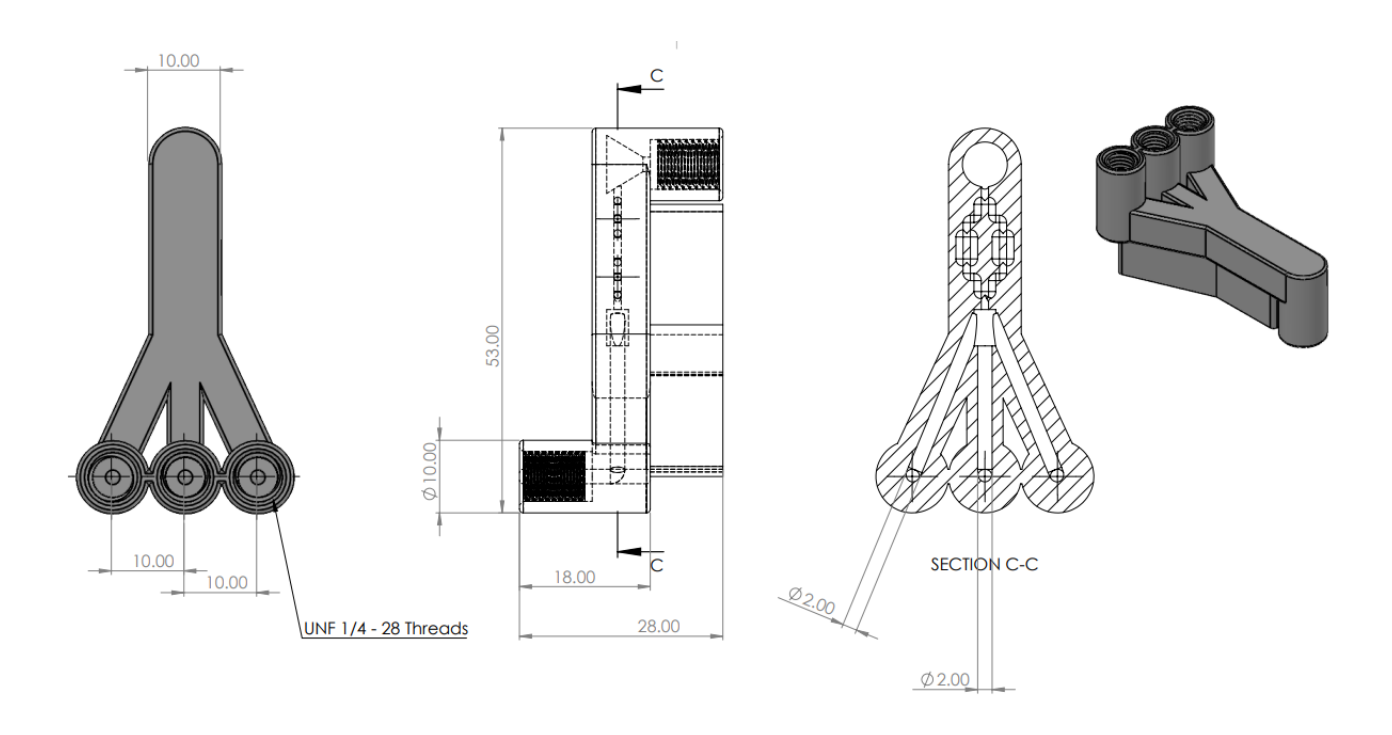
Fitting Material	PEEK	
Connection Type	HPLC/Chromatography	
Thread size UNF(F) (port 1) (in)	1/4-28 Flat Bottom	
Compression Size / Tube Od (Port 2) (in)	1/16	
Compression Size / Tube Od (Port 2) (mm)	1.6	
Color	Natural	
Max Operating Pressure (PSI)	1000	
Orifice Dimensions (mm)	0.5	
Description	Low-Pressure Y Connector Assembly, Natural PEEK, 0.020\" Bore, 1/16\" OD Tubing, 1/4-28 Flat Bottom; 1/EA	

Design 2 reactor



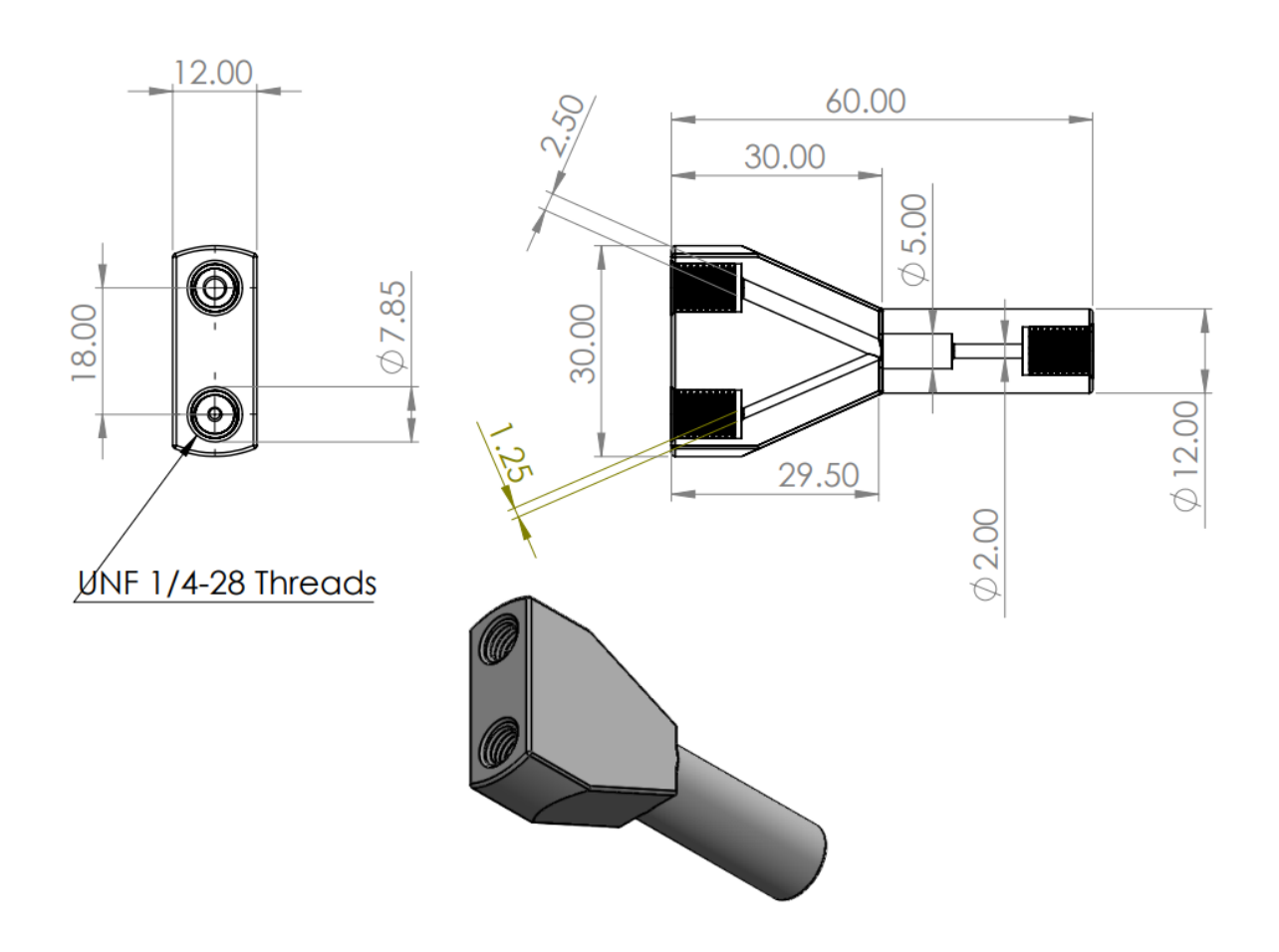
Fitting Material	ETFE	
Connection Type	HPLC/Chromatography	
Thread size UNF(F) (port 1) (in)	1/4-28 Flat Bottom	
Compression Size / Tube Od (Port 2) (in)	1/16	
Compression Size / Tube Od (Port 2) (mm)	1.6	
Color	Natural	
Max Operating Pressure (PSI)	1000	
Orifice Dimensions (mm)	0.5	
Description	Low-Pressure Tee Assembly, Natural ETFE, 0.020\" Bore, 1/16\" OD Tubing, 1/4-28 Flat Bottom; 1/EA	

Design 3 reactor



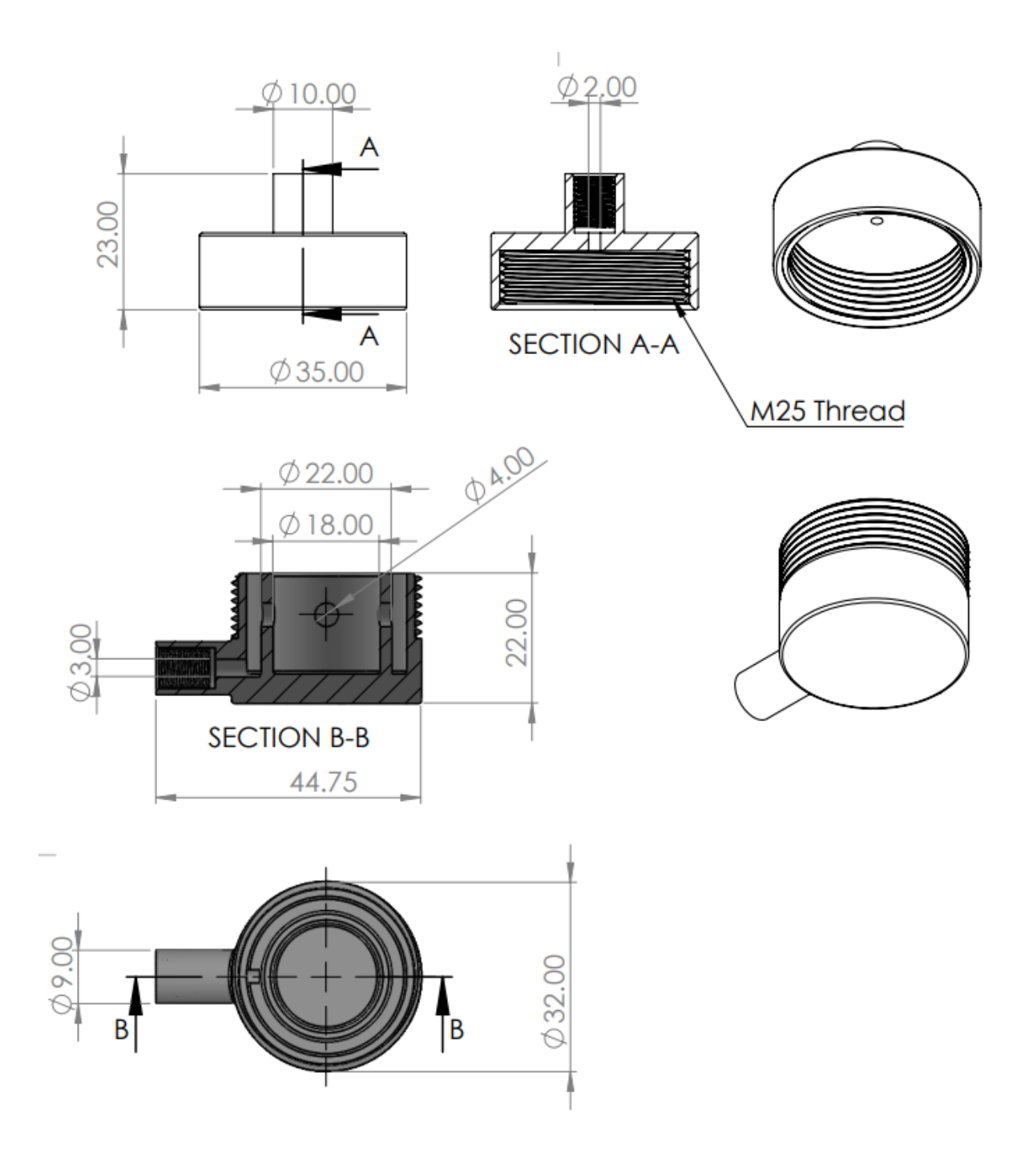
All dimensions in mm

Design 4 reactor



All dimensions in mm

Modular mixing reactor



All dimensions in mm

Publications and Presentations

Publications

- Mughal, B.; Zaidi, S.Z.J.; Zhang, X.; Hassan, S.U. Biogenic Nanoparticles: Synthesis, Characterisation and Applications. *Appl. Sci.* 2021, *11*, 2598. https://doi.org/10.3390/app11062598
- Mughal, B., Zhang, X., Stulz, E.. Optimisng Batch Synthesis of Silver Nanorods for NIR Absorbance using Seed-Mediated Methods. (in draft)
- Mughal, B., Zhang, X., Stulz, E.. Synthesis of Silver Nanorods using flow reactors for NIR Absorbance. (in draft)
- Mughal, B., Zhang, X., Stulz, E.. Development of AgNR/PMMA Nanocomposite for NIR Absorbance. (in draft)

Presentations

- Poster presentation: Development of Silver Nanomaterials for Spectrally Selective Absorption. Dstl Advanced Materials Programme Defence Materials Forum. 8-9th November 2022, Leicester, UK
- Poster presentation: Development of Silver Nanomaterials as Spectrally Selective Absorbers. The 25th International Conference on Miniaturized Systems for Chemistry and Life Sciences (μTAS 2021) 10-14th October 2021, California, USA (Virtual)
- Oral presentation: Development of Silver Nanomaterials as Spectrally Selective Absorbers. Defence Materials Forum. 19th May 2021, Australia (Online)
- Oral presentation: Development of Silver Nanomaterials for Optically
 Active Materials. PGR Conference. 1-3rd September 2020, Southampton, UK
- Poster presentation: Developing Silver Nanoparticle Production for Optically Active Materials. Materials Research Exchange (MRE) 2020. 18-20th February 2020, London, UK
- Poster presentation: Nanocomposite Coatings for Infrared Signature
 Management. Dstl Partnership Event. 11th September 2019, Southampton,
 UK

References

- [1] W. Gutowski and H. Dodiuk, *Nanomaterials and Nanocomposites*. 2014. doi: 10.1201/b16347-22.
- [2] M. Meyyappan, J. Li, J. Li, and A. Cassell, "Nanotechnology: An overview and integration with MEMS," *Proceedings of the IEEE International Conference on Micro Electro Mechanical Systems (MEMS)*, vol. 2006, no. January, pp. 1–3, 2006, doi: 10.1109/memsys.2006.1627721.
- [3] M. Giersig and G. B. Khomutov, *Nanomaterials for Application in Medicine and Biology: Preface*. 2008.
- [4] S. Saallah and I. W. Lenggoro, "Nanoparticles carrying biological molecules: Recent advances and applications," *KONA Powder and Particle Journal*, vol. 2018, no. 35, pp. 89–111, 2018, doi: 10.14356/kona.2018015.
- [5] G. M. Meheretu, D. Cialla, and J. Popp, "Surface Enhanced Raman Spectroscopy on Silver Nanoparticles," *International Journal of Biochemistry and Biophysics*, vol. 2, no. 4, pp. 63–67, 2014, doi: 10.13189/ijbb.2014.020403.
- [6] G. Franci *et al.*, "Silver nanoparticles as potential antibacterial agents," *Molecules*, vol. 20, no. 5, pp. 8856–8874, 2015, doi: 10.3390/molecules20058856.
- [7] Á. L. Mudarra, S. Martínez De Salinas, and M. H. Pérez-Temprano, "Beyond the traditional roles of Ag in catalysis: The transmetalating ability of organosilver(i) species in Pd-catalysed reactions," *Org Biomol Chem*, vol. 17, no. 7, pp. 1655–1667, 2019, doi: 10.1039/c8ob02611d.
- [8] X. Y. Dong, Z. W. Gao, K. F. Yang, W. Q. Zhang, and L. W. Xu, "Nanosilver as a new generation of silver catalysts in organic transformations for efficient synthesis of fine chemicals," *Catal Sci Technol*, vol. 5, no. 5, pp. 2554–2574, 2015, doi: 10.1039/c5cy00285k.
- [9] G. Liao, W. Zhao, Q. Li, Q. Pang, and Z. Xu, "Novel poly (acrylic acid)-modified tourmaline/silver composites for adsorption removal of Cu(II) ions and catalytic reduction of methylene blue in water," *Chem Lett*, vol. 46, no. 11, pp. 1631–1634, 2017, doi: 10.1246/cl.170785.

- [10] Y. Mei *et al.*, "High catalytic activity of platinum nanoparticles immobilized on spherical polyelectrolyte brushes," *Langmuir*, vol. 21, no. 26, pp. 12229–12234, 2005, doi: 10.1021/la052120w.
- [11] Z. Wu et al., "Knitting Aryl Network Polymers-Incorporated Ag Nanoparticles: A Mild and Efficient Catalyst for the Fixation of CO2 as Carboxylic Acid," ACS Sustain Chem Eng, vol. 5, no. 11, pp. 9634–9639, 2017, doi: 10.1021/acssuschemeng.7b02678.
- [12] T. Dang-Bao, D. Pla, I. Favier, and M. Gómez, "Bimetallic nanoparticles in alternative solvents for catalytic purposes," *Catalysts*, vol. 7, no. 7, 2017, doi: 10.3390/catal7070207.
- [13] B. R. Cuenya, "Synthesis and catalytic properties of metal nanoparticles: Size, shape, support, composition, and oxidation state effects," *Thin Solid Films*, vol. 518, no. 12, pp. 3127–3150, 2010, doi: 10.1016/j.tsf.2010.01.018.
- [14] Y. Q. He, S. P. Liu, L. Kong, and Z. F. Liu, "A study on the sizes and concentrations of gold nanoparticles by spectra of absorption, resonance Rayleigh scattering and resonance non-linear scattering," vol. 61, pp. 2861–2866, 2005, doi: 10.1016/j.saa.2004.10.035.
- [15] K. L. Kelly, E. Coronado, L. L. Zhao, and G. C. Schatz, "The optical properties of metal nanoparticles: The influence of size, shape, and dielectric environment," *Journal of Physical Chemistry B*, vol. 107, no. 3, pp. 668–677, 2003, doi: 10.1021/jp026731y.
- [16] and M. S. Ü. Derin Sevenler, Neşe Lortlar Ünlü, "Nanoparticle Biosensing with Interferometric Reflectance Imaging," in *Nanobiosensors and Nanobioanalyses*, no. January, 2015, pp. 1–379. doi: 10.1007/978-4-431-55190-4.
- [17] T. Huang and X. H. N. Xu, "Synthesis and characterization of tunable rainbow colored colloidal silver nanoparticles using single-nanoparticle plasmonic microscopy and spectroscopy," *J Mater Chem*, vol. 20, no. 44, pp. 9867–9876, 2010, doi: 10.1039/c0jm01990a.

- [18] H. Jiang *et al.*, "Butterfly-wing hierarchical metallic glassy nanostructure for surface enhanced Raman scattering," *Nano Res*, vol. 12, no. 11, pp. 2808–2814, 2019, doi: 10.1007/s12274-019-2517-2.
- [19] N. Reznikov, M. Bilton, L. Lari, M. M. Stevens, and R. Kröger, "Fractal-like hierarchical organization of bone begins at the nanoscale," *Science* (1979), vol. 360, no. 6388, 2018, doi: 10.1126/science.aao2189.
- [20] J. E. M. Haverkort, E. C. Garnett, and E. P. A. M. Bakkers, "Fundamentals of the nanowire solar cell: Optimization of the open circuit voltage," *Appl Phys Rev*, vol. 5, no. 3, 2018, doi: 10.1063/1.5028049.
- [21] W. Quispe-Tintaya, "Shaping the Future of Nanomedicine: Anisotropy in Polymeric Nanoparticle Design," *Physiol Behav*, vol. 176, no. 3, pp. 139–148, 2017, doi: 10.1002/wnan.1348.Shaping.
- [22] A. Klug, "The tobacco mosaic virus particle: structure and assembly," *Phil. Trans. R. Soc. Lond. B*, no. 354, pp. 1–6, 1999.
- [23] A. J. Shnoudeh *et al.*, *Synthesis, Characterization, and Applications of Metal Nanoparticles*. Elsevier Inc., 2019. doi: 10.1016/B978-0-12-814427-5.00015-9.
- [24] L. Meng, J. Zhang, H. Li, W. Zhao, and T. Zhao, "Preparation and Progress in Application of Gold Nanorods," *J Nanomater*, vol. 2019, 2019, doi: 10.1155/2019/4925702.
- [25] S. D. Anderson, V. V. Gwenin, and C. D. Gwenin, "Magnetic Functionalized Nanoparticles for Biomedical, Drug Delivery and Imaging Applications," *Nanoscale Res Lett*, vol. 14, 2019, doi: 10.1186/s11671-019-3019-6.
- [26] J. Stone, S. Jackson, and D. Wright, "Biological applications of gold nanorods," *Wiley Interdiscip Rev Nanomed Nanobiotechnol*, vol. 3, no. 1, pp. 100–109, 2011, doi: 10.1002/wnan.120.
- [27] N. G. Khlebtsov and L. A. Dykman, "Optical properties and biomedical applications of plasmonic nanoparticles," *J Quant Spectrosc Radiat Transf*, vol. 111, no. 1, pp. 1–35, 2010, doi: 10.1016/j.jqsrt.2009.07.012.
- [28] J. E. Ortiz-Castillo, R. C. Gallo-Villanueva, M. J. Madou, and V. H. Perez-Gonzalez, "Anisotropic gold nanoparticles: A survey of recent synthetic

- methodologies," *Coord Chem Rev*, vol. 425, p. 213489, 2020, doi: 10.1016/j.ccr.2020.213489.
- [29] W. Quispe-Tintaya, "Shaping the Future of Nanomedicine: Anisotropy in Polymeric Nanoparticle Design," *Physiol Behav*, vol. 176, no. 3, pp. 139–148, 2017, doi: 10.1002/wnan.1348.Shaping.
- [30] B. Wiley, Y. Sun, and Y. Xia, "Synthesis of silver nanostructures with controlled shapes and properties," *Acc Chem Res*, vol. 40, no. 10, pp. 1067–1076, 2007, doi: 10.1021/ar7000974.
- [31] B. RE, *The fundamentals of aircraft combat survivability analysis and design*, 2nd ed. New York: AIAA Education Series, 2003.
- [32] Y. A. Razumova, N. A. Toropov, and A. Tigran, "Chemically synthesized silver nanorods intended for near IR applications," vol. 1067233, no. May 2018, 2019, doi: 10.1117/12.2306852.
- [33] A. K. Ojha, S. Forster, S. Kumar, S. Vats, S. Negi, and I. Fischer, "Synthesis of well dispersed silver nanorods of different aspect ratios and their antimicrobial properties against gram positive and negative bacterial strains," pp. 1–7, 2013.
- [34] P. Merkl *et al.*, "Plasmonic Coupling in Silver Nanoparticle Aggregates and Their Polymer Composite Films for Near Infrared Photothermal Biofilm Eradication," *ACS Appl Nano Mater*, vol. 4, no. 5, pp. 5330–5339, May 2021, doi: 10.1021/acsanm.1c00668.
- [35] L. Jauffred, A. Samadi, H. Klingberg, P. M. Bendix, and L. B. Oddershede, "Plasmonic Heating of Nanostructures," *Chem Rev*, vol. 119, no. 13, pp. 8087–8130, Jul. 2019, doi: 10.1021/acs.chemrev.8b00738.
- [36] K. Wang, C. Wang, Y. Yin, and K. Chen, "Modification of Al pigment with graphene for infrared/visual stealth compatible fabric coating," *J Alloys Compd*, vol. 690, pp. 741–748, 2017, doi: 10.1016/j.jallcom.2016.08.171.
- [37] X. li Chen, C. hui Tian, Z. xin Che, and T. ping Chen, "Selective metamaterial perfect absorber for infrared and 1.54 µm laser compatible stealth technology," *Optik* (*Stuttg*), vol. 172, no. July, pp. 840–846, 2018, doi: 10.1016/j.ijleo.2018.07.091.

- [38] K. E. Andersson and C. Åkerlind, "A review of materials for spectral design coatings in signature management applications," *Optics and Photonics for Counterterrorism, Crime Fighting, and Defence X; and Optical Materials and Biomaterials in Security and Defence Systems Technology XI*, vol. 9253, p. 92530Y, 2014, doi: 10.1117/12.2067167.
- [39] P. L. Suryawanshi, S. P. Gumfekar, B. A. Bhanvase, S. H. Sonawane, and M. S. Pimplapure, "A review on microreactors: Reactor fabrication, design, and cutting-edge applications," *Chem Eng Sci*, vol. 189, pp. 431–448, 2018, doi: 10.1016/j.ces.2018.03.026.
- [40] J. C. Maxwell, P. Trans, and R. S. Lond, "A Dynamical Theory of the Electromagnetic Field," pp. 459–512, 1865, doi: 10.1098/rstl.1865.0008.
- [41] J. Jana, M. Ganguly, and T. Pal, "Enlightening surface plasmon resonance effect of metal nanoparticles for practical spectroscopic application," 2016, *Royal Society of Chemistry*. doi: 10.1039/c6ra14173k.
- [42] G. Heness, "Metal-polymer nanocomposites," in *Advances in Polymer Nanocomposites: Types and Applications*, Woodhead Publishing Limited, 2012, pp. 164–177. doi: 10.1533/9780857096241.1.164.
- [43] E. Petryayeva and U. J. Krull, "Localized surface plasmon resonance: Nanostructures, bioassays and biosensing-A review," 2011, *Elsevier B.V.* doi: 10.1016/j.aca.2011.08.020.
- [44] C. F. Bohren, *Absorption and scattering of light by small particles*. 1983. doi: 10.1088/0031-9112/35/3/025.
- [45] X. Huang, S. Neretina, and M. A. El-Sayed, "Gold nanorods: From synthesis and properties to biological and biomedical applications," *Advanced Materials*, vol. 21, no. 48, pp. 4880–4910, 2009, doi: 10.1002/adma.200802789.
- [46] E. Hutter and J. H. Fendler, "Exploitation of localized surface plasmon resonance," *Advanced Materials*, vol. 16, no. 19, pp. 1685 1706, 2004, doi: 10.1002/adma.200400271.

- [47] J. Cao, T. Sun, and K. T. V. Grattan, "Gold nanorod-based localized surface plasmon resonance biosensors: A review," *Sens Actuators B Chem*, vol. 195, pp. 332–351, 2014, doi: 10.1016/j.snb.2014.01.056.
- [48] C. R. Rekha, V. U. Nayar, and K. G. Gopchandran, "Synthesis of highly stable silver nanorods and their application as SERS substrates," *Journal of Science: Advanced Materials and Devices*, vol. 3, no. 2, pp. 196–205, 2018, doi: 10.1016/j.jsamd.2018.03.003.
- [49] A. J. Frank, N. Cathcart, K. E. Maly, and V. Kitaev, "Synthesis of Silver Nanoprisms with Variable Size and Investigation of Their Optical Properties: A First-Year Undergraduate Experiment Exploring Plasmonic Nanoparticles," *J Chem Educ*, vol. 87, no. 10, pp. 1098–1101, Oct. 2010, doi: 10.1021/ed100166g.
- [50] I. Freestone, N. Meeks, M. Sax, and C. Higgitt, "The Lycurgus Cup A Roman nanotechnology," *Gold Bull*, vol. 40, no. 4, pp. 270–277, 2008, doi: 10.1007/BF03215599.
- [51] G. A. López-Muñoz, J. A. Pescador-Rojas, J. Ortega-Lopez, J. S. Salazar, and J. Abraham Balderas-López, "Thermal diffusivity measurement of spherical gold nanofluids of different sizes/concentrations," *Nanoscale Res Lett*, vol. 7, no. July, 2012, doi: 10.1186/1556-276X-7-423.
- [52] K. M. Mayer and J. H. Hafner, "Localized surface plasmon resonance sensors," *Chem Rev*, vol. 111, no. 6, pp. 3828–3857, 2011, doi: 10.1021/cr100313v.
- [53] M. Hu et al., "Gold nanostructures: Engineering their plasmonic properties for biomedical applications," Chem Soc Rev, vol. 35, no. 11, pp. 1084–1094, 2006, doi: 10.1039/b517615h.
- [54] D. D. E. Jr and G. Chumanov, "Synthesis and Optical Properties of Silver Nanoparticles and Arrays," vol. 29634, pp. 1221–1231, 2005, doi: 10.1002/cphc.200500113.
- [55] N. L. Pacioni, C. D. Borsarelli, V. Rey, and A. V Veglia, *Silver Nanoparticle Applications*, no. May 2016. 2015. doi: 10.1007/978-3-319-11262-6.

- [56] J. M. GL Hornyak, HF Tibbals, J Dutta, *Introduction to nanoscience and nanotechnology*. Taylor & Francis Group, 2008.
- [57] X. F. Zhang, Z. G. Liu, W. Shen, and S. Gurunathan, "Silver nanoparticles: Synthesis, characterization, properties, applications, and therapeutic approaches," *Int J Mol Sci*, vol. 17, no. 9, 2016, doi: 10.3390/ijms17091534.
- [58] S. H. Lee and B. H. Jun, "Silver nanoparticles: Synthesis and application for nanomedicine," 2019. doi: 10.3390/ijms20040865.
- [59] T. M. Tolaymat, A. M. El, A. Genaidy, K. G. Scheckel, T. P. Luxton, and M. Suidan, "Science of the Total Environment An evidence-based environmental perspective of manufactured silver nanoparticle in syntheses and applications: A systematic review and critical appraisal of peer-reviewed scienti fi c papers," Science of the Total Environment, The, vol. 408, no. 5, pp. 999–1006, 2010, doi: 10.1016/j.scitotenv.2009.11.003.
- [60] B. Pietrobon, V. Kitaev, R. V April, V. Re, M. Recei, and V. May, "Photochemical Synthesis of Monodisperse Size-Controlled Silver Decahedral Nanoparticles and Their Remarkable Optical Properties," no. 22, pp. 5186–5190, 2008.
- [61] A. Zielińska, E. Skwarek, A. Zaleska, M. Gazda, and J. Hupka, "Preparation of silver nanoparticles with controlled particle size," in *Procedia Chemistry*, 2009, pp. 1560–1566. doi: 10.1016/j.proche.2009.11.004.
- [62] M. M. Oliveira, D. Ugarte, D. Zanchet, and A. J. G. Zarbin, "Influence of synthetic parameters on the size, structure, and stability of dodecanethiol-stabilized silver nanoparticles," *J Colloid Interface Sci*, vol. 292, no. 2, pp. 429–435, 2005, doi: 10.1016/j.jcis.2005.05.068.
- [63] N. R. Jana, L. Gearheart, and C. J. Murphy, "Wet chemical synthesis of high aspect ratio cylindrical gold nanorods," *Journal of Physical Chemistry B*, vol. 105, no. 19, pp. 4065–4067, 2001, doi: 10.1021/jp0107964.
- [64] N. R. Jana, L. Gearheart, and C. J. Murphy, "Wet chemical synthesis of silver nanorods and nanowires of controllable aspect ratio," *Chemical Communications*, no. 7, pp. 617–618, 2001, doi: 10.1039/b100521i.

- [65] G. Nanorods, B. B. D. Busbee, S. O. Obare, and C. J. Murphy, "An Improved Synthesis of High-Aspect-Ratio Gold Nanorods**," no. 5, pp. 2002–2004, 2003.
- [66] C. J. Murphy *et al.*, "Anisotropic metal nanoparticles: Synthesis, assembly, and optical applications," *Journal of Physical Chemistry B*, vol. 109, no. 29, pp. 13857–13870, 2005, doi: 10.1021/jp0516846.
- [67] G. J. Lee, S. Il Shin, Y. C. Kim, and S. G. Oh, "Preparation of silver nanorods through the control of temperature and pH of reaction medium," *Mater Chem Phys*, vol. 84, no. 2–3, pp. 197–204, 2004, doi: 10.1016/j.matchemphys.2003.11.024.
- [68] T. K. Sau and C. J. Murphy, "Seeded high yield synthesis of short Au nanorods in aqueous solution," *Langmuir*, vol. 20, no. 15, pp. 6414–6420, 2004, doi: 10.1021/la049463z.
- [69] C. Ni, P. A. Hassan, and E. W. Kaler, "Structural characteristics and growth of pentagonal silver nanorods prepared by a surfactant method," *Langmuir*, vol. 21, no. 8, pp. 3334–3337, 2005, doi: 10.1021/la046807c.
- [70] S. Bhattacharya and J. Biswas, "Role of spacer lengths of gemini surfactants in the synthesis of silver nanorods in micellar media," *Nanoscale*, vol. 3, no. 7, pp. 2924–2930, 2011, doi: 10.1039/c1nr10141b.
- [71] N. Garg, C. Scholl, A. Mohanty, and R. Jin, "The role of bromide ions in seeding growth of Au nanorods," *Langmuir*, vol. 26, no. 12, pp. 10271–10276, 2010, doi: 10.1021/la100446q.
- [72] Z. H. Chieng, M. E. Mohyaldinn, Anas. M. Hassan, and H. Bruining, "Experimental Investigation and Performance Evaluation of Modified Viscoelastic Surfactant (VES) as a New Thickening Fracturing Fluid," *Polymers* (*Basel*), vol. 12, no. 7, p. 1470, Jun. 2020, doi: 10.3390/polym12071470.
- [73] N. R. Jana, L. Gearheart, and C. J. Murphy, "Seed-mediated growth approach for shape-controlled synthesis of spheroidal and rod-like gold nanoparticles using a surfactant template," *Advanced Materials*, vol. 13, no. 18, pp. 1389– 1393, 2001, doi: 10.1002/1521-4095(200109)13:18<1389::AID-ADMA1389>3.0.CO;2-F.

- [74] J. Jiu, K. Murai, D. Kim, K. Kim, and K. Suganuma, "Preparation of Ag nanorods with high yield by polyol process," *Mater Chem Phys*, vol. 114, no. 1, pp. 333–338, 2009, doi: 10.1016/j.matchemphys.2008.09.028.
- [75] J. Patarroyo, A. Genç, J. Arbiol, N. G. Bastús, and V. Puntes, "One-pot polyol synthesis of highly monodisperse short green silver nanorods," *Chemical Communications*, vol. 52, no. 73, pp. 10960–10963, 2016, doi: 10.1039/c6cc04796c.
- [76] D. Chen and L. Gao, "Large-scale growth and end-to-end assembly of silver nanorods by PVP-directed polyol process," *J Cryst Growth*, vol. 264, no. 1–3, pp. 216–222, 2004, doi: 10.1016/j.jcrysgro.2003.12.019.
- [77] Y. Sun, Y. Yin, B. T. Mayers, T. Herricks, and Y. Xia, "Uniform silver nanowires synthesis by reducing AgNO3 with ethylene glycol in the presence of seeds and poly(vinyl pyrrolidone)," *Chemistry of Materials*, vol. 14, no. 11, pp. 4736–4745, 2002, doi: 10.1021/cm020587b.
- [78] Y. Sun, B. Mayers, T. Herricks, and Y. Xia, "Polyol synthesis of uniform silver nanowires: A plausible growth mechanism and the supporting evidence," *Nano Lett*, vol. 3, no. 7, pp. 955–960, 2003, doi: 10.1021/nl034312m.
- [79] A. Nekahi, S. P. H. Marashi, and D. H. Fatmesari, "High yield polyol synthesis of round- and sharp-end silver nanowires with high aspect ratio," *Mater Chem Phys*, vol. 184, pp. 130–137, 2016, doi: 10.1016/j.matchemphys.2016.09.033.
- [80] B. Wiley, Y. Sun, and Y. Xia, "Synthesis of silver nanostructures with controlled shapes and properties," *Acc Chem Res*, vol. 40, no. 10, pp. 1067–1076, 2007, doi: 10.1021/ar7000974.
- [81] Z. C. Li, Q. F. Zhou, X. H. He, and K. Feng, "Synthesis of silver nanocubes and nanorods through sodium-bromide-assisted polyol route," *Micro Nano Lett*, vol. 6, no. 4, p. 261, 2011, doi: 10.1049/mnl.2011.0056.
- [82] T. Maiyalagan, "Synthesis, characterization and electrocatalytic activity of silver nanorods towards the reduction of benzyl chloride," *Appl Catal A Gen*, vol. 340, no. 2, pp. 191–195, 2008, doi: 10.1016/j.apcata.2008.02.016.

- [83] C. Chen *et al.*, "Study on the growth mechanism of silver nanorods in the nanowire-seeding polyol process," *Mater Chem Phys*, vol. 107, no. 1, pp. 13–17, 2008, doi: 10.1016/j.matchemphys.2007.06.048.
- [84] Y. Y. Yu, S. S. Chang, C. L. Lee, and C. R. C. Wang, "Gold nanorods: electrochemical synthesis and optical properties," *Journal of Physical Chemistry B*, vol. 101, no. 34, pp. 6661–6664, 1997, doi: 10.1021/jp971656q.
- [85] M. Törnblom and U. Henriksson, "Effect of solubilization of aliphatic hydrocarbons on size and shape of rodlike C16TABr micelles studied by 2H NMR relaxation," *Journal of Physical Chemistry B*, vol. 101, no. 31, pp. 6028– 6035, 1997, doi: 10.1021/jp970899f.
- [86] S. S. Chang, C. W. Shih, C. D. Chen, W. C. Lai, and C. R. C. Wang, "The Shape Transition of Gold Nanorods," *Langmuir*, vol. 15, no. 3, pp. 701–709, 1999, doi: 10.1021/la980929I.
- [87] S. P. Stagon and H. Huang, "Syntheses and applications of small metallic nanorods from solution and physical vapor deposition," *Nanotechnol Rev*, vol. 2, no. 3, pp. 259–267, 2013, doi: 10.1515/ntrev-2013-0001.
- [88] J. J. Zhu, X. H. Liao, X. N. Zhao, and H. Y. Chen, "Preparation of silver nanorods by electrochemical methods," *Mater Lett*, vol. 49, no. 2, pp. 91–95, 2001, doi: 10.1016/S0167-577X(00)00349-9.
- [89] F. Kim, J. H. Song, and P. Yang, "Photochemical synthesis of gold nanorods," *J Am Chem Soc*, vol. 124, no. 48, pp. 14316–14317, 2002, doi: 10.1021/ja028110o.
- [90] T. Placido *et al.*, "Photochemical synthesis of water-soluble gold nanorods: The role of silver in assisting anisotropic growth," *Chemistry of Materials*, vol. 21, no. 18, pp. 4192–4202, 2009, doi: 10.1021/cm900721r.
- [91] Y. Zhou, S. H. Yu, C. Y. Wang, X. G. Li, Y. R. Zhu, and Z. Y. Chen, "A novel ultraviolet irradiation photoreduction technique for the preparation of single-crystal Ag nanorods and Ag dendrites," *Advanced Materials*, vol. 11, no. 10, pp. 850–852, 1999, doi: 10.1002/(SICI)1521-4095(199907)11:10<850::AID-ADMA850>3.0.CO;2-Z.

- [92] J. Zhang, M. R. Langille, and C. A. Mirkin, "Synthesis of silver nanorods by low energy excitation of spherical plasmonic seeds," *Nano Lett*, vol. 11, no. 6, pp. 2495–2498, 2011, doi: 10.1021/nl2009789.
- [93] F. K. Liu, Y. C. Chang, F. H. Ko, and T. C. Chu, "Microwave rapid heating for the synthesis of gold nanorods," *Mater Lett*, vol. 58, no. 3–4, pp. 373–377, 2004, doi: 10.1016/S0167-577X(03)00504-4.
- [94] M. Tsuji, M. Hashimoto, Y. Nishizawa, M. Kubokawa, and T. Tsuji, "Microwave-assisted synthesis of metallic nanostructures in solution," *Chemistry A European Journal*, vol. 11, no. 2, pp. 440–452, 2005, doi: 10.1002/chem.200400417.
- [95] M. Tsuji *et al.*, "The role of adsorption species in the formation of Ag nanostructures by a microwave-polyol route," *Bull Chem Soc Jpn*, vol. 81, no. 3, pp. 393–400, 2008, doi: 10.1246/bcsj.81.393.
- [96] G. Linfeng, M. Chipara, and J. M. Zaleski, "Convenient, rapid synthesis of Ag nanowires," *Chemistry of Materials*, vol. 19, no. 7, pp. 1755–1760, 2007, doi: 10.1021/cm070160a.
- [97] C. A. Foss, G. L. Hornyak, J. A. Stockert, and C. R. Martin, "Optical properties of composite membranes containing arrays of nanoscopic gold cylinders," *Journal of Physical Chemistry*, vol. 96, no. 19, pp. 7497–7499, 1992, doi: 10.1021/j100198a004.
- [98] L. Vigderman, B. P. Khanal, and E. R. Zubarev, "Functional gold nanorods: Synthesis, self-assembly, and sensing applications," *Advanced Materials*, vol. 24, no. 36, pp. 4811–4841, 2012, doi: 10.1002/adma.201201690.
- [99] B. M. I. van der Zande, M. R. Bohmer, L. G. Fokkink, and C. Schonenberger, "Aqueous gold sols of rod-shaped particles," *Journal of Physical Chemistry B*, vol. 101, no. 6, pp. 852–854, 1997, doi: 10.1021/jp963348i.
- [100] J. C. Hulteen, "A general template-based method for the preparation of nanomaterials," *J Mater Chem*, vol. 7, no. 7, pp. 1075–1087, 1997, doi: 10.1039/a700027h.

- [101] V. M. Cepak et al., "Fabrication and characterization of concentric-tubular composite micro- and nanostructures using the template-synthesis method," J Mater Res, vol. 13, no. 11, pp. 3070–3080, Nov. 1998, doi: 10.1557/JMR.1998.0419.
- [102] G. Sauer *et al.*, "Highly ordered monocrystalline silver nanowire arrays," *J Appl Phys*, vol. 91, no. 5, pp. 3243–3247, Mar. 2002, doi: 10.1063/1.1435830.
- [103] X. Li *et al.*, "Controllable synthesis of Ag nanorods using a porous anodic aluminum oxide template," *Appl Surf Sci*, vol. 255, no. 17, pp. 7529–7531, 2009, doi: 10.1016/j.apsusc.2009.04.020.
- [104] Y. Shi, L. Lv, and H. Wang, "A facile approach to synthesize silver nanorods capped with sodium tripolyphosphate," *Mater Lett*, vol. 63, no. 30, pp. 2698–2700, 2009, doi: 10.1016/j.matlet.2009.09.046.
- [105] J. Zhou, G. Zhou, R. Wang, and M. Lu, "Synthesis in aqueous phase and characterization of silver nanorods and nanowires," *Materials Science- Poland*, vol. 27, no. 1, pp. 73–78, 2009.
- [106] K. K. Caswell, C. M. Bender, and C. J. Murphy, "Seedless, surfactantless wet chemical synthesis of silver nanowires," *Nano Lett*, vol. 3, no. 5, pp. 667–669, 2003, doi: 10.1021/nl0341178.
- [107] Z. Wang, J. Liu, X. Chen, J. Wan, and Y. Qian, "A simple hydrothermal route to large-scale synthesis of uniform silver nanowires," *Chemistry A European Journal*, vol. 11, no. 1, pp. 160–163, 2005, doi: 10.1002/chem.200400705.
- [108] J. Xu, J. Hu, C. Peng, H. Liu, and Y. Hu, "A simple approach to the synthesis of silver nanowires by hydrothermal process in the presence of gemini surfactant," *J Colloid Interface Sci*, vol. 298, no. 2, pp. 689–693, 2006, doi: 10.1016/j.jcis.2005.12.047.
- [109] H. G. Scheibel and J. Porstendörfer, "Generation of monodisperse Ag- and NaCl-aerosols with particle diameters between 2 and 300 nm," *J Aerosol Sci*, vol. 14, no. 2, pp. 113–126, 1983, doi: 10.1016/0021-8502(83)90035-6.
- [110] J. H. Jung, H. Cheol Oh, H. Soo Noh, J. H. Ji, and S. Soo Kim, "Metal nanoparticle generation using a small ceramic heater with a local heating area,"

- *J Aerosol Sci*, vol. 37, no. 12, pp. 1662–1670, 2006, doi: 10.1016/j.jaerosci.2006.09.002.
- [111] M. H. Magnusson, K. Deppert, J. Malm, J. Bovin, and L. Samuelson, "<JNanopartRes_1999_v1_n2_p243-251_Magnusson.pdf>," pp. 243–251, 1999.
- [112] A. S. Gurav, T. T. Kodas, L.-M. Wang, E. I. Kauppinen, and J. Joutsensaari, "Generation of nanometer-size fullerene particles via vapor condensation," *Chem Phys Lett*, vol. 218, no. 4, pp. 304–308, Feb. 1994, doi: 10.1016/0009-2614(93)E1491-X.
- [113] M. Procházka, J. Štěpánek, B. Vlčková, I. Srnová, and P. Malý, "Laser ablation: Preparation of 'chemically pure' Ag colloids for surface-enhanced Raman scattering spectroscopy," *J Mol Struct*, vol. 410–411, no. 96, pp. 213–216, 1997, doi: 10.1016/S0022-2860(96)09467-7.
- [114] R. C. Issac *et al.*, "Dynamics of laser produced silver plasma under film deposition conditions studied using optical emission spectroscopy," *Appl Surf Sci*, vol. 125, no. 2, pp. 227–235, 1998, doi: 10.1016/S0169-4332(97)00415-7.
- [115] A. L. Stepanov, D. E. Hole, A. A. Bukharaev, P. D. Townsend, and N. I. Nurgazizov, "Reduction of the size of the implanted silver nanoparticles in float glass during excimer laser annealing," *Appl Surf Sci*, vol. 136, no. 4, pp. 298–305, 1998, doi: 10.1016/S0169-4332(98)00349-3.
- [116] S. Kim *et al.*, "Catalytic effect of laser ablated Ni nanoparticles in the oxidative addition reaction for a coupling reagent of benzylchloride and bromoacetonitrile," *J Mol Catal A Chem*, vol. 226, no. 2, pp. 231–234, 2005, doi: 10.1016/j.molcata.2004.10.038.
- [117] M. Kawasaki and N. Nishimura, "1064-nm laser fragmentation of thin Au and Ag flakes in acetone for highly productive pathway to stable metal nanoparticles," Appl Surf Sci, vol. 253, no. 4, pp. 2208–2216, 2006, doi: 10.1016/j.apsusc.2006.04.024.
- [118] A. H. Hamad, "Effects of Different Laser Pulse Regimes (Nanosecond, Picosecond and Femtosecond) on the Ablation of Materials for Production of

- Nanoparticles in Liquid Solution," in *High Energy and Short Pulse Lasers*, 2016. doi: 10.5772/63892.
- [119] S. Zhang, Z. Liang, W. Hang, Z. Yang, B. Yu, and W. Wang, "Comparison of nanosecond and femtosecond laser-induced tip-enhanced ablations by experimental and theoretical methods," *Nucl Instrum Methods Phys Res B*, vol. 440, no. December 2018, pp. 146–155, 2019, doi: 10.1016/j.nimb.2018.12.025.
- [120] R. Anugrahwidya, N. Yudasari, and D. Tahir, "Optical and structural investigation of synthesis ZnO/Ag Nanoparticles prepared by laser ablation in liquid," *Mater Sci Semicond Process*, vol. 105, no. August 2019, 2020, doi: 10.1016/j.mssp.2019.104712.
- [121] J. Simon, V. P. N. Nampoori, and M. Kailasnath, "Facile synthesis of Au-Ag core shell and nanoalloy using femtosecond laser ablation and their optical characterization," *Optik (Stuttg)*, vol. 195, no. May, p. 163168, 2019, doi: 10.1016/j.ijleo.2019.163168.
- [122] M. Malekzadeh, K. L. Yeung, M. Halali, and Q. Chang, "Synthesis of nanostructured Ag@SiO2-Penicillin from high purity Ag NPs prepared by electromagnetic levitation melting process," *Materials Science and Engineering* C, vol. 102, no. December 2018, pp. 616–622, 2019, doi: 10.1016/j.msec.2019.04.083.
- [123] M. Elango, M. Deepa, R. Subramanian, and G. Saraswathy, "Synthesis, structural characterization and antimicrobial activities of polyindole stabilized Ag-Co3O4nanocomposite by reflux condensation method," *Mater Chem Phys*, vol. 216, no. August 2017, pp. 305–315, 2018, doi: 10.1016/j.matchemphys.2018.05.049.
- [124] A. G. El-Shamy, W. M. Attia, and K. M. Abd El Kader, "Enhancement of the conductivity and dielectric properties of PVA/Ag nanocomposite films using γ irradiation," *Mater Chem Phys*, vol. 191, pp. 225–229, 2017, doi: 10.1016/j.matchemphys.2017.01.026.
- [125] M. E. Koleva et al., "Laser-assisted approach for synthesis of plasmonic Ag/ZnO nanostructures," Superlattices Microstruct, vol. 109, pp. 886–896, 2017, doi: 10.1016/j.spmi.2017.06.007.

- [126] Q. Xiao, Z. Yao, J. Liu, R. Hai, H. Y. Oderji, and H. Ding, "Synthesis and characterization of Ag-Ni bimetallic nanoparticles by laser-induced plasma," Thin Solid Films, vol. 519, no. 20, pp. 7116–7119, 2011, doi: 10.1016/j.tsf.2011.04.201.
- [127] S. Iravani, H. Korbekandi, S. V Mirmohammadi, and B. Zolfaghari, "Synthesis of silver nanoparticles: Chemical, physical and biological methods," 2014.
- [128] M. Zhang, K. Zhang, B. De Gusseme, W. Verstraete, and R. Field, "The antibacterial and anti-biofouling performance of biogenic silver nanoparticles by Lactobacillus fermentum," *Biofouling*, vol. 30, no. 3, pp. 347–357, 2014, doi: 10.1080/08927014.2013.873419.
- [129] S. Priyadarshini, V. Gopinath, N. M. Priyadharsshini, D. Mubarakali, and P. Velusamy, "Colloids and Surfaces B: Biointerfaces Synthesis of anisotropic silver nanoparticles using novel strain, Bacillus flexus and its biomedical application," *Colloids Surf B Biointerfaces*, vol. 102, pp. 232–237, 2013, doi: 10.1016/j.colsurfb.2012.08.018.
- [130] S. Gurunathan *et al.*, "Biosynthesis, purification and characterization of silver nanoparticles using Escherichia coli," *Colloids Surf B Biointerfaces*, vol. 74, no. 1, pp. 328–335, 2009, doi: 10.1016/j.colsurfb.2009.07.048.
- [131] S. Sadhasivam, P. Shanmugam, and K. S. Yun, "Biosynthesis of silver nanoparticles by Streptomyces hygroscopicus and antimicrobial activity against medically important pathogenic microorganisms," *Colloids Surf B Biointerfaces*, vol. 81, no. 1, pp. 358–362, 2010, doi: 10.1016/j.colsurfb.2010.07.036.
- [132] M. A. Shenashen, S. A. El-safty, and E. A. Elshehy, "Synthesis, Morphological Control, and Properties of Silver Nanoparticles in Potential Applications," pp. 293–316, 2014, doi: 10.1002/ppsc.201300181.
- [133] S. Iravani, "Green synthesis of metal nanoparticles using plants," 2011. doi: 10.1039/c1gc15386b.
- [134] A. R. Vilchis-Nestor, V. Sánchez-Mendieta, M. A. Camacho-López, R. M. Gómez-Espinosa, M. A. Camacho-López, and J. A. Arenas-Alatorre, "Solventless synthesis and optical properties of Au and Ag nanoparticles using

- Camellia sinensis extract," *Mater Lett*, vol. 62, no. 17–18, pp. 3103–3105, 2008, doi: 10.1016/j.matlet.2008.01.138.
- [135] N. A. Begum, S. Mondal, S. Basu, R. A. Laskar, and D. Mandal, "Biogenic synthesis of Au and Ag nanoparticles using aqueous solutions of Black Tea leaf extracts," *Colloids Surf B Biointerfaces*, vol. 71, no. 1, pp. 113–118, 2009, doi: 10.1016/j.colsurfb.2009.01.012.
- [136] P. L. Suryawanshi, S. P. Gumfekar, B. A. Bhanvase, S. H. Sonawane, and M. S. Pimplapure, "A review on microreactors: Reactor fabrication, design, and cutting-edge applications," *Chem Eng Sci*, vol. 189, pp. 431–448, Nov. 2018, doi: 10.1016/j.ces.2018.03.026.
- [137] R. L. Hartman, J. P. McMullen, and K. F. Jensen, "Deciding whether to go with the flow: Evaluating the merits of flow reactors for synthesis," *Angewandte Chemie - International Edition*, vol. 50, no. 33, pp. 7502–7519, 2011, doi: 10.1002/anie.201004637.
- [138] E. A. Mansur, M. YE, Y. WANG, and Y. DAI, "A State-of-the-Art Review of Mixing in Microfluidic Mixers," *Chin J Chem Eng*, vol. 16, no. 4, pp. 503–516, 2008, doi: 10.1016/S1004-9541(08)60114-7.
- [139] V. Sans, L. Porwol, V. Dragone, and L. Cronin, "A self optimizing synthetic organic reactor system using real-time in-line NMR spectroscopy," *Chem Sci*, vol. 6, no. 2, pp. 1258–1264, 2015, doi: 10.1039/c4sc03075c.
- [140] C. J. Richmond et al., "A flow-system array for the discovery and scale up of inorganic clusters," Nat Chem, vol. 4, no. 12, pp. 1037–1043, 2012, doi: 10.1038/nchem.1489.
- [141] B. G. Zukas and N. R. Gupta, "Interphase Synthesis of Zinc Oxide Nanoparticles in a Droplet Flow Reactor," *Ind Eng Chem Res*, vol. 56, no. 25, pp. 7184–7191, Jun. 2017, doi: 10.1021/acs.iecr.7b00407.
- [142] H. Huang *et al.*, "Continuous flow synthesis of ultrasmall gold nanoparticles in a microreactor using trisodium citrate and their SERS performance," *Chem Eng Sci*, vol. 189, pp. 422–430, Nov. 2018, doi: 10.1016/j.ces.2018.06.050.

- [143] N. T. K. Thanh, N. Maclean, and S. Mahiddine, "Mechanisms of Nucleation and Growth of Nanoparticles in Solution," *Chem Rev*, vol. 114, no. 15, pp. 7610– 7630, Aug. 2014, doi: 10.1021/cr400544s.
- [144] R. L. Hartman and K. F. Jensen, "Microchemical systems for continuous-flow synthesis," *Lab Chip*, vol. 9, no. 17, p. 2495, 2009, doi: 10.1039/b906343a.
- [145] A. M. Nightingale and J. C. deMello, "Segmented Flow Reactors for Nanocrystal Synthesis," *Advanced Materials*, vol. 25, no. 13, pp. 1813–1821, Apr. 2013, doi: 10.1002/adma.201203252.
- [146] C.-Y. Lee, C.-L. Chang, Y.-N. Wang, and L.-M. Fu, "Microfluidic Mixing: A Review," Int J Mol Sci, vol. 12, no. 5, pp. 3263–3287, May 2011, doi: 10.3390/ijms12053263.
- [147] C. N. R. Rao, G. U. Kulkarni, P. J. Thomas, and P. P. Edwards, "Metal nanoparticles and their assemblies," *Chem Soc Rev*, vol. 29, no. 1, pp. 27–35, 2000, doi: 10.1039/a904518j.
- [148] A. Jahn, J. E. Reiner, W. N. Vreeland, D. L. DeVoe, L. E. Locascio, and M. Gaitan, "Preparation of nanoparticles by continuous-flow microfluidics," *Journal of Nanoparticle Research*, vol. 10, no. 6, pp. 925–934, 2008, doi: 10.1007/s11051-007-9340-5.
- [149] J. Boleininger, A. Kurz, V. Reuss, and C. Sönnichsen, "Microfluidic continuous flow synthesis of rod-shaped gold and silver nanocrystals," *Physical Chemistry Chemical Physics*, vol. 8, no. 33, pp. 3824–3827, 2006, doi: 10.1039/b604666e.
- [150] X. Z. Lin, A. D. Terepka, and H. Yang, "Synthesis of silver nanoparticles in a continuous flow tubular microreactor," *Nano Lett*, vol. 4, no. 11, pp. 2227–2232, 2004, doi: 10.1021/nl0485859.
- [151] J. B. Edel, R. Fortt, J. C. DeMello, and A. J. DeMello, "Microfluidic routes to the controlled production of nanoparticles," *Chemical Communications*, vol. 2, no. 10, pp. 1136–1137, 2002, doi: 10.1039/b202998g.
- [152] J. Wagner, T. Kirner, G. Mayer, J. Albert, and J. M. Köhler, "Generation of metal nanoparticles in a microchannel reactor," *Chemical Engineering Journal*, vol. 101, no. 1–3, pp. 251–260, 2004, doi: 10.1016/j.cej.2003.11.021.

- [153] J. Wagner and J. M. Köhler, "Continuous synthesis of gold nanoparticles in a microreactor," *Nano Lett*, vol. 5, no. 4, pp. 685–691, Apr. 2005, doi: 10.1021/nl050097t.
- [154] A. Singh, M. Shirolkar, N. P. Lalla, C. K. Malek, and S. K. Kulkarni, "Room temperature, water-based, microreactor synthesis of gold and silver nanoparticles," *Int J Nanotechnol*, vol. 6, no. 5–6, pp. 541–551, 2009, doi: 10.1504/IJNT.2009.024645.
- [155] D. Jeevarathinam, A. K. Gupta, B. Pitchumani, and R. Mohan, "Effect of gas and liquid flowrates on the size distribution of barium sulfate nanoparticles precipitated in a two phase flow capillary microreactor," *Chemical Engineering Journal*, vol. 173, no. 2, pp. 607–611, 2011, doi: 10.1016/j.cej.2011.08.010.
- [156] H. Liu *et al.*, "Microfluidic biosynthesis of silver nanoparticles: Effect of process parameters on size distribution," *Chemical Engineering Journal*, vol. 209, pp. 568–576, Oct. 2012, doi: 10.1016/j.cej.2012.08.049.
- [157] M. Jiao, J. Zeng, L. Jing, C. Liu, and M. Gao, "Flow Synthesis of Biocompatible Fe 3 O 4 Nanoparticles: Insight into the Effects of Residence Time, Fluid Velocity, and Tube Reactor Dimension on Particle Size Distribution," *Chemistry of Materials*, vol. 27, no. 4, pp. 1299–1305, Feb. 2015, doi: 10.1021/cm504313c.
- [158] J. Sui, J. Yan, D. Liu, K. Wang, and G. Luo, "Continuous Synthesis of Nanocrystals via Flow Chemistry Technology," *Small*, vol. 16, no. 15, Apr. 2020, doi: 10.1002/smll.201902828.
- [159] A.-G. Niculescu, C. Chircov, A. C. Bîrcă, and A. M. Grumezescu, "Nanomaterials Synthesis through Microfluidic Methods: An Updated Overview," *Nanomaterials*, vol. 11, no. 4, p. 864, Mar. 2021, doi: 10.3390/nano11040864.
- [160] B. G. Zukas and N. R. Gupta, "Interphase Synthesis of Zinc Oxide Nanoparticles in a Droplet Flow Reactor," *Ind Eng Chem Res*, vol. 56, no. 25, pp. 7184–7191, Jun. 2017, doi: 10.1021/acs.iecr.7b00407.
- [161] X. Zhao *et al.*, "Microwave-assisted synthesis of silver nanoparticles using sodium alginate and their antibacterial activity," *Colloids Surf A Physicochem Eng Asp*, vol. 444, pp. 180–188, Mar. 2014, doi: 10.1016/j.colsurfa.2013.12.008.

- [162] B. Nikoobakht and M. A. El-Sayed, "Preparation and Growth Mechanism of Gold Nanorods (NRs) Using Seed-Mediated Growth Method," *Chemistry of Materials*, vol. 15, no. 10, pp. 1957–1962, May 2003, doi: 10.1021/cm020732I.
- [163] Z. M. Xiu, Q. B. Zhang, H. L. Puppala, V. L. Colvin, and P. J. J. Alvarez, "Negligible particle-specific antibacterial activity of silver nanoparticles," *Nano Lett*, vol. 12, no. 8, pp. 4271–4275, 2012, doi: 10.1021/nl301934w.
- [164] S. Pal, Y. K. Tak, and J. M. Song, "Does the antibacterial activity of silver nanoparticles depend on the shape of the nanoparticle? A study of the gramnegative bacterium Escherichia coli," *Appl Environ Microbiol*, vol. 73, no. 6, pp. 1712–1720, 2007, doi: 10.1128/AEM.02218-06.
- [165] J. Helmlinger *et al.*, "Silver nanoparticles with different size and shape: Equal cytotoxicity, but different antibacterial effects," *RSC Adv*, vol. 6, no. 22, pp. 18490–18501, 2016, doi: 10.1039/c5ra27836h.
- [166] S. Agnihotri, S. Mukherji, and S. Mukherji, "Size-controlled silver nanoparticles synthesized over the range 5-100 nm using the same protocol and their antibacterial efficacy," *RSC Adv*, vol. 4, no. 8, pp. 3974–3983, 2014, doi: 10.1039/c3ra44507k.
- [167] R. Qin, G. Li, L. Pan, Q. Han, Y. Sun, and Q. He, "Preparation of SiO 2 @Ag Composite Nanoparticles and Their Antimicrobial Activity," *J Nanosci Nanotechnol*, vol. 17, no. 4, pp. 2305–2311, Apr. 2017, doi: 10.1166/jnn.2017.13042.
- [168] Y. Zhou *et al.*, "PLLA microcapsules combined with silver nanoparticles and chlorhexidine acetate showing improved antibacterial effect," *Materials Science and Engineering C*, vol. 78, pp. 349–353, 2017, doi: 10.1016/j.msec.2017.04.100.
- [169] S. Chen, Y. Quan, Y. L. Yu, and J. H. Wang, "Graphene Quantum Dot/Silver Nanoparticle Hybrids with Oxidase Activities for Antibacterial Application," ACS Biomater Sci Eng, vol. 3, no. 3, pp. 313–321, 2017, doi: 10.1021/acsbiomaterials.6b00644.

- [170] M. Kujda *et al.*, "Charge stabilized silver nanoparticles applied as antibacterial agents," *J Nanosci Nanotechnol*, vol. 15, no. 5, pp. 3574–3583, 2015, doi: 10.1166/jnn.2015.9727.
- [171] M. Meng, H. He, J. Xiao, P. Zhao, J. Xie, and Z. Lu, "Controllable in situ synthesis of silver nanoparticles on multilayered film-coated silk fibers for antibacterial application," *J Colloid Interface Sci*, vol. 461, pp. 369–375, 2016, doi: 10.1016/j.jcis.2015.09.038.
- [172] R. Yamada *et al.*, "Ag nanoparticle–coated zirconia for antibacterial prosthesis," *Materials Science and Engineering C*, vol. 78, pp. 1054–1060, 2017, doi: 10.1016/j.msec.2017.04.149.
- [173] J. Z. Guo, H. Cui, W. Zhou, and W. Wang, "Ag nanoparticle-catalyzed chemiluminescent reaction between luminol and hydrogen peroxide," *J Photochem Photobiol A Chem*, vol. 193, no. 2–3, pp. 89–96, 2008, doi: 10.1016/j.jphotochem.2007.04.034.
- [174] C. B. Wang, G. Deo, and I. E. Wachs, "Interaction of Polycrystalline Silver with Oxygen, Water, Carbon Dioxide, Ethylene, and Methanol: In Situ Raman and Catalytic Studies," *Journal of Physical Chemistry B*, vol. 103, no. 27, pp. 5645–5656, 1999, doi: 10.1021/jp984363I.
- [175] Z. J. Jiang, C. Y. Liu, and L. W. Sun, "Catalytic properties of silver nanoparticles supported on silica spheres," *Journal of Physical Chemistry B*, vol. 109, no. 5, pp. 1730–1735, 2005, doi: 10.1021/jp046032g.
- [176] T. Kamal, I. Ahmad, S. B. Khan, and A. M. Asiri, "Synthesis and catalytic properties of silver nanoparticles supported on porous cellulose acetate sheets and wet-spun fibers," *Carbohydr Polym*, vol. 157, pp. 294–302, 2017, doi: 10.1016/j.carbpol.2016.09.078.
- [177] R. Mout, D. F. Moyano, S. Rana, and V. M. Rotello, "Surface functionalization of nanoparticles for nanomedicine," *Chem Soc Rev*, vol. 41, no. 7, pp. 2539– 2544, 2012, doi: 10.1039/c2cs15294k.
- [178] H. Liao and J. H. Hafner, "Gold nanorod bioconjugates," *Chemistry of Materials*, vol. 17, no. 18, pp. 4636–4641, 2005, doi: 10.1021/cm050935k.

- [179] D. Pissuwan, S. M. Valenzuela, M. C. Killingsworth, X. Xu, and M. B. Cortie, "Targeted destruction of murine macrophage cells with bioconjugated gold nanorods," *Journal of Nanoparticle Research*, vol. 9, no. 6, pp. 1109–1124, 2007, doi: 10.1007/s11051-007-9212-z.
- [180] H. Takahashi, Y. Niidome, and S. Yamada, "Controlled release of plasmid DNA from gold nanorods induced by pulsed near-infrared light," *Chemical Communications*, no. 17, pp. 2247–2249, 2005, doi: 10.1039/b500337g.
- [181] J. Chen et al., "Gold nanocages: Bioconjugation and their potential use as optical imaging contrast agents," Nano Lett, vol. 5, no. 3, pp. 473–477, 2005, doi: 10.1021/nl047950t.
- [182] H. Liao, C. L. Nehl, and J. H. Hafner, "Biomedical applications of plasmon resonant metal nanoparticles," *Nanomedicine*, vol. 1, no. 2, pp. 201–208, Aug. 2006, doi: 10.2217/17435889.1.2.201.
- [183] A. K. Salem, P. C. Searson, and K. W. Leong, "Multifunctional nanorods for gene delivery," *Nat Mater*, vol. 2, no. 10, pp. 668–671, 2003, doi: 10.1038/nmat974.
- [184] M. Hu et al., "Gold nanostructures: Engineering their plasmonic properties for biomedical applications," Chem Soc Rev, vol. 35, no. 11, pp. 1084–1094, 2006, doi: 10.1039/b517615h.
- [185] S. E. Skrabalak *et al.*, "Gold nanocages: Synthesis, properties, and applications," *Acc Chem Res*, vol. 41, no. 12, pp. 1587–1595, 2008, doi: 10.1021/ar800018v.
- [186] M. Hu *et al.*, "Ultrafast laser studies of the photothermal properties of gold nanocages," *Journal of Physical Chemistry B*, vol. 110, no. 4, pp. 1520–1524, 2006, doi: 10.1021/jp0571628.
- [187] X. Huang, I. H. El-Sayed, W. Qian, and M. A. El-Sayed, "Cancer cell imaging and photothermal therapy in the near-infrared region by using gold nanorods," *J Am Chem Soc*, vol. 128, no. 6, pp. 2115–2120, 2006, doi: 10.1021/ja057254a.
- [188] A. R. Lowery, A. M. Gobin, E. S. Day, N. J. Halas, and J. L. West, "Immunonanoshells for targeted photothermal ablation of tumor cells," *Int J*

- *Nanomedicine*, vol. 1, no. 2, pp. 149–154, 2006, doi: 10.2147/nano.2006.1.2.149.
- [189] X. Huang, I. H. El-Sayed, W. Qian, and M. A. El-Sayed, "Cancer cell imaging and photothermal therapy in the near-infrared region by using gold nanorods," *J Am Chem Soc*, vol. 128, no. 6, pp. 2115–2120, 2006, doi: 10.1021/ja057254a.
- [190] H. Wang *et al.*, "In vitro and in vivo two-photon luminescence imaging of single gold nanorods," *Proc Natl Acad Sci U S A*, vol. 102, no. 44, pp. 15752–15756, 2005, doi: 10.1073/pnas.0504892102.
- [191] N. J. Durr, T. Larson, D. K. Smith, B. A. Korgel, K. Sokolov, and A. Ben-Yakar, "Two-photon luminescence imaging of cancer cells using molecularly targeted gold nanorods," *Nano Lett*, vol. 7, no. 4, pp. 941–945, 2007, doi: 10.1021/nl062962v.
- [192] K. C. Black *et al.*, "Gold nanorods targeted to delta opioid receptor: Plasmon-resonant contrast and photothermal agents," *Mol Imaging*, vol. 7, no. 1, pp. 50–57, 2008, doi: 10.2310/7290.2008.0007.
- [193] J. Q. Hu *et al.*, "A Simple and Effective Route for the Synthesis of Crystalline Silver Nanorods and Nanowires," *Adv Funct Mater*, vol. 14, no. 2, pp. 183–189, 2004, doi: 10.1002/adfm.200304421.
- [194] C. J. Orendorff, A. Gole, T. K. Sau, and C. J. Murphy, "Surface-enhanced Raman spectroscopy of self-assembled monolayers: Sandwich architecture and nanoparticle shape dependence," *Anal Chem*, vol. 77, no. 10, pp. 3261–3266, 2005, doi: 10.1021/ac048176x.
- [195] Y. Yang, S. Matsubara, L. Xiong, T. Hayakawa, and M. Nogami, "Solvothermal synthesis of multiple shapes of silver nanoparticles and their SERS properties," *Journal of Physical Chemistry C*, vol. 111, no. 26, pp. 9095–9104, 2007, doi: 10.1021/jp068859b.
- [196] M. J. Banholzer, J. E. Millstone, L. Qin, and C. A. Mirkin, "Rationally designed nanostructures for surface-enhanced Raman spectroscopy," *Chem Soc Rev*, vol. 37, no. 5, pp. 885–897, 2008, doi: 10.1039/b710915f.

- [197] L. Jensen, C. M. Aikens, and G. C. Schatz, "Electronic structure methods for studying surface-enhanced Raman scattering," *Chem Soc Rev*, vol. 37, no. 5, pp. 1061–1073, 2008, doi: 10.1039/b706023h.
- [198] M. Mulvihill, A. Tao, K. Benjauthrit, J. Arnold, and P. Yang, "Surface-enhanced Raman spectroscopy for trace arsenic detection in contaminated water," *Angewandte Chemie International Edition*, vol. 47, no. 34, pp. 6456–6460, 2008, doi: 10.1002/anie.200800776.
- [199] P. D. O'Neal, G. L. Coté, M. Motamedi, J. Chen, and W.-C. Lin, "Feasibility study using surface-enhanced Raman spectroscopy for the quantitative detection of excitatory amino acids," *J Biomed Opt*, vol. 8, no. 1, p. 33, 2003, doi: 10.1117/1.1528208.
- [200] C. Gu and T. Y. Zhang, "Electrochemical synthesis of silver polyhedrons and dendritic films with superhydrophobic surfaces," *Langmuir*, vol. 24, no. 20, pp. 12010–12016, 2008, doi: 10.1021/la802354n.
- [201] Y. Sun and R. Qiao, "Facile tuning of superhydrophobic states with Ag nanoplates," *Nano Res*, vol. 1, no. 4, pp. 292–302, 2008, doi: 10.1007/s12274-008-8030-7.
- [202] P. R. Sajanlal and T. Pradeep, "Mesoflowers: A new class of highly efficient surface-enhanced Raman active and infrared-absorbing materials," *Nano Res*, vol. 2, no. 4, pp. 306–320, 2009, doi: 10.1007/s12274-009-9028-5.
- [203] P. R. Sajanlal and T. Pradeep, "Electric-field-assisted growth of highly uniform and oriented gold nanotriangles on conducting glass substrates," *Advanced Materials*, vol. 20, no. 5, pp. 980–983, 2008, doi: 10.1002/adma.200701790.
- [204] A. G. Rao and S. P. Mahulikar, "Integrated review of stealth technology and its role in airpower PhD Student, 2 Assistant Professor Department of Aerospace Engineering," no. December 2002, 2018.
- [205] V. Kapur, Stealth Technology and Its Effect on Aerial Warfare, no. 33. 2014.
- [206] J. Anselmo, "State of Stealth," Aviation Week & Space Technology. Accessed: Jun. 09, 2019. [Online]. Available: https://aviationweek.com/site-

- files/aviationweek.com/files/uploads/2017/12/12/State of Stealth FINAL 121317.pdf
- [207] G. Montambaux, "Generalized Stefan-Boltzmann Law," *Found Phys*, vol. 48, no. 4, pp. 395–410, 2018, doi: 10.1007/s10701-018-0153-4.
- [208] G. Overton, "PHOTONICS APPLIED: DEFENSE: IR countermeasures aim for safer flights." Accessed: Nov. 14, 2020. [Online]. Available: https://www.laserfocusworld.com/lasers-sources/article/16548073/photonicsapplied-defense-ir-countermeasures-aim-for-safer-flights
- [209] K. H. Wu, Y. C. Chang, C. C. Yang, Y. J. Gung, and F. C. Yang, "Synthesis, infrared stealth and corrosion resistance of organically modified silicate-polyaniline/carbon black hybrid coatings," *Eur Polym J*, vol. 45, no. 10, pp. 2821–2829, 2009, doi: 10.1016/j.eurpolymj.2009.07.008.
- [210] H. Yu, G. Xu, X. Shen, X. Yan, C. Shao, and C. Hu, "Effects of size, shape and floatage of Cu particles on the low infrared emissivity coatings," *Prog Org Coat*, vol. 66, no. 2, pp. 161–166, 2009, doi: 10.1016/j.porgcoat.2009.07.002.
- [211] H. Yu, G. Xu, X. Shen, X. Yan, and C. Cheng, "Low infrared emissivity of polyurethane/Cu composite coatings," *Appl Surf Sci*, vol. 255, no. 12, pp. 6077–6081, 2009, doi: 10.1016/j.apsusc.2009.01.019.
- [212] T. Wang *et al.*, "Electromagnetic wave absorption and infrared camouflage of ordered mesoporous carbon-alumina nanocomposites," *Microporous and Mesoporous Materials*, vol. 134, no. 1–3, pp. 58–64, 2010, doi: 10.1016/j.micromeso.2010.05.007.
- [213] X. Yan and G. Xu, "Corrosion and mechanical properties of polyurethane/Al composite coatings with low infrared emissivity," *J Alloys Compd*, vol. 491, no. 1–2, pp. 649–653, 2010, doi: 10.1016/j.jallcom.2009.11.030.
- [214] C. Guo, S. Yin, L. Huang, L. Yang, and T. Sato, "Discovery of an excellent IR absorbent with a broad working waveband: Cs x WO 3 nanorods," *Chemical Communications*, vol. 47, no. 31, pp. 8853–8855, 2011, doi: 10.1039/c1cc12711j.

- [215] Y. Xia, Y. Xiong, B. Lim, and S. E. Skrabalak, "Shape-Controlled Synthesis of Metal Nanocrystals: Simple Chemistry Meets Complex Physics?," *Angewandte Chemie International Edition*, vol. 48, no. 1, pp. 60–103, Jan. 2009, doi: 10.1002/anie.200802248.
- [216] D. Paramelle, A. Sadovoy, S. Gorelik, P. Free, J. Hobley, and D. G. Fernig, "A rapid method to estimate the concentration of citrate capped silver nanoparticles from UV-visible light spectra," *Analyst*, vol. 139, no. 19, pp. 4855–4861, 2014, doi: 10.1039/c4an00978a.
- [217] A. Mirzaei, K. Janghorban, B. Hashemi, M. Bonyani, S. G. Leonardi, and G. Neri, "Characterization and optical studies of PVP-capped silver nanoparticles," *J Nanostructure Chem*, vol. 7, no. 1, pp. 37–46, 2017, doi: 10.1007/s40097-016-0212-3.
- [218] J. Liu, J. B. Lee, D. H. Kim, and Y. Kim, "Preparation of high concentration of silver colloidal nanoparticles in layered laponite sol," *Colloids Surf A Physicochem Eng Asp*, vol. 302, no. 1–3, pp. 276–279, 2007, doi: 10.1016/j.colsurfa.2007.02.040.
- [219] C. Wu, X. Zhou, and J. Wei, "Localized Surface Plasmon Resonance of Silver Nanotriangles Synthesized by a Versatile Solution Reaction," *Nanoscale Res Lett*, vol. 10, no. 1, pp. 1–6, 2015, doi: 10.1186/s11671-015-1058-1.
- [220] C. Wang, T. Wang, Z. Ma, and Z. Su, "PH-tuned synthesis of gold nanostructures from gold nanorods with different aspect ratios," *Nanotechnology*, vol. 16, no. 11, pp. 2555–2560, 2005, doi: 10.1088/0957-4484/16/11/015.
- [221] Y. Zhong *et al.*, "Preparation of triangular silver nanoplates by silver seeds capped with citrate-CTA+," *RSC Adv*, vol. 8, no. 51, pp. 28934–28943, 2018, doi: 10.1039/c8ra04554b.
- [222] M. Carboni, L. Capretto, D. Carugo, E. Stulz, and X. Zhang, "Microfluidics-based continuous flow formation of triangular silver nanoprisms with tuneable surface plasmon resonance," *J Mater Chem C Mater*, vol. 1, no. 45, pp. 7540–7546, 2013, doi: 10.1039/c3tc31335b.

- [223] H. Zhang, J. Yang, R. Sun, S. Han, Z. Yang, and L. Teng, "Microfluidics for nanodrug delivery systems: From fundamentals to industrialization," *Acta Pharm Sin B*, vol. 13, no. 8, pp. 3277–3299, Aug. 2023, doi: 10.1016/j.apsb.2023.01.018.
- [224] S. E. Lohse, "Size and shape control of metal nanoparticles in millifluidic reactors," *Physical Sciences Reviews*, vol. 3, no. 11, Nov. 2018, doi: 10.1515/psr-2017-0120.
- [225] S. Marre and K. F. Jensen, "Synthesis of micro and nanostructures in microfluidic systems," Chem Soc Rev, vol. 39, no. 3, p. 1183, 2010, doi: 10.1039/b821324k.
- [226] A. J. Capel, R. P. Rimington, M. P. Lewis, and S. D. R. Christie, "3D printing for chemical, pharmaceutical and biological applications," *Nat Rev Chem*, vol. 2, no. 12, pp. 422–436, Nov. 2018, doi: 10.1038/s41570-018-0058-y.
- [227] P. J. LaNasa and E. L. Upp, "Basic Flow Measurement Laws," in *Fluid Flow Measurement*, Elsevier, 2014, pp. 19–29. doi: 10.1016/B978-0-12-409524-3.00002-2.
- [228] O. Okafor, A. Weilhard, J. A. Fernandes, E. Karjalainen, R. Goodridge, and V. Sans, "Advanced reactor engineering with 3D printing for the continuous-flow synthesis of silver nanoparticles," *React Chem Eng*, vol. 2, no. 2, pp. 129–136, 2017, doi: 10.1039/C6RE00210B.
- [229] V. Singh, "3D-printed device for synthesis of magnetic and metallic nanoparticles," *J Flow Chem*, vol. 11, no. 2, pp. 135–142, Jun. 2021, doi: 10.1007/s41981-020-00124-3.
- [230] A. D. Stroock, S. K. W. Dertinger, A. Ajdari, I. Mezić, H. A. Stone, and G. M. Whitesides, "Chaotic Mixer for Microchannels," *Science* (1979), vol. 295, no. 5555, pp. 647–651, Jan. 2002, doi: 10.1126/science.1066238.
- [231] D. K. Avasthi, Y. K. Mishra, D. Kabiraj, N. P. Lalla, and J. C. Pivin, "Synthesis of metal-polymer nanocomposite for optical applications," *Nanotechnology*, vol. 18, no. 12, 2007, doi: 10.1088/0957-4484/18/12/125604.
- [232] M. N. Siddiqui, H. H. Redhwi, E. Vakalopoulou, I. Tsagkalias, M. D. Ioannidou, and D. S. Achilias, "Synthesis, characterization and reaction kinetics of

- PMMA/silver nanocomposites prepared via in situ radical polymerization," *Eur Polym J*, vol. 72, pp. 256–269, 2015, doi: 10.1016/j.eurpolymj.2015.09.019.
- [233] B. Karthikeyan, M. Anija, and R. Philip, "In situ synthesis and nonlinear optical properties of Au:Ag nanocomposite polymer films," *Appl Phys Lett*, vol. 88, no. 5, pp. 1–3, 2006, doi: 10.1063/1.2168667.
- [234] I. Armentano, M. Dottori, E. Fortunati, S. Mattioli, and J. M. Kenny, "Biodegradable polymer matrix nanocomposites for tissue engineering: A review," *Polym Degrad Stab*, vol. 95, no. 11, pp. 2126–2146, 2010, doi: 10.1016/j.polymdegradstab.2010.06.007.
- [235] M. R. Vengatesan and V. Mittal, "Nanoparticle- and Nanofiber-Based Polymer Nanocomposites: An Overview," pp. 1–38, 2016.
- [236] G. G. Carbone, A. Serra, A. Buccolieri, and D. Manno, "A silver nanoparticle-poly(methyl methacrylate) based colorimetric sensor for the detection of hydrogen peroxide," *Heliyon*, vol. 5, no. 11, p. e02887, 2019, doi: 10.1016/j.heliyon.2019.e02887.
- [237] U. Ali, K. J. B. A. Karim, and N. A. Buang, "A Review of the Properties and Applications of Poly (Methyl Methacrylate) (PMMA)," *Polymer Reviews*, vol. 55, no. 4, pp. 678–705, 2015, doi: 10.1080/15583724.2015.1031377.
- [238] M. A. Awad, A. A. Hendi, K. M. O. Ortashi, A. B. Alanazi, B. A. ALZahrani, and D. A. Soliman, "Greener synthesis, characterization, and antimicrobiological effects of helba silver nanoparticle-PMMA nanocomposite," *Int J Polym Sci*, vol. 2019, 2019, doi: 10.1155/2019/4379507.
- [239] N. Singh and P. K. Khanna, "In situ synthesis of silver nano-particles in polymethylmethacrylate," *Mater Chem Phys*, vol. 104, no. 2–3, pp. 367–372, 2007, doi: 10.1016/j.matchemphys.2007.03.026.
- [240] Y. Deng, Y. Sun, P. Wang, D. Zhang, H. Ming, and Q. Zhang, "In situ synthesis and nonlinear optical properties of Ag nanocomposite polymer films," *Physica E Low Dimens Syst Nanostruct*, vol. 40, no. 4, pp. 911–914, 2008, doi: 10.1016/j.physe.2007.11.018.

- [241] A. Gescher, "Metabolism of N,N-dimethylformamide: Key to the understanding of its toxicity," *Chem. Res. Toxicol.*, 1993.
- [242] A. Panáček *et al.*, "Silver Colloid Nanoparticles: Synthesis, Characterization, and Their Antibacterial Activity," *J Phys Chem B*, vol. 110, no. 33, pp. 16248–16253, Aug. 2006, doi: 10.1021/jp063826h.
- [243] Jr.; O. C. A. C. V. S. K. A. Biswas; H. Eilers; F. Hidden, "Large broadband visible to infrared plasmonic absorption from Ag nanoparticles with a fractal structure embedded in a Teflon AF® matrix," *Appl. Phys. Lett.* 88, 013103, 2006, doi: https://doi.org/10.1063/1.2161401.
- [244] S. K. L. K. J. C. C. K. K. D. W. S. Y.-H. K. C. S. Yoon, "Surface-plasmon resonance of Ag nanoparticles in polyimide," *J. Appl. Phys.* 98, 084309, 2005, doi: https://doi.org/10.1063/1.2106019.
- [245] A. K. Sarychev and V. M. Shalaev, "Electromagnetic field fluctuations and optical nonlinearities in metal-dielectric composites," *Phys Rep*, vol. 335, no. 6, pp. 275–371, 2000, doi: https://doi.org/10.1016/S0370-1573(99)00118-0.
- [246] C. G. Granqvist, "Solar Energy Materials," *Advanced Materials*, vol. 15, no. 21, pp. 1789–1803, 2003, doi: 10.1002/adma.200300378.
- [247] M. Carboni, M. Carravetta, X. L. Zhang, and E. Stulz, "Efficient NIR light blockage with matrix embedded silver nanoprism thin films for energy saving window coating," *J Mater Chem C Mater*, vol. 4, no. 8, pp. 1584–1588, 2016, doi: 10.1039/c6tc00026f.
- [248] H. Kimpton, D. A. Cristaldi, E. Stulz, and X. Zhang, "Thermal performance and physicochemical stability of silver nanoprism-based nanofluids for direct solar absorption," *Solar Energy*, vol. 199, no. January, pp. 366–376, 2020, doi: 10.1016/j.solener.2020.02.039.
- [249] O. Velgosova, L. Mačák, M. Lisnichuk, and M. Vojtko, "Synthesis and Analysis of Polymorphic Silver Nanoparticles and Their Incorporation into the Polymer Matrix," *Polymers (Basel)*, vol. 14, no. 13, p. 2666, Jun. 2022, doi: 10.3390/polym14132666.